



UNIVERSITÀ DEGLI STUDI DI PAVIA
DOTTORATO IN SCIENZE CHIMICHE
E FARMACEUTICHE
XXIX CICLO

Coordinatore: Chiar.mo Prof. Mauro Freccero

COATED GOLD NANO-OBJECTS AS
FLEXIBLE TOOLS FOR BIOLOGICAL
APPLICATIONS

Tutore

Chiar.mo Prof. Angelo Taglietti

Tesi di Dottorato di

BARBARA BASSI

a.a. 2015- 2016

SUMMARY

CHAPTER 1: INTRODUCTION	6
1.1 NANOCHEMISTRY AND NANOPARTICLES	7
1.2 GOLD NANOPARTICLES	10
1.3 ANISOTROPIC GOLD NANOPARTICLES	15
1.3.1 GOLD LSB-NANOSTAR (GNS)	21
1.3.2 TRITONX-100 SHRINKED NANOSTAR (SGNS)	30
1.4 OPTICAL PROPERTIES OF NANOSTARS	35
1.5 SURFACE-ENHANCED RAMAN SCATTERING (SERS)	38
1.5.1 ELECTROMAGNETIC ENHANCEMENT	40
1.5.2 CHEMICAL ENHANCEMENT	43
1.5.3 ENHANCEMENT FACTOR	45
1.6 PHOTOTHERMAL EFFECT	48
CHAPTER 2: GNSs GRAFTED ON GLASS: SILICA COATING	51
2.1 ANTIBACTERIAL APPLICATION	52
2.1.1 INTRODUCTION	52
2.1.2 EXPERIMENTAL DETAIL: SYNTHESIS AND CHARACTERIZATION	56
2.1.2.1 MATERIALS AND INSTRUMENTATION	56
2.1.2.2 GLASSWARE PRE-TREATMENT	58
2.1.2.3 PREPARATION AND CHARACTERIZATION OF GLASSES	58
2.1.3 RESULT AND DISCUSSIONS	65
2.1.3.1 CHARACTERIZATION	65
2.1.3.2 PHOTOTHERMAL RESPONSE	77
2.1.3.3 ANTIMICROBIAL ACTIVITY	82
2.1.3.4 CONCLUSION	87
2.2 SERS CHIPS	89
2.2.1 INTRODUCTION	89
2.2.2 EXPERIMENTAL DETAIL: SYNTHESIS AND CHARACTERIZATION	95
2.2.2.1 MATERIALS AND INSTRUMENTATION	95
2.2.2.2 GLASSWARE PRE-TREATMENT	96

2.2.2.2	PREPARATION AND CHARACTERIZATION OF SERS CHIPS	97
2.2.3	RESULT AND DISCUSSIONS	99
2.2.3.1	GNSs MONOLAYER ON GLASS	99
2.2.3.2	COATING WITH SILICA	103
2.2.3.3	SERS MEASURES: A PROOF OF CHEMICAL STABILITY OF CHIPS	106
2.2.3.4	EFFECT OF THICKNESS OF SILICA COATING ON SERS RESPONSE.....	108
2.2.3.5	TESTING REUSABILITY	120
2.2.3.5	CONCLUSION	121
 CHAPTER 3: GNSs: ADDING FUNCTIONS WITH TAILORED COATING		122
 3.1 SENSING Pb.....		123
3.1.1	INTRODUCTION	123
3.1.2	EXPERIMENTAL DETAIL: SYNTHESIS AND CHARACTERIZATION	128
3.1.2.1	MATERIALS AND INSTRUMENTATION	128
3.1.2.2	GLASSWARE PRE-TREATMENT	129
3.1.2.3	PREPARATION AND CHARACTERIZATION OF THE SENSORY SYSTEM	129
3.1.3	RESULT AND DISCUSSIONS	132
3.1.3.1	COATING OF GNSs WITH GLUTATHIONE	132
3.1.3.2	BEHAVIOUR OF GNSs-GSH WITH METAL CATIONS: Pb ²⁺ DETECTION	135
3.1.3.3	CONCLUSION	146
 3.2 TAILORING OF GNS SURFACE FOR SERS TAG		148
3.2.1	INTRODUCTION	148
3.2.2	EXPERIMENTAL DETAIL: SYNTHESIS AND CHARACTERIZATION	159
3.2.2.1	MATERIALS AND INSTRUMENTATION	159
3.2.2.2	GLASSWARE PRETRATMENT	160
3.2.2.3	PREPARATION AND CHARACTERIZATION OF COATED GNSs	160
3.2.3	RESULT AND DISCUSSIONS	164
3.2.3.1	NATIVE GNSs CHARACTERIZATION	164
3.2.3.2	GNSs TITRATION	164
3.2.3.3	CHARACTERIZATION OF GNSs COATED WITH MIXED MONOLAYERS	167
3.2.3.4	PAH COATING OF GNSs COATED WITH MIXED MONOLAYERS	171
3.2.3.5	SERS MEASUREMENTS ON COLLOIDAL SUSPENSIONS OF GNSs	173
3.2.3.6	BIOCOMPATIBILITY STUDIES	177
3.2.3.7	SERS IMAGING IN CELLS.....	178

3.2.3.8 CONCLUSION	181
3.3 SERS TAGS AS THERANOSTIC DEVICES	183
3.3.1 INTRODUCTION	183
3.3.2 EXPERIMENTAL DETAIL: SYNTHESIS AND CHARACTERIZATION	187
3.3.2.1 MATERIALS AND INSTRUMENTATION	187
3.3.2.2 GLASSWARE PRE-TREATMENT	188
3.3.2.3 PREPARATION AND CHARACTERIZATION OF THERANOSTIC DEVICE	188
3.3.3 RESULT AND DISCUSSION	193
3.3.3.1 NATIVE GNSS AND SHRINKED GNSS	193
3.3.3.2 TITRATION OF GNSS AND sGNSS WITH HS-PEG₃₀₀₀-NH₂	194
3.3.3.3 COATING WITH A MIXED MONOLAYER OF HS-PEG₃₀₀₀-NH₂ AND MMC	196
3.3.3.4 RELATIONSHIP BETWEEN Z POTENTIAL AND PH	200
3.3.3.5 EVALUATION OF SERS RESPONSE OF THE SERS TAG	203
3.3.3.6 FUNCTIONALIZATION WITH FOLIC ACID	204
3.3.3.7 RELATIONSHIP BETWEEN Z POTENTIAL AND PH OF FINAL SERS TAG	207
3.3.3.8 FT-IR CHARACTERIZATION	209
3.3.3.9 SERS RESPONSE AFTER FUNCTIONALIZATION WITH FOLIC ACID	210
3.3.3.10 TEM CHARACTERIZATION OF sGNS SERS TAGS	212
3.3.3.11 AN ALTERNATIVE PATHWAY: REACTION BETWEEN HS-PEG-NH₂ AND FOLIC ACID FOR SUBSEQUENT FUNCTIONALIZATION OF GNSS	213
3.3.3.12 EVALUATION OF THE PHOTOTHERMAL EFFECT	214
3.3.3.13 CYTOTOXICITY OF SERS TAG	217
3.3.3.14 IMAGING OF HELA CELLS WITH GNSS SERS TAGS	218
3.3.3.15 IMAGING OF HELA CELLS WITH SHRINKED GNSS SERS TAGS	220
3.3.3.16 IMAGING HELA CELLS IN ABSENCE OF FOLIC ACID	222
3.3.3.17 IMAGING OF DI TCN1 CELLS WITH GNS SERS TAGS	223
3.3.3.18 EVALUATION OF THE PHOTO-THERMAL EFFECT ON HELA CELLS	225
3.3.3.20 CONCLUSION	227
CHAPTER 4: CONCLUSIONS	229

Note to the reader: in order to make this document more easy to read, the numbering of references, figures, tables and equations is started from the beginning for every independent section (introduction, chapters 2.1, 2.2, 3.1, 3.2, 3.3). For the same reasons some repetitions (for example in the experimental sections) were needed.

CHAPTER 1: INTRODUCTION

1.1 NANOCHEMISTRY AND NANOPARTICLES

In 1999, the National Science and Technology Council of the USA (STFC), one of USA's largest multidisciplinary research organisations, presented a nanotechnology's action plan and designated the 21st century as the century of nanosciences.¹ In recent years, nanotechnology has been embraced by industrial sectors due to its applications in the fields of electronic storage systems,² biotechnology,³ magnetic separation and preconcentration of target analytes, targeted drug delivery,^{4,5} and vehicles for gene and drug delivery.⁶ Nanotechnology is closely related to nanoscience, that concerns the study of materials and structures on the scale of nanometers. Nanoscale structures have existed in nature long before scientists began studying them in laboratories, for example: a single strand of DNA, the building block of all living things, is about three nanometers wide; the scales on a morpho butterfly's wings contain nanostructures that change the way light waves interact with each other, giving the wings brilliant metallic blue and green hues; peacock feathers and soap bubbles also get their iridescent coloration from light interacting with structures just tens of nanometers thick. The essence of nanoscience is the ability to work on these levels in order to generate larger structures with fundamentally new molecular organization. Why work on nanostructures? Because almost all of the atoms in a nanostructure are on the surface. This aspect implicates particular chemical and physical properties that differ from individual molecules or bulk material. In order to create this kind of structures a relatively new branch of chemistry was born: the nanochemistry. In 1991, Geoffrey Ozin⁷, a pioneer in this field, created the notion of "nanochemistry" generating one of the most cited concept articles in the field of materials science. He described the field as "*an emerging subdiscipline of solid-state chemistry that emphasizes the synthesis rather than the engineering aspects of preparing little pieces of matter with nanometer sizes in one, two or three dimensions. The nanochemist can be considered to work towards this goal from the atom 'up', whereas the nanophysicist tends to operate from the bulk 'down'*". In other words nanochemistry is an active new field that deals with confinement of chemical products that are of nanometer dimensions, the challenge is to be able to use chemical approaches that would reproducibly provide a precise control of composition, size and shape of the nano-objects

¹ M. Antonietti; K. Landfester; Y. Mastai; *Israel Journal of Chemistry*, **2001**, 41, 1-5.

² Y.S. Kang; S. Risbud; J.F. Rabolt; P. Stroeve; *Chem. Mater.*, **1996**, 8, 2209–2211.

³ Q.A. Pankhurst; J. Connolly; S.K. Jones; J. Dobson; *J. Phys. D. Appl. Phys.*, **2003**, 36, R167.

⁴ J. Dobson; *Gene Ther.*, **2006**, 13, 283–287.

⁵ S. Rudge; C. Peterson; C. Vessely; J. Koda; S. Stevens; L. Catterall; *J. Control. Release*, **2001**, 74, 335–340.

⁶ T. Appenzeller; *Science*, **1991**, 254, 1300.

⁷ G.A. Ozin; *Advanced Material*, **1992**, 4, 10, 612–649.

formed.⁸ An important class of nano-materials are nanoparticles (NP). In nanotechnology, a nanoparticle is defined as an ultrafine particle with lengths in two or three dimensions greater than 1 nm and smaller than 100 nm. The research in this field is currently very dynamic due to a wide variety of potential applications in biomedical, optical and electronic fields. Attractive and important features of nanoparticles are: i) their surface area to volume ratio, which is much larger than in a bulk material; surface atoms on the surface of a material are more reactive than those in the centre, so the material is more reactive; ii) nanoparticles may have their surface modified, depending on the presence of reactants and adsorbing compounds, which may instantaneously change with changing compounds and thermodynamic conditions; iii) last but not least, nanoparticles have a large and functional surface that can bind, adsorb and carry other compounds. On the other hand, a nanoparticles has a surface chemically more reactive compared to their bulk analogues. There are different kinds of nanoparticles that suit different purposes. The composition of engineered nanoparticles may vary, source materials may be of biological origin like lipids, phospholipids, chitosan, or have chemical origin like polymers, silica and noble metals as gold, silver and copper.

Two approaches have been developed in the preparation of nanoparticles (summarized in Figure 1): the first one is the top-down method, which consists in an external force applied to a solid that leads to its break-up into smaller particles; the second one is the bottom-up method, which implies that the nanostructures are synthesized onto the substrate by stacking atoms onto each other, giving rise to crystal planes further stack onto each other, resulting in the synthesis of the nanostructures. A bottom-up approach can thus be viewed as a synthetic approach where the building blocks are added onto the substrate in order to form the nanostructures material.⁹

⁸ M. Antonietti; C.G. Göltner; *Angewandte Chemie International Edition*, **1997**, 36, 910.

⁹ S. Horikoshi; N. Serpone; *Microwaves in Nanoparticle Synthesis: Fundamentals and Applications*, Wiley-VCH Verlag GmbH & Co., **2013**.

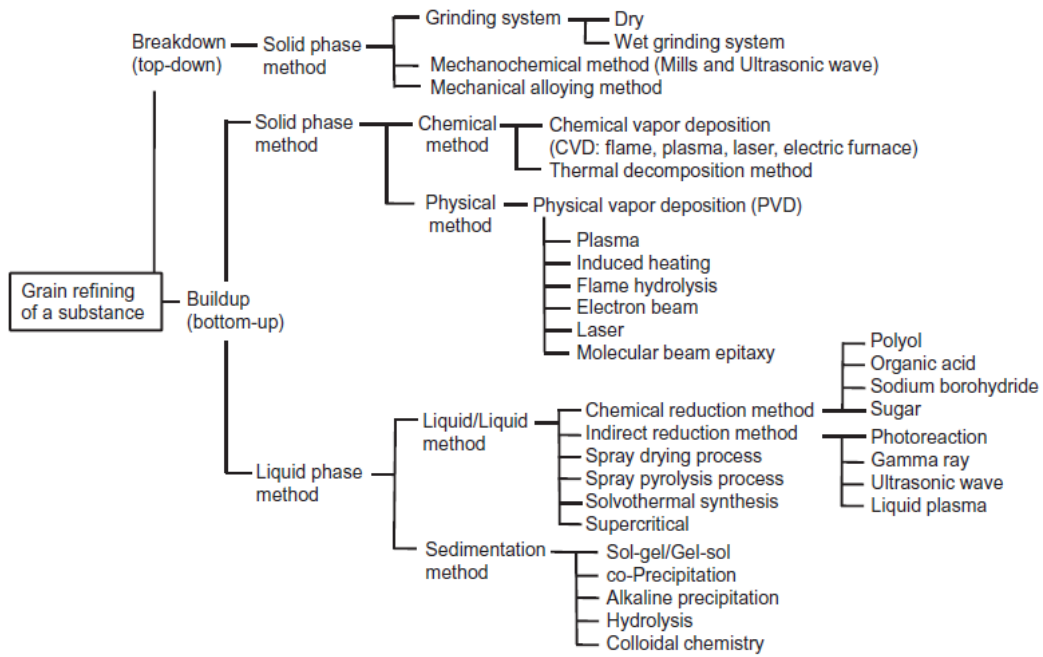


Figure 1: common synthetic method for bottom up and top down approaches.⁹

The bottom-up approach is more advantageous than the top-down, because the former has a better chance of producing nanostructures with less defects, more homogenous chemical composition, and better short- and long-range ordering. All the preparations carried out in this work belong to the bottom-up approach.

1.2 GOLD NANOPARTICLES

Colloidal gold, also known as gold nanoparticles (AuNP), is a term used for a suspension of nanometer-sized particles of gold. The history of these colloidal solutions dates back to Roman times when they were used to stain glass for decorative purposes.¹⁰ The modern era of AuNP synthesis began over 150 years ago with the work of Michael Faraday, when he observed that the colloidal gold solutions have properties that differ from the bulk gold.^{11,12}



Figure 2: a slide used by Faraday in his lecture on gold sols, in 1858.

The preparation of gold sol that Faraday studied was ruby-red in colour as shown in Figure 2. He described the colloid in these terms: "*part of the gold is reduced in exceedingly fine particles, which becoming diffused, produce a beautiful ruby fluid*". He could not explain the reason why changing the size of the gold particles altered the colour, but described his work as "*a useful experimental entrance into certain physical investigations respecting the nature and action of a ray of light*".¹³ Now we know that the optical properties reported by Faraday are due to the interaction of gold nanoparticles with light. This phenomenon arises from a resonant oscillation of free electrons of the surface atoms in the presence of light, also known as Localized Surface Plasmon Resonance (LSPR, described in detail in Chapter 1.5).¹⁴ Spherical gold nanoparticles, with particle diameter of 15 nm, show an absorption maximum at 520 nm in aqueous solution due to their LSPR (Figure 3b).

There are many reasons for choosing this kind of nanoparticles as a smart material for several tasks. Just to cite a few: i) gold is known for being chemically inert, so AuNPs are

¹⁰ D.A. Giljohann; D.S. Seferos; W.L. Daniel; M.D. Massich; P.C. Patel; C.A. Mirkin; *Angewandte Chemie International Edition*, **2010**, 49, 3280-3294.

¹¹ M.A. Hayat; *Academic Press*, **1989**.

¹² P.P. Edwards; J.M. Thomas; *Angewandte Chemie*, **2007**, 46, 5480-5486.

¹³ M. Faraday; *Philosophical Transactions of the Royal Society of London*, **1847**, 147, 145-181.

¹⁴ P.K. Jain; X.I. Huang; I.H. El-Sayed; M.A. El-Sayed; *Accounts of Chemical Research*, **2008**, 41, 12, 1578-1586.

more stable in respect to other metal nanoparticles, ii) AuNP are resistant to strong oxidizing or highly acidic environment, iii) they can interact with thiol moiety of organic compound, so their surface can be efficiently functionalized to improve stabilization or to insert molecules or receptors for specific purposes.

The synthetic method used to obtain spherical AuNPs was pioneered by J. Turkevich et al. in 1951¹⁵ and refined by G. Frens in the 1973¹⁶ and is the simplest and the best known synthesis of nanoparticles available. This approach uses the chemical reduction of small amounts of hot solution of gold salts such as hydrogen tetrachloroaurate (HAuCl₄), using sodium citrate as reducing and capping agent. This method produces monodisperse spherical gold nanoparticles in the range of 10–20 nm in diameter (Figure 3a).

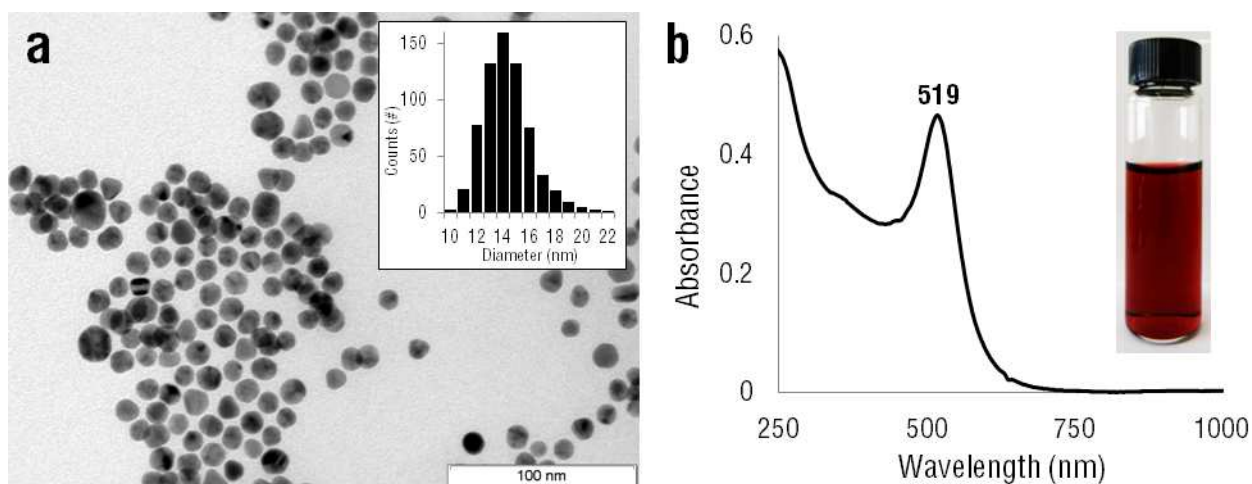


Figure 3: a) TEM image and size distribution histogram (inset) showing an average diameter of ~15 nm. b) UV-Vis spectra of the synthesized gold nanoparticles with a characteristic surface plasmon resonance peak at 519 nm and a representative photograph of the same nanoparticles (inset).

The progress made in nanochemistry allowed the synthesis of nanoparticles of different shapes, known as "anisotropic nanoparticles".

The chemical growth of this kind of nano-objects consists in a crystallization of a solid phase from a solution. There is a known solubility for a solute in a particular solvent, whereby addition of any excess solute will produce formation of nanocrystals: this phenomenon is called nucleation; therefore, in order to obtain nucleation, the solution must be supersaturated: this condition can be obtained by directly dissolving the solute

¹⁵ J. Turkevich; P.C. Stevenson; J. Hillier; *Discuss. Faraday Soc.*, **1951**, 11, 55–75.

¹⁶ G. Frens; *Colloid & Polymer Science*, **1972**, 250, 736–741.

at high temperature and the cooling to low temperatures, or by adding the necessary reactants during the reaction¹⁷. There are three type of nucleation: homogeneous, heterogeneous and secondary nucleation.¹⁸ Homogeneous nucleation take place in absence of a solid interface by combining solute molecules to give nuclei: the driven force is the thermodynamics of the process, in fact the super-saturated solution is not stable in energy. The overall free energy variation is the total amount of the free energy due to the formation of a new volume (favourable contribution) and the free energy due to the new surface created (unfavourable contribution).

In the case of the spherical particles the free energy variation can be calculated thanks to this equation:

$$\Delta G = - \frac{4}{3} \pi r^3 K_B T \ln(S) + 4\pi r^2 \gamma \quad (1)$$

where V is the volume of the crystallized species, r is the radius of the nuclei, K_B is the Boltzmann constant, S is the saturation ratio and γ is the surface free energy per unit area. When $S > 1$, ΔG has a maximum at the critical size r^* . This maximum free energy is the activation energy for nucleation phenomenon. The critical nuclei size r^* can be obtained by setting $d\Delta G/dr=0$:

$$r^* = \frac{2V\gamma}{3K_B T \ln(S)} \quad (2)$$

For a given value of S, all particles with $r > r^*$ will grow and all particles with $r < r^*$ will dissolve. The higher is the saturation ratio the smaller the critical nuclei size r^* is. Homogeneous nucleation continues until the concentration of the reactants drops below the critical level. Then heterogeneous nucleation occur, with the addition of new material on the pre-formed nuclei. At this stage, the smaller particles grow more rapidly than the larger ones because the free energy driving force is larger for smaller particles than for larger particles, so focusing in size occurs. However, continuing with the reaction, the saturation ratio decreases and consequently r^* increases. At this stage the larger particles continue to grow and the smaller ones get smaller and finally dissolve: this is the so called ‘‘Ostwald ripening’’ or defocussing. Once the reaction goes into this stage it is difficult to get monodisperse particles.

From an experimental point of view, to obtain monodisperse samples it is necessary either to quickly interrupt the process of growth (for example decreasing temperature) or

¹⁷ C.B. Murray; C.R. Kagan; M.G. Bawendi; *Annual Review of Materials Research*, **2000**, 30, 545-610.

¹⁸ C. Burda; X. Chen; R. Narayanan; M.A. El-Sayed; *Chemical Reviews*, **2005**, 105, 1025-1102.

to provide reactants continuously so to maintain saturation regime during all the reaction.

In addition, particles can grow by aggregation with other particles: this process is called secondary growth. Secondary growth is the most important cause of thermodynamic instability in colloidal solution (the rate of particle growth by aggregation is much larger than that by molecular addition).

In order to produce stable nanoparticles, usually the synthetic step is followed by a functionalization step in order to stabilize the surface of the nano-objects, alternatively, sometimes is possible to introduce the capping agent directly during the synthetic reaction.^{19,20}

When crystal growth is under thermodynamic control, surface energy plays a crucial role in determining the morphology of gold nanocrystals since the surface area-to-volume ratio is high for nanoparticles, and a crystal at the equilibrium tends to have the lowest surface energy for a given volume of material. Isotropic growth of nanocrystals is preferred under thermodynamic control, because the sphere is the morphology associated to the low surface energy. For this reason, obtaining an anisotropic growth requires some fine expedients for moving from a spherical morphology to asymmetric nanoparticles. Available shape of gold nanoparticles are for example: spherical, rod, triangular, polygonal rods, stars ect.^{21,22,23}

The properties and applications of colloidal gold nanoparticles also depend upon their shape (as described in detail in Chapter 1.3). Moreover, the gold surface offers a unique opportunity to conjugate ligands such as oligonucleotides, proteins, and antibodies containing functional groups such as thiols, mercaptans, phosphines, and amines, which demonstrates a strong affinity for gold surface.²⁴ The realization of such gold nanoconjugates coupled with LSPR gold nanoparticles have found applications in simple but powerful imaging techniques such as dark-field imaging, Surface Enhancement Raman Spectroscopy (SERS), and optical imaging for the diagnosis of various disease states.²⁵ These are not the only applications of nanoparticles: in fact, many examples

¹⁹ M. Benkovičová; K. Vegso; P. Siffalovic; M. Jergel; E. Maj-ova; S. Luby; A. Sa-ta; *Chemical Papers*, **2013**, 67, 9, 1225–1230.

²⁰ F. Dumur; A. Guerlin; E. Dumas; D. Bertin; D. Gignes; C.R. Mayer; *Gold Bulletin*, **2011**, 44, 119-137.

²¹ N.R. Jana; L. Gearheart; C.J. Murphy; *Adv Mater.*, **2001**, 13, 1389–1393.

²² N.R. Jana; L. Gearheart; C.J. Murphy; *J. Phys. Chem. B*, **2001**, 105, 4065–4067.

²³ K. Subrata; P. Sudipa; P. Snigdhamayee; B. Soumen; K.G. Sujit; P. Anjali; *Nanotechnology*, **2007**, 18, 075712

²⁴ A.P. Alivisatos; K.P. Johnsson; X. Peng; T.E. Wilson; C.J. Loweth; M.P. Bruchez; *Nature*, **1996**, 382, 609–611.

²⁵ I.H. El-Sayed; X. Huang; M.A. El-Sayed; *Nano Lett.*, **2005**, 5, 829-834.

exist of highly sensitive and selective assays based upon gold nanoconjugates. In recent years, nanotechnological research focus has turned to therapeutic possibilities for such materials (as shown in Figure 4): gene-regulating agents, drug carriers, imaging agents, and photoresponsive therapeutics in many debilitating diseases have been widely investigated.²⁶

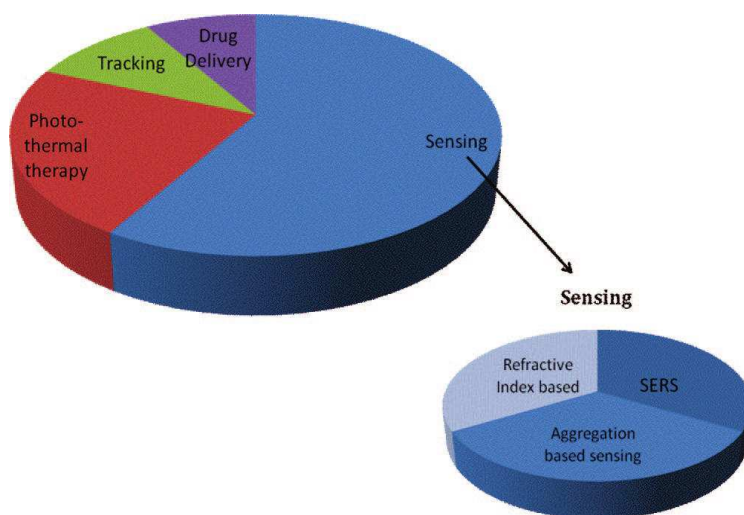


Figure 4: pie chart depicting the different biomedical applications of gold nanoparticles.²⁶

²⁶ C.J. Murphy; A.M. Gole; J.W. Stone; P.N. Sisco; A.M. Alkilany; E.C. Goldsmith; S.C. Baxter; *Accounts of Chemical Research*, **2008**, 41, 12, 1721-1730.

1.3 ANISOTROPIC GOLD NANOPARTICLES

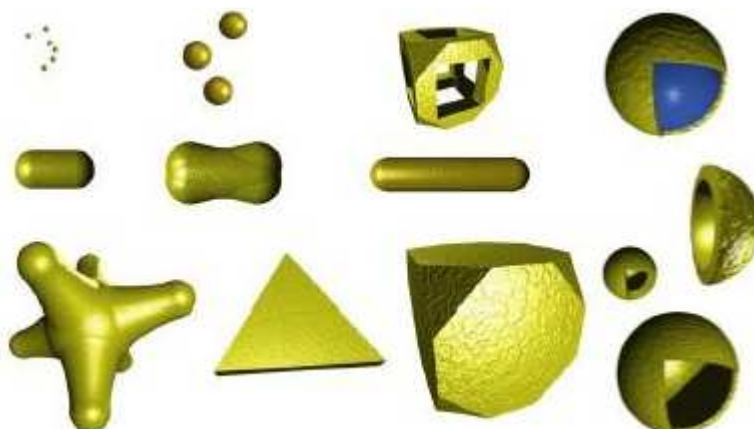


Figure 5: different shapes of gold nanoparticles.

Anisotropic gold nanoparticles are of considerable current interest, due to various shape-dependent properties (examples of different shape are shown in Figure 5).^{27,28} Controlling the length-to-width ratio and the uniformity of the length and width distributions of metal nanoparticles, as well as synthesizing particles with a width dimension below 10 nm, is a quite challenging task when using large-scale bench top methods.²⁹ Anyway, solution-based approaches can be successful for the synthesis of anisotropic nanoparticles.³⁰ Such syntheses need a really fine control of growth conditions, and key parameters in shape control are: i) control of nucleation and growth, restricting the size to the nanometer regime; ii) maintaining a high monomer concentration that induces better stability of anisotropic nanoparticle embryos, and iii) use of a suitable surfactant or capping agent that selectively adsorbs on specific planes of growing particles.

The simplest approaches for anisotropic nanoparticle synthesis rely on various surfactant-based methods.²⁷ Our experience in the synthesis of anisotropic nanoparticles takes inspiration from the one of gold nanorods³¹ (AuNRs, the most simple and the more investigated kind of anisotropic gold nanoparticle) which exploit a modified surfactant-based El-Sayed's protocol.³² This kind of approach is called "seed-growth" and is a popular example of synthesis of AuNRs, which are the most simple and the more investigated kind of anisotropic gold nanoparticle. AuNRs exhibit two absorption bands,

²⁷ M.A. El-Sayed; *Acc. Chem. Res.*, **2001**, 34, 257–264.

²⁸ N. R. Jana; *Angew. Chem.*, **2004**, 116, 1562–1566;

²⁹ T.S. Ahmadi; Z.L. Wang; T.C. Green; A. Henglein; M.A. El-Sayed; *Science*, **1996**, 272, 1924–1926.

³⁰ Y. Sun; B. Mayers; T. Herricks; Y. Xia; *Nano Lett.*, **2003**, 3, 955–960.

³¹ A. Donà; Synthesis and functionalization of anisotropic gold nanoparticles; *Doctorate Thesis in Chemistry*, **2013-2014**.

³² B. Nikoobakht; M.A. El-Sayed; *Chemistry of Materials*, **2003**, 15, 1957-1962.

one at 510 – 530 nm (related to the transversal electron oscillation) and another in the 750 – 1100 nm near-infrared (nIR) range (related with the longitudinal electron oscillation): this band λ_{\max} is strongly influenced by the aspect ratio (AR) and directly proportional to it. As AuNRs efficiently convert the absorbed nIR radiation into heat, and as in the nIR blood, skin, and tissues are semitransparent, in vivo applications of gold NRs for photothermal therapy against tumors³³ and multidrug-resistant bacterial infections³⁴ have been considered.

Usually, rod-shaped metal nanoparticles are synthesized in rigid templates or in the presence of surfactants, in the former case metal ions are reduced inside cylindrical pores of oxide³⁵ or polymeric membranes.³⁶ In the latter method, neutral or charged surfactants are used for growth of the nanoparticles.³⁷ In non-aqueous media, surfactants such as tetraoctylphosphine oxide and oleic acid have been used to grow cobalt nanorods in the direction parallel to the {101} planes.³⁸ In aqueous media, hexadecyltrimethylammonium bromide (CTAB, Figure 6) has been one of the most popular molecules used in the synthesis of metal nanoparticles, although so far this has been limited to only gold and silver.³⁹

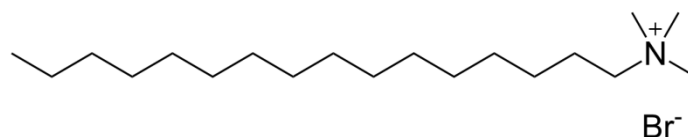


Figure 6: hexadecyltrimethylammonium bromide's (CTAB) structure.

As already mentioned in Chapter 1.2, the first step in the formation of the nanocrystals is nucleation, which consists in the crystallization of solid nuclei from a solution. Nuclei further evolve into seeds⁴⁰ which, in specific conditions, will grow to form nanoparticles with the desired shape. Due to their small size and their continuous evolution in time, very little is known about the nuclei during a synthesis. Seeds can be viewed as nascent,

³³ S. Link; M.A. El-Sayed; *Int. Rev. Phys. Chem.*, **2000**, 19, 409–453.

³⁴ D. Pissuwan; C.H. Cortie; S.M. Valenzuela; M.B. Cortie; *Trends Biotechnol.*, **2010**, 28, 207–213.

³⁵ C.R. Martin; *Chem. Mater.*, **1996**, 8, 8, 1739–1746.

³⁶ T. Thurn-Albrecht; J. Schotter; G.A. Kastle; N. Emley; T. Shibauchi; L. Krusin-Elbaum; K. Guarini; C.T. Black; M.T. Tuominen; T.P. Russel; *Science*, **2000**, 290, 5499, 2126–2129.

³⁷ M. Brust; M. Walker; D. Bethell; D.J. Schiffrin; R.J. Whyman; *Chem. Soc. Chem. Commun.*, **1994**, 801–802.

³⁸ V.F. Puentes; K.M. Krishnan; A.P. Alivisatos; *Science*, **2001**, 291, 5511, 2115–2117

³⁹ Y. Ying; S.S. Chang; C.L. Lee; C.R.C. Wang; J., *Phys. Chem. B*, **1997**, 101, 34, 6661–6664.

⁴⁰ Y. Xia; Y. Xiong; B. Lim; S.E. Skrabalak; *Angew. Chem. Int. Ed.*, **2009**, 48, 60–103.

faceted nanocrystals, larger than the nuclei. Once a cluster has grown past a critical size, in fact, structural fluctuations become so energetically costly that it becomes locked into a well-defined structure. In general, the seeds can be single crystals, single twinned or multiple twinned structures and all of these may co-exist in a typical synthesis. In a one pot synthesis, the seeds are formed *in situ* in the reaction mixture; instead, in a two-step synthesis, the seeds are prepared first and added later into a growth solution. This two-step process is the cited "seed-mediated growth" approach. While the one-pot synthesis is more convenient, the seed-mediated approach effectively isolates seed formation and growth as separate steps, and this is particularly advantageous as the condition necessary for the nucleation are exactly the opposite to those required for the selective growth of facets. The small seed particles are usually generated under conditions of high chemical supersaturation. This conditions are contraindicated for shape control as they ensure rapid growth of all crystal surfaces. For this reason the seed-growth method is more indicated for the shape control of gold nanocrystals, as it allows a rational design of the nanocrystal shape through the choice of seeds structure and growth conditions.

Once the seeds are formed, they can grow in size through the addition of metal atoms; so, the shape of the final crystals is largely determined by the structure of the seeds.

The different structure of the nanorods obtained from El-Sayed and co-workers and Murphy and co-workers can be taken as a typical example of how the structure of the seed influences the final structure of the nanocrystal.⁴¹

⁴¹ X. Huang; S. Neretina; M.A. El-Sayed; *Adv. Mater.*, **2009**, 21, 4880-4910.

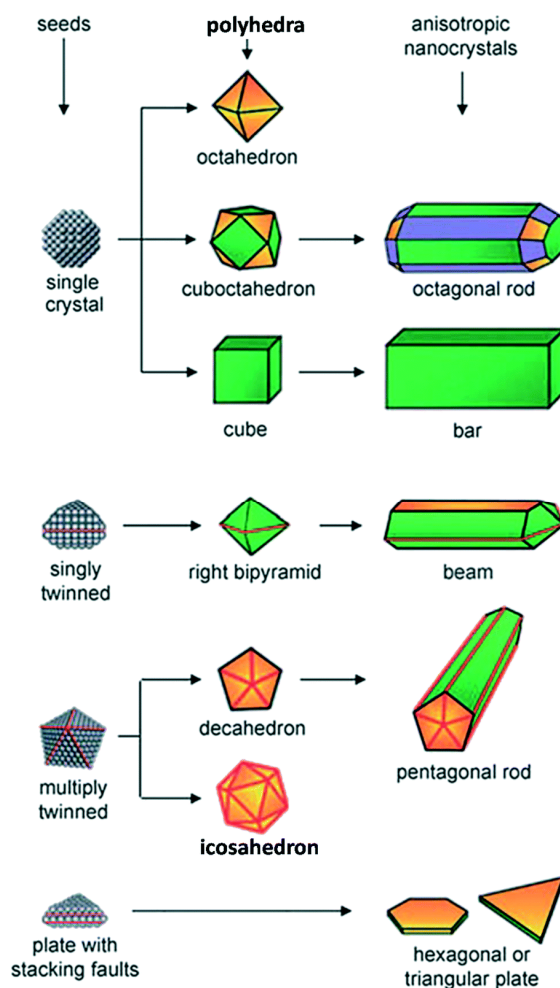


Figure 7: example of a relationship between the structure of the seed and the structure of the nanoparticles.⁴²

In the seed mediated growth method proposed by El-Sayed's group,⁴¹ a growth solution is prepared adding Ag(I), ascorbic acid, a mild reducing agent, to an aqueous CTAB solution of HAuCl₄ to reduce Au(III) to Au(I) following this reaction:



where DHA represent dehydroascorbic acid, the oxidized form of H₂Asc, the L-ascorbic acid.⁴³ This step is followed by the addition of the seed solution of CTAB-capped gold nanoparticle, which catalyse the reduction of Au(III) on the seed surface. The addition of Ag(I) leads to an increase in the yield, aspect ratio and reproducibility of gold nanorods.

⁴² L. Polavarapu; S. Mourdikoudis; I. Pastoriza-Santos; J. Pérez-Juste; *Cryst. Eng. Comm.*, **2015**,17, 3727-3762.

⁴³ M. Luty-Blocho; K. Paclawski; M. Wojnicki; K. Fitzner; *Inorganica Chimica Acta*, **2013**, 395, 189-196.

The seed growth method is the preferential choice in the preparation of gold nanorods and other anisotropic nanoparticles in general. However, it requires a fine control over a high number of parameters, which influence the monodispersity, the yield and the reproducibility of the synthesis. Thanks to the fine control of the synthetic parameters, for example the quantity of ascorbic acid, is possible to tune the aspect ratio of the nano-objects and consequently the LSPR band's position in the UV-Vis-nIR field (Figure 8).

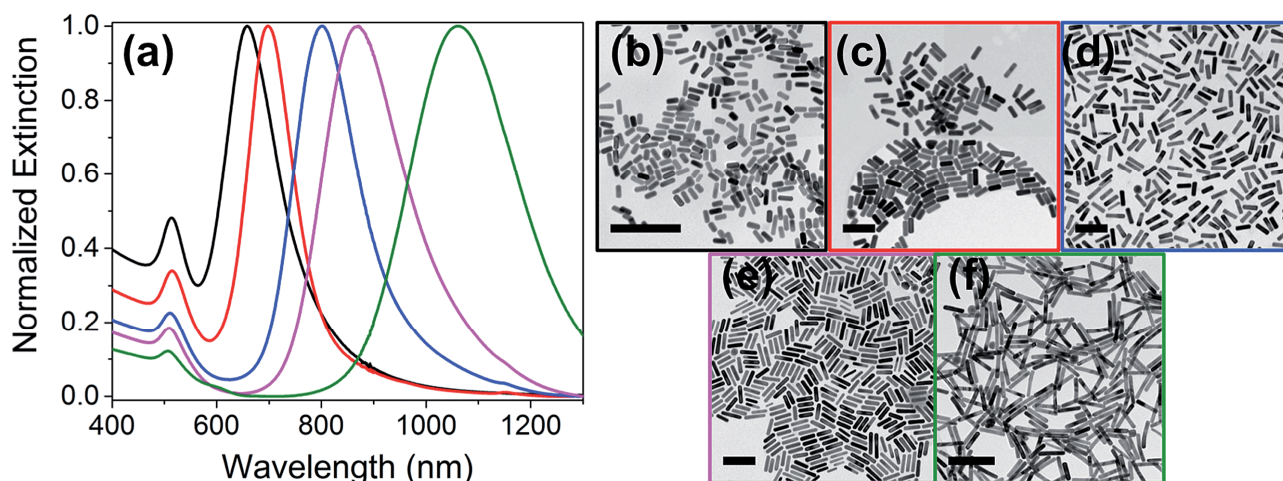


Figure 8: typical TEM images of gold NRs with different plasmon band energies. The scale bar is 50 nm.⁴⁴

The major problem of this kind of “surfactant-based methods” is the cytotoxicity of the surfactant⁴⁵: *in vivo* stability, cytotoxicity and clearance by the immune system are issues to be considered before the application of any kind of nano-object. This issue implies that CTAB has to be completely removed from gold nano-objects before *in vivo* use. Nano-objects can be coated with polyethylene glycol (PEG), which is a non-toxic polymer, to confer stability against aggregation and to prevent macrophage recognition.^{46,47,48,49} In our experimental experience we have noted that it is difficult to completely remove CTAB because it remains strongly linked to the tips of the objects.⁵⁰ This issue is the main reason that lead us to work on the preparation of anisotropic nanoparticles avoiding the use of this problematic surfactant. To prepare gold

⁴⁴ J.G. Hinman; A.J. Stork; J.A. Varnell; A.A. Gewirth; C.J. Murphy; *Faraday Discuss.*, **2016**.

⁴⁵ A.M. Alkilany; P.K. Nagaria; C.R. Hexel; T.J. Shaw; C.J. Murphy; M.D. Wyatt; *Small*, **2009**, 5, 6, 701–708.

⁴⁶ R. Gref; Y. Minamitake; M.T. Peracchia; V. Trubetskoy; V. Torchilin; R. Langer; *Science*, **1994**, 263, 1600–1603.

⁴⁷ S. Stolnik; S.E. Dunn; M.C. Garnett; M.C. Davies; A.G.A. Coombes; D.C. Taylor; M.P. Irving; S.C. Purkiss; T.F. Tadros; S.S. Davis; L. Illum; *Pharmaceutical Research*, **1994**, 11, 1800–1808.

⁴⁸ D. Bazile; C. Prud'Homme; M.T. Bassoulet; M. Marland; M. Spenlehauer; M. Veillard; *Journal of Pharmaceutical Sciences*, **1995**, 84, 493–498.

⁴⁹ D.E. Owens; N.A. Peppas; *International Journal of Pharmaceutics*, **2006**, 307, 93–102.

⁵⁰ B. Thierry; J. Ng; T. Krieg; H.J. Griesser; *Chemical Communications*, **2009**, 1724–1726.

asymmetric nanocrystals with easily removable surfactant, we moved to a zwitterionic surfactant: N,N-dimethyl-3ammonio-1-propanesulfonate (LSB) to a non-ionic surfactant: TritonX-100. The replacement of CTAB with the zwitterionic surfactant LSB in El-Sayed's modified protocol leads to the formation of a mixture of monocrystalline gold nanostars (GNSs) and pentatwinned gold asymmetric nanostars (ANSs) instead of gold nanorods. In the case of replacement with a non-ionic surfactant like TritonX-100, the synthesis lead to the formation of hexapodal gold nanostar (GNSs).

Gold nanostars and in general multibranch gold nano-objects have received a lot of attention in the field of biotechnology. In most cases GNSs were synthesized using modification of the previously reported seed-growth methods for the synthesis of gold nanorods.³² Further examples of modified synthesis is the capping and directing agent with polyvinylpyrrolidone^{51,52,53} or synthesis with other different surfactants like bis-(p-sulfonatophenyl) phenylphosphine dihydrate dipotassium (BSPP)⁵⁴ and sodium dodecyl sulfate (SDS).⁵⁵ There are also seedless and surfactantless synthesis.⁵⁶

The use of branched gold nanoparticles has been designed mainly for sensing applications thanks to their huge surface-enhanced Raman spectroscopy (SERS) enhancement factors^{57,58} and plasmonic photothermal therapy (PPTT)⁵⁹ (these topics will be explained in detail in Chapter 1.5 and 1.6 respectively).

⁵¹ S. Barbosa; A. Agrawal; L. Rodriguez-Lorenzo; I. Pastoriza-Santos; R.A. Alvarez-Puebla; A. Kornowski; H. Weller; L.M. Liz-Marzan; *Langmuir*, **2010**, 26, 14943-14950.

⁵² G.H. Jeong; Y.W. Lee; M. Kim; S.W. Han; *Journal of Colloid and Interface Science*, **2009**, 329, 97-102.

⁵³ M. Yamamoto; Y. Kashiwagi; T. Sakata; H. Mori; M. Nakamoto; *Chemistry of Materials*, **2005**, 17, 5391-5393.

⁵⁴ E. Hao; R.C. Bailey; G.C. Schatz; J.T. Hupp; S. Li; *Nano Letters*, **2004**, 4, 327-330.

⁵⁵ C.H. Kuo; M.H. Huang; *Langmuir*, **2005**, 21, 2012-2016.

⁵⁶ J. Xie; J.Y. Lee; D.I.C. Wang; *Chemistry of Materials*, **2007**, 19, 2823-2830.

⁵⁷ E.S. Allgeyer; A. Pongan; M. Browne; M.D. Mason; *Nano Letters*, **2009**, 9, 3816-3819.

⁵⁸ A. Guerrero-Martinez; S. Barbosa; I. Pastoriza-Santos; L.M. Liz-Marzan; *Current Opinion in Colloid & Interface Science*, **2011**, 16, 118-127.

⁵⁹ H. Yuan; C.G. Khoury; C.M. Wilson; G.A. Grant; A.J. Bennett; T. Vo-Dinh; *Nanomedicine: Nanotechnology, Biology, and Medicine*, **2012**, 8, 1355-1363.

1.3.1 GOLD LSB-NANOSTAR (GNS)

Anisotropic gold nano-objects have been the subject of a large number of papers during the past 15 years, and this is especially true for gold nanorods (AuNRs) after the discovery of their seed-growth synthesis in aqueous solution, developed and improved by El-Sayed and Murphy.⁶⁰ As has been wrote in Chapter 1.3 this powerful and simple technique requires two steps: i) the preparation of tiny spherical gold nanoparticles (size <5 nm) called "seeds" and ii) the addition of a small volume of this seeds to a growth solution, in which Au^{III} complex (AuCl₄) is reduced first to Au^I by a weak reductant, generally ascorbic acid (AA), and then to Au⁰ by the catalytic action of the seeds, in the presence of a surfactant. A typical example of surfactant, used to obtain AuNRs, is CTAB, which adheres preferentially on the highest free-energy facets of the seeds in order to form an interdigitated double layer,⁶¹ thereby leaving the other facets free to add the reduced Au atoms. The crystals grow along preferential directions and cylinder-like NRs are obtained, characterized by their AR. The seed-growth preparation with CTAB⁶² has been used as the standard by many scientists who are interested in the biomedical applications of gold NRs.⁶³ These are directly related to their localized surface plasmon resonance (LSPR), a typical optical feature of this kind of nanoparticles (which are fully discussed in Chapter 1.4). Typically this kind of nanoparticles, have to be coated with *polyethylene glycol* (PEG), a nontoxic polymer, that imparts to the coated nano-objects solubility in water, stability against aggregation, and masks them from macrophage recognition.⁶⁴ Furthermore, CTAB is cytotoxic⁶⁵ so it has to be completely removed from AuNRs before *in vivo* use but, unfortunately, it is very strongly bound to the gold surface.

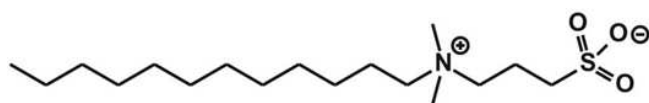


Figure 9: Molecular structure of *N,N*-dimethyl-3ammonio-1-propanesulfonate, LSB.

As has been previuos mentioned, in order to solve this issue our research group developed an alternative seed-growth method in order to prepare gold anisotropic nanoparticles with easily

removable surfactant with a lauryl sulfobetaine zwitterionic surfactant (LSB).⁶⁶

⁶⁰ N.R. Jana; L. Gearheart; C.J. Murphy; *Chem. Commun.*, **2001**, 617–618.

⁶¹ B. Nikoobakht; M.A. El-Sayed; *Langmuir*, **2001**, 17, 6368 – 6374.

⁶² N.R. Jana; L. Geraheart; S.O. Obare; C.J. Murphy; *Langmuir*, **2002**, 18, 922–927.

⁶³ P.K. Jain; I.H. El-Sayed; M.A. El-Sayed; *Nano Today*, **2007**, 2, 18–29.

⁶⁴ R. Gref; Y. Minamitake; M.T. Peracchia; V. Trubetskoy; V. Torchilin; R. Langer; *Science*, **1994**, 263, 1600–1603.

⁶⁵ C.J. Murphy; A.M. Gole; J.W. Stone; P.N. Sisco; A.M. Alkilany; E.C. Goldsmith; S.C. Baxter; *Acc. Chem. Res.*, **2008**, 41, 1721–1730.

⁶⁶ A. Casu; E. Cabrini; A. Donà; A. Falqui; Y. Diaz-Fernandez; C. Milanese; A. Taglietti; P. Pallavicini; *Chem. Eur. J.*, **2012**, 18, 9381–9390.

As already sketched, the products of the LSB-directed synthesis are not rod-like nanoparticles, but a mixture of branched nanostructures, the so called gold nanostars (GNSs). More in detail, by using LSB we obtain a mixture of monocrystalline gold nanostars (MNSs) and pentatwinned gold asymmetric nanostars (ANSs) (see Figure 10-11).

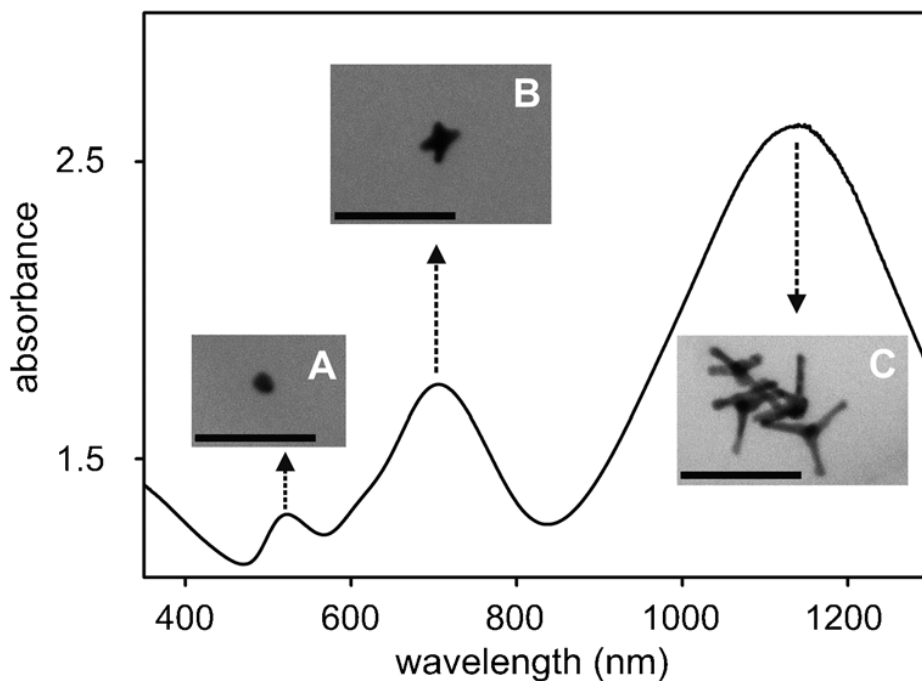


Figure 10: UV-Vis extinction spectrum of a colloid of GNSs prepared with a modified El Sayed protocol. Insets: TEM images displaying the typologies of the objects that generate A) short, B) intermediate, and C) long LSPR. Scale bar: 100 nm.

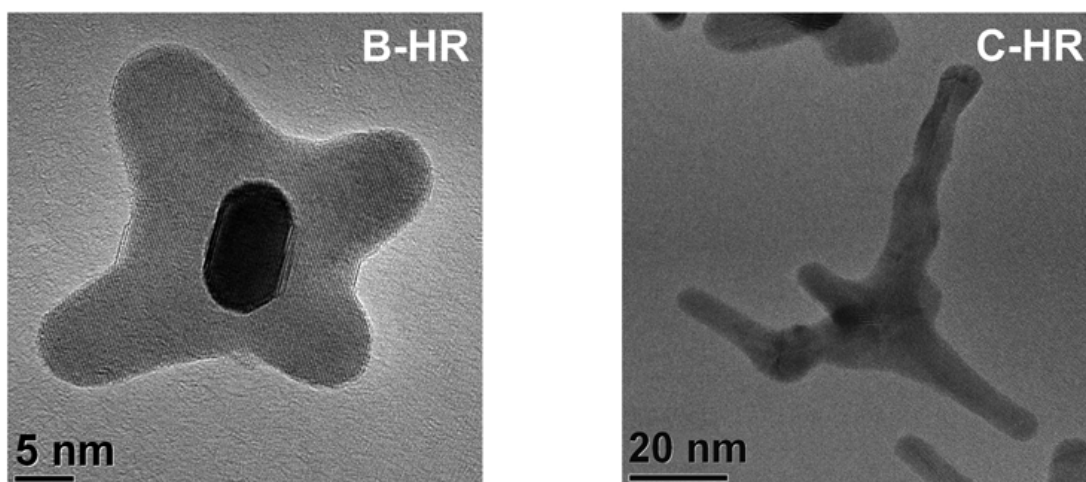


Figure 11: HRTEM images of MNS (B-HR) and ANS (C-HR).

In brief, the modified synthesis consist in two steps: (i) Au nano-seeds are generated from AuCl₄ by means of NaBH₄, reduction in solutions at high LSB concentration, (ii) a few μL of the seeds are added to a growth solution containing LSB at the same concentration of the seed solution, AuCl₄, Ag⁺, and a variable concentration of ascorbic acid.⁶⁶ The growth process is fast and completion is obtained in less than 60 min, generating an intensely blue coloured colloid. The Au^{III} to GNSs conversion yield is 60 – 70%.

The general appearance of the final extinction spectrum (Figure 10) is a three-band profile with a weak “short” band centered at 520 - 530 nm, an “intermediate” band that falls in the 690 - 720 nm range, and a “long” band, usually the most intense, that falls in the 750 - 1150 nm range. The short band can be attributed to two contributions: the first has to be ascribed to the presence of almost spherical nano-objects of 15 - 20 nm diameter, whereas the second one is characteristic of gold nanostars, and it has been attributed to a dipolar resonance localized at the central particle core;⁶⁷ both contributions coexist. The “intermediate” band owes itself to the first kind of anisotropic objects, the regular monocrystalline nanostars (MNSs) equipped with large branches. This observation is consistent with previously reported literature in comparison with the monocrystalline nanostars described by other authors.^{68,69} Finally, the “long” band can be ascribed to pentatwinned nanostar (ANSs), which are characterized by narrow long branches of high aspect ratio (Figure 12).⁷⁰

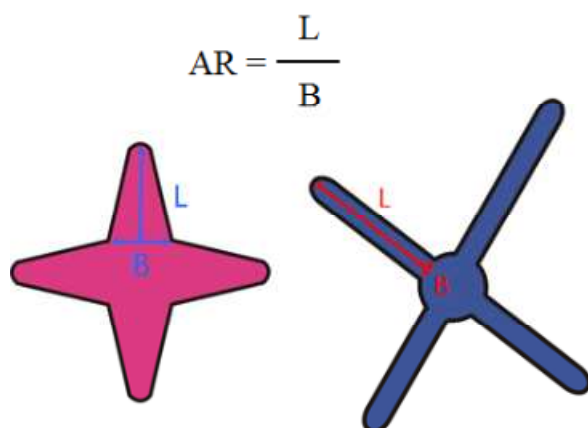


Figure 12: schematic representation of MNS and ANS and of the definition of Aspect Ratio.

⁶⁷ F. Hao; C.L. Nel; J.H. Nordlander; *Nano Lett.*, **2007**, 7, 729-732.

⁶⁸ J. Xie; J.Y. Lee; D.I.C. Wang; *Chem. Mater.*, **2007**, 19, 2823-2830.

⁶⁹ Q. Su; X. Ma; J. Dong; C. Jiang; W. Qian; *Appl. Mater. Interfaces*, **2011**, 3, 1873-1879.

⁷⁰ C.G. Khoury; J. Vo-Dinh; *J. Phys. Chem. C*, **2008**, 112, 18849-18859.

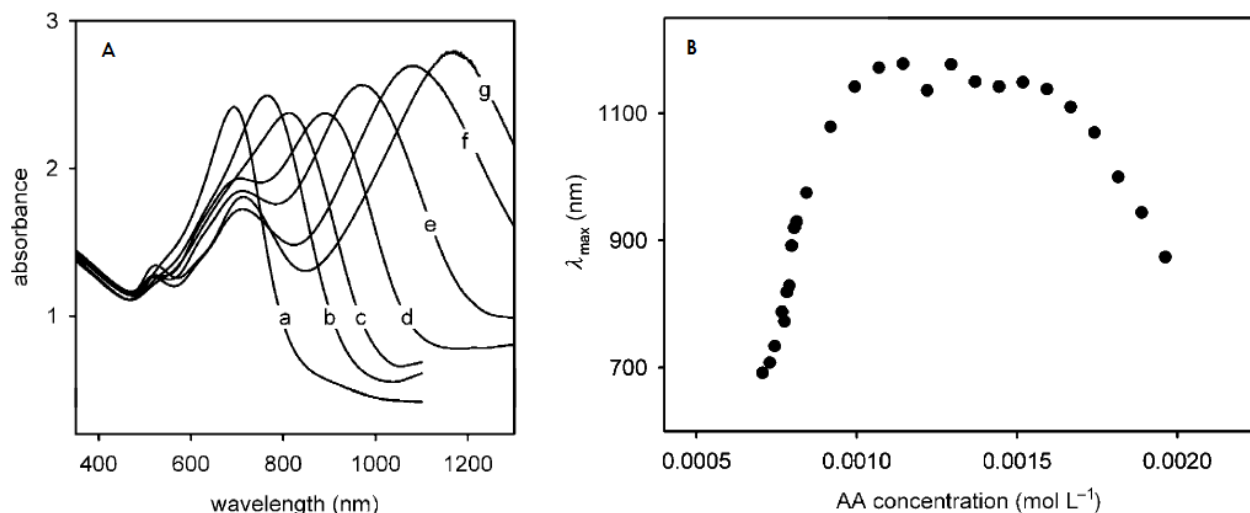


Figure 13: A) series of UV-Vis spectra from preparations obtained in 0.1M LSB by varying the AA concentration in the growth solution. B) Position of the long LSPR maximum for the same series of preparations as a function of AA concentration.

As shown in Figure 13, given a constant LSB concentration, the variation of the amount of ascorbic acid influences the LSPR position in the UV-Vis spectra of the samples, in particular the position of the “long” band ascribed to ANSs. Figure 13 represents the general trend of the position of “long” LSPR band: a three-zone behaviour as a function of ascorbic acid concentration can be observed.

In the first zone, increasing the ascorbic acid concentration leads to a red-shift in the position of the “long” LSPR band. At the beginning the “intermediate” band appears as a shoulder of the “long” band but further incrementing the amount of ascorbic acid in this range, the “intermediate” and “long” bands become separated, because the intermediate band does not significantly change position, while the long band continues to red-shift. The regulation of this synthetic parameter in this range is very interesting because it allows to fine tune the position of “long” LSPR band. In the third zone increasing ascorbic acid shifts back the maximum of the “long” band to shorter wavelengths and the intensity of the band gradually decreases; the intermediate band also shifts to the blue and the absorbance between 500 and 600 nm increases. This suggests that at high concentration of ascorbic acid the formation of isotropic morphologies returns to be favourite over anisotropic growth.

The Ag⁺ concentration used in this synthesis was chosen after the decision to use synthetic conditions as similar as possible to those that led to the highest aspect ratio gold nanorods in the case of CTAB as directing agent. Silver ions are necessary to obtain

anisotropic growth but the mechanism involved in this process is not demonstrate; we propose that the role of this reactant might also be able to decrease the quantity of Cl^- in solution by precipitation of AgCl , thereby disfavoring Cl^- competition with the $-\text{SO}_3^-$ moiety of LSB for the direct interaction with the Au surface of the nanostars.

As already reported, a typical sample of gold nanostars is a mixture of two kind of objects: MNSs and ANSs. HR-TEM of these kind of nanoparticles has already been shown in Figure 11 and these images discloses typical features that can be ascribed to a tridimensional structure of GNSs. The Figure 14 shows an evident darker spot in the center of the MNS, which corresponds to a branch that points towards the observer (a sixth branch may be hidden behind the structure). The generation of these anisotropic objects is due to the ability of LSB to bind and selectively protect the $\{111\}$ face of the gold lattice,⁶⁶ whereas CTAB bind to the $\{100\}$ face.³² In all cases, HR-TEM shows that MNSs are single crystals, while ANSs are pentatwinned crystals with branches of different length. The products are crystalline with fcc (face centered cubic) structure.

In Figure 14 growth directions are highlighted.

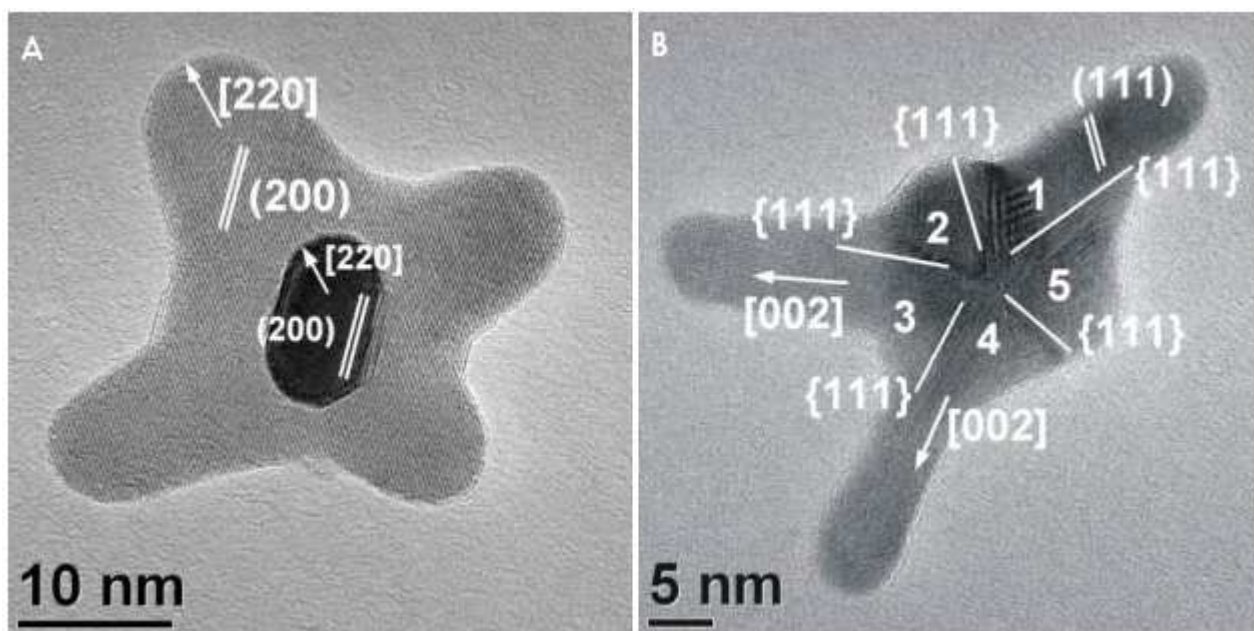


Figure 14: A) HR-TEM of a monocrystalline gold nanostar, (MNSs) and B) a penta-twinned branched particle, (ANSs). MNSs are monocrystalline with four or five visible branches grown along the $[220]$ or $[200]$ directions. ANSs are always twinned crystals with $\{111\}$ contact planes, with branches grown along $[220]$ or $[002]$ directions.

ICP-OES measurements of typical GNSs show that silver is present with a percentage of 10-15% in respect to gold. The average yields of gold and silver in samples of GNSs are

60% and 70%, respectively. These measurements suggest that silver does not only promote the anisotropic growth but it is also included in the structure of the particles.

TEM images of samples prepared with different concentrations ascorbic acid were deeply analyzed and the percentages of different typologies of objects were counted. The analysis was performed through the use of the software ImageJ. An example of these results is summarized in Table 1.

Table 1: example of a summary of the count of objects for sample prepared with different ascorbic acid concentrations.

LSB [M]	AA [M]	% MNS	% ASN
0.1 M	$7.3 \cdot 10^{-4}$	30	23
	$8.0 \cdot 10^{-4}$	35	29
	$1.1 \cdot 10^{-3}$	32	47
	$1.3 \cdot 10^{-3}$	20	70

The percentage of MNSs in a typical colloid of GNSs, is almost constant and independent of ascorbic acid concentration, with an approximately 30% value. By regulating the amount of ascorbic acid, at a chosen concentration of LSB, it is possible to make ANSs the most abundant species. It is well established that the final shape of a nanocrystal is largely determined by the initial structure of the seed (see Chapter 1.3). The single-crystals objects, MNSs, are approximately the same under all the examined conditions and this strongly suggests that the composition of the seed is identical, independent of LSB concentration, and contains approximately 70% twinned and 30% monocrystalline seeds.

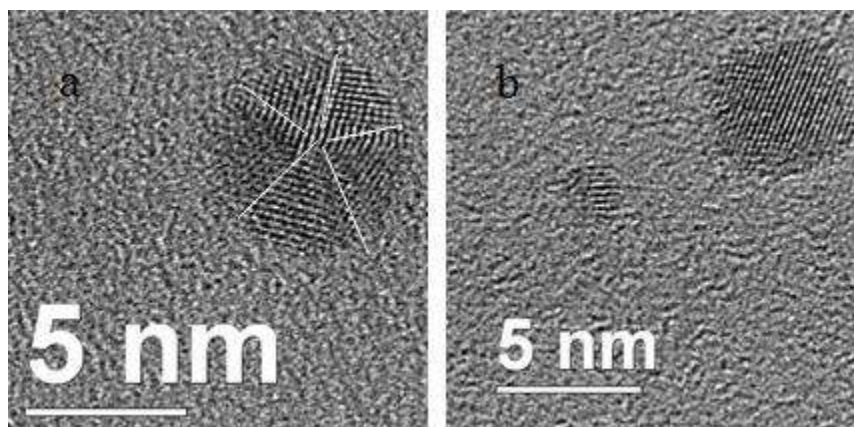


Figure 15: HR-TEM of a pentatwinned (a) and a single-crystal (b) seed nanoparticles.

With an analysis of the dimensions of the nanostructures, it was found that the aspect ratio of the MNSs is maintained constant at 1.3 - 1.4 upon changing ascorbic acid concentration; for MNS, the dimensions at the base of the branches is 10.8(0.8) nm and the medium length of the branches is 14(2) nm. The increase of ascorbic acid drives the development of the twinned seeds into ANSs structure with higher aspect ratio, varying from 2.2 to 4.⁶⁶ A possible consideration about the growth mechanism is that there is a preferential binding mechanism with: LSB sulfate moiety could adsorb preferentially on the {111} Au face, thanks to the Au-Au distance in this face (2.35 Å) well matches with the O-O bite (2.37 Å) in the sulfate moiety of LSB. The Au-Au distance in {220} face is instead 1.44 Å.

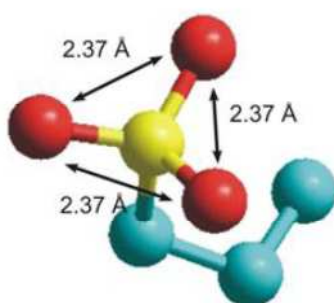


Figure 16: Molecular model obtained using method AM1 with the HyperChem 7.5 program.³¹

According to this model, LSB preferentially adsorb on {111} faces and Au⁽⁰⁾ is preferentially deposited on the direction [220] and [200], leading to the anisotropic growth of the branches. In comparison with the model proposed by C.J. Murphy for

CTAB-directed synthesis of gold nanorods, the monolayer of LSB can interdigitate a second layer of surfactant molecules to form a double layer, thanks to this arrangement the dodecyl chains self-interact and are not exposed to the aqueous environment. Furthermore, the sulphate moiety of the second layer are instead exposed to water, imparting a negative charge to the nanoparticles: $-14(2)$ mV.³¹

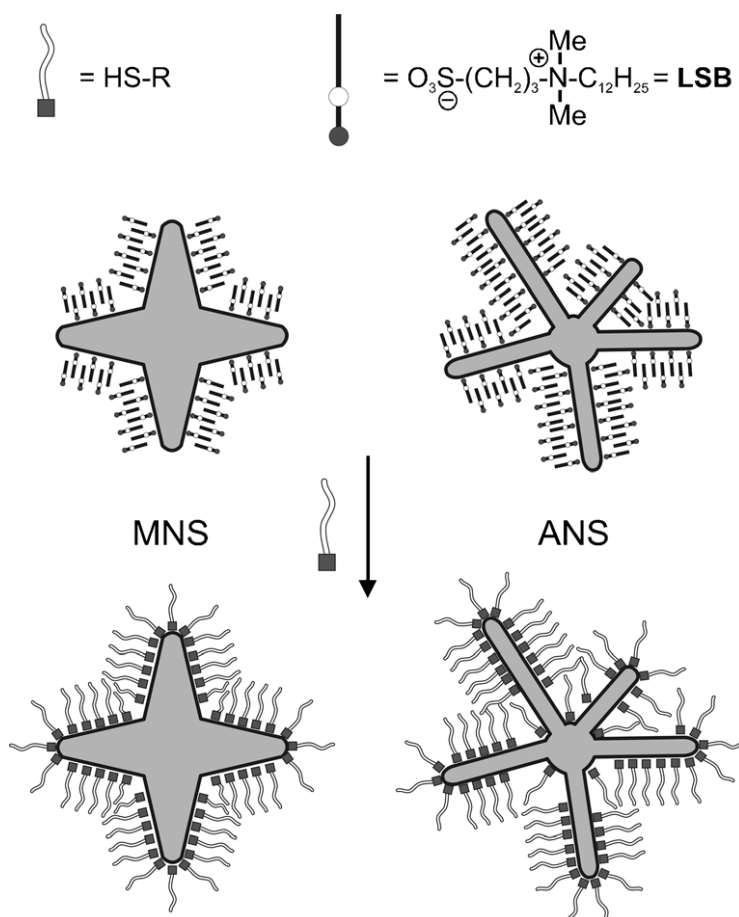


Figure 17: Formula and pictorial representation of the molecular and nanospecies discussed in this Chapter. Please note that the drawing of MNSs is to be considered a projection, as these nanocrystals have two further branches perpendicular to the plane of the illustration.

The weakly bound LSB surfactant can be fully removed by the surface when using PEG-thiol as a coating agent, with a straightforward “mix and coat” procedure (Figure 17). The PEG-coated MNSs and ANSs are perfectly stable in water as well as in a range of organic solvents and in similar to *in vivo* conditions.

Probably, the most important feature of these ANSs species comes from the possibility to tune the position of the long-band in the 750 – 1200 nm range, also called “biologic transparent window”, a feature made possible by the regulation of a synthetic parameter

(e.g. ascorbic acid concentration). That is the main reason why gold nanostars and in general multibranched gold nano-objects have received a lot of attention over these past years.⁷¹ This kind of NPs can be excellent alternatives to AuNRs for *in vivo* use, photothermal therapy, and targeted drug delivery. Moreover, their targeted use for *in vivo* SERS detection of tumors can be easily imagined.⁷²

⁷¹ A.G. Martinez; S. Barbosa; I.P. Santos; L.M. Liz-Marzàn; *Curr. Opin. Colloid Interface Sci.*, **2011**, 16, 118–127.

⁷² X. Qian; X.H. Peng; D.O. Ansari; Q.Y. Goen; G.Z. Chen; D.M. Shin; L. Yang; A.N. Young; M.D. Wang; S. Nie; *Nat. Biotechnol.*, **2008**, 26, 83–90.

1.3.2 TRITONX-100 SHRINKED NANOSTAR (SGNS)

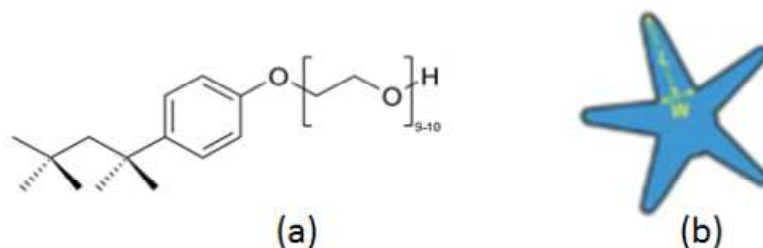


Figure 18: a) molecular structure of TritonX-100 and schematic representation of b) 5-branched gold nanostars obtained with the TX-100 seed-growth method.

Continuing with weaker coating agents, in order to replace the traditional cationic surfactant (CTAB), also the non-ionic surfactant TritonX-100 (TX-100, Figure 18a) was evaluated, obtaining mainly regular 5-branched gold nanostars (Figure 18b). Also this synthetic approach is based on a modified seed-growth El Sayed's protocol.³² The seed-growth synthesis of this kind of Triton-based GNSs uses the same conditions that lead to gold nanorods with CTAB³² and to gold nanostars (GNSs) with LSB.⁶⁶ In brief: i) gold spherical seeds are generated from $AuCl_4^-$ thanks to the strong reducing agent $NaBH_4$, in solutions of TX-100 surfactant; ii) a few amount of the seeds are added to a growth solution containing: TX-100 at the same concentration of the seed solution, $AuCl_4^-$, Ag^+ and a variable concentration of ascorbic acid.

The growth process is complete in less than 60 minutes, generating intensely blue-colored solution, in which the Au(III) to GNSs conversion yield is 60–70%.

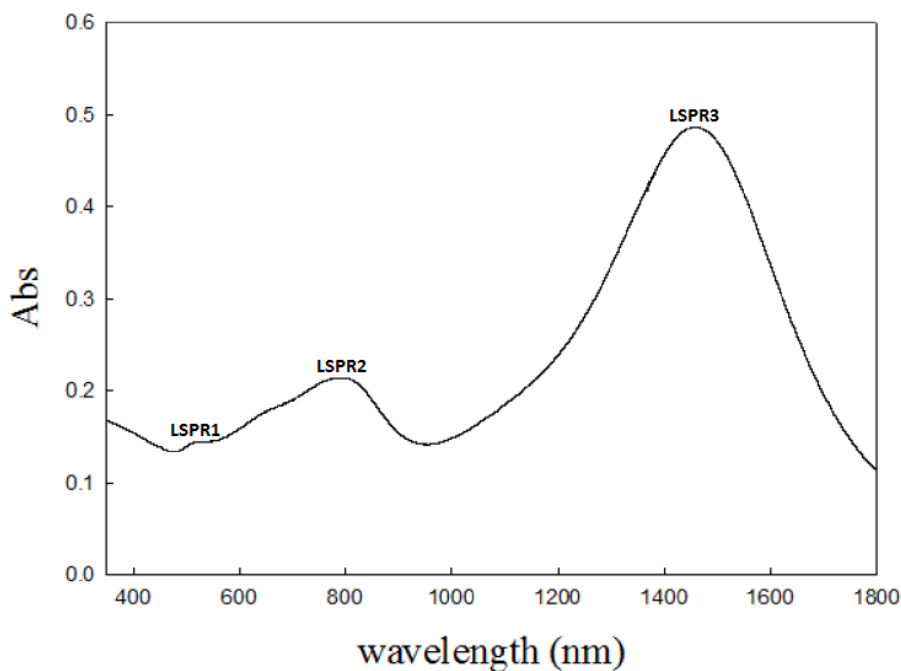


Figure 19: UV-Vis-nIR spectrum of a typical TX100-GNSs colloid.

These gold nanostars have the uncommon feature of three LSPR in the 530 – 1800 nm range (as shown in Figure 19): a very weak one at 530 – 560 nm (LSPR1 or “short band”), an intense one in the 600 – 900 nm range (LSPR2 or “intermediate band”), and the most intense in the 1100 – 1600 nm range (LSPR3 or “long band”).

LSPR2 and LSPR3 depend strongly on the aspect ratio of the objects and span the entire nIR range. It is a unique feature for anisotropic gold nano-objects to have two more resonant band in addition to LSPR1, both shifting to the red with aspect ratio and with the longest one reaching the surprising wavelengths of 1500/1600 nm. It was proposed that these observations could be due to the peculiar shape of these objects: in each nanoparticle there are co-linear branches and the longitudinal oscillation along these aligned branches could be responsible for LSPR3, but there are also branches which form an angle with all the other branches, remaining not coupled and generating LSPR2 (see Figure 20).

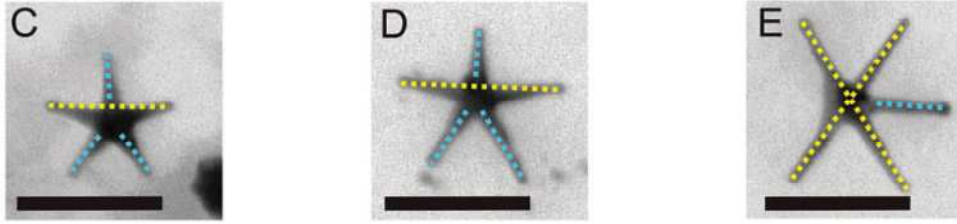


Figure 20: TEM images of TX100-GNSs. Yellow and azure dotted lines show co-linear and uncoupled branches. Scale bar 80 nm.

This is explained in figure 20: in each object at least two branches are co-linear (Figure 20 evidenced by the yellow dotted lines), and the longitudinal oscillation of the electrons along these aligned branches is responsible for the long LSPR. On the other hand, at least one branch forms an angle with all the other remaining branches (Figure 20 azure dotted lines), thus generating the intermediate LSPR through the longitudinal oscillation of the electrons along its length. Besides GNSs, some undeveloped, roughly spherical nanoparticles are also found and are irregular polycrystals; at high ascorbic acid concentration they become a negligible percentage of the products (they are co-responsible for the 520 – 560 nm short band). Furthermore, GNSs are crystalline with a face-centered cubic (fcc) structure and the five-branched nanostars are pentatwinned crystals (Figure 21). The growth of the branches takes place along the $\{111\}$ twinning boundaries of the crystal core, giving place to mirror planes along the growth direction.

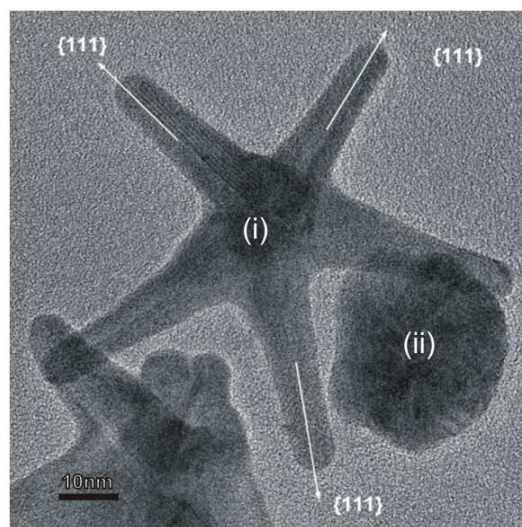


Figure 21: i) HR-TEM on a TX-100 based GNSs ii): a polycrystalline spherical nanoparticle.

TX-100 is a non-ionic surfactant that has been rarely used in Au nanoparticles synthesis,⁷³ leading mostly to spherical or highly symmetric objects, and the use in the seed-growth approach was quite a novelty, at a first sight difficult to explain. However, TX-100 has a feature resembling PVP, i.e., the repeating sequence of oxygen atoms in its hydrophilic head, made of nine $-\text{CH}_2\text{CH}_2\text{O}-$ units. It can be proposed in that similarly to PVP it adheres to the $\{111\}$ Au faces, lowering their energy and promoting their development. As already mentioned the TX-100 adhesion is weak, so these GNSs are poorly stable if coated only with this surfactant, as ultracentrifugation induces aggregation.⁷⁴ The addition of a PEG at the end of the growth induces the simple displacement of the surfactant, and these coated GNSs can be ultra-centrifuged, separated, re-dissolved in water and centrifuged again many times, in order to remove any residual TX-100.

B. Devika Chithrani et al.⁷⁵ studied the size dependence of gold nanoparticle uptake into mammalian cells and found that the maximum uptake by a cell occurred at a nanoparticle size of 50 nm (Figure 22), while Osaki et al.⁷⁶ qualitatively showed that 50 nm nanoparticles entered cells via receptor-mediated endocytosis more efficiently than greater or smaller dimensions.

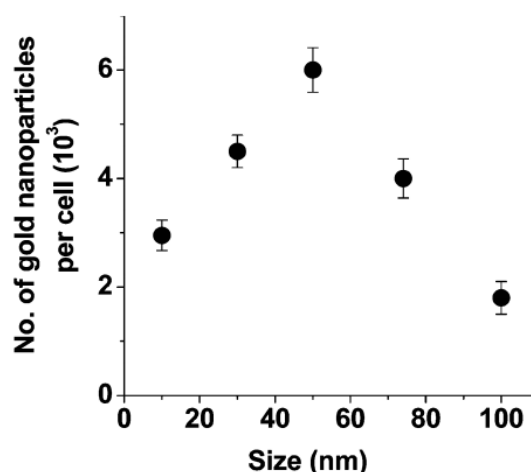


Figure 22: dependence of cellular uptake of gold nanoparticles as a function of size.⁷⁶

⁷³ A. Pal; *Curr. Sci.*, **1998**, 74, 14–16.

⁷⁴ P. Pallavicini; A. Donà; A. Casu; G. Chirico; M. Collini; G. Dacarro; A. Falqui; C. Milanese; L. Sironi; A. Taglietti; *Chem. Commun.*, **2013**, 49, 6265–6267.

⁷⁵ B.D. Chithrani; A.A. Ghazani; W.C.W. Chan; *Nano Lett.*, **2006**, 6, 4,662–668.

⁷⁶ F. Osaki; T. Kanamori; S. Sando; T. Sera; Y.J. Aoyana; *Am. Chem. Soc.*, **2004**, 126, 6520–6521.

Chithrani et al. hypothesized that the uptake of standard gold nanoparticles is mediated by nonspecific adsorption of serum proteins onto the gold surface, these proteins induce the nanoparticles to enter into cells via the mechanism of receptor-mediated endocytosis. So, in order to promote the cellular uptake of TX100-GNSs into cells we developed a modified protocol of the classical synthesis⁷⁴ to shrink the dimension of the nanoparticles from 80 nm to 40 nm.⁷⁷ This advance was due by changing synthetic parameters during the preparation of the colloid (experimental details are provided in Paragraph 2.2.2.3). We call these particles: “shrunk GNSs” (sGNSs).

The Figure 23 shown a general UV-Vis spectrum of a typical shrunk GNSs colloid.

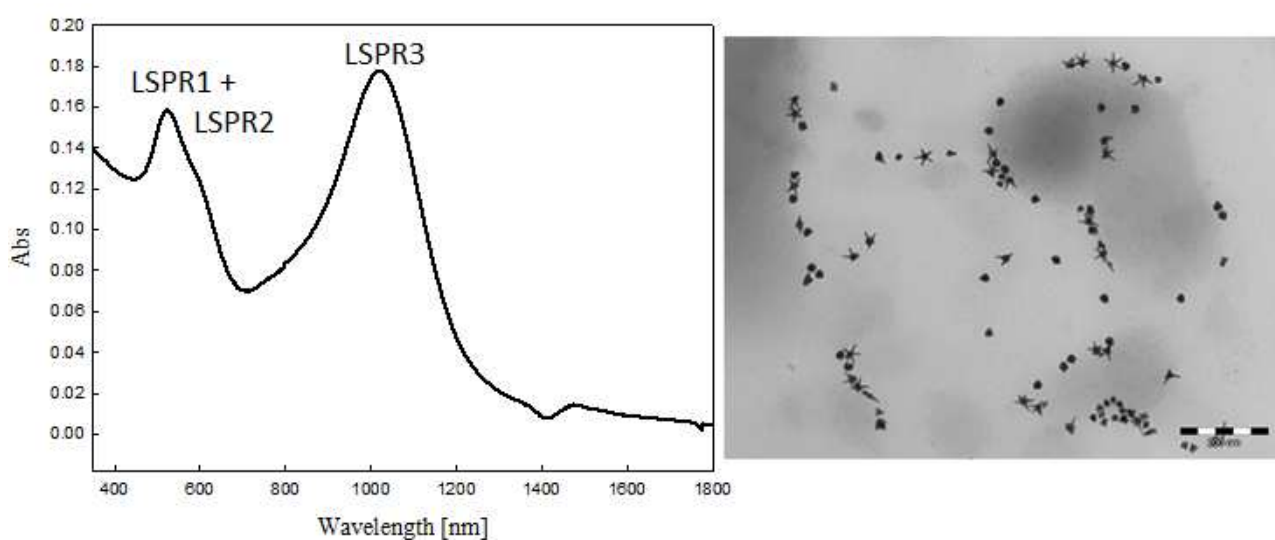


Figure 23: UV-Vis-nIR spectrum of a typical “shrink” TX100-GNSs colloid and relative TEM image. Scale bar: 200 nm.

These shrunk GNSs shown two intense LSPR's band: the “short” one and the “intermediate”, fuse together, resulting a band that fall in the 530 – 560 nm, instead the long band shifted in UV-Vis region in 900 – 1100 nm range. Thanks to this modified approach we obtain a mixture of nanosphere and regular 5-branched gold nanostars with 2.8 aspect ratio, moreover the long band fall in the biological window, ideal for biological applications that require internalization into the cells.⁷⁶

⁷⁷ S. Bertani; *Sintesi e separazione di nanostelle d'oro di dimensioni ridotte e morfologia controllata*; Master Thesis in Chemistry, **2014-2015**.

1.4 OPTICAL PROPERTIES OF NANOSTARS

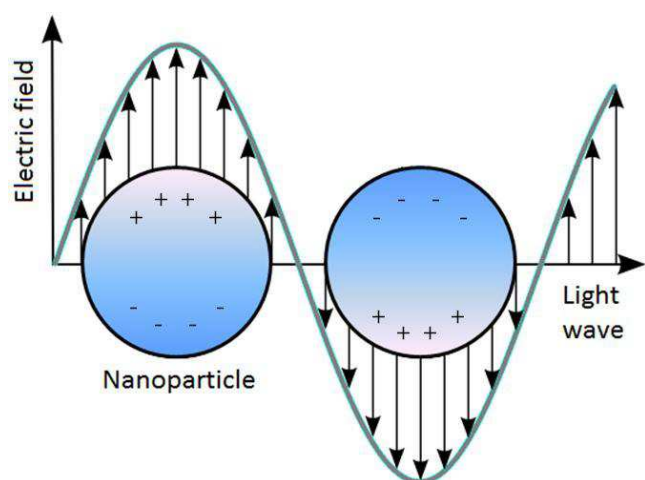


Figure 24: schematic of localized surface plasmon resonance (LSPR) where the free conduction electrons in the metal nanoparticle are driven into oscillation due to strong coupling with incident light.

Gold nanoparticles have been extensively used for applications both in biology and technology due to their unique optical properties. These properties are conferred by the interaction of light with electrons on the gold nanoparticle surface, this kind of event provokes a phenomenon called: localized surface plasmon resonance (LSPR).⁷⁸ LSPR is an optical phenomenon that causes a collective oscillation of valence electrons and subsequent absorption within the ultraviolet-visible (UV-Vis) band, due to interactions

between the incident photons and the conduction band of a noble metal nanostructure.⁷⁹ This classical effect was theoretically described by Mie⁸⁰ in 1908 by solving Maxwell's equations for a plane wave incident on a metal sphere surrounded by a dielectric medium, given the dielectric function of the metal. Mie theory provides an exact analytical solution for nanosphere LSPR in terms of a multipole expansion. For nanospheres whose diameters are less than about one tenth the incident radiation wavelength, only the dipole term in the expansion is significant, and the extinction simplifies to:

$$\sigma = \frac{18\pi V \epsilon_m}{\lambda} \frac{\epsilon_2}{(\epsilon_1 + 2\epsilon_m)^2 + \epsilon_2^2}$$

where σ is the extinction cross section, V is the nanoparticle volume, λ is wavelength, ϵ_m is the dielectric constant of the medium, and $\epsilon_1 + i\epsilon_2$ is the complex dielectric function of the metal.⁸¹ The resonance condition is met when $\epsilon_1 = -2\epsilon_m$, which occurs in the visible for gold and silver nanospheres. The sharpness of the resonance is determined by the imaginary part of the dielectric function, ϵ_2 . Silver, having a smaller imaginary component than gold, exhibits sharper, brighter resonances.⁸² One can see that in the dipole approximation, LSPR has no dependence on the size of the nanosphere. The

⁷⁸ F. Hao; C.L. Nehl; J.H. Hafner; P. Nordlander; *Nanoletters*, **2007**, 7, 3, 729-732.

⁷⁹ J.L. Hammond; N. Bhalla; S.D. Rafiee; P. Estrela; *Biosensors*, **2014**, 4, 172-188.

⁸⁰ G. Mie; *Ann.Phys.*, **1908**, 330, 377-445.

⁸¹ S. Link; M.A. El-Sayed; *Journal of Physical Chemistry B.*, **1999**, 103, 4212-4217.

⁸² P.B. Johnson; R. W. Christy; *Phys. Rev. B*, **1972**, 6, 4370-4379.

resonant condition is purely determined by the dielectric functions of the metal and the medium. However, for larger nanospheres where the higher multipoles become important, there is a modest red shift with size. LSPR can occur only when the incident light can induce a dipole (or quadrupole on bigger NP) on the surface of the nanoparticle, and this condition is verified only when the particles are smaller than the wavelength of the incident light. These plasmon resonances give rise to surface plasmon absorption bands. Instead of other transition metals, which show broad absorption bands in the UV range, noble metals (copper, silver and gold) have LSPR frequencies that lie in the visible region.⁸³ Since copper is easily oxidized, silver and gold nanostructures are the most attractive from the point of view of the use of such features. Gold nanospheres in the 10 nm size range have a strong maximum around 520 nm in water (which confers the characteristic red colour) and silver nanoparticles in the same size range show a LSPR peak around 390 nm (responsible of the characteristic bright yellow of AgNPs).

As it will be described later in this work, in many biological applications, especially *in vivo* studies, it is desirable to work in the near infrared region, especially in the 750 - 950 nm range, because this window is characterized by low absorption of tissues, blood and water. One way of tuning LSPR absorption into this region is to move from gold nanosphere to anisotropic gold nanoparticles, whose simplest examples are gold nanorods. As previously mentioned, rod-shaped nanoparticles have two resonances, in fact, when spherical symmetry is lost, the oscillation are no longer univocal and electrons can oscillate along the short axis (transverse mode) or long axis (longitudinal mode), giving rise to two plasmon absorption bands: a first one, centred around 530 nm, which is related to the transverse mode and the second one, more intense, which can be placed in the near infrared, related to the longitudinal mode. The longitudinal plasmon resonance band is sensible to the aspect ratio of the object (i.e. length-to-width ratio), so it can be tuned to longer wavelength increasing the AR. The optical properties of metal nanorods can be theoretically described using the Gans' theory, an extension of Mie's theory. Inducing anisotropy in gold nanoparticles is the strategy chosen to obtain nIR absorbing nano-objects. Another key attribute of the surface plasmon resonance is that its frequency depends on the dielectric constant, that is the refractive index (RI) of the medium surrounding the nanoparticle.⁸⁴ Increasing the refractive index of the medium, a red-shift of LSPR will be obtained, so changes in the nanoparticle environment can be sensed. In order to sense chemical/biological species, for example, the nanoparticles could be conjugated with recognition units for a target analyte; at the same time

⁸³ U. Kreibig; M. Vollmer; *Optical Properties of Metal Clusters*, Springer, Berlin **1995**, 25.

⁸⁴ S. Underwood; P. Mulvaney; *Langmuir*, **1994**, 10, 3427-3430.

appropriate surface capping is required to minimize non-specific binding. In this way, only the binding of the target molecule will cause a plasmon band shift due to a local RI change, and the system can be used as an optical sensing tool.⁸⁵ Interestingly, geometries that offer plasmon tunability also offer high plasmon sensitivity: among these there are anisotropic species with sharp surface curvatures and tips (nanorods, nanostars, etc) or junctions (metal nanoshells).

The strongly enhanced tunable absorption and scattering of noble metal nanocrystals has made them a novel class of optical and spectroscopic tags for biological sensing⁸⁶ and imaging⁸⁷ and biomedical therapeutics⁸⁸ with the potential to replace conventional chromophores and fluorophores.⁸⁹

⁸⁵ A.J. Haes; R.P. Van Duyne; *J.Am.Chem.Soc.*, **2002**, 124, 10596-10604.

⁸⁶ N.L. Rosi; C.A. Mirkin; *Chem. Rev.*, **2005**, 105, 1547-1556.

⁸⁷ I.H. El-Sayed; X. Huang; M.A. El-Sayed; *Nano. Lett.*, 2005, 5, 829-841.

⁸⁸ X. Huang; I.H. El-Sayed; W. Qian; M.A. El-Sayed; *J. Am. Chem. Soc.*, **2006**, 128, 2115-2156.

⁸⁹ P.K. Jain; X. Huang; I.H. El-Sayed; A.M. El-Sayed; *Plasmonics*, **2007**, 2, 107-118.

1.5 SURFACE-ENHANCED RAMAN SCATTERING (SERS)

Raman scattering of molecules is an inelastic scattering process whose cross-section is around 10^{-29} cm²/molecule.⁹⁰ When compared to cross-section of other optical processes, such as fluorescence (10^{-19} cm²/molecule), Raman scattering is thus a very weak phenomenon. This had hindered the usage of Raman scattering in applications where the background fluorescence was eminent. One of the effective ways to overcome this disadvantage is through Surface Enhanced Raman Scattering (SERS). Upon adsorption/proximity of molecules on/to plasmonic nanostructures, the Raman signal intensity can be enhanced by many orders of magnitude.⁹¹ This phenomenon has emerged as one of the most active fields of research in plasmon enhanced optical spectroscopy. The first observations of the Raman spectra of pyridine on roughened silver electrodes were made in 1974;⁹² and the increment in the Raman signal was attributed to a large number of molecules on the corrugated surface of the electrode. In 1977, two different reports by Jeanmarie et al.⁹³ and Albercht et al.⁹⁴ showed that an enhancement in the Raman signal was due to a localized electromagnetic field around the metallic nanostructure. Since then, interest in SERS and related uses has grown exponentially (Figure 25) especially in the context of its applications in molecular detection and bio-sensing also because SERS effect is accompanied by a simultaneous quenching of fluorescence process likely activated in biological samples using visible light.⁹⁵

⁹⁰ R.F. Aroca; *Surface-Enhanced Vibrational Spectroscopy*, Wiley, West Sussex, **2006**.

⁹¹ E.C. Le Ru; P.G. Etchegoin; *Principles of Surface-Enhanced Raman Spectroscopy and Related Plasmonic Effects*, Elsevier, Amsterdam, **2009**.

⁹² M. Fleischmann; P.J. Hendra; A.J. McQuillan; *Chem. Phys. Lett.*, **1974**, 26, 163-166.

⁹³ D.L. Jeanmaire; R.P. Van Duyne; *J. Electroanal. Chem.*, **1977**, 84, 1-20.

⁹⁴ M.G. Albrecht; J.A. Creighton; *J. Am. Chem. Soc.*, **1977**, 99, 5215-5217.

⁹⁵ B. Sharma; R.R. Frontiera; A.I. Henry; E. Ringe; R.P. Van Duyne; *Materials Today*, **2012**, 15, 1, 16-25.

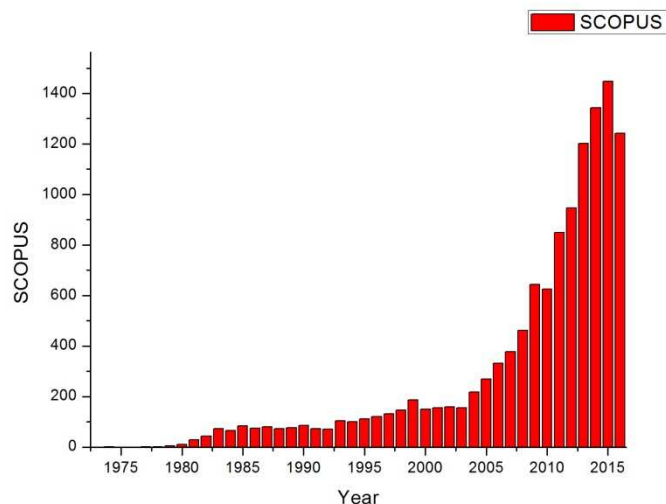


Figure 25: growing popularity of the surface enhanced Raman technique.

SERS has been observed for a very large number of molecules adsorbed on the surfaces of relatively few metals in a variety of morphologies and physical environments. Silver, copper and gold are the dominant SERS substrates used, but some investigations have been reported on alkali metals and a few others substrates. The largest enhancements occur for surfaces which are rough on the nanoscale (10 – 100 nm). These include electrode surfaces roughened by one or more oxidation–reduction cycles, monolayers of nanoparticles deposited on glass surfaces, colloids, and arrays of such particles prepared by lithographic techniques. This phenomenon differs in a number of ways from ordinary Raman spectroscopy of molecules and solids and even from unenhanced surface Raman spectroscopy.⁹⁶ Surface Enhanced Raman Scattering is a surface technique which imparts a very high enhancement to the usually weak Raman effect thanks mainly to the peculiar interactions of EM radiation with plasmonic features of metallic nano-objects. When a EM radiation impinges on a undisturbed molecule the induced dipole moment is $\mu = \alpha E$, when the molecule is placed in proximity or bounded to a metal nano-object the above relation for the induced dipole moment must be generally rewritten as follows:

$$\mu_{ind(mol)}^* = \alpha_{mol}^* E_{out}(\omega_{inc})$$

In this formula two different physical phenomena are included, from one side the molecule experiences an increased EM field due to plasmonic resonances effects, on the other side the polarizability of the molecules can be affected by chemical or electron

⁹⁶ B.S. Rabinovitch; J.M. Schurr; H.L. Strauss; *Annual Reviews Inc.*, Palo Alto, CA, **1985**, 549.

interactions with metal. Many mechanisms were proposed in the early days of SERS, a number of them turned out simply to be wrong and those that survived were quickly sorted into two classes which were called electromagnetic and chemical enhancement.

1.5.1 ELECTROMAGNETIC ENHANCEMENT

The collective excitation of the electron gas of a conductor is called a plasmon; if the excitation is confined to the near surface region it is called a surface plasmon. Surface plasmons can either be propagating, on the surface of a grating, e.g., or localized, on the surface of a spherical particle (LSPR, see Chapter 1.4), e.g..

Surface nanometric roughness or curvature is required for the excitation of surface plasmons by light. Perhaps the most familiar example of this phenomenon is Wood's anomaly, in which the reflectivity of a grating dips sharply at the frequency which excites the surface plasmon. The electromagnetic field of the light at the surface can be greatly enhanced under conditions of surface plasmon excitation; the amplification of both the incident laser field and the scattered Raman field through their interaction with the surface constitutes the electromagnetic SERS mechanism. There have been many versions of the electromagnetic theory developed over the years which treat physical situations of varying complexity at different levels of completeness. Model systems which have been treated include isolated spheres, isolated ellipsoids, interacting spheres, interacting ellipsoids, randomly rough surfaces treated as collections of hemispherical bumps or gratings and fractal surfaces, for example. These systems have been analysed with different degrees of details and complexity. The simplest treatments invoke the electrostatic approximation using sharp boundaries and local, bulk dielectric functions for the substrate. Full electrodynamic calculations have been carried out for the simpler systems and the effects of a non-local dielectric response have been discussed. These issues have been critically reviewed in the comprehensive article by Moskovits.⁹⁷ The essential physics which underlies the electromagnetic mechanism is well-illustrated by the textbook example of a metal sphere in an external electric field. For a spherical particle whose radius is much smaller than the wavelength of light, the electric field is uniform across the particle and the electrostatic (Rayleigh) approximation is a good one. The field induced at the surface of the sphere is related to the applied, external (LASER) field by equation (1) below.

$$E_{Induced} = \{[\epsilon_1(\omega) - \epsilon_2]/[\epsilon_1(\omega) - 2\epsilon_2]\} E_{LASER} \quad (1)$$

⁹⁷ M. Moskovits; *Rev. Mod. Phys.*, **1985**, 57, 3, 783-826.

where $\epsilon_1(\omega)$ is the complex, frequency dependent dielectric function of the metal and ϵ_2 is the relative permittivity of the ambient phase. This function is resonant at the frequency for which $\text{Re}(\epsilon_1) = -2\epsilon_2$. Excitation of the surface plasmon greatly increases the local field experienced by a molecule adsorbed on the surface of the particle. A very physical way to visualize this phenomenon is to consider the particle as having localized the plane wave of the light as a dipole field centred in the sphere which then decays with the dipole decay law away from the surface in all directions. Due to the small energy shifts involved in Raman processes, the particle is able to enhance not only the incident LASER field but also the Raman scattered field. It acts as an antenna which amplifies the scattered light intensity. It is easy to see from the above discussion why small increases in the local field produce such large enhancements in the Raman scattering; assuming the invariance of EF for incident and Raman fields it is commonly accepted that the overall enhancement scales roughly as E^4 .

This simple model rationalizes, at least qualitatively, most of the experimental observations. The arguments which follow apply generally to the wide variety of surface morphologies which have been used in SERS research; the numerical factor of 2 (sphere)



Figure 26: scheme representing the enhancement of a electric field along a sharp tip.

in the resonance equation will simply be different for different structures. The dominance of the coinage metals and the alkali metals as SERS substrates arises simply because the resonance condition is satisfied at the visible frequencies commonly used for Raman spectroscopy. Other metals have their surface plasmon resonances in different regions of the electromagnetic spectrum and can, in principle, support SERS at those frequencies. In addition, the imaginary part of the dielectric function (which measures losses in the solid) for the coinage and alkali metals is very small at the resonance frequency. Low loss materials sustain sharper and more intense resonances than those where scattering and other dissipative mechanisms are important. The materials requirement is fulfilled simply by selecting an excitation frequency for which $\text{Re} \epsilon_1$ satisfies a resonance condition and $\text{Im} \epsilon_1$ is as close to zero as possible.

The dipole decay law explains the range dependence of the phenomenon and the early controversy over that

issue. The enhancement falls off as $G=[r/(r+d)]^{12}$ for a single molecule located a distance d from the surface of a sphere of radius r , or $G=[r/(r+d)]^{10}$ for a monolayer of molecules. For large radii of curvature the effect looks long-ranged whereas for small radii it can appear to be a surface effect. The fact that the enhancement can be long ranged provided strong evidence for the electromagnetic mechanism. The depolarization is easily explained by considering a SERS-active surface to be a heterogeneous collection of roughness features of different sizes and shapes onto which the molecules adsorb in a variety of orientations. The lack of motional averaging and the opportunity for multiple scattering both contribute to depolarization.

When an object has an electrical charge, its electric fields are strongest at the sharpest features of that object. For example, electric fields are strongest at the sharp tip of a lightning rod, hence the name of the effect. This phenomenon also occurs at the nanoscale, where particles of metals such as gold or silver can produce LSPR and tends to concentrate the field lines at any sharp points of highly conducting materials (see Figure 26).⁹⁸ In this regard too, our GNSs and shranked GNSs, thanks to their many sharp tips, represent an ideal nanosubstrate for SERS applications.

⁹⁸ R.E. White; C.G. Vayenas; *Modelling and Numerical Simulations II*, Mordechai Schlesinger, **2009**.

1.5.2 CHEMICAL ENHANCEMENT

Electromagnetic theories related to plasmonic effects predict a maximum EF equal to about 10^{12} nevertheless several works report on higher EF (10^{14} - 10^{15}). This experimental evidences require to invoke additional enhancement process which operates independently of the electromagnetic event; this is so called chemical enhancement. As discussed below, it has been very difficult to separate these effects on systems which support electromagnetic enhancement. The early evidence for the existence of chemical enhancement was, therefore, mostly inferential. Electromagnetic enhancement should be a non-selective amplifier for Raman scattering by all molecules adsorbed on a particular surface yet the molecules CO and N₂ differ by a factor of 200 in their SERS intensities under the same experimental conditions. This result is very hard to explain invoking only electromagnetic enhancement. The polarizabilities of the molecules are nearly identical and even the most radical differences in orientation upon adsorption could not produce such a large difference. A second line of evidence in support of the presence of a chemical mechanism comes from potential-dependent electrochemical experiments. If the potential is scanned at a fixed laser frequency, or the laser frequency is scanned at fixed potential, broad resonances are observed.⁹⁹

These observations can be explained by a resonance Raman mechanism in which either

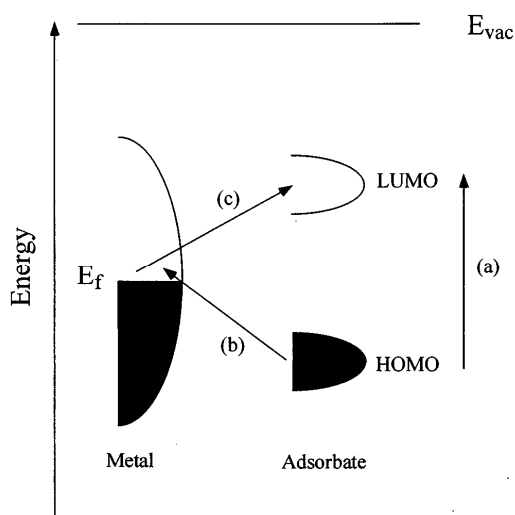


Figure 27: typical energy level diagram for a molecule adsorbed on a metal surface. The occupied and unoccupied molecular orbitals are broadened into resonances by their interaction with the metal states; orbital occupancy is determined by the Fermi energy. Possible charge transfer excitations are shown.

(a) the electronic states of the adsorbate are shifted and broadened by their interaction with the surface or (b) new electronic states which arise from chemisorption serve as resonant intermediate states in Raman scattering. It is not uncommon that the highest occupied molecular orbital (HOMO) and lowest unoccupied molecular orbital (LUMO) of the adsorbate are symmetrically disposed in energy with respect to the Fermi level of the metal (Figure 27). In this case charge transfer excitations (either from the metal to the molecule or vice versa) can occur at about half the energy of the intrinsic intramolecular excitations of the adsorbate. Molecules commonly studied by SERS typically have their lowest-lying electronic

⁹⁹ E.C. Le Ru; E. Blackie; M. Meyer; P.G. Etchegoin; *J. Phys. Chem. C*, **2007**, 111, 13794-13803.

excitations in the near ultraviolet which would put the charge transfer excitations of this simple model in the visible region of the spectrum. Lombardi et al.¹⁰⁰ have developed a theory which accounts for the potential-dependent excitation profiles mentioned above.¹⁰¹

¹⁰⁰ J.R. Lombardi; R.L. Birke; T. Lu; J. Xu; *J. Chem. Phys.*, **1986**, 84, 4174.

¹⁰¹ A. Campion; P. Kambhampati; *Chemical Society Reviews*, **1998**, 27, 241-250.

1.5.3 ENHANCEMENT FACTOR

One of the important parameters which is needed to characterize the efficiency of the SERS substrates is the enhancement factor (EF).¹⁰² Depending on the structure of the supporting plasmonic material, electromagnetic enhancement for SERS is theoretically calculated to be able to reach factors of $\sim 10^{10}$ – 10^{11} .¹⁰³ The main reasons for the disparity in the SERS EFs encountered in the literature probably derives from the lack of rigorous definitions. This problem was in fact pinpointed as one of four outstanding issues for SERS research and applications.¹⁰⁴ Scientists are attempting to address this issue by proposing and discussing a number of possible rigorous definitions for EFs. They particularly emphasize two crucial points, which probably have so far not drawn the attention they deserve: i) the necessity of including the non-SERS properties (in particular Raman cross-sections) of the investigated molecular probes in the definition, ii) the importance of distinguishing between EF definitions that are sensitive to the exact experimental conditions and to the SERS probe and those that are more intrinsic to the SERS substrate and therefore truly represent its performance. The diversity of situations that can arise in SERS, such as single molecules, multiple molecules, experimental limitations (e.g., not knowing the exact number of molecules), averages over time, spatial distribution, orientations of the probe on the surface, etc. make a single general definition of the EF impossible; the number of possible definitions is commensurate with this complexity. The most important definitions are three: the Single Molecule Enhancement Factor (SMEF), the SERS Substrate Enhancement Factor (SSEF) and the Analytical Enhancement Factor (AEF).

The SMEF is the enhancement felt by a given molecule at a specific point. It is, in general, dependent upon the Raman tensor of the probe and its orientation on the SERS substrate and with respect to the local field at that point. It is also dependent upon the orientation of the SERS substrate with respect to the incident laser polarization and direction. Hence, it requires the exact definition of the SERS substrate geometry and of the exact position and orientation of the probe on it. Because of these constraints, this definition is much more suited to theoretical estimations of the EF, rather than experimental measurements. The definition of the single molecule enhancement factor (SMEF) is shown in equation 2:

¹⁰² E.C. Le Ru; E. Blackie; M. Meyer; P.G. Etchegoin; *J. Phys. Chem. C*, **2007**, 111, 13794–13803.

¹⁰³ J.P. Camden; J.A. Dieringer; Y. Wang; D.J. Masiello; L.D. Marks; G.C. Schatz; R.P. Van Duyne; *J. Am. Chem. Soc.*, **2008**, 130, 38, 12616–12617.

¹⁰⁴ M. Natan; *Faraday Discuss.*, **2006**, 132, 321–328.

$$\mathbf{SMEF} = \frac{I_{SERS}^{SM}}{\langle I_{RS}^{SM} \rangle} \quad (2)$$

where I_{SERS}^{SM} is the SERS intensity of the single molecule under consideration, whereas $\langle I_{RS}^{SM} \rangle$ is the average Raman intensity per molecule for the same probe. In most cases, what is really important is the maximum SMEF on a SERS substrate. This is particularly true for experiments where Single Molecule signals may only be detectable from the points of highest enhancements (hot-spots).

For many SERS applications and experiments, the detailed distribution of the SMEF on the substrate, or even its maximum value, is irrelevant because one is mainly dealing with average SERS signals. It is, therefore, equally important to define SERS Substrate Enhancement Factor (SSEF), which can be used to compare the average SERS enhancements across different substrates. The most widely used definition is the equation 3:

$$\mathbf{SSEF} = \frac{I_{SERS}/N_{surf}}{I_{RS}/N_{vol}} \quad (3)$$

where $N_{vol} = c_{RS}V$ is the average number of molecules in the scattering volume (V) for the Raman (non-SERS) measurement, and N_{surf} is the average number of adsorbed molecules in the scattering volume for the SERS experiments. This expression resembles the commonly used average EF.^{105,106}

The definitions introduced so far (i.e. SMEF and SSEF) have attempted to emphasize the intrinsic characteristics of the substrate and are not always straightforward for relating to experimental results. For many applications, however, one is mostly concerned with the simple question of how much more signal can be expected from SERS as compared to normal Raman under similar, given experimental conditions. To address this question, scientists introduce another definition, which is fairly intuitive and particularly relevant for analytical chemistry applications. Let us consider an analyte solution with concentration c_{RS} , which produces a Raman signal I_{RS} under non-SERS conditions. Under identical experimental conditions (LASER wavelength, LASER power, microscope objective or lenses, spectrometer, etc.), and for the same preparation conditions, the same analyte in presence of a SERS substrate, with concentration which can be different (c_{SERS}), now gives a SERS signal I_{SERS} . The analytical enhancement factor (AEF) can then be defined by equation 4:

¹⁰⁵ A.D. McFarland; M.A. Young; J.A. Dieringer; R.P.V. Duyne; *Phys. Chem. B*, **2005**, 109, 11279-11287.

¹⁰⁶ N. Félidj; J. Aubard; G. Le´vi; J.R. Krenn; M. Salerno; G. Schider; B. Lamprecht; A. Leitner; F.R. Aussenegg; *Phys. Rev. B*, **2002**, 65, 075419.

$$\mathbf{AEF} = \frac{I_{SERS}/c_{SERS}}{I_{RS}/c_{SERS}} \quad (4)$$

This definition, although useful for specific practical applications, tends to strongly depend on many factors, in particular, on the adsorption properties and surface coverage (monolayer vs multilayer) of the probe: c_{SERS} obviously does not fully characterize the number of adsorbed molecules. It is also strongly dependent upon the sample preparation procedure for 2D planar substrates (e.g., spin-coating, dipping, or drying). The AEF, effectively, ignores the fact that SERS is a type of surface spectroscopy, which means that only the adsorbed molecules contribute to the signal and that the effect is distance-dependent.^{107,108} For this reason, it is not a good characterization of the SERS substrate itself, and it cannot be used to easily compare the performances of different substrates. However, provided all experimental procedures are clearly stated and sub-monolayer coverage of the SERS surface is ensured, the AEF represents a simple figure for the SERS EF, whose measurement is easily reproducible. From its definition, it is also clear that the AEF is particularly suited to the case of SERS active liquids (e.g., colloidal solutions).¹⁰⁹

¹⁰⁷ R. Aroca; *Surface Enhanced Vibrational Spectroscopy*; Wiley, Chichester, **2006**.

¹⁰⁸ S. Lal; N.K. Grady; G.P. Goodrich; N.J. Halas; *Nano Lett.*, **2006**, 6, 2338–2343.

¹⁰⁹ E.C. Le Ru; E. Blackie; M. Meyer; P.G. Etchegoin; *J. Phys. Chem. C*, **2007**, 111, 13794–13803.

1.6 PHOTOTHERMAL EFFECT

Probably, one of the most charming properties of gold nanoparticle is the ability of plasmon oscillation to relax non-radiatively: in fact, the non-radiative component is efficiently converted to heat on the time scale of picoseconds.¹¹⁰ The event concerns hot electrons that relax by collision with lattice ions, resulting in heating the gold nanocrystal lattice homogeneously via electron-phonon interaction, this occurs in ~ 1 ps. The lattice cools by giving its heat to the surrounding medium via phonon-phonon relaxation in ~ 100 ps.²⁷ This phenomenon can be readily exploited to produce a localized heating of the medium immediately surrounding the nanoparticle, by employing light radiation with an appropriate frequency overlapping with the nanoparticle LSPR absorption. Light can be absorbed by nanoparticles at the frequency of their LSPR and the energy be returned as heat. Depending on LASER energy, different phenomena can be obtained: at fast rate of energy deposition relative to lattice cooling, the photothermal heating can result in the desorption of surface-capping molecules¹¹¹ (a phenomenon which can be useful in drug delivery) or it may melt and reshape the nanoparticles.¹¹² At slower rate the lattice cools via phonon-phonon processes, leading to the localized heating of the medium surrounding the nanoparticle. In these conditions gold nanoparticles can be considered “light activated nanoscopic heaters” and they can be used, for example to reach selective (if conjugation of nanoparticles with proper targeting groups is used) LASER photothermolysis of bacteria or cancer cells. In nanomedicine, this technique is known as plasmonic photothermal therapy (PPTT),¹¹³ and can be applied to cancer and other disorders, e.g., bacterial infections.¹¹⁴ The use of intense pulsed LASERs for the thermal ablation/hyperthermia of tumors has gained increasing interest in recent times.^{115,116} In traditional photothermal therapy, the PPT agents can be natural chromophores already present in the tissue or externally added dye molecules.^{117,118} However, a common hindrance is that water and chromophores present in tissues absorb radiation along the light path, thus reducing the speed and effectiveness of heat diffusion within the cancer cells, and increasing non-specific injury

¹¹⁰ S. Link; M.A. El-Sayed; *J. Phys. Chem. B*, **1999**, 103, 8410-8426.

¹¹¹ P.K. Jain; W. Qian; M.A. El-Sayed; *J. Am. Chem. Soc.*, **2006**, 128, 2426-2433.

¹¹² S. Link; C. Burda; B. Nikoobakht; M.A. El-Sayed; *Chem. Phys. Lett.*, **1999**, 315, 12-18.

¹¹³ X. Huang; K.J. Prashant; I.H. El-Sayed; M.A. El-Sayed; *Lasers Med. Sci.*, **2008**, 23, 217-228.

¹¹⁴ V.P. Zharov; K.E. Mercer; E.N. Galitovskaya; M.S. Smeltzer; *Biophys. J.*, **2006**, 90, 619-623.

¹¹⁵ Z. Amin; J.J. Donald; A. Masters; R. Kant; A.C. Steger; S.G. Bown; W.R. Lees; *Radiology*, **1993**, 187, 339-343.

¹¹⁶ C.P. Nolsoe; S. Torp-Pedersen; F. Burcharth; T. Horn; S. Pedersen; N.E. Christensen; E.S. Olldag; P.H. Andersen; S. Karstrup; T. Lorentzen; *Radiology*, **1993**, 187, 333-343.

¹¹⁷ R.R. Anderson; J.A. Parrish; *Science*, **1983**, 200, 524-527.

¹¹⁸ W.R. Chen; R.L. Adams; E. Heaton; D.T. Dickey; K.E. Bartels; R.E. Nordquist; *Cancer Lett.*, **1995**, 88, 15-19.

of adjacent healthy tissue. Strong photoabsorbers, such as dyes, which can be selectively located within the cancerous region allow for increased heat production within the tumor at lower LASER irradiation energies, may render the method less invasive. Whereas strongly absorbing dyes have been conventionally employed for this purpose, the strongly LSPR enhanced absorption of metal nanoparticles makes them much more potent agents for photothermal therapy at much lower LASER intensities. For instance, the plasmon absorption of 40 nm AuNPs has a molar coefficient of $\sim 8 \times 10^9 \text{ M}^{-1}\text{cm}^{-1}$,¹¹⁹ a value that is almost six orders of magnitude larger than the molar coefficient of extinction of $\sim 10^4 \text{ M}^{-1}\text{cm}^{-1}$ for indocyanine green,¹²⁰ a dye commonly used in PPTT. In addition, AuNPs can be conjugated using well-established surface chemistries,¹²¹ Au-thiol binding or electrostatic adsorption, to various antibodies/proteins selected to specifically target molecular markers on the diseased cells. Selective targeting provides increase in the specific delivery of the nanoparticle absorbers to the diseased cells as compared to healthy cells. In a reported example, the LASER energy required for photodamage of the cancer cells (20 W/cm^2) was significantly lower than that required for the non-malignant cells (57 W/cm^2). This was attributable to the selective binding of the nanoparticle conjugates to the cancer cell surface and the strong SPR absorption of the nanoparticles at the LASER frequency, and demonstrated that nanoparticles are ideal agents for selective laser photothermal therapy, although, in this example, limited to near-surface or skin-type cancers.¹²² For clinical therapy applications involving tumors located deep within bodily tissue, there is the need to use LASER light in the near-infrared (nIR) region of the so called “biological window”, the 700 – 900 nm range (Figure 28). For this reason, in order to perform PPTT in deep tissues it is necessary the use of nIR absorbing gold nanostructures, like anisotropic gold nanostar; moreover, gold nanostar have high photostability, and in the condition of PPTT treatment they don't suffer from photobleaching, which can usually hamper the limit the effectiveness of classic organic dyes.

¹¹⁹ P.K. Jain; K.S. Lee, I.H. El-Sayed; M.A. El-Sayed; *J. Phys. Chem. B*; **2006**, 110, 7238-7248.

¹²⁰ K. Urbanska; B.R. Dixon; Z. Matuszak; J. Oszejca; P.N. Sliwinska; G. Stochel; *Acta Biochim. Pol.*, **2002**, 43, 387-391.

¹²¹ E. Katz; I. Willner; *Angew Chem. Int. Ed.*, **2004**, 43, 6042-6108.

¹²² I.H. El-Sayed; X. Huang; M.A. El-Sayed; *Cancer Lett.*, **2006**, 239, 129-135.

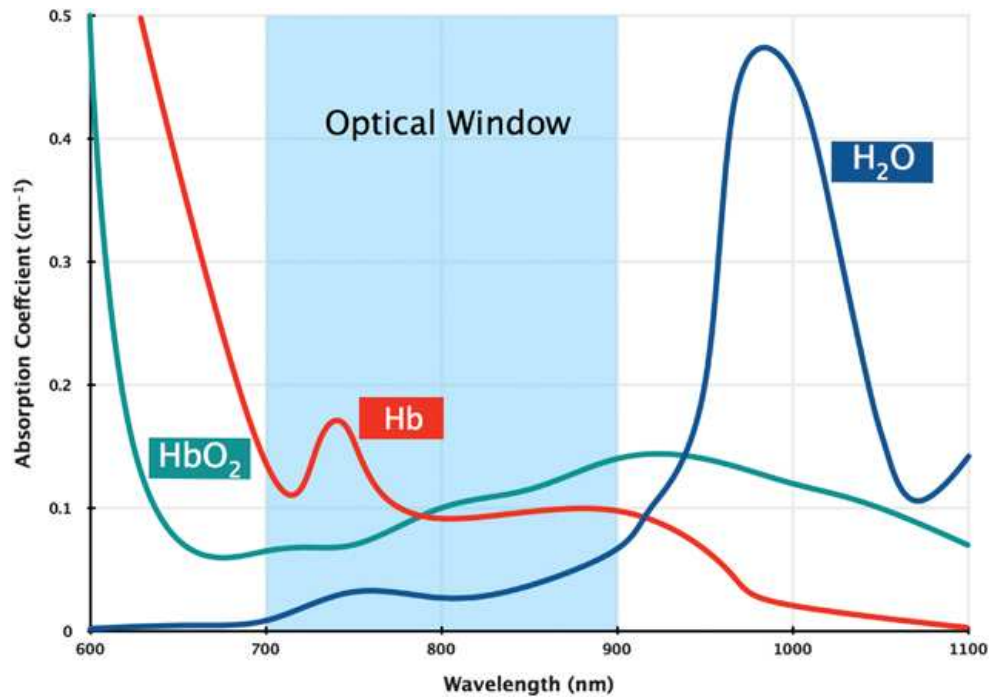


Figure 28: The absorption spectra of major tissue light absorbers hemoglobin and water. In the “optical window” between 700 and 900 nm there is little single-photon absorption (except by melanin that has a high absorption coefficient and may be present in lymphnodes and spleens of non-albino mice). Biological tissues are considered optically transparent in this commonly used imaging window.

However, the approach of using noble metal nanoparticles for targeting, imaging and therapy is general and versatile. Cancer is only one example. The use of plasmonic nanoparticles can be extended to other biological applications, for example, controlled denaturation of proteins, controlled release of drugs, destruction of viruses and bacteria, etc.¹²³

¹²³ V.P. Zharov; K.E. Mercer; E.N. Galtovskaya; M.S. Smeltzer; *Biophys. J.*, **2006**, 90, 619-627.

CHAPTER 2: GNSs GRAFTED ON GLASS: SILICA COATING

2.1 ANTIBACTERIAL APPLICATION

2.1.1 INTRODUCTION

It is acknowledged that medical device related infections account for a substantial morbidity, as well as causing a sharp increase in health-care costs. Implanted synthetic medical devices, especially, demonstrate a significant number of infections: although the rate of infection is relatively low, the sheer volume of medical devices accounts for a large number of infections.^{1,2,3} An example of device that has been associated with a high number of bloodstream infections is the central venous catheter.^{4,5} It is estimated that in the United States alone at least 80,000 catheter related bloodstream infections (CRBSI) occur annually in intensive care units. These CRBSIs are associated with 24,000 patient deaths and increased health care costs ranging from approximately \$10,000 to \$63,000 per case. Infection of medical implants and devices can be traced back to different sources of the infectious agent: i) a contaminated implant/device surface; ii) the hands of the surgical staff during implantation/application; iii) the patient's own skin or mucus membrane; iv) distant local infections in the patient; v) contaminated disinfectants; vi) contact with other patients in the hospital, or family members after intervention.⁶ Many of these risk factors can be easily avoided by stricter hygiene procedures in the hospitals. However, infections can never be completely avoided and therefore strategies to purposely avoid infection by either inhibiting adhesion of the pathogens or by killing adhesive microorganisms have to be pursued. Nano-technological advances will likely have a greater impact to prevent and nurse bacterial infections. A significant proportion of the research, in the nanoparticles field, focuses on silver nanoparticles, thanks to their well-known antibacterial features. In this chapter I'm going to describe a new interesting nanomaterial, that can be applied to contribute to solve the problem of infection related with medical devices, combining the antibacterial features of silver nanoparticles with the photo-thermal response of GNSs. This goal is reached using a multilayer coating technique. In order to design optimal strategies for the battle against medical device related infections, a good understanding of this bacterial infection is of critical importance. Upon implantation of the device (see Figure 1): A) proteins from the blood's

¹ R. Gradinger; R. Graf; J. Grifka; J. Löhr; *Der. Orthopäde*, **2008**, 3, 257-269.

² M. Hellmann; S.D. Mehta; D.M. Bishai; S.C. Mears; J.M. Zenilman; *J. Athroplasty*, **2010**, 25, 66-771.

³ A.J. Tokarczyk; S.B. Greenberg; J.S. Vender; *Crit. Care Med.*, **2009**, 37, 2320-2321.

⁴ S. Noimark; C.W. Dunnill; M. Wilson; I.P. Parkin; *Chem. Soc. Rev.*, **2009**, 38, 3435-3448.

⁵ A. David; D.C. Risitano; G. Mazzeo; L. Sinardi; F.S. Venuti; A.U. Sinardi; *Minerva Anesthesiol.*, **2005**, 71, 561-564.

⁶ V.D. Rosenthal; D.G. Maki; N. Graves; *Am. J. Infect. Control*, **2008**, 36, e1-e12.

patient rapidly adsorb onto the surface of an implanted device and form a good substrate for planktonic, free-swimming bacteria to adhere to; B) the sessile bacteria will recruit additional bacteria from the direct environment and also proliferate on the surface; C) the adhered bacteria change gene expression patterns and start producing the extracellular polymeric substance, the main component of the biofilm; D) the biofilm slowly grows and microcolonies of bacteria form inside the biofilm; E) finally, small parts of the biofilm can break off and planktonic bacteria escape from the biofilm and can invade new, clean surfaces at distant sites.

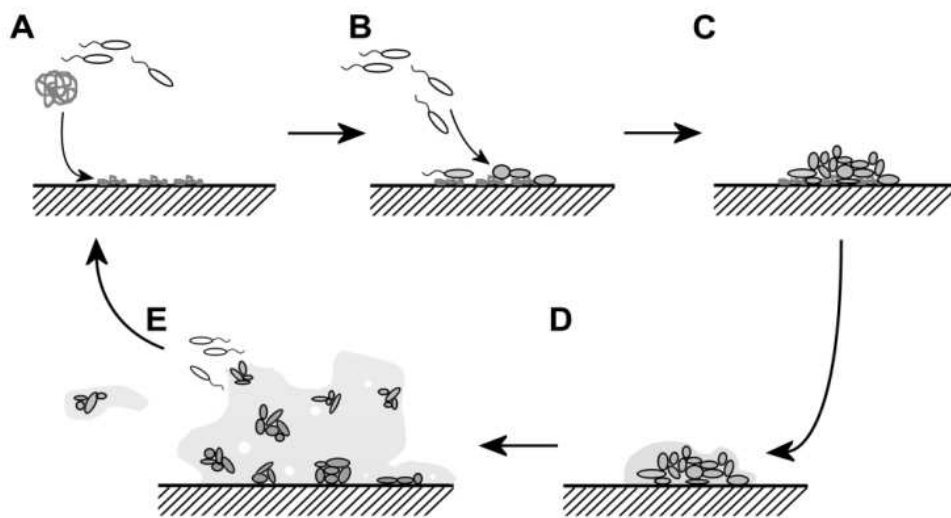


Figure 1: Schematic representation of biofilm formation.

This phenomenon is called “biofilm formation” and the biofilm is a protective sheet around the sessile bacteria that will protect them from shear stress, attack by the host’s immune system and (bad for the patient) against antibiotic substances.^{7,8} Knowing the important steps in surface invasion and biofilm formation, the number of possible strategies to avoid these phenomena is limited. The post-biofilm formation treatment of the infection is very difficult because of the slimy nature of the biofilm. The systemically administered antibiotics will not penetrate and therefore the bacteria will not be killed.⁷ So, to be able to prevent the adhesion of bacteria above the surface of the implanted device it means to be able to prevent a possible infection. It is clear that the topological and chemical characteristics of a medical device surface are important for the rate of microorganism adhesion. The application of silver as a preserving and antimicrobial

⁷ N. Hoiby; T. Bjarnsholt; M. Givskov; S. Molin; O. Ciofy; *Int. J. Antimicrob. Agents*, **2010**, 35, 322-332.

⁸ L. Hall-Stoodley; P. Stoodley; *Cell. Microbiol.*, **2009**, 11, 1034-1043.

agent goes back to 4000 BC. To that extent, examples are: i) silver vessels used to transport water during military campaigns ii) silver salts used to preserve water and food iii) silver coin in water or milk as a preservation method.⁹ The use of silver and silver salts to clean wounds and promote healing remained even into the 20th century. Silver was (and still is) used in wound dressings and successfully applied on open infected wounds, skin ulcers, compound fractures, and burn injuries.¹⁰ The efficacy of silver nanoparticles in reducing or preventing biofilm formation in venous catheters was demonstrated;¹¹ so the strategies to prevent device implantation failure have focused on development of surface coatings with silver nanoparticles, metallic silver, silver salts, or silver sulfadiazine.¹²

One of the research activity in the laboratory where I graduated and where I worked during my Ph.D is focused on the development of innovative nano-materials endowed with anti-infective properties, applying ground-breaking technologies to finish biomaterial surfaces with bactericidal layers. In particular our lab was successful in functionalization of glass surfaces with self-assembled monolayers of silane and nanoparticles.¹³ During my Ph.D I completed the work started during my “Laurea magistrale” thesis, taking advantage of this ability in order to obtain glass surfaces with a coating layer capable of both static and photo-switchable antibacterial activity, prepared using sequential chemical grafting and functionalizations. Some of the work here presented has been already described in my “Laurea magistrale” thesis, and is reported here because we started from those results to prepare new samples to complete the evaluation of the antibacterial and antibiofilm results, getting a complete explanation of the observed behaviour. Multi-layered coating we proposed bears a monolayer of gold nanostars (GNSs), covered by a thin layer of SiO₂ decorated on top by silver nanoparticles (AgNPs). These surfaces exerted bactericidal activity on *Escherichia coli* and *Staphylococcus aureus* (represented in Figure 2), due to the release of silver ions.

⁹ J.W. Alexander; *Surg. Infect.*, **2009**, 10, 289-292.

¹⁰ B.S. Atiyeh; M. Costagliola; S.N. Hayek; S.A. Dibo; *Burns*, **2007**, 33, 139-148.

¹¹ D. Roe; B. Karandikar; N. Bonn-Savage; B. Gibbins; J.B. Rouillet; *J. Antimicrob. Chemther.*, **2008**, 61, 869-876.

¹² L.W. Menno-Knetsch; L.H. Koole; *Polymers*, **2011**, 3, 340-366.

¹³ A. Taglietti; C.R. Arciola; A. D'Agostino; G. Dacarro; L. Montanaro; D. Campoccia; L. Cucca; M. Vercellino; A. Poggi; P. Pallavicini; L. Visai; *Biomaterials*, **2014**, 35, 1779-1788.

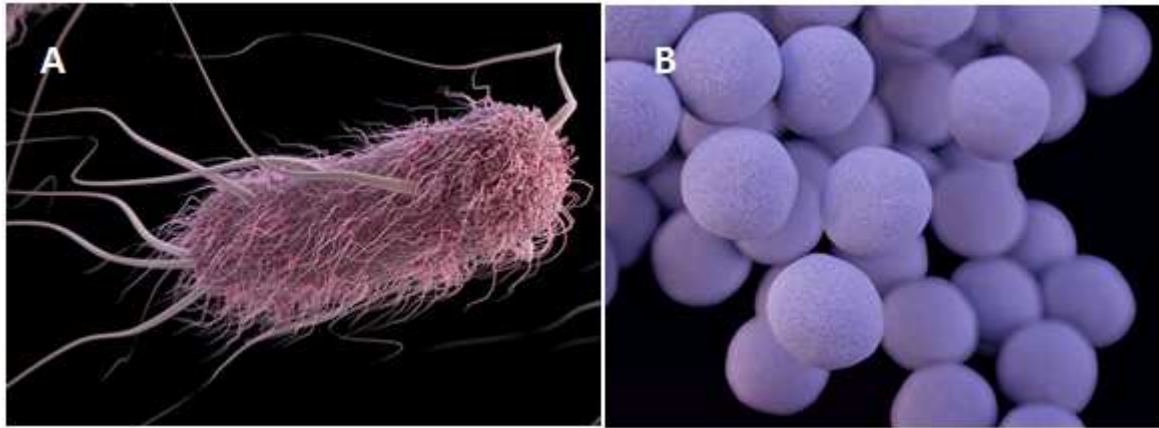


Figure 2: A) coloured scanning electron micrograph (SEM) of *Escherichia coli* bacterium. B) coloured scanning electron micrograph (SEM) of *Staphylococcus aureus* bacteria.

The underlying GNSs added a local bactericidal effect based upon nIR LASER irradiation, attributed to the photo-thermal response. Complementary microbiological and imaging evaluation of the effects on both planktonic and surface-attached bacteria allowed us to unravel an unprecedented synergy between these photo-thermal and intrinsic bactericidal effects.

2.1.2 EXPERIMENTAL DETAIL: SYNTHESIS AND CHARACTERIZATION

2.1.2.1 MATERIALS AND INSTRUMENTATION

Reagents

Gold(III) chloride trihydrate (~30wt% in HCl 99.99%), sodium borohydride (98%), L-ascorbic acid (AA) (≥99%), silver nitrate (99.8%), sodium citrate (≥99%), hydrochloric acid (≥37%), nitric acid (≥65%), sulfuric acid (95%), hydrogen peroxide (30 wt%), ethanol (≥99.7%), N-Dodecyl-N,N-dimethyl-3-ammonium-1-propanesulfonate (LSB) (≥99.7%), (3-aminopropyl)trimethoxysilane (APTES) (≥98.0%), sodium silicate solution (Na₂O(SiO₂)₃₋₅ 27%wt % SiO₂), (3-mercaptopropyl)trimethoxysilane (MPTS) (≥98.0%), were purchased from Aldrich. Amberlite IR120 hydrogenated was purchased from Fluka Analytical. Microscopy cover glass slides 21x26 mm were purchased from DEL Chimica. All reagents were used as received. All the preparation are made with bidistilled water.

Instrumentation

UV-Vis Spectroscopy. UV-Vis-nIR absorption on functionalized slides at normal incidence were measured in air using a Varian Cary 50 UV/Vis spectrophotometer. The wavelength scan range was 300-1100 nm. The samples were placed in a special holder enabling transmission measurement of the same spot on the slide during all experimental stages.

Contact Angle. Static contact angle determinations were made with a KSV CAM200 instrument, with the water sessile drop method.

High-Resolution Scanning Electron Microscopy (HR-SEM). Images were obtained by a SIGMA high-resolution scanning electron microscope (Carl Zeiss) based on the GEMINI® column which features a high brightness Schottky field emission source, beam booster, and in-lens secondary electron detector. Measurements were conducted in low acceleration potential mode (≤2 kV) with a working distance of about 2 mm thus allowing the use of uncoated samples.

Determination of Ag and Au by ICP-OES spectroscopy. The Ag and Au content in solution was then determined by Inductively Coupled Plasma (ICP) atomic emission spectroscopy. Measures were repeated three times, and mean values are given. ICP data were collected with an ICP-OES OPTIMA 3000 Perkin Elmer instrument.

Atomic Force Microscopy (AFM). AFM images were taken from an Auto Probe CP Research Thermomicroscopes scanning system in tapping mode using a Au coated Si probe with a typical spring constant $k=1.74 \text{ Nm}^{-1}$ (NSG03 probes from NT-MDT). Images were analysed using Image Processing 2.1 provided by Thermomicroscopes.

Cross-section imaging using Scanning Electron Microscopy Back Scattering Detector (SEM-BDS). The cross sections of photoactive surfaces were imaged using a JEOL SEM 7001 instrument that provides simultaneous SEM-BDS and Secondary Electron detector images of the same sample spot. Before imaging, the samples were mechanically broken applying slight pressure with a diamond knife on one end of the sample, and avoiding any damage of the cross-section area of interest. The cut samples were then coated on the top with 10 nm thin Cr layer, to increase electrical and thermal conductivity, and minimise radiation damage. The top-coating on the flat extended surfaces of the samples did not significantly interfere with the lateral cross-section morphology and chemical composition, allowing BSD observation of electron-density contrast between gold nano-stars and SiO_2 . The samples were glued on aluminium stabs using conductive carbon tape and silver paint. Imaging was performed on a 90° tilted sample holder with short working distance to increase BSD signal. Several experimental conditions were explored, finding an optimal acceleration voltage of 15 kV for high contrast images.

Transmission electron microscopy (TEM). TEM images of the used GNSs were taken on a Jeol JEM-1200 EX II instrument on 1:10 diluted GNSs solution, with a 10 μL sample dropped on Copper grids (300 mesh) coated with a Parlodion membrane.

Thermograms. We employed a ThermaCAM SC3000 (FLIR Systems; Italy) camera (320 x 240 microbolometers array) operating in the spectral range of 8-9 μm and a numerical aperture 0.46 x 0.34. The acquisition frequency is 9 Hz with a sensitivity of 0.1°C and an accuracy of $\pm 0.2^\circ\text{C}$. The thermocamera measured the heating of the surface of the slides. The profiles of temperature as a function of time were obtained from a ROI selected on the thermal image.

2.1.2.2 GLASSWARE PRE-TREATMENT

All the glassware that come in contact with GNSs was always pre-treated before use: a wash in *aqua regia* for 30 min, then washed and filled with bi-distilled water and ultrasonicated for 3 minutes before discarding water. The bi-distilled water/ultrasound treatment was repeated three times. Then the glassware were dried in an oven for 1 hour at 140°C.

Prior to APTES grafting, microscopy cover glass slides (21x26 mm) were treated with piranha solution (3:1 sulfuric acid 95% and hydrogen peroxide 30 wt%) for 30 minutes. Then the slides were washed in water under sonication for three minutes, three times. Then the glasses were dried in an oven for 1 hour at 140°C.

2.1.2.3 PREPARATION AND CHARACTERIZATION OF GLASSES

Synthesis of Gold Nanostar (GNSs)

The seeds were prepared in a vial by adding 5.0 mL of LSB aqueous solution (0.2 M) and 5.0 mL of HAuCl₄ aqueous solution (5×10^{-4} M). Subsequently, 600 μ L of an ice-cooled solution of NaBH₄ in water (0.01 M) were added to the pale yellow solution of AuCl₄⁻ obtained in the previous step. As prepared brown-orange solution was gently hand-shaken for a couple of second; this solution is efficient for the growth procedure of GNSs for 180 minutes from preparation if kept cold. The growth solution was prepared with 50 mL of LSB solution in water at the same concentration chosen for the seed solution (0.2 M), 1800 μ L of AgNO₃ in water (0.004 M), 50 mL of aqueous HAuCl₄ (0.001 M) and 820 μ L of an aqueous L-ascorbic acid solution (0.078 M) mixed to obtain a colourless solution just after a few seconds of gentle mixing. Then 120 μ L of seed solution were added to give a blue colloid, the intensity of which rapidly increased. The solution was allowed to react without agitation for 1 h. The colloidal suspensions were stored in the preparation flask, maintained in the dark and used within 7 days from preparation.

Synthesis of silver nanoparticles (AgNP)

Briefly, to 100 mL of ice cooled water the following solutions were added in sequence under vigorous stirring 1 mL of 1% (wt/v) AgNO₃ solution, after a minute 1 mL of 1% (wt/v) sodium citrate and, after a further minute, 0.500 mL of a ice-cooled solution 0.075%wt in NaBH₄ and 1%wt in sodium citrate. After the last addition, stirring was immediately stopped, in order to avoid coagulation. The colloidal suspensions were stored in the preparation flask, maintained in the dark and used within 3 days from preparation.

Preparation of tipe 0 glass

The pre-treated cover glass were fully immersed in a solution of APTES 10% (v/v) in ethanol and allowed to react for 5 minutes at 60°C. The amino-modified glasses were washed three times under sonication with ethanol. After this step, the samples were gently dried under N₂ flux.

Preparation of tipe I glass

Type 0 glass slides were fully immersed in the GNSs solution for 14 hours. After immersion, the slides were washed three times in water without sonication and carefully dried in N₂ stream. Dried samples (Type I) were stored in the dark in a desiccator.

Preparation of tipe II glass

The dried type I glasses were fully immersed in a MPTS ethanol solution 5% (v/v) for 10 minutes. After this step, the samples were washed three times with fresh ethanol and dried by N₂ flux. For silica deposition, the slides were then dipped for 4 hour in a 1.5wt % sodium silicate solution (after dilution of a 27%wt SiO₂ solution with water) kept at 90°C in a stove. The strongly acidic cation exchanger Amberlite IR-120 was used for the adjustment of the solution pH to 8.5-9. The silica-coated substrates (Type II) were washed three times in ethanol under sonication and dried in N₂ stream.

Preparation of tipe III glass

The type II slides were treated again with APTES like the initial step, then fully immersed in the colloidal suspensions of silver nanoparticles for 15 minutes at room-temperature. After this time the slides were washed three times with water and dried under N₂ flux. Dried samples were stored in the dark in a desiccator.

Preparation of glass to ICP-OES analisys (total quantity of Ag and Au)

The total Ag and Au content on type I, type II and type III samples was determined by quantitatively oxidizing the silver and gold NPs linked on a single slide (21x26 mm coated on both sides, total coated surface 10.92 cm²) by dipping it in 3 mL of *aqua regia* diluted 4:25 with bi-distilled water in a vial and keeping it overnight on a Heidolph Promax 1020 reciprocating platform shaker. The Ag and Au content in solution was then determined by Inductively Coupled Plasma (ICP) atomic emission spectroscopy.

Preparation of glass to ICP-OES analisys (release of Ag and Au at different time)

Quantities of noble metal released, after different immersion time in bi-distilled water for the three different types of samples, expressed as released micrograms per area unit. The release of Ag and Au versus time was followed on slides (21x26 mm coated on both sides, total coated surface 10.92 cm²). Each slide was immersed in 3 mL of bi-distilled water. Slides were taken off the water after 5 and 24 h (during this time the samples keeping on a Heidolph Promax 1020 reciprocating platform shaker). The content of Ag and Au in the 3 mL water volume was determined by ICP. Measures were repeated three times, and mean values are given. ICP data were collected with Inductively Coupled Plasma (ICP) atomic emission spectroscopy.

Studies of Microbicidal Effect (ME)

The antibacterial activity of the glasses was investigated against *Staphylococcus aureus* ATCC 6538 (Gram-positive) and *Escherichia coli* ATCC 10356 (Gram-negative). The microorganisms were grown overnight in Tryptone Soya Broth (Oxoid; Basingstoke, Hampshire, England) at 37°C. Washed cells were re-suspended in Dulbecco's PBS 10% and optical density (OD) was adjusted to 0.2, at 600 nm wavelength corresponding

approximately to 1×10^8 Colony Forming Units (CFU/mL). Bacterial suspensions (10 μ L) were deposited on a standard microscope slide (76 \times 26 mm); subsequently the microbial suspensions were covered with a functionalized glass (24 \times 24 mm), forming a thin film between the slides that facilitated direct contact of the microorganisms with the active NP surface. The two assembled glasses were introduced in a Falcon test-tube (50 mL) containing 1 mL of PBS to maintain a damp environment. For each bacterial strain two equivalent modified glasses were prepared; the slides were maintained in contact with the liquid films containing bacteria at room temperature for 5 and 24 h, respectively; for each time of contact an unmodified glass slide was processed in parallel as a control sample. After different times of contact, 9 mL of PBS were introduced in each Falcon test-tube under a gentle shaking to detach the assembled glass slides. Bacterial suspensions were then grown in Tryptone Soya Agar (Oxoid; Basingstoke, Hampshire, England) to count viable cells. The decimal-log reduction rate, a.k.a microbicidal effect (ME), was calculated using the formula:

$$\mathbf{ME = \log NC - \log NE} \quad \mathbf{(1)}$$

Where NC is the number of CFU/mL developed on the unmodified control glasses, and NE the number of CFU/mL counted after exposure to modified glasses. The results expressed as ME represent the average of six equivalent determinations.

Microbicidal Effect on nIR Irradiation (T-ME)

The antibacterial activity on NIR irradiation of the glasses was investigated against *S. aureus* ATCC 6538 (Gram-positive) and *E. coli* ATCC 10356 (Gram-negative). The microorganisms were grown overnight in Tryptone Soya Broth (Oxoid; Basingstoke, Hampshire, England) at 37°C. Washed cells were resuspended in Dulbecco's PBS 10% and optical density (OD) was adjusted to 0.2, at 600 nm wavelength corresponding approximately to 1×10^8 Colony Forming Units (CFU/mL). Bacterial suspensions (10 μ L) were deposited in little wells (20 \times 20 mm); subsequently glass slides (24 x 26 mm) were cut in four portion (each 10 \times 10 mm) and one of these portions was laid down upon the bacterial suspensions, forming a thin film between the slides that facilitates direct contact of the microorganisms with the active NP surface. Subsequently, the slides were irradiated with continuous LASER sources tuned on 806 nm for 30 minutes using an irradiance of 0.25W/cm² and a beam waist of 1.00 cm (multimode AlGaAs LASER diode, L808P200, Thorlabs GmbH, power of radiation 200 mW). After irradiation the inoculum was re-suspended in 1mL of Dulbecco's PBS 10%; these bacterial suspensions were

serially diluted in PBS and were then grown in Tryptone Soya Agar (Oxoid; Basingstoke, Hampshire, England) to count viable cells. The decimal-log reduction rate, microbicidal effect (T-ME), was calculated using the formula:

$$\mathbf{T-ME = \log NC_M - \log NT} \quad \mathbf{(2)}$$

(NC_M is the number of CFU/mL developed on the modified but not irradiated control glasses; NT the number of CFU/mL counted after exposure to modified and irradiated glasses).

Preparation of biological samples for localised irradiation experiments

S. aureus (DSM-346) and *E. coli* (ATCC-10798) were transferred from the stock to a fresh agar plate and incubated overnight at 37°C. Three colonies were taken from the agar plate for each bacterial strains, and independently transferred to fresh nutrient broth medium (Oxoid, Ltd-Thermo Fisher) to be grown overnight in a shaking incubator (200 rpm, at 37°C). The bacterial cell concentrations were adjusted to 10⁵ colony forming units per millilitre (CFU/mL) in sterile nutrient broth. Control glass and photoactive surfaces were sterilized with 70% ethanol, dried and placed in separate wells within 24-well plates. 1 mL of 10⁵ CFU/mL bacterial suspensions in nutrient broth were added to each well containing the samples and then incubated at 37°C for 24 h. After incubation, the supernatant was removed and the samples were carefully rinsed with 5% glucose pH 7.59 phosphate buffer.

Localised laser irradiation experiments

For the localised LASER irradiation experiments, the samples were dried at room temperature in vertical position. The drying time was less than 5 min. Subsequently, the samples were transferred onto the confocal Raman microscope stage (Renishaw InVia Raman Spectrometer) and overall bright-field images were assembled, using a 20x objective lens over a 2000x2000 µm grid (see Figure 3). Taking these bright-field images as surface maps, specific spots within each sample were irradiated for 10 sec using a 785 nm continuous LASER (maximum power at the sample 70 mW). The spots were set following straight line paths containing no more than 12 spots, separated at least by 180 µm. The separation between individual lines within the same sample was at least 1000 µm. Different relative power intensities (100%, 50%, 10%) and objective lenses (Leica 5x

and Leica 20x) were combined to control the power density at the sample surface. After irradiation, a second bright-field map was recorded to ensure steady positioning of the samples during each experiment. The whole process from drying, irradiation to mapping was performed within 30 minutes for each individual sample. The non-irradiated zones of the sample were considered a “dark” control. When the irradiation was completed, the samples were immediately fixed with 4% paraformaldehyde and 2.5% glutaraldehyde in 0.1 M phosphate buffer and stored at 4°C.

Sample preparation and imaging with Scanning Electron Microscopy (SEM)

For SEM processing, the samples were fixed overnight at 4°C with 4% paraformaldehyde and 2.5% glutaraldehyde in 0.1 M phosphate buffer. Subsequent fixation and staining steps were carried out in water using 2% osmium tetroxide for 1 h, 1% tannic acid for 1 h, and 2% osmium tetroxide for 1 h. Between these steps, the samples were rinsed several times with DI-water. Then, staining overnight at 4°C with 1% uranyl acetate in water was performed. After this last staining step, the samples were rinsed with DI-water, and progressively dehydrated with increasing ethanol concentrations (*i.e.* 30%, 50%, 70%, 90% and 100%). After dehydration, the samples were critical-point dried in CO₂ (Quorum Technologies K850) and coated with 10 nm of Au/Pd (Quorum Technologies Q150T).

SEM imaging was performed using a JEOL SEM 7001 instrument (acceleration voltage 10 kV). The localisation of laser-irradiated zones was achieved adapting a mapping method published before. Starting with a bright-field confocal image map (see Figure 3a), obtained as described above, the irradiated areas were identified at low magnification SEM (see Figure 3b), and then re-localised at increasing magnifications.

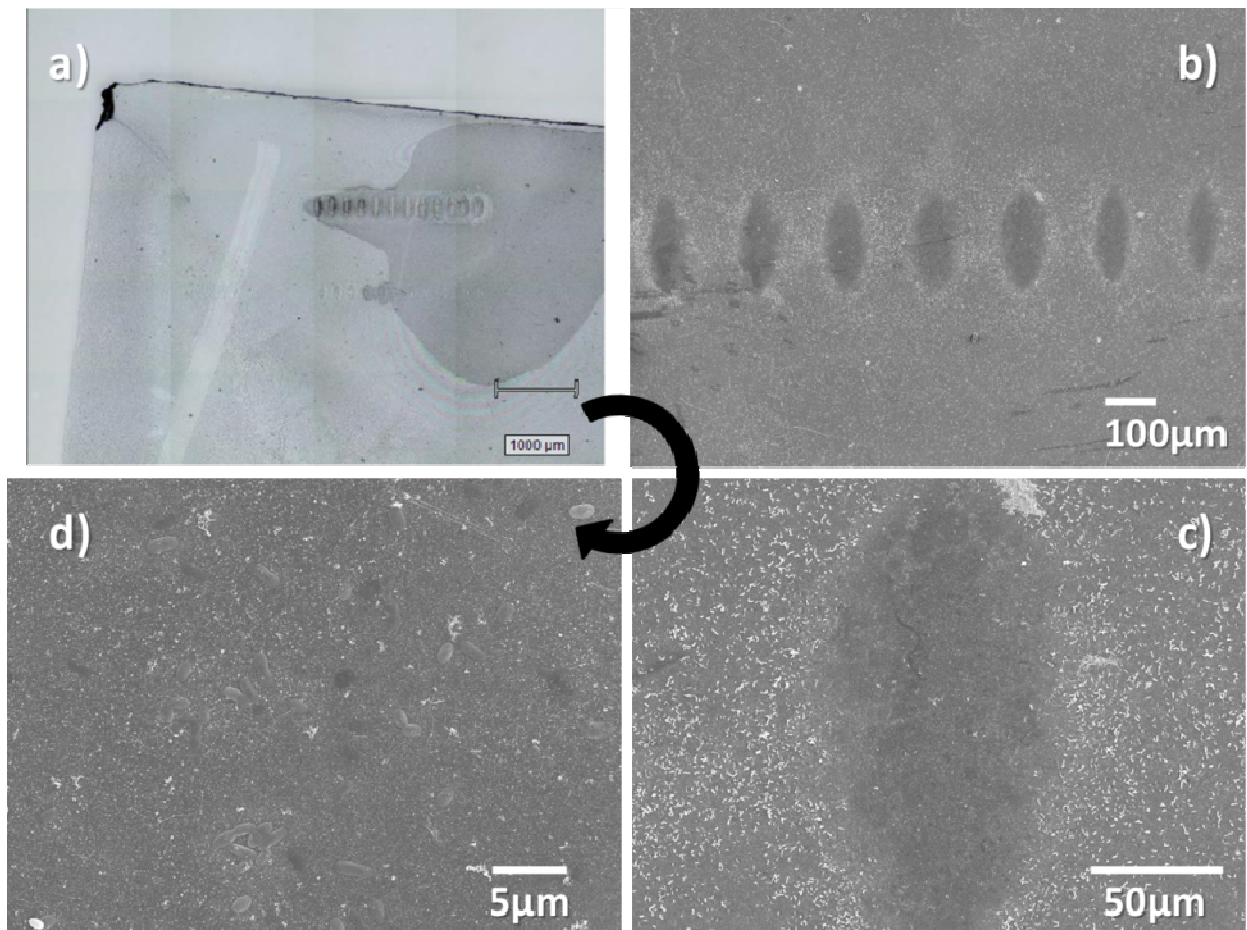


Figure 3: typical confocal (a) and SEM images (c-d) of *E. coli* on Type III surfaces irradiated with 100% laser power and 5x objective lens, showing the process of localisation of the irradiated spots using the mapping method based on increasing magnifications.¹⁴ Equivalent mapping processes were performed for all the samples.

¹⁴ S. Syrenova; C. Wadell; F.A.A. Nugroho; T.A. Gschneidner; Y.A.D. Fernandez; G. Nalin; D. Świtlik; F. Westerlund; T.J. Antosiewicz; V.P. Zhdanov; K. Moth-Poulsen; C. Langhammer; *Nature Materials*, **2015**, 14, 1236–1244.

2.1.3 RESULT AND DISCUSSIONS

2.1.3.1 CHARACTERIZATION

As already stated in the introduction, the most of the inorganic antibacterial surfaces are based on the release of metal cations with intrinsic biocidal properties;¹⁵ a typical example of this approach, is the sustained action of Ag⁺ release from a monolayers of silver nanoparticles (AgNPs) anchored on the surface of a bulk materials.¹⁶ A classic example coming from our laboratory is represented by systems which can be prepared by functionalizing the surfaces with self-assembled monolayers featuring grafting functions for the bulk material and suitable adhesive functional groups for silver nanoparticles (e.g. *mercaptopropyltrimethoxy silane* - MPTS;¹⁷ *aminopropyltrimethoxy silane* - APTES¹³), followed by surface dip-coating in AgNPs colloidal solutions. These surfaces reduce of 5-7 orders of magnitude the colony forming units (CFU) of planktonic *Escherichia coli* (*E. coli*) and *Staphylococcus aureus* (*S. aureus*)¹⁹ and of 5 orders of magnitude the surviving fraction of *Staphylococcus epidermidis* (*S. epidermidis*) biofilms.¹⁴ Recently, a photo-thermal approach for antibacterial surfaces also emerged, using monolayers of gold nanostars (GNSs) grafted on MPTS-coated glass surfaces.¹⁸ GNSs are biologically inert but, as it was explained in Chapter 1, have at least one localized surface plasmon resonance (LSPR) band which can be placed in the bio-transparent nIR window.¹⁹ These GNSs irradiated through tissues with a 800 nm laser undergo thermal relaxation and local temperature increase leading to eradication of *S. epidermidis* biofilms.¹⁹

The idea of combining favourable features of different nanoparticles in the same nanomaterial, led us to imagine innovative glass surfaces integrating both approaches, and featuring a dramatically enhanced antibacterial activity against *S. aureus* and *E. coli*, attributed to the synergy between the AgNPs monolayer and the local temperature increase upon nIR irradiation of the underlying GNSs monolayer. The glass slides go through a multi-step coating process sketched in Figure 4. GNSs were prepared in bi-distilled water using our established seed-growth method,²⁰ yielding colloidal

¹⁵ S. Chernousova; M. Epple; *Angew. Chem. Int. Ed.*, **2013**, 52, 1636–1653.

¹⁶ M.L.W. Knetsch; L.H. Koole; *Polymers* **2011**, 3, 340-366.

¹⁷ P. Pallavicini; A. Taglietti; G. Dacarro; Y.A.D. Fernandez; M. Galli; P. Grisoli; M. Patrini; G.S. De Magistris; R. Zanoni; *J. Colloid Interf. Sci.*, **2010**, 350, 110-116.

¹⁸ P. Pallavicini; A. Donà; A. Taglietti; P. Minzioni; M. Patrini; G. Dacarro; G. Chirico; L. Sironi; N. Bloise; L. Visai; L. Scarabelli; *Chem. Commun.*, **2014**, 50, 1969-1971.

¹⁹ V.G. Martinez; S. Barbosa; I.P. Santos; L.M.L. Marzán; *Curr. Opin. Colloid Interface Sci.*, **2011**, 16, 118–127.

²⁰ A. Casu; E. Cabrini; A. Donà; A. Falqui; Y.D. Fernandez; C. Milanese; A. Taglietti; P. Pallavicini; *Chem. Eur. J.*, **2012**, 18, 9381-9390.

suspensions of asymmetric penta-twinned branched gold nanoparticles (Figure 5A) with main LSPR centred at ~800 nm (Figure 5B, grey dashed line).

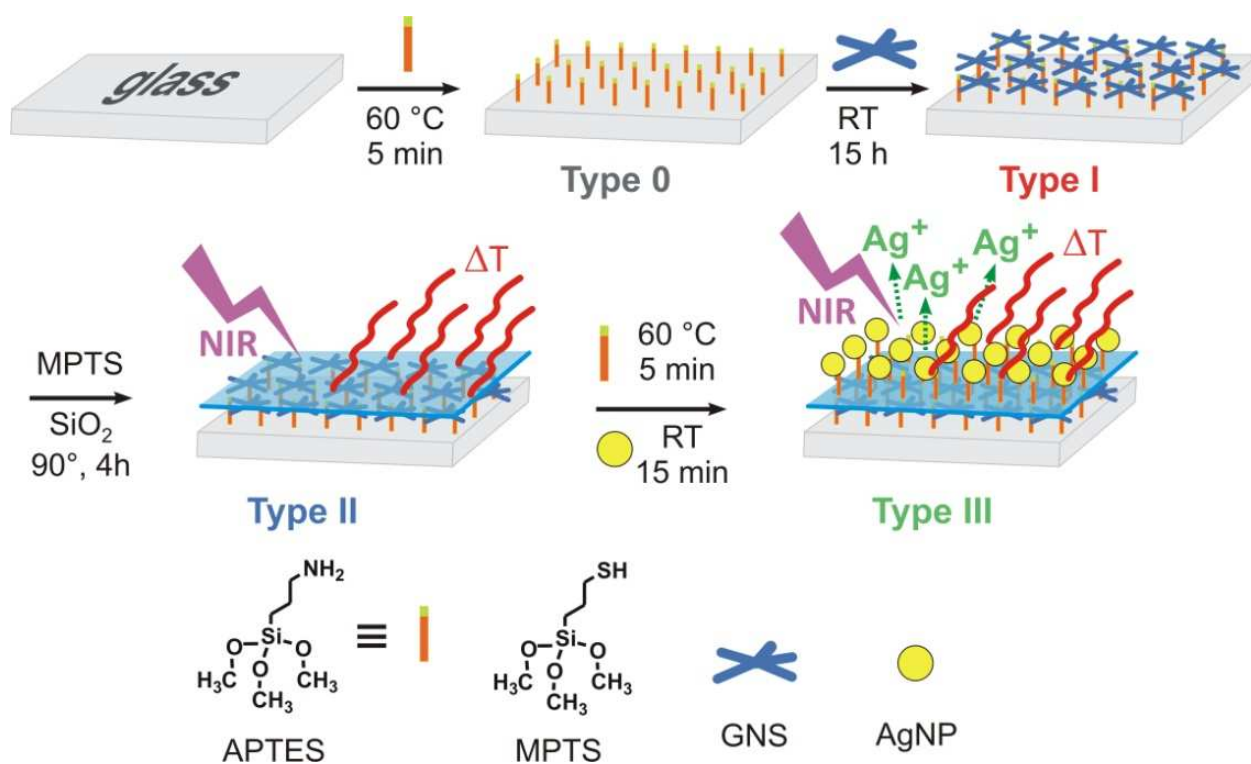


Figure 4: Synthetic scheme of the preparation of Type I-III glasses.

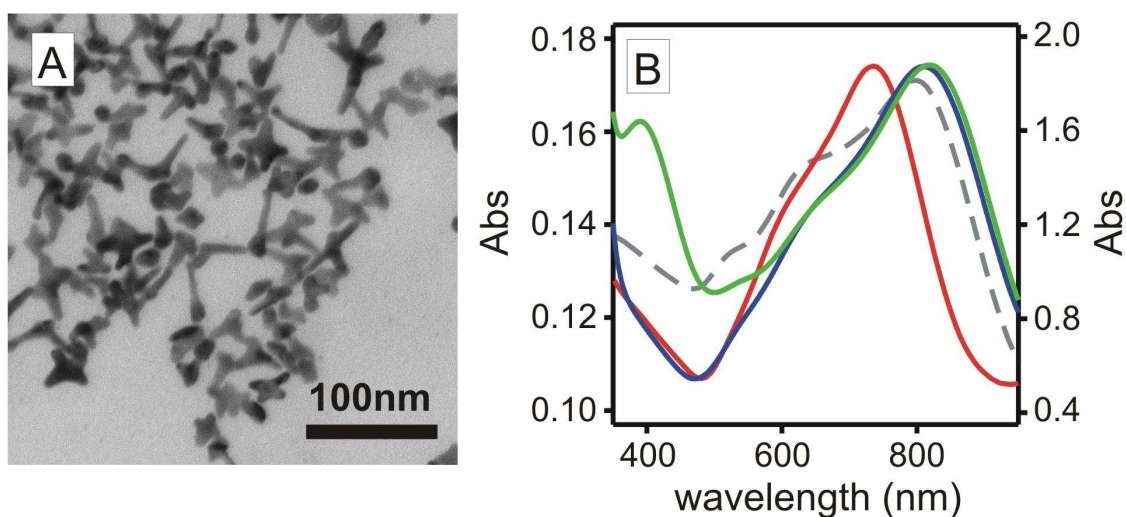


Figure 5: A) TEM image of a typical colloid of GNSs used in this work. B) UV-Vis spectrum of typical GNSs colloidal solution (grey dashed line). UV-Vis spectrum of Type I glass (red full line). UV-Vis spectrum of Type II glass (blue full line). UV-Vis spectrum of Type III glass (green full line).

Table 1: list of abbreviation.

TYPE	Description
0	<i>Glass APTES</i>
I	<i>Glass APTES GNSs</i>
II	<i>Glass APTES GNSs MPTS SiO₂</i>
III	<i>Glass APTES GNSs MPTS SiO₂ APTES AuNPs</i>

Type 0 slides were prepared as reported in paragraph 2.1.2.3. Use of APTES allows a significant time shortening of the procedures as compared with MPTS monolayer formation. Efficiency of silanization was routinely controlled with contact angle measurements: a sensible increase in hydrophobicity was obtained, showing a mean value of 55(6)°, which is in good agreement with data reported in literature for the formation of an -NH₂ self-assembled monolayer (SAM).²¹ After this step, amino terminated glass slides were immersed in a colloidal suspension of GNSs (Au = 0.06 - 0.07 g/L) described in Paragraph 1.3.1.

Type I slides were thus obtained thanks to the electrostatic interaction of the negatively charged GNSs ($Z = -12$ mV) with the positively charged amino-groups of grafted APTES, that are protonated at the acidic pH (~3) of the GNSs colloid. The weak nature of the LSB-Au²² interaction favours the facile LSB surface displacement by the APTES ammonium groups and efficient GNSs adhesion. The first indication of the deposition of objects on the APTES functionalized slides comes from direct observation of the blue colour of the slides. The quantity of grafted GNSs was controlled by setting the dipping time, showing an increase of absorbance vs time in the UV-Vis-nIR spectra of Type I slides (Figure 6), and confirmed by quantitative analysis of grafted gold and silver (10% Ag vs Au atoms, as in the growth solution of the GNSs).

²¹ J.A. Howarter; J.P. Youngblood; *Langmuir*, **2006**, 22, 26, 11142e7.

²² L. Sironi; S. Freddi; M. Caccia; P. Pozzi; L. Rossetti; P. Pallavicini; A. Donà; E. Cabrini; M. Gualtieri; I. Rivolta; A. Panariti; L. D'Alfonso; M. Collini; G. Chirico; *Journal of Physical Chemistry C*, **2012**, 116, 34, 18407-18418.

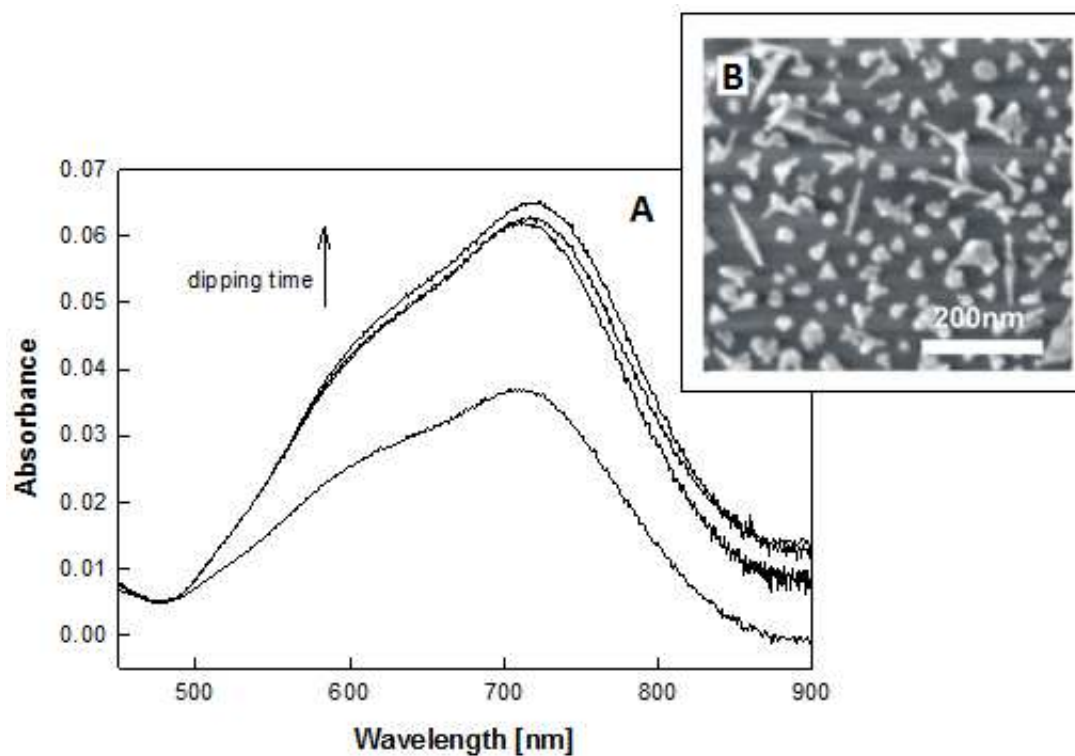


Figure 6: A) Absorption spectra (Abs vs wavelength, normalized at 480 nm) on Type I slides removed from the GNSs solution jar at different times (1, 3, 14 and 24 hours) B) HR-SEM image of Type I glass.

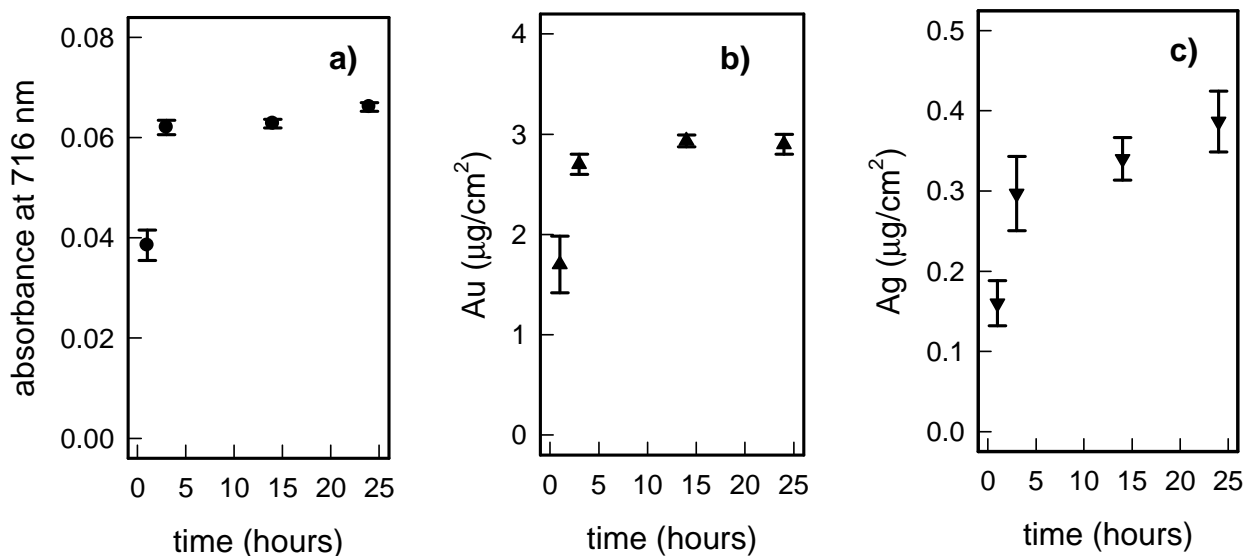


Figure 7: a) absorbance of Type I samples at λ_{max} as a function of immersion time; b) surface concentration of gold as a function of immersion time for the same series (mean values on 3 samples removed from GNSs solution at the same time); c) surface concentration of silver as a function of immersion time for the same series (mean values on 3 samples removed from GNSs solution at the same time)

Maximum surface density was reached after 3-6 h, but to ensure saturation, we adopted a 14 h dipping time, obtaining as shown in Figure 6 and 7, Au surface concentrations of 3.0(0.5) $\mu\text{g}/\text{cm}^2$ (average of 16 samples).

In figure 5B a spectra measured with a simple UV-Vis spectrophotometer on a Type I sample, obtained after 14 hours of dipping in the colloidal suspension, is shown (full red line spectra), and compared with the original spectra of the colloidal suspension used (grey dashed line spectra): a LSPR blue shift of 58(9) nm (average on 48 glass samples, six preparations coming from three different colloidal suspension) is observed when moving from the colloidal suspension in water to the monolayer on glass in air, due to change of local refractive index. Contact angle measurements on these samples gave a value of 37(4) $^\circ$. SEM images of a type I samples after 14 hours of dipping are reported in Figure 6B, showing the unchanged objects morphology and the very uniform, continuous and homogeneous distribution which is obtained for a typical preparation, features which were already observed for similar monolayers of the same objects grafted on a MPTS functionalized glass, or for different anisotropic gold nano-object grafted on amino-terminated ITO glass samples.²³ Type I samples are stable in air for at least a couple of weeks, while after one month we observed changes in colour and LSPR spectra, moreover they are sensitive to rubbing, mechanical scratching and humidity.²⁴

On Type I surfaces, a monolayer of MPTS was then self-assembled: contact angle was measured after this step, and the value moved to 66(4) $^\circ$, demonstrating the formation of the layer, with the sulphur atoms being reasonably bound to gold surfaces and the alcoxysilane moieties exposed to the solution. The $-\text{Si}(\text{OCH}_3)_3$ groups of the alcoxysilane terminations are reactive towards Na_4SiO_4 aqueous solution, and can form a SiO_2 overlayer, according to previously described methods which are reported to give a silica layer of about 4-5 nm thickness under proper conditions.²⁵ Through this synthetic step it is possible to obtain the Type II slides. UV-Vis spectra showed a red shift of about 60(15) nm as shown in Figure 5B (blue full line), calculated on the basis of 12 samples coming from three different preparation batches (as compared to relative starting Type I samples), as expected from the increase in the effective refractive index of the adjacent medium, which turns to be silica instead of air.²⁶ Interestingly, prolonged sonication in water or scratching with hard surfaces did not have any effect on the samples integrity,

²³ Q. Su; X. Ma; J. Dong; C. Jiang; W. Qian; *Acs Applied Materials & Interfaces*, **2011**, 3, 6, 1873-1879.

²⁴ B. Bassi; Funzionalizzazione multistrato di vetri: nano materiali complessi per applicazioni antibatteriche; *Master Thesis in Chemistry*, **2012-2013**.

²⁵ N. Irit; T.A. Bendikov; I. Doron-Mor; Z. Barkay; A. Vaskevich; I. Rubinstein; *J. Am. Chem. Soc.*, **2007**, 129, 84-92.

²⁶ T.A. Bendikov; A. Rabinkov; T. Karakouz; A. Vaskevich; I. Rubinstein; *Analytical Chemistry*, **2008**, 80, 19, 7487-7498.

evidencing that the silica treatment is effective in protecting the GNSs monolayer from detachment, as they are placed under a silica coating (see Figure 8a).

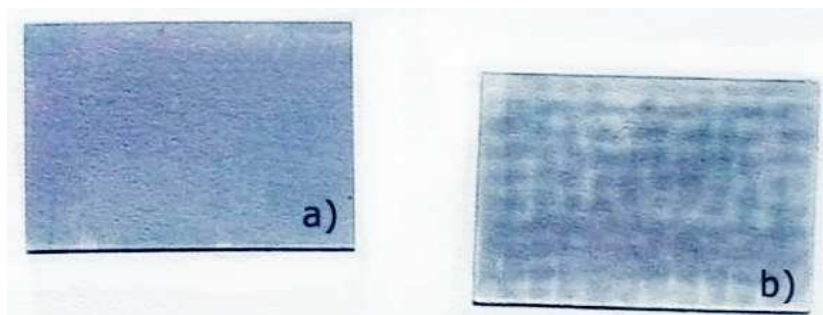


Figure 8: photograph of Type II (a) and Type I (b) glasses after 1 minute of sonication.

Contact angle on Type II samples gave non-measurable values: the water drop did completely spread over the surface, indicating a very high hydrophilicity, caused by the presence of an high number of active $-OH$ groups on the surface after the silanization step. These slides were further over-coated with APTES by the same procedure described above to silanize glass slide to obtain the Type I, in order to produce samples named glass|APTES|GNSs|MPTS| SiO_2 |APTES. Exploiting the positive charge caused by the presence of ammonium groups brought by the layer obtained with APTES, it was then possible to graft on top a further layer of negatively charged citrate-coated AgNPs ($d=9$ nm),²⁷ obtaining Type III surfaces (UV-Vis spectrum are shown in Figure 5B green full line).

Summing up, as shown in Figure 5B, these multiple synthetic steps were clearly followed by changes in UV-Vis-NIR spectra: GNSs undergo a LSPR blue shift ($\Delta\lambda = -58(9)$ nm) from colloidal solution (grey dotted line) to Type I monolayers on glass (red line), attributed to the decrease of local refractive index from water ($n=1.3339$) to air ($n=1.0003$) at the interface.²⁸ Addition of MPTS gives a $\Delta\lambda = +8(2)$ nm (spectrum not shown), and the formation of the SiO_2 over layer in Type II glasses produces a further red shift ($\Delta\lambda = +60(15)$ nm, blue line in Figure 5B) due to the local n increase ($n=1.4585$ for SiO_2). The SiO_2 coating of Type II slides was analysed by AFM imaging, and a thickness of $\sim 4-5$ nm was estimated (Figure 9).

²⁷ R.M. Bright; M.D. Musick; M.J. Natan; *Langmuir*, **1998**, *14*, 5695-5701.

²⁸ K.M. Mayer; J.H. Hafner; *Chem. Rev.*, **2011**, *111*, 3828-3857.

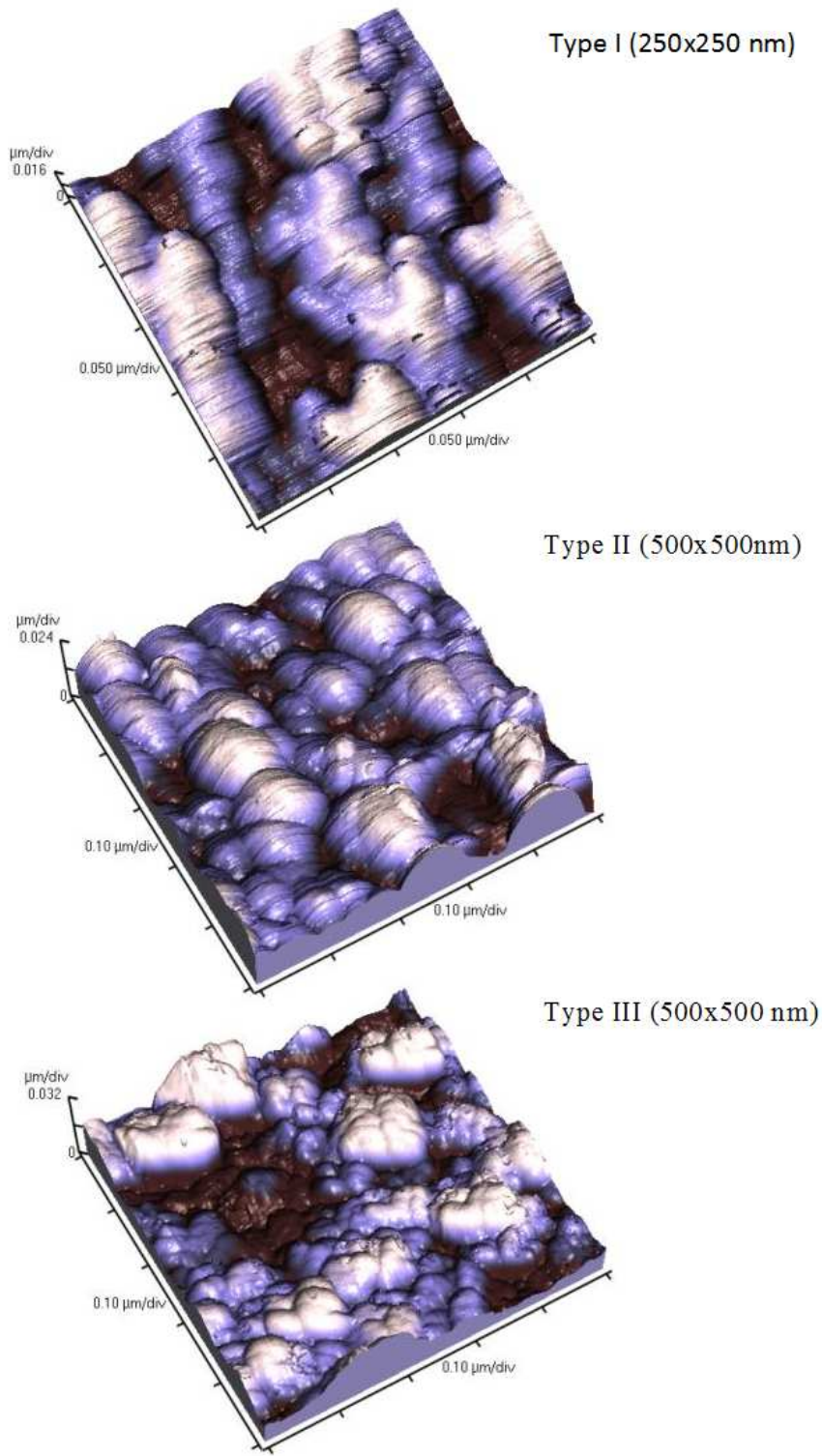


Figure 9: AFM images of different type of glasses.

In the AFM images above (Figure 9), changes in morphology, between Type I and Type II, and between Type II and Type III are evident. In particular, on stepping from Type I to Type II larger and smoother hills are observed. The average height of these hill-shaped

objects is 20(4.1) nm (ten objects were measured with a line analysis of the image). This value can be compared with an average height of 16(4.6) nm measured on the anisotropic objects present in Type I, allowing a rough estimation of silica layer thickness of about 4-5 nm. It has to be noted that in AFM imaging, the size of nano-objects is apparently larger, due to the well-known convolution effect of AFM tips on nanometer size objects.²⁹

Table 2: line analysis of AFM images.

Line analysis heights of object [nm]	
Type I	Type II
8.2	23.5
16.6	20.7
22.8	22.0
13.0	26.9
14.7	16.1
22.5	17.1
15.1	16.4
13.3	
13.2	
20.1	
average: 16.0 nm	average: 20.4 nm
st. dev: 4.6	sd dev: 4.1

²⁹ K.C. Grabar; K.R. Brown; C.D. Keating; S.J. Stranick; S.L. Tang; M.J. Natan; *Anal. Chem.*, **1997**, 69, 471-483.

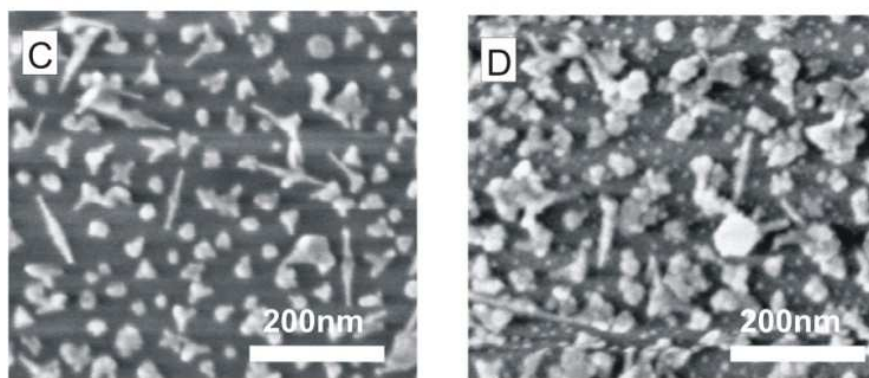


Figure 10: HR-SEM image of (C) Type II and (D) Type III surfaces.

Large shifts and shape variations in LSPR bands are predicted for spherical and rod-like Ag and Au nanoparticles aligned at short distances (<10 nm).^{30,31} This is not observed here. Although by AFM imaging we can only approximately estimate the SiO₂ layer thickness, SEM images support a thickness compatible to 4 nm calculated value. Both the different nature of Ag and Au and the particular geometry of the AgNPs-GNSs arrangement (small spheres on large branches sides) may lead to poor plasmon resonances hybridization³¹ and to the negligible spectral changes observed here. However, absorption spectra of Type III slides (green line, Figure 5B) showed the additional LSPR band of AgNPs at 394 nm.¹⁷ Analysis of Type III surfaces after full oxidation with *aqua regia* (Table 3) confirmed Ag surface concentration a 0.6 $\mu\text{g}/\text{cm}^2$.

³⁰ L.L. Zhao; K.L. Kelly; G.C. Schatz; *J. Phys. Chem. B*, **2003**, 107, 7343-7350.

³¹ S.D. Liu; M.T. Cheng; *J. Appl. Phys.*, **2010**, 108, 034313.

Table 3: quantities of noble Ag and Au found in solution (ICP-OES measurements) after treatment of samples in *aqua regia*, expressed as micrograms per area unit on the samples. Data are averages of least three independent samples. Standard deviations for each data set are reported between parenthesis.

sample	Au ($\mu\text{g}/\text{cm}^2$)	Ag ($\mu\text{g}/\text{cm}^2$)
Type I	3.0 (0.5)	0.32 (0.03)
Type II	2.7 (0.3)	0.30 (0.03)
Type III	2.8 (0.3)	0.90 (0.1)

This value is comparable to the silver concentration on AgNPs grafted on APTES-functionalised flat glass ($0.73 \mu\text{g}/\text{cm}^2$).¹³ A full monolayer of AgNPs gave a contact angle of 32° , therefore also in this case a mixed surface can be hypothesised, having a sub-monolayer of AgNPs and SiO_2 still exposed at the interface.

AgNPs have an average diameter of 9 nm (comparable to the typical dimension of this kind of nanoparticles)¹³ and a volume of $3.81 \times 10^{-19} \text{ cm}^3$ for one AgNPs, corresponding to $4.00 \times 10^{-18} \text{ g}$ per AgNP (Ag density = $10.49 \text{ g}/\text{cm}^3$). According to ICP-OES, the Ag surface density is $0.60 \mu\text{g}/\text{cm}^2$, equivalent to $1.5 \times 10^{11} \text{ AgNPs}/\text{cm}^2$.

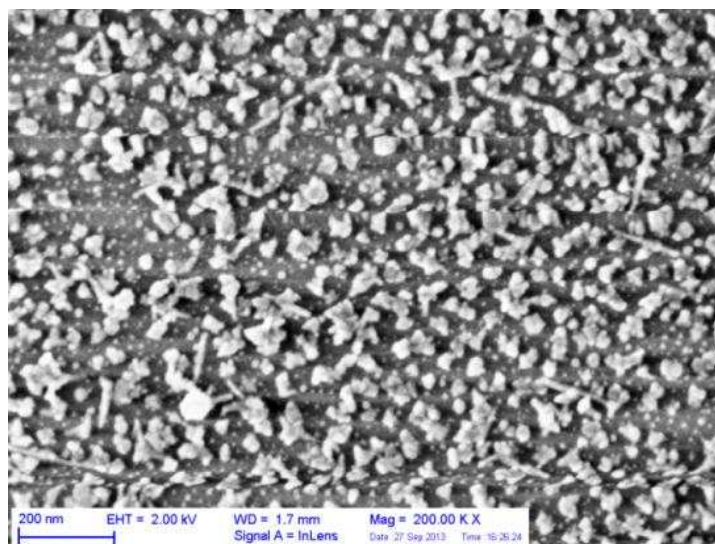


Figure 11: HR-SEM image of a Type III slide.

Using HR-SEM images (Figure 11) we have attempted to count the number of AgNPs on a $200 \times 200 \text{ nm}$ area ($4.00 \times 10^{-10} \text{ cm}^2$, $\sim 45 \text{ NPs}$), focusing primarily on the SiO_2 zones, since

on top of GNSs the contrast was not sufficiently high to individuate the AgNPs. With this direct SEM measurement, we have estimated a surface density of 1.13×10^{11} AgNPs/cm², in good agreement with the ICP-OES data discussed above. Curiously, these values are slightly lower than the surface density reported before for AgNPs monolayers on APTES functionalised flat glass (1.83×10^{11}).¹³

SEM BSD (backscattered electron detection) on Type II and Type III surfaces (Figure 12), allowed direct observation of the GNSs monolayer within the cross-section of the samples.

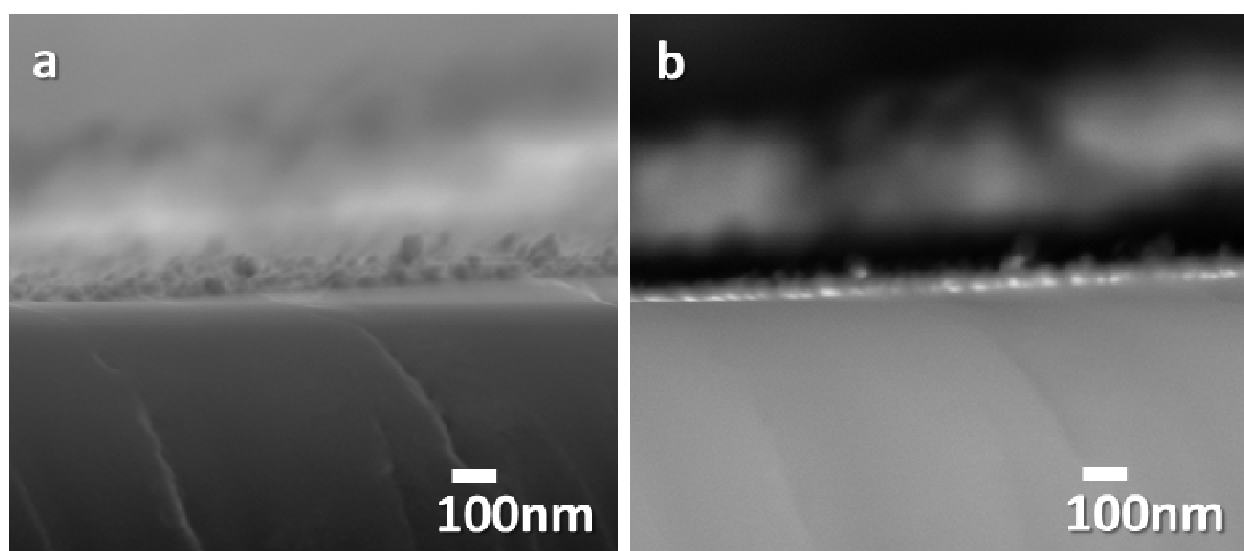


Figure 12: SEM BSD imaging for type III surfaces. Representative cross-section Scanning Electron Microscopy images of type II surfaces. a) Secondary electron detector image showing the topography of the surface. b) Back Scattering Detector (SEM-BSD) image showing electron density contrast at the cross section. The brightest spots in (b) represent the gold nano-stars on the glass surface (bottom), immersed on the SiO₂ coating. Images were taken with acceleration voltage 15 kV.

The electron dense GNSs appeared in the SEM BSD images as bright spots aligned to the sample surface and inserted within the multilayer structure (Figure 12B). In the cross-section view, the increased roughness of the SiO₂ could be also observed, while AgNPs were too small to be imaged.

As already described above, the SiO₂ layer on Type II slides drastically increases the mechanical stability of the GNSs monolayer from scratching and ultrasound treatment. Moreover, GNSs over-coated with SiO₂ in Type II surfaces do not release Ag⁺ cations from Ag⁰ contained within the GNSs Au lattice.¹⁹ Type II slides were kept in 3 mL of water for 5 h and 24 h and no Ag (or Au) was detected in the aqueous phase (see Table 4).

Table 4: Metal release from Type I-III surfaces in water. Quantities of noble metal released, after different immersion time in bi-distilled water for the three different types of samples, expressed as released micrograms per area unit. The value means an average values coming from at least three samples and standard deviations reported between parenthesis. u.d.l. indicate a quantity under detection limit of the instrument.

Sample (immersion time)	Au ($\mu\text{g}/\text{cm}^2$)	Ag ($\mu\text{g}/\text{cm}^2$)
Type I (5 hours)	u.d.l.	0.026 (0.02)
(24 hours)	0.006 (0.004)	0.028 (0.02)
Type II (5 hours)	u.d.l.	u.d.l.
(24 hours)	u.d.l.	u.d.l.
Type III (5 hours)	u.d.l.	0.18 (0.03)
(24 hours)	u.d.l.	0.21 (0.01)

Similar experiments on Type III slides (bearing AgNPs directly exposed to water) yielded an Ag^+ release of $0.18(0.03) \mu\text{g}/\text{cm}^2$ and $0.21(0.01) \mu\text{g}/\text{cm}^2$ after 5h and 24h, respectively. These Ag^+ concentrations correspond to 30% and 35% of the total silver contained in the AgNPs over-layer.

2.1.3.2 PHOTOTHERMAL RESPONSE

On the other hand, the UV-Vis-nIR transparent SiO₂ layer did not inhibit the photo-thermal response of the GNSs monolayer upon nIR irradiation (800 nm). By using a continuous LASER source tuned on the LSPR maximum, able to deliver variable irradiances (0.2–2.5 W/cm²), we have tested Type I-III samples containing the same GNSs surface concentration. Upon LASER irradiation, the surfaces experienced a time-dependent temperature increase that was directly measured using a thermocamera. The efficient photo-thermal properties of the GNSs used in this work have been already demonstrated in their colloidal solutions when grafted on a SAM obtained with MPTS on glass.¹⁸ In this work type I, type II and type III samples were tested, coming from the same preparation set. The slides were irradiated with continuous LASER sources tuned on the proper λ_{\max} of LSPR, using increasing irradiation power. The thermogram profiles (Figure 13) are characterised by a sharp temperature increase, followed by a plateau, that can be rationalised considering the balance between photo-thermal conversion of incident light and heat dissipation from the surface.

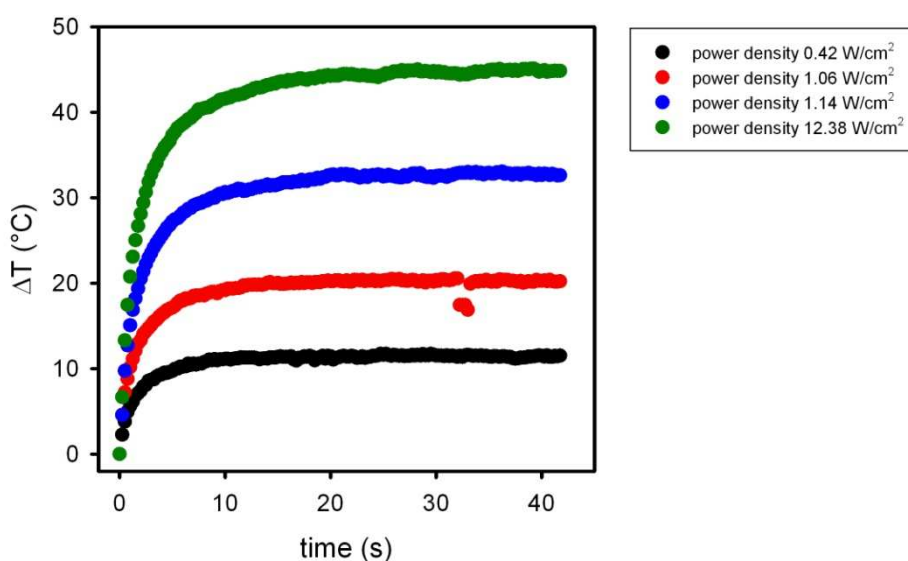


Figure 13: thermograms (ΔT vs time) for Type II surfaces at different irradiances (see figure for legend). ΔT are calculated from thermocamera data, i.e. from the temperature read on the slide surface at the plateau, with respect to starting T . Similar ascending/plateau profiles were observed for all Type I-III surfaces, at all irradiance (power density) values investigated.

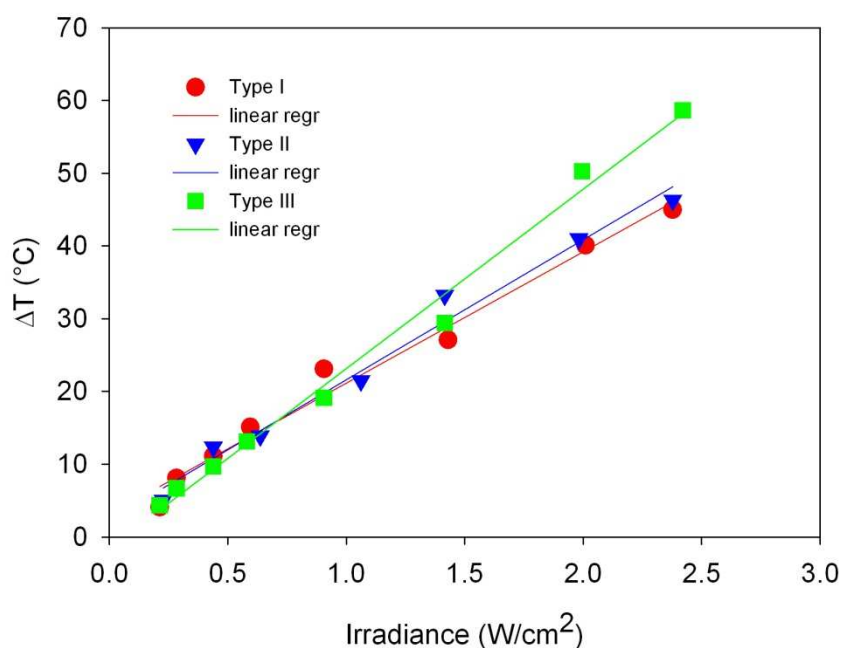


Figure 14: trends of T_{\max} vs power density (irradiance) for Type I-III slides. Linear regression lines evidence almost superimposable trends.

ΔT linearly increases from 2-3 to more than 40°C when applied LASER power increases from 15 to 171 mW (with irradiances ranging between 0.44 and 5.4 W/cm²). Steep ascending-plateau profiles with a rapidly reached maximum equilibrium temperature (<20 s) is observed. The most interesting observation is that no variations in the relation between applied power and temperature increase are observed when changing the sample type (as shown in Figure 14), providing that the irradiation wavelength is tuned on the λ_{\max} of LSPR. The three slopes between applied laser power and temperature reached are almost identical for all the three type of sample. In other words, LASER irradiation of the GNSs monolayer at their nIR LSPR results in the same, efficient photo-thermal conversion, independently from the presence of further coatings (with MPTS, SiO₂, APTES and AgNPs), which do not affect at all the photo-thermal features of the GNSs grafted layer.

The thermograms in Figure 13 can be explained considering a very simple physical model that accounts for the photo-thermal conversion of the incident light and the heat dissipation from the surface. Under linear regime, considering constant incident irradiance P and constant ambient temperature T_0 , the heat conservation balance leads to the following time-dependent differential equation for the temperature change at the surface:

$$\frac{\partial \Delta T}{\partial t} = \sigma \cdot P - \theta \cdot \Delta T \quad (3)$$

Where ΔT represents the temperature increase at the surface with respect to the surroundings, and the constants σ and θ accounts for the photo-thermal conversion efficiency of the surface and the heat dissipation from the surface, respectively. This differential equation has an analytical solution that can be expressed in terms of the irradiance-dependent plateau temperature (T_{max}):

$$\Delta T = T_{max} (1 - e^{-\theta \cdot t}) \quad (4)$$

The equation above describes the main features of the thermograms shown in Figure 13: starting with $\Delta T=0$ for $t=0$, followed by a very sharp increase in temperature, until reaching a plateau at T_{max} . Another interesting feature of this expression is that the time dependent term is influenced by the thermal properties of the material, while the plateau temperature (T_{max}) is determined by the equilibrium between heat dissipation and photo-thermal conversion, according to the expression:

$$\theta \cdot T_{max} = \sigma \cdot P \quad T_{max} = \frac{\sigma}{\theta} \cdot P \quad (5)$$

can be re-written as

Describing the linear dependence, experimentally observed, between T_{max} and P , as depicted in Figure 14. Moreover, this expression provides physical meaning for the slopes of these linear trends in Figure 14, as being the ratio between the photo-thermal efficiency and the heat dissipation constants determining the thermogram profiles. Interestingly, the slopes in Figure 14 for Type I, Type II, and Type III surfaces are very similar, suggesting that the presence of thin over-layers is not significantly interfering with the photo-thermal behaviour of the surfaces, when irradiated by a LASER in the nIR spectral region. However, in previous work^{32,33} it was demonstrated that these thermogram profiles can be better described by a double exponential growth, with two growth periods (τ_1 and τ_2) and two characteristic plateau temperatures (ΔT_1 and ΔT_2):

³² P. Pallavicini; S. Basile; G. Chirico; G. Dacarro; L. D'Alfonso; Alice Donà; M. Patrini; Andrea Falqui; L. Sironi; A. Taglietti; *Chem. Commun.*, **2015**, 51, 12928-12930.

³³ S. Freddi; L. Sironi; R. D'Antuono; D. Morone; A. Donà; E. Cabrini; L. D'Alfonso; M. Collini; P. Pallavicini; G. Baldi; D. Maggioni; G. Chirico; *Nano Lett.*, **2013**, 13, 5, 2004-2010.

$$\Delta T = \Delta T_1 \left(1 - e^{-\frac{t}{\tau_1}}\right) + \Delta T_2 \left(1 - e^{-\frac{t}{\tau_2}}\right) \quad (6)$$

In this expression, the increase of the overall plateau temperature at the surface is:

$$T_{\max} - T_0 = \Delta T_1 + \Delta T_2 \quad (7)$$

To account for this experimental evidence, here we have introduced a non-linear perturbation in our model, by considering the increase of the temperature at the interface in close proximity with the surface (e.g. glass and air). Therefore, the heat-balance differential equation can be re-written:

$$\frac{\partial(T - T_0)}{\partial t} = \sigma \cdot P - \theta \cdot [T - T_{int}(t)] \quad (8)$$

It is important to note that in this expression, T_0 is the initial ambient temperature (i.e. before irradiation), while $T_{int}(t)$ is the time-dependent interface temperature of the surroundings of the surface (i.e. $T_{int}(0) = T_0$), where the heat exchange takes place. Combining the empirical double exponential growth equation above and this modified differential equation, we obtained an expression for the interface temperature as a function of time:

$$T_{int}(t) = T_0 - \Delta T_1 \left(1 - \frac{1}{\theta \cdot \tau_1}\right) e^{-\frac{t}{\tau_1}} - \Delta T_2 \left(1 - \frac{1}{\theta \cdot \tau_2}\right) e^{-\frac{t}{\tau_2}} \quad (9)$$

Where the following condition must be satisfied (equivalent to the assumption $T_{int}(0) = T_0$):

$$\theta = \frac{\Delta T_1 / \tau_1 + \Delta T_2 / \tau_2}{\Delta T_1 + \Delta T_2} \quad (10)$$

Substituting this expression in the equation for $T_{int}(t)$, we obtain the general expression:

$$T_{int}(t) = T_0 + \alpha \left[e^{-\frac{t}{\tau_1}} - e^{-\frac{t}{\tau_2}} \right] \quad (11)$$

Where the parameter α is related to the empirical fitting constants as follows:

$$\alpha = \frac{\Delta T_1 \cdot \Delta T_2 (\tau_2 - \tau_1)}{\tau_2 \cdot \Delta T_1 + \tau_1 \cdot \Delta T_2} \quad (12)$$

From the expression for $T_{\text{int}}(t)$ it is clear that irrespectively of the value of α , the exponential terms cancel each other at $t=0$, and the condition $T_{\text{int}}(0)= T_0$ is satisfied. Additionally, since the exponential terms between brackets and the parameter α have always opposite signs, the behaviour of the function describing the interface temperature is characterised by a sharp increase, until reaching a maximum at:

$$t_m = \frac{\tau_1 \cdot \tau_2}{\tau_1 - \tau_2} \ln \left(\frac{\tau_1}{\tau_2} \right) \quad (13)$$

And then $T_{\text{int}}(t)$ experiences an exponential decrease until reaching again the limiting value of T_0 . We interpreted this peculiar behaviour of $T_{\text{int}}(t)$ as the result of overheating in the first few seconds of irradiation when, due to the thermal conversion of the intense and coherent laser light, the temperature rises too fast to allow the surrounding material (glass, air) to dissipate the local heat. This situation is then equilibrated, and the overheating effect vanishes at longer times, as the plateau equilibrium temperature is achieved and the system reaches stationary conditions, resembling the non-perturbed linear behaviour. The maximum equilibrium temperatures indicated in Figure 13 were reached within 10 s, and the absolute increase ($\Delta T = T_{\text{plateau}} - T_0$) varied from 5 to $\sim 50^\circ\text{C}$ at different LASER power densities, with no significant differences between Type I-III surfaces.

2.1.3.3 ANTIMICROBIAL ACTIVITY

The intrinsic antimicrobial activity of Type III surfaces against *E. coli* and *S. aureus* was investigated in absence of irradiation. In order to study the antibacterial abilities of functionalized surfaces, an experimental protocol to evaluate the microbicidal effect (ME)¹³ within thin liquid films in contact with functionalized surfaces can be used:

$$ME = \log N_C - \log N_E \quad (14)$$

where N_C and N_E are the number of CFU/mL developed on non-functionalised control glass and on active surfaces, respectively.

Table 5: microbicidal effect on planktonic bacteria for non-irradiated surfaces (ME) and after laser irradiation (TME).

	ME (Type III) 5 h	ME (Type III) 24h	TME (Type II) 0.5 h	TME (Type III) 0.5 h
<i>E. coli</i>	1.7	5.4	1.6	> 6.0
<i>S. aureus</i>	0.7	1.6	1.2	> 6.0
	Static Ag ⁺ release		Photo-thermal	Combined

For Type III slides, after contact times of 5 h and 24 h, a significant bactericidal effect was observed (Table 5), as expected from the presence of the AgNPs over-layer on these surfaces. Longer contact times (24 h vs 5 h) are needed to obtain larger ME values, and the effects are stronger against *E. coli* with respect to *S. aureus*, as previously reported.¹⁸ Control experiments with Type II slides (SiO₂ contact surface, absence of Ag⁺ release) show negligible ME (<<0.5) after 5 h and 24 h for both bacterial strains investigated.

The microbicidal effect exerted against planktonic bacteria by photo-thermal action upon nIR irradiation, was then investigated for Type II and Type III samples. Surface irradiation was carried out for 0.5 h with a 800 nm continuous LASER source (irradiance 0.25 W/cm², $\Delta T = +5^\circ\text{C}$ measured at the air interface for all surfaces). In this case, the photo-thermal microbicidal effect, TME, was calculated as:

$$TME = \log N_{C_M} - \log N_T \quad (15)$$

where NT and NC_M are the number of CFU/mL developed on the modified glasses with and without LASER irradiation, respectively. When Type II slides were used, we exclusively observed the effect of local photo-thermal action, as no Ag^+ is released from these surfaces. At contact-irradiation times as short as 0.5 h, Type II slides, showed measurable TME values (1.2 and 1.6 for *S. aureus* and *E. coli*, respectively; Table 5). Irradiation control experiments performed using unmodified glass showed negligible TME values, suggesting that the photo-thermal effect arises from the GNSs and that direct LASER-radiation damage is not significant under our experimental conditions. Remarkably on Type III slides, after 0.5 h of irradiation, considerably higher TME values (>6) were observed for both *S. aureus* and *E. coli* (Table 5). This is an impressive effect, considering that: i) the static AgNPs action required much longer contact times (over 24 h) on Type III samples to reach ME values of 5.4 and 1.6 for *E. coli* and *S. aureus*, respectively; ii) the net photo-thermal action on Type II samples gave much lower TME values after 0.5 h. Therefore, the enhancement of TME observed for irradiated Type III slides must be due to the synergy between the local photo-thermal effect and the AgNPs antimicrobial action on both *E. coli* and *S. aureus*.

In addition to the planktonic experiments, we have investigated the antimicrobial effect on cells directly attached to the surfaces using SEM imaging, this aspect is particularly relevant considering that attached bacterial cells and biofilms play a critical role in infections associated with medical devices and are particularly difficult to eradicate *in vivo*. The morphology of attached bacterial cells before and after irradiation was investigated using recently developed SEM fixation and staining procedures,³⁴ able to preserve delicate biological structures at interfaces. Sterilised surfaces were covered with nutrient broth containing 10^5 CFU/mL of bacteria. The samples were protected from light, incubated at 37°C for 24 h, and then carefully rinsed with glucose buffer. The samples were subsequently kept in glucose buffer for immediate use. For each bacterial strain, three kinds of samples were investigated: i) control (non-functionalised glass), ii) Type II and iii) Type III surfaces. Selected areas of the samples were irradiated for 10 s using a 785 nm LASER installed in a Renishaw InVia Raman Spectrometer (shorter irradiation times were chosen to compensate for the higher power density of this LASER). Adapting a previously published surface-mapping method,³⁵ visible-light mapping of sample morphology was performed to aid the identification of the irradiated

³⁴ A. Susarrey-Arce; I. Sorzabal-Bellido; A. Oknianska; F. McBride; A.J. Beckett; J.G.E. Gardeniers; R. Raval; R.M. Tiggelaar; Y.A.D. Fernandez; *J. Mater. Chem. B*, **2016**, 4, 3104-3112.

³⁵ S. Syrenova; C. Wadell, F.A.A. Nugroho; T.A. Gschneidtner, Y.A.D. Fernandez; G. Nalin; K. Moth-Poulsen; C. Langhammer; *Nat. Mater.*, **2015**, 14, 1236-1244.

areas (Figure 3), adapting a surface-mapping method published before.³⁶ After irradiation, the samples were immediately processed for SEM. The localized irradiation of selected zones of the samples allowed us to utilise the remaining non-irradiated area as a dark-control.

SEM showed that in the absence of irradiation, the morphology of *E. coli* cells attached to the photoactive surfaces Type II and III was preserved (Figure 15a-c).

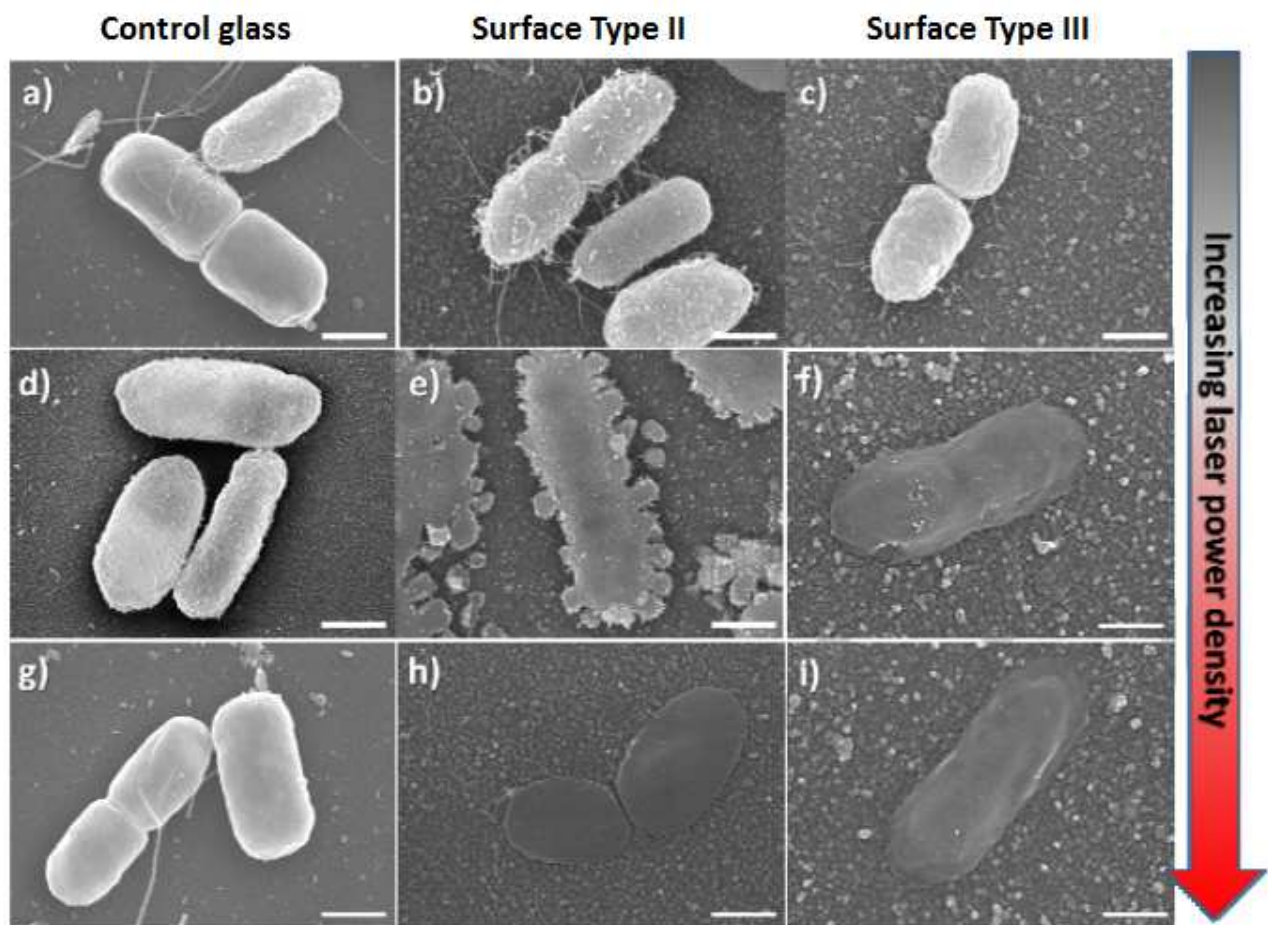


Figure 15: Representative SEM images showing the effect of LASER irradiation on *E. coli* cells attached to: (by column) a,d,g) Control glass; b,e,h) Type II surfaces (glass/GNSs/SiO₂); c,f,i) Type III surfaces (glass/GNSs/SiO₂/AgNP). Increasing power density: (by row) a,b,c) Non irradiated samples; Samples irradiated with: d,e,f) 5x objective lens; g,h,i) 20x objective lens. All scale bars are 500 nm.

We noted that the surface density of *E. coli* cells on the non-irradiated photoactive surfaces Type III was considerably lower than the cell density on control glass (Figure

³⁶ S. Syrenova; C.Wadell; F.A.A. Nugroho; T.A. Gschneidtner; Y.A.D. Fernandez; G. Nalin; D. Świtlik; F. Westerlund; T.J. Antosiewicz; V.P. Zhdanov; K. Moth-Poulsen; C. Langhammer; *Nat. Mater.*, **2015**, 14, 1236–1244.

16a-b), and attributed this to the intrinsic antimicrobial effect of AgNPs against *E. coli*. For *S. aureus*, no significant difference was observed between non-irradiated Type III and control glass surfaces (Figure 16c-d).

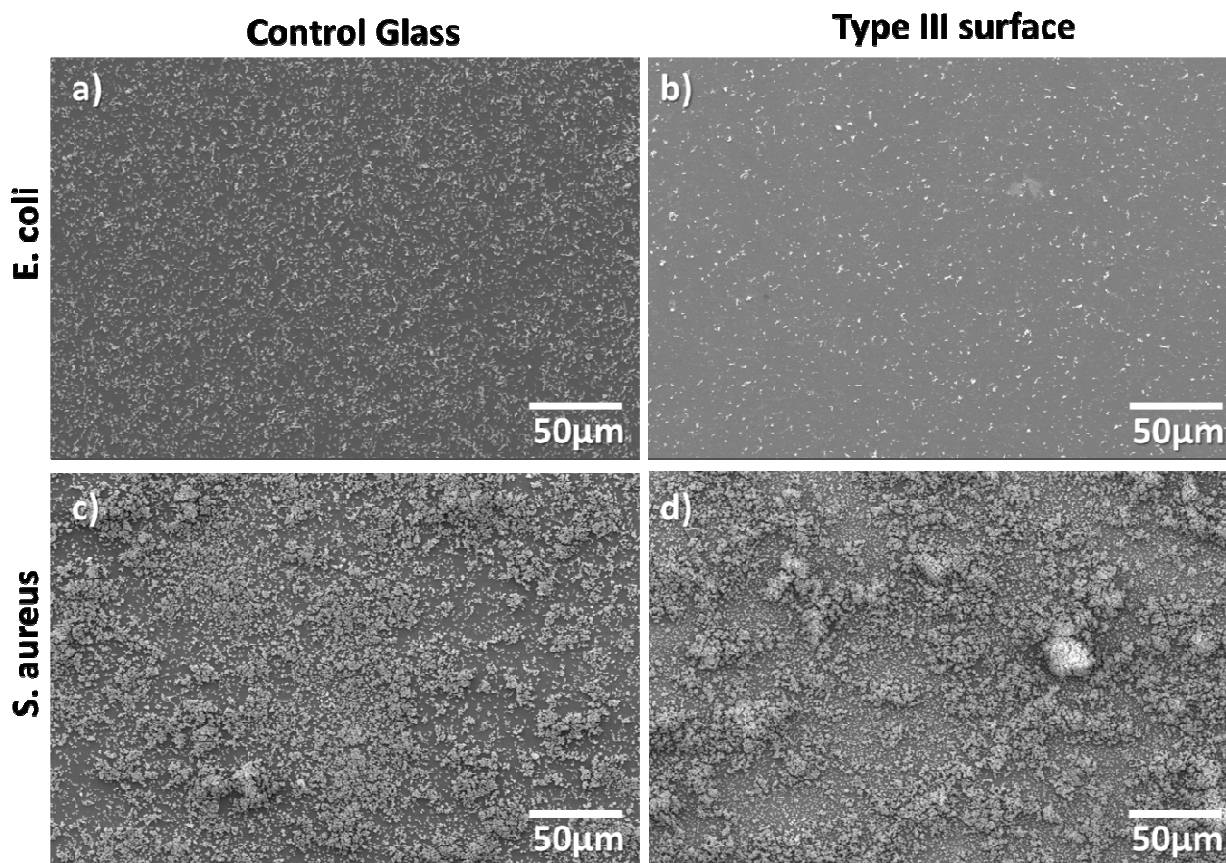


Figure 16: representative SEM of a) *E. coli* on non-functionalised control glass, b) *E. coli* on Type III glass, c) *S. aureus* on non-functionalised control glass, d) *S. aureus* on Type III glass. A considerable reduction in cell density for *E. coli* on Type III surfaces was observed due to the intrinsic antibacterial activity of AgNPs. Surprisingly, this effect was not observed for *S. aureus*, probably due to the well-known higher resistance of Gram-positive bacteria towards AgNPs. Moreover, in these experiments, the samples were incubated in nutrient broth for 24h, therefore we would expect the AgNPs on Type III surfaces to be capped by proteins from the rich growing media. Under these experimental conditions, the activity of AgNPs attached to the surface could be considerably reduced if compare with the non-coated AgNPs in our planktonic experiments in PBS. Similar effects have been reported before.³⁷

We then performed LASER-irradiation experiments with increasing power densities on biofilms of *E. coli* and *S. aureus* attached to control glass surfaces (Figure 15a,d,g). On these non-functionalised glass samples, even at the highest power density used, we do not observe any adverse effect on cell morphology. This confirms that under our

³⁷ A. Taglietti; Y.A.D. Fernandez; E. Amato; L. Cucca; G. Dacarro; P. Grisoli; V. Necchi; P. Pallavicini; L. Pasotti; M. Patrini; *Langmuir*, **2012**, 28, 21, 8140–8148.

experimental conditions direct LASER-radiation damage is negligible. When Type II surfaces containing only GNS were irradiated in the nIR, we observed a remarkable disruption of *E. coli* cells morphology as the laser power density increased, going from intact cells (Figure 15b), to cells displaying a granular-like membrane disruption (Figure 15e), to complete collapse of the cell structure (Figure 15h). These results demonstrate that the photo-thermal effect on Type II surfaces is significantly effective on bacterial cells attached to the surface. Interestingly, the irradiation of Type III surfaces led to complete *E. coli* cell disruption at lower power density (Figure 15f). Comparing Type II and Type III surfaces at intermediate power density in Figure 15d-f, we clearly observed an enhanced effect emerging from the combination of photo-switchable GNS and Ag⁺ release from AgNPs on Type III samples. This enhancement is remarkable, considering that the temperature increase at the surface for both Type II and III samples is the same, irrespectively of the presence of the AgNPs. This surface-located effect also correlates with the synergistic antimicrobial activity observed in the planktonic state for Type III surfaces. Similar results were obtained for *S. aureus*, showing progressive disruption of cell morphology on Type III surfaces. In this case the intermediate state was characterised by increasing number of pores on the rigid *S. aureus* cell wall, ultimately leading to the collapse and coalescence of neighbouring cell membranes. For this gram-positive bacterium higher power densities were required to produce complete disruption of cell morphology even on Type III surfaces (Figure 17).

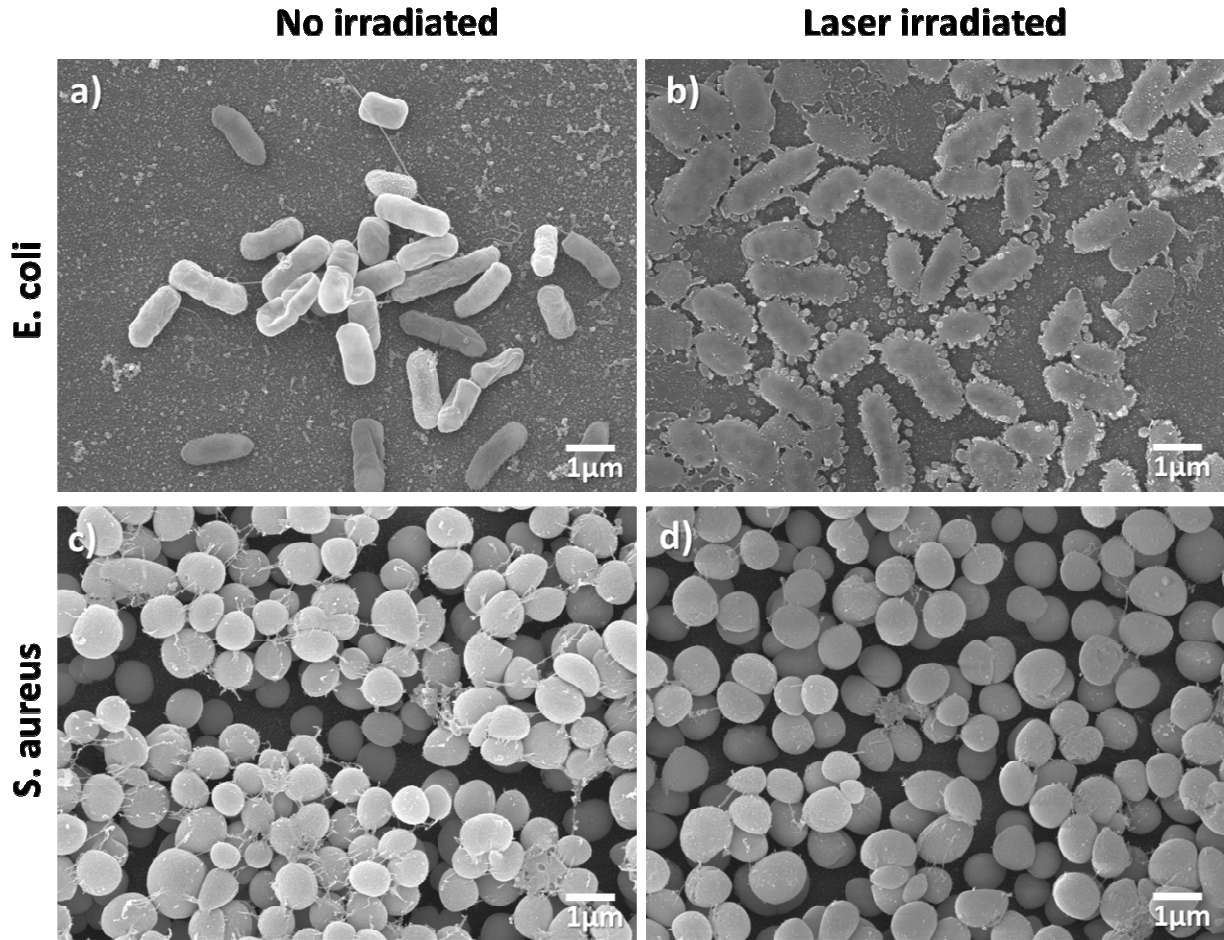


Figure 17: representative SEM images showing cell morphology on Type II surfaces for: a) non-irradiated *E. coli*, b) laser irradiated *E. coli*, c) non-irradiated *S. aureus*, d) laser irradiated *S. aureus*. Samples b & d were irradiated with 5x objective lens and 100% relative density power. Comparing these images, we can conclude that the cell architecture of *S. aureus* attached to photoactive surfaces Type II is more resistant than *E. coli* cellular structure upon LASER irradiation. These results can be explained considering the thick peptidoglycan cell wall of Gram-negative *S. aureus*, compared with the thin cellular membrane of *E. coli* cells.

2.1.3.4 CONCLUSION

In conclusion, our surfaces present a novel architecture with an external layer of AgNPs and an underlying GNSs monolayer, separated by a thin SiO₂ coating. This design preserves the photo-thermal properties of GNSs upon nIR irradiation.

The intrinsic bactericidal action of AgNP and the photo-switchable bactericidal hyperthermia of the irradiated GNS cooperate leading to a synergistic antibacterial effect. Such modular constructions, combining nano-objects with different functionalities, may pave the way towards a new generation of multimodal antimicrobial surfaces that incorporate both static and photo-switchable components. Implanted medical devices

could benefit from the synergistically-enhanced bactericidal action that can be activated externally by using harmless nIR LASER irradiation through living tissues to tackle post-surgical infections and bacterial re-colonization of internalised devices.

2.2 SERS CHIPS

2.2.1 INTRODUCTION

Biochemical and genetic diagnostic tests often require large numbers of samples either to test a large number of variables or to screen large sample populations. The reagents used in these assays can be very expensive and the sample itself may not be available in large quantities; therefore, smaller reaction volumes are essential. Surface-Enhanced Raman Scattering (SERS) is a non-destructive analytical method based on vibrational spectroscopy, which can give a characteristic spectrum of a specific molecules or bioagents;¹ SERS also offers a high degree of sensitivity and specificity.² Different strategy are usually used to exploit SERS signal in biosensing as shown in Figure 1.

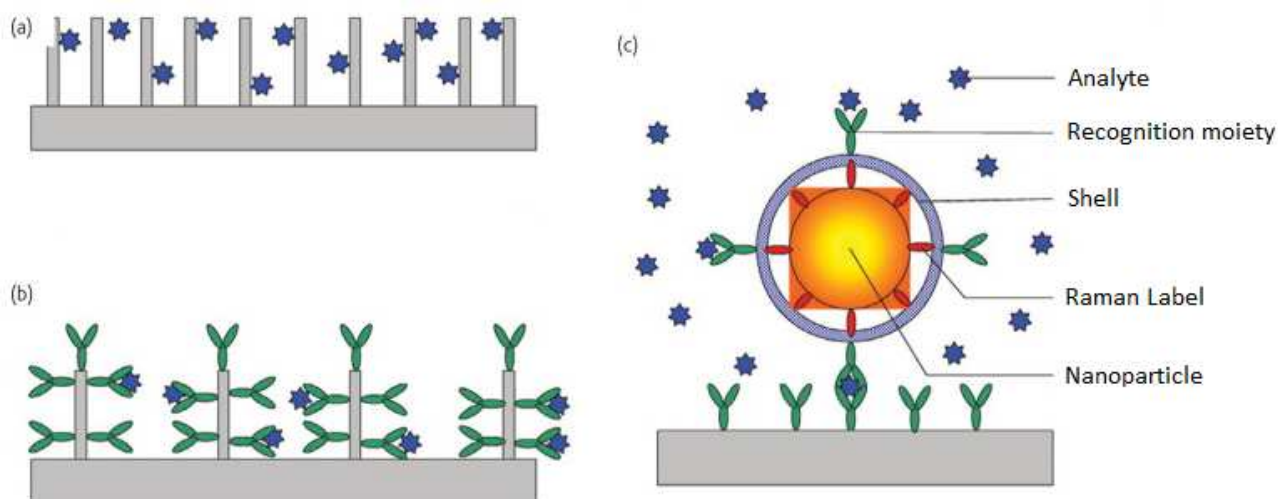


Figure 1: different SERS detection configurations: (a) direct intrinsic detection; (b) indirect intrinsic detection; and (c) extrinsic detection.³

In the so-called intrinsic detection (Figure 1a) the analyte can be directly applied to the nanostructured surfaces and the inherent Raman spectrum of the biomolecule directly measured to identify the specimen. To allow for capture and to aid specificity of detection, antibodies, aptamers, or related molecules can be immobilized onto nanostructured surfaces as shown in Figure 1b, and the Raman spectral differences

¹ M. Fleischmann; P.J. Hendra; A.J. McQuillan; *Chem. Phys. Lett.*, **1974**, 26, 163–166.

² P.R. Carey; *Biochemical Applications of Raman and Resonance Raman Spectroscopies*, Academic Press, New York, **1982**.

³ A.R. Tripp; A.R. Dluhyb; Y. Zhaoc; *Nanotoday*, **2008**, 3, 3–4, 31–37.

before and after capture of the specimen can be used to identify the species. In extrinsic detection, a Raman reporter molecule is used to generate a signal for detection. For example, a gold nanoparticle may be used as the SERS-active substrate to which a Raman reporter molecule is immobilized as shown in Figure 1c, by coating this structure with another layer of dielectrics such as SiO₂, TiO₂, or a polymer, a core-shell complex is formed in which the outer-shell may be decorated with capture molecules such as antibodies. Thus, specimens may be captured and detected via a sandwich structure. This extrinsic SERS detection method has been successfully used for in vivo SERS imaging of unique or rare cancer cells.⁴

Regardless the configuration, the ideal SERS substrate must be the best compromise between different requirements: i) highest enhancement factor as possible, ii) reproducible and uniform on the whole substrate surface, iii) a stable shelf-life, and iv) simple to fabricate, cheap and reusable. In the following section, we describe the realization and performances of a SERS chip based on intrinsic detection that in principle could be used to detect an extended range of analytes, satisfying the above mentioned characteristics. A couple of examples of devices based on the extrinsic detection scheme will be reported in Chapter 3. In view of the points already described, during this period of research, we decided to exploit, as a reproducible method to realize recyclable Surface Enhanced Raman Spectroscopy (SERS) active glass chips, the grafting strategy already described in Chapter 2.1. Using this approach, (i.e. grafting GNSs on glass by means of electrostatic interactions, after a functionalization of glass chips with APTES) it was possible to obtain homogeneous coatings, giving rise to reproducible SERS responses for the model compound Rhodamine 6G. However, as these substrates suffer of an intrinsically low mechanical and chemical stability, the introduction of a silica layer coating, once again as described in Chapter 2.1, was performed to obtain increased stability: these coatings allowed to preserve a good Enhancement Factor (EF) and thus ensure a good sensitivity and in the same time giving an extreme robustness leading to reusability of chips. Moreover, the preparation of the protective layers with two different thickness allowed to better understand the relationship between the thickness of the insulating layer and the SERS response.

⁴ X. Qian; X.H. Peng; D.O. Ansari; Q. Yin-Goen; G.Z. Chen; D.M. Shin; L. Yang; A.N. Young; M.D. Wang; S. Nie; *Nature Biotechnology*, **2008**, 26, 83-90.

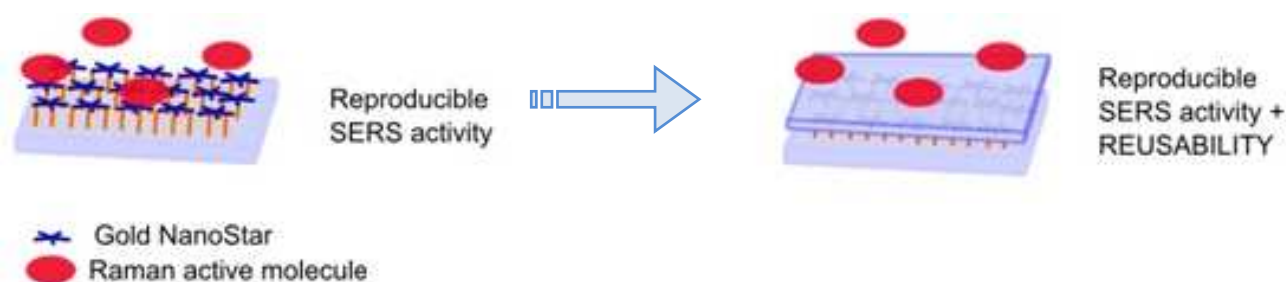


Figure 2: schematic representation of the approach to the realization of re-usable SERS chips.

As already told, SERS spectroscopy is receiving a huge and increasing attention as a powerful analytical tool. In SERS techniques, the intrinsic ability of Raman spectroscopy to recognize a molecule exploiting its vibrational fingerprint is coupled with the strong increase in signal intensity: the overall result is that SERS effects allow a rare combination of sensitivity and specificity, a fact which is leading to several successful applications in chemical and biochemical optical sensing.⁵ In any case a key role is played by the SERS substrate. For analytical purposes, the major challenge is to obtain a SERS substrate (i.e. an analysis chip to be used routinely⁶) with the following features: i) an homogeneous structure, in order to give point to point repeatability (the deviation in enhancement over the whole surface should be less than 20%) ii) sample-to-sample reproducibility; even after a long shelf time, the enhancement effect must be maintained and the deviation in the enhancement should be less than 20% for different batches of substrates prepared by the same method, iii) large scale applicability of a low cost synthetic pathway, iv) stability, and, with an obvious importance from an economic point of view, v) re-usability. Although the constantly increasing number of studies on SERS substrates, it's hard to find examples meeting all these criteria.^{6,7} The best compromise between above mentioned requirements must be obviously accompanied by the highest possible Enhancement Factor (EF)⁸ The currently accepted theories state that the enhancement of Raman signals close to noble metal nanostructured surfaces arises by the combined action of a chemical and of an electromagnetic effect,^{9,10,11} the latter occurring as a consequence of the action of a near optical field (usually coming from a

⁵ D. Ciialla; A. Marz; R. Bohme; F. Theil; K. Weber; M. Schmitt; J. Popp; *Anal. and Bioanal. Chem.*, **2012**, 403, 1, 27-54.

⁶ J.A. Huang; Y.L. Zhang; H. Ding; H.B. Sun; *Advanced Optical Materials*, **2015**, 3, 5, 618-633.

⁷ X.M. Lin; Y. Cui; Y. Xu; B. Ren; Z.Q. Tian; *Anal. and Bioanal. Chem.*, **2009**, 394, 7, 1729-1745.

⁸ E.C. Le Ru; E. Blackie; M. Meyer; P.G. Etchegoin; *J. of Phys. Chem. C*, **2007**, 111, 37, 13794-13803.

⁹ A. Otto; I. Mrozek; H. Grabhorn; W. Akemann; *Journal of Physics-Condensed Matter*, **1992**, 4, 5, 1143-1212;

¹⁰ M. Moskovits; *Reviews of Modern Physics*, **1985**, 57, 3, 783-826.

¹¹ E.C. Le Ru; E. Blackie; M. Meyer; P.G. Etchegoin; *Journal of Physical Chemistry C*, **2007**, 111, 37, 13794-13803.

LASER source), which is amplified as a result of LSPR phenomena which are typical of noble metal NPs. The specific frequency of LSPR absorption bands is a variable depending from the conductivity of the metal, the dielectric properties of the surrounding medium and from NPs morphology (size and shape), with anisotropic particles usually showing red-shifted LSPR and even leading to near IR absorption. Also the localization and intensity of amplified electromagnetic fields causing SERS is strongly influenced by NP shape and dimensions. The efforts for increasing EF factors open the way to the synthesis of asymmetric, branched, shaped metal nano-objects. Indeed as electromagnetic fields generated in proximity of NPs surfaces rapidly decrease as function of distance from surface. EF⁸ in Raman response arising from LSPR phenomena can hugely increase only near to noble metal NPs surfaces, especially in close proximity of sharp edges and tips of anisotropic NPs (the so called “lightning rod effect”), or in small spaces comprised between two protruding edges of nano-objects. These confined spatial zones are called “hot spots”: in general this definition includes highly localized regions formed within the interstitial spaces present in metallic nanostructures, in which, as it is claimed, enhancement obtained can reach up to 10¹⁵ orders of magnitude of SERS response compared to normal Raman signal,¹² as a result of focusing of field energy in narrow spatial regions.¹³ Among anisotropic structures which can give high EF, gold nanostars (GNSs) have emerged as excellent SERS active NPs, as their branches and terminal tips usually provide huge field enhancement and “hot spots”,¹⁴ showing higher SERS response when compared to spherical or other anisotropic structures such as nanorods and nanocubes.¹⁵ The possibility to build up a high-EF SERS sensing chips based on branched GNSs on flat bulk surface has been explored by several recent investigations, using different synthetic approaches^{16,17,18} Surface assembly of noble metal nanoparticles driven by electrostatical interactions is a promising and economic approach used to realize SERS active substrates. A bulk, inexpensive surface such glass or ITO glass is coated with a Self Assembled Monolayer of an amine bearing alcoxysilane, for example APTES, and subsequently, in the proper conditions, negatively charged nano-objects can interact with positively charged ammonium groups present on the bulk

¹² A. Indrasekara; S. Meyers; S. Shubeita; L.C. Feldman; T. Gustafsson; L. Fabris; *Nanoscale*, **2014**, 6, 15, 8891-8899.

¹³ K. Kneipp; M. Moskovits; H. Kneipp; *Surface-Enhanced Raman Scattering: Physics and Applications*, Springer Science & Business Media, **2006**.

¹⁴ A.G. Martinez; S. Barbosa; I.P. Santos; L.M. Marzan; *Current Opinion in Colloid & Interface Science*, **2011**, 16, 2, 118-127.

¹⁵ E.N. Esenturk; A.R.H. Walker; *Journal of Raman Spectroscopy*, **2009**, 40, 1, 86-91.

¹⁶ L.P. Mayen; J. Oliva; A.T. Castro; E. De la Rosa; *Nanoscale*, **2015**, 7, 22, 10249-58.

¹⁷ Q. Su; X. Ma; J. Dong; C. Jiang; W. Qian; *Acs Applied Materials & Interfaces*, **2011**, 3, 6, 1873-1879.

¹⁸ A. Indrasekara; S. Meyers; S. Shubeita; L.C. Feldman; T. Gustafsson; L. Fabris; *Nanoscale*, **2014**, 6, 15, 8891-8899.

surfaces, allowing the preparation of uniform and reproducible substrates.^{19,20} Anyway, several critical issues for this type of materials may arise from the mechanical and chemical instability of the grafted GNSs monolayer. Electrostatic interactions are quite weak, and one should carefully check the behaviour when coated devices are handled: detachment of objects and mechanical removal, following manipulation, scratching or ultrasounds treatments, must be taken into account. Moreover, competition with substances dissolved in analyzed fluids (especially those of biological origin) which could lead to competitive interaction and eventually GNSs detachment and release in analysed media must be considered. Last but not least, there is a problem which is independent from the approach used for the substrate assembly, and potentially affects all SERS substrates: chemical reactivity with contaminants and in general substances showing high affinity towards noble metal surfaces (e.g. thiols) can of course affect substrate stability, response and/or re-usability.²¹ All these issues represent limits of striking evidence from the point of view of synthetic reproducibility, robustness, reusability and, as a consequence, economy of routine applications.

Examples of substrates possessing the ability of regeneration of the SERS active surface for reuse are often based on photocatalytic degradation of molecules adsorbed on substrate, and usually exploit the presence of TiO₂,^{22,23} ZnO,²⁴ or other components like mesoporous silica:²⁵ in all cases, anyway, the sample must undergo some specific treatment and be irradiated in the UV to gain re-usability. Few examples report about different approaches: for example flower-like silver structures electrodeposited on ITO glass were found to partially regenerate after a very long (44 hours) immersion in ethanol solution²⁶ while in other lithographically constructed systems recyclability was obtained through a complex sequence of steps, including chemical etching and plasma cleaning.²⁷ In another example, silicon substrates bearing Gold nanoparticles were recycled after thermal treatments of one hour at 330 °C.²⁸ A more straightforward idea is to chemically stabilize and protect the GNSs monolayer from the surrounding environment with a layer

¹⁹ O. Seitz; M.M. Chehimi; E.C. Deliry; S. Truong; N. Felidj; C. Perruchot; S.J. Greaves; J.F. Watts; *Colloids and Surfaces a-Physicochemical and Engineering Aspects*, **2003**, *218*, 1-3, 225-239.

²⁰ M. Wang; X. Cao; W. Lu; L. Tao; H. Zhao; Y. Wang; M. Guo; J. Dong; W. Qian; *Rsc Advances*, **2014**, *4*, 109, 64225-64234.

²¹ X.M. Lin; Y. Cui; Y.H. Xu; B. Ren; Z.Q. Tian; *Analytical and Bioanalytical Chemistry*, **2009**, *394*, 7, 1729-1745.

²² X. Li; G. Chen; L. Yang; Z. Jin; J. Liu; *Advanced Functional Materials*, **2010**, *20*, 17, 2815-2824.

²³ Y. Chen; G. Tian; K. Pan; C. Tian; J. Zhou; W. Zhou; Z. Ren; H. Fu; *Dalton Transactions*, **2012**, *41*, 3, 1020-1026.

²⁴ G. Sinha; L.E. Depero; I. Alessandri; *Acs Applied Materials & Interfaces*, **2011**, *3*, 7, 2557-2563.

²⁵ X. Yan; L. Wang; D. Qi; J. Lei; B. Shen; T. Sen; J. Zhang; *Rsc Advances*, **2014**, *4*, 101, 57743-57748.

²⁶ J. Bian; S. Shu; J. Li; C. Huang; Y.Y. Li; R.Q. Zhang; *Applied Surface Science*, **2015**, *333*, 126-133.

²⁷ A. Gopalakrishnan; M. Chirumamilla; F. De Angelis; A. Toma; R.P. Zaccaria; R. Krahne; *Acs Nano*, **2014**, *8*, 8, 7986-7994.

²⁸ H. Lin; Q. Shao; F. Hu; R. Que; M. Shao; *Thin Solid Films*, **2012**, *526*, 133-138.

of silica, trying to maintain an appreciable SERS enhancement in spite of the dielectric gap between nano-object and Raman active molecules. In a recent example, gold nanoparticles grafted on a capillary tube were coated with a layer of silica through APTES²⁹ in these case a reducing agent (sodium borohydride) must be present in a flowing washing solution to ensure regeneration of the surface for SERS based sensing purposes. Furthermore some authors³⁰ observed a high EF even at longer distances using silica spacers. These results seems to indicate a unexpected persistence of SERS effect beyond tens of nanometers.

Along these lines, in this work we have prepared a monolayer of GNS grafted on bulk glass surfaces silanized with APTES, adding a further thin silica layer grown on the GNS monolayer. To do this, we followed a methodology (which we have already used in the previous chapter) and was widely employed, for example in order to protect gold island based transmission localized surface plasmon resonance (T-LSPR) sensing substrates^{31,32} Using this approach we obtained a complete stabilization, as well protection and separation from the solution, inertness towards mechanical removal and chemical reactivity, conserving a good EF of SERS response. These surfaces, after easy and simple washing with bi-distilled water, can be repeatedly re-used, acting a prototype of a low cost, homogeneous, reproducible, robust and reusable SERS substrate.

²⁹ W. Wang; Q. Guo; M. Xu; Y. Yuan; R. Gu; J. Yao; *Journal of Raman Spectroscopy*, **2014**, 45, 736–744.

³⁰ V.I. Kukushkin; A.B. Van'kov; I.V. Kukushkin; *Jetp Letters*, **2013**, 98, 2, 64-69.

³¹ N. Irit; T.A. Bendikov; I.D. Mor; Z. Barkay; A. Vaskevich; I. Rubinstein; *Journal of the American Chemical Society*, **2007**, 129, 1, 84-92.

³² Y. Chaikin; O. Kedem; J. Raz; A. Vaskevich; I. Rubinstein; *Analytical Chemistry*, **2013**, 85, 21, 10022-10027.

2.2.2 EXPERIMENTAL DETAIL: SYNTHESIS AND CHARACTERIZATION

2.2.2.1 MATERIALS AND INSTRUMENTATION

Reagents

Gold(III) chloride trihydrate (~30wt% in HCl 99.99%), sodium borohydride (98%), L-ascorbic acid (AA) ($\geq 99\%$), silver nitrate (99.8%), hydrochloric acid ($\geq 37\%$), nitric acid ($\geq 65\%$), sulfuric acid (95%), hydrogen peroxide (30 wt %), ethanol ($\geq 99.7\%$), N-dodecyl-N,N-dimethyl-3-ammonium-1-propanesulfonate (LSB) ($\geq 99.7\%$), (3-aminopropyl)trimethoxysilane (APTES) ($\geq 98.0\%$), sodium silicate solution ($\text{Na}_2\text{O}(\text{SiO}_2)_{3-5}$ 27%wt SiO_2), (3-mercaptopropyl)trimethoxysilane (MPTS) ($\geq 98.0\%$), were purchased from Aldrich. Amberlite® IR120 hydrogenated was purchased from Fluka Analytical. Microscopy cover glass slides 21x26 mm were purchased from DEL Chimica. All reagents were used as received. All the preparation are made with bi-distilled water.

Instrumentation

UV-Vis Spectroscopy. UV-Vis spectra on functionalized slides at normal incidence were measured in air using a Varian Cary 50 UV/Vis spectrophotometer. The wavelength scan range was 300-1000 nm. The samples were placed in a special holder enabling transmission measurement of the same spot on the slide during all experimental stages.

Contact Angle. Static contact angle determinations were made with a KSV CAM200 instrument, with the water sessile drop method.

Scanning Electron Microscopy (SEM). SEM images were taken from Tescan Mira XMU variable pressure Field Emission Scanning Electron Microscope – FEG SEM (Tescan USA Inc., USA) located at the Arvedi Laboratory, CISRiC, Pavia. Slides were mounted onto Aluminum stubs using double sided carbon adhesive tape and were then made electrically conductive by coating in vacuum with a thin layer of Pt/Pd (3-5 nm). Observations were made in backscattered electrons mode (BSE) at 30 kV and with InBeam secondary electron detector for higher spatial resolution.

High-Resolution Scanning Electron Microscopy (HR-SEM). Images were obtained by a SIGMA high-resolution scanning electron microscope (Carl Zeiss) based on the GEMINI® column which features a high brightness Schottky field emission source, beam booster, and in-lens secondary electron detector. Measurements were conducted in low acceleration potential mode (≤ 2 kV) with a working distance of about 2 mm thus allowing the use of uncoated samples.

ICP-OES spectroscopy. The Ag and Au content in solution was then determined by Inductively Coupled Plasma (ICP) atomic emission spectroscopy with an ICP-OES OPTIMA 3000 Perkin Elmer instrument.

SERS measurements. SERS measurement were carried out at room temperature by using a Labram Dilor spectrometer equipped with an Olympus microscope HS BX40. The LASER beam was the He-Ne red light at 632.8 nm. The exciting LASER power was kept at a low level of about 1 mW to avoid bleaching the dyes. The SERS spectra of aqueous solutions with concentrations ranging between 1 and 1000 mM were collected, depositing 20 μ L of R6G solution at a desired concentration on the SERS substrate, and spreading the drop on the functionalized surface by placing a “blank” (not functionalized) clean glass coverslip. In this way, a very thin film of solution is confined between two glass surfaces: a lower functionalized one and an upper blank (completely transparent) one.

2.2.2.2 GLASSWARE PRE-TREATMENT

All the glassware that come into contact with GNSs was always pre-treated before use: a wash in *aqua regia* for 30 minutes, then washed and filled with bi-distilled water and ultrasonicated for three minutes before discarding water. The bi-distilled water/ultrasound treatment was repeated three times. Then the glassware were dried in an oven for 1 hour at 140°C.

Prior to APTES grafting, microscopy cover glass slides (21x26 mm) were treated with piranha solution (3:1 sulfuric acid 95% and hydrogen peroxide 30%wt) for 30 minutes. Then the slides were washed in water under sonication for three minutes, and dried in an oven for 1 hour at 140°C.

2.2.2.2 PREPARATION AND CHARACTERIZATION OF SERS CHIPS

Preparation of GNSs

The seeds were prepared in a vial by adding 5.0 mL of LSB aqueous solution (0.2 M) and 5.0 mL of HAuCl_4 aqueous solution (5×10^{-4} M). Subsequently, 600 μL of an ice-cooled solution of NaBH_4 in water (0.01 M) were added to the pale yellow solution of AuCl_4^- obtained in the previous step. As prepared brown-orange solution was gently hand-shaken for a couple of second; this solution is efficient for the growth procedure of GNSs for 180 minutes from preparation if kept cold. The growth solution was prepared with 50 mL of LSB solution in water at the same concentration chosen for the seed solution (0.2 M), 1800 μL of AgNO_3 in water (0.004 M), 50 mL of aqueous HAuCl_4 (5×10^{-4} M) and 820 μL of an aqueous L-ascorbic acid solution (0.078 M) mixed to obtain a colourless solution just after a few seconds of gentle mixing. Then 120 μL of seed solution were added to give a blue coloured colloid, the intensity of which rapidly increased. The solution was allowed to react without agitation for 1h.

Preparation of ZERO glass samples

The pre-treated slides (typically eight slides for each preparations) are fully immersed in a solution of APTES 10% (v/v) in ethanol contained in a Hellendhal type glass staining jar, for 5 minutes at 60°C . The obtained amino-modified glasses were washed three times with ethanol under sonication. After this step, the samples were gently dried under N_2 flux. The slides were then fully immersed in the GNSs colloidal suspension for 14 hours. After immersion, the slides were washed three times in water without sonication and carefully dried in N_2 stream. Dried samples were stored in the dark in a box with dryers.

Determination of Ag and Au by ICP-OES spectroscopy

The total Ag and Au content on all kind of samples was determined by quantitatively oxidizing the grafted GNSs on a single slide (21x26 mm coated on both sides, total coated surface 10.92 cm^2) by dipping it in 3 mL of *aqua regia* diluted 4:25 with bi-distilled water in a vial, and keeping it overnight on a Heidolph Promax 1020 reciprocating platform shaker. Typically, one or two slide for every batch of 8 slides preparation was analyzed. Measures were repeated three times, and mean values were used.

Preparation of "FOUR" samples

Typically, seven dried "ZERO" samples were fully immersed in a MPTS ethanol solution 5% (v/v) for 10 minutes. After this step, the samples were washed three times with fresh ethanol and dried by N₂ flux. For silica deposition, the slides were then dipped for one or four hours in a 1.5%wt sodium silicate solution (after dilution of a 27%wt SiO₂ solution with water) kept at 90°C. The strongly acidic cation exchanger Amberlite IR-120 was used for the adjustment of the solution pH to 8.5-9. After the chosen immersion time, the silica-coated substrates were washed three times in ethanol under sonication and dried in N₂ stream. All steps are performed in Hellendhal type glass staining jars.

Preparation of samples for SERS measurements with MMC

The chosen glass samples (ZERO samples and FOUR samples) were placed in a Hellendhal type glass staining jar containing a 10⁻³ M solution of MMC in ethanol. After one hour, glass samples were washed by 5 minutes immersion in fresh ethanol and dried under gentle flux of N₂. This washing procedure was repeated three times. A carefully dried in N₂ stream. Dried samples were stored in Hellendhal type glass staining jar kept in the dark in presence of dryers.

Preparation of samples for SERS measurements with R6G

The typical experimental setup for all samples investigated was performed placing on the 21x26 mm functionalized glass sample a 20 µL drop of a water solution of R6G at the desired concentration. After this, a blank and clean 21x26 mm glass slide was placed to cover functionalized glass in order to spread completely the drop and to obtain an almost homogeneous film of R6G solution between the two glass slides. The so-assembled sample was then used quickly for Raman analysis. For the re-usability tests, in the used samples the blank cover glass slide were removed after the Raman measure, while the functionalized glass was washed with bi-distilled water, wiped with a lab tissue paper, and then used again in the same way as fresh samples.

2.2.3 RESULT AND DISCUSSIONS

2.2.3.1 GNSs MONOLAYER ON GLASS

Formation of an APTES monolayer on glass slides was obtained using a reported procedure.³³ This step allows short functionalization times and ensures a good quality monolayer formation: efficiency of silanization is routinely controlled with contact angle measurements: the value moves from $<10^\circ$ for cleaned glass samples (piranha solutions, see experimental), to a value of $52(5)^\circ$, a data consistent with those found in the literature for the formation of a monolayer of APTES on bulk glass.³⁴ GNSs were prepared in water using an seed-growth method already published and exploited for several purposes,^{35,36,37} composition of these colloidal suspension has been extensively characterized and described in our paper³⁸ and in Paragraph 1.3.1. Their extinction spectrum in solution is dominated by the LSPR of the main component, whose maximum can be positioned in the 700-1150 nm range as a function of synthetic parameters (e.g. ascorbic acid concentration). As geometrical features such the number and sharpness of edges and tips, play a fundamental role in SERS responses, and as LSPR are strongly dependent from these geometrical features, we have used such reaction conditions as to obtain colloidal solutions with a LSPR of the main population centred always close to a same value (between 840 and 860 nm) in order to maximize reproducibility of Raman measures. A representative spectrum of the preparations used is shown in Figure 3 (blue line).

³³ A. Taglietti; C.R. Arciola; A. D'Agostino; G. Dacarro; L. Montanaro; D. Campoccia; L. Cucca; M. Vercellino; A. Poggi; P. Pallavicini; L. Visai; *Biomaterials*, **2014**, 35, 6, 1779-1788.

³⁴ X. Zeng; G. Xu; Y. Gao; Y. An; *Journal of Physical Chemistry B*, **2011**, 115, 3, 450-454.

³⁵ A. Casu; E. Cabrini; A. Donà; A. Falqui; Y.D. Fernandez; C. Milanese; A. Taglietti; P. Pallavicini; *Chemistry-a European Journal*, **2012**, 18, 30, 9381-9390.

³⁶ A. D'Agostino; A. Taglietti; B. Bassi; A. Donà; P. Pallavicini; *Journal of Nanoparticle Research*, **2014**, 16, 10.

³⁷ B. Bassi; A. Taglietti; P. Galinetto; N. Marchesi; A. Pascale; E. Cabrini; P. Pallavicini; G. Dacarro; *Nanotechnology*, **2016**, 27, 26.

³⁸ A. Casu; E. Cabrini; A. Donà; A. Falqui; Y. Diaz-Fernandez; C. Milanese; A. Taglietti; P. Pallavicini; *Chem. Eur. J.*, **2012**, 18, 9381-9390.

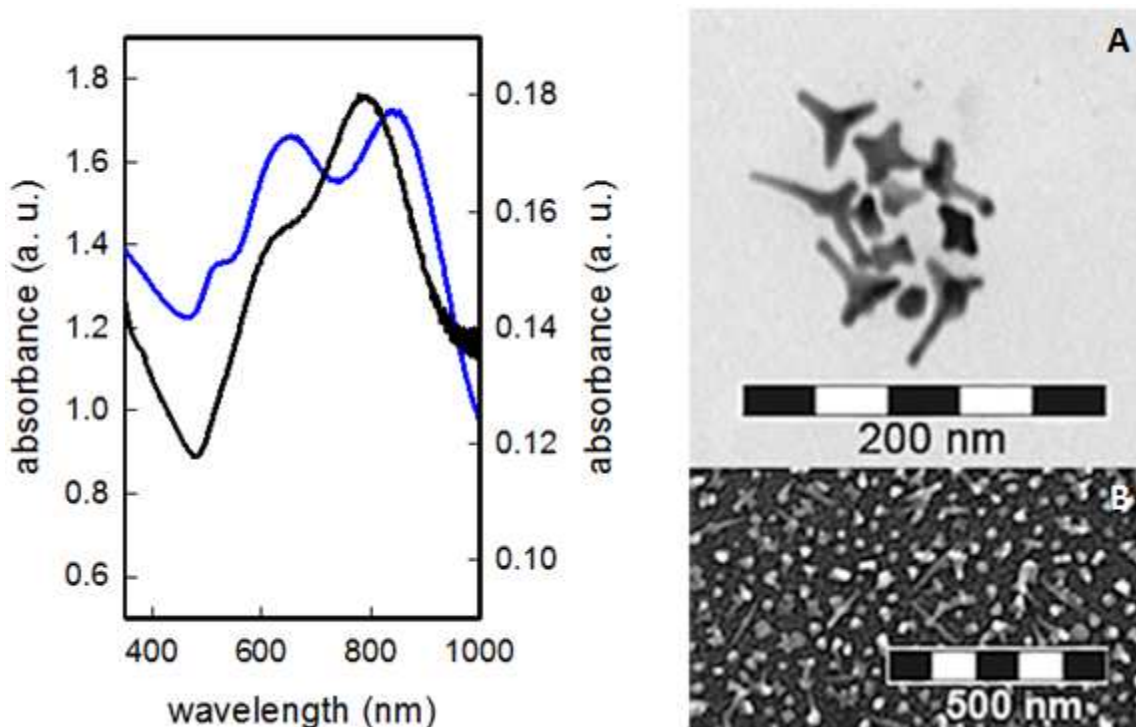


Figure 3: spectrum of typical GNSs colloidal suspension used in this work (blue line, right scale) compared with the spectrum of GNSs layer on amino-terminate glass (ZERO sample, black line, left scale); A) detail of a TEM image of the colloid suspension giving the blue line spectrum; B) detail of SEM image of ZERO sample giving the black line spectrum.

As we have described in Paragraph 1.3.1, at the end of the growth process GNSs are coated on their surface by a double layer of LSB molecules, giving to objects an overall negative surface charge, which can be quantified by Dynamic Light Scattering (DLS) measurements in a Z potential of -15 mV. Thus, immersion of APTES-terminated bulk glass samples in the colloidal GNSs suspension for 14 hours yields the so called “ZERO” samples, where a GNSs layer formation is obtained, due to their electrostatic interaction with the positively charged amino-groups, which are in protonated form, as GNSs colloidal solutions are slightly acidic (pH=3) because of the presence of excess ascorbic acid from the growth process. Success of GNSs grafting on the APTES functionalized slides can be visually perceived directly, as slides turn to an evident blue colour. These glass samples were gently washed with ethanol and water, and then dried under nitrogen stream.

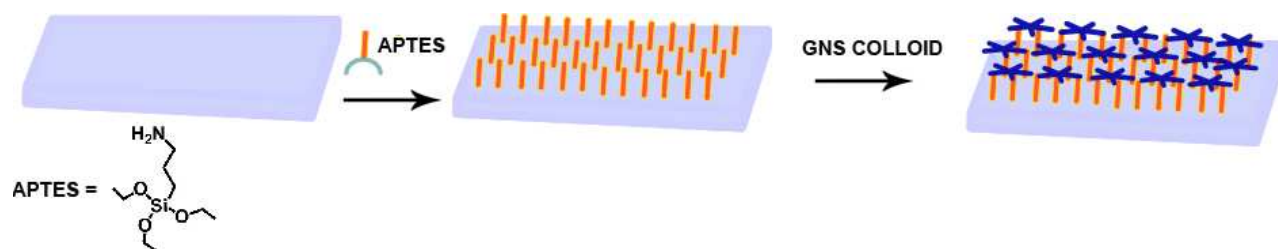


Figure 4: pictorial of synthetic process of the ZERO type glasses.

Success of GNSs grafting on the APTES functionalized slides can be visually perceived directly, as slides turn to an evident blue colour. SEM images of the obtained samples (Figure 3) show unchanged objects morphology with respect to the corresponding TEM image from the parent colloidal solution, as well a continuous and homogeneous coating of the slides with GNSs. This was already observed for monolayers of the same GNSs grafted on a MPTS functionalized glass.³⁹ This was already observed for monolayers of the same GNSs grafted on a MPTS functionalized glass, for different GNSs grafted on APTES-functionalised ITO glass samples¹⁹ or tethered on smooth gold-coated Si surfaces by means of a self assembled monolayer with 6-aminohexane-1-thiol.¹²

In figure 3 the UV-Vis spectrum for a typical ZERO type glass (black line), is compared with the one of the GNSs colloidal suspension (blue line), while in Figure 3A a detail of a TEM image taken for a sample of the colloidal suspension is compared with a detail of SEM (Figure 3B) for one of the glass samples obtained. A LSPR blue shift of about 60(10) nm (average of 32 glass samples, coming four preparations based on four slightly different starting colloidal suspensions: an example of reproducibility of the preparation is reported in Figure 5) is observed moving from the colloidal suspension in water to the monolayer on glass, as already reported for similar samples discussed in Chapter 2.1. This shift is due to the decrease of the local refractive index (n) on passing from water ($n_{\text{water}}=1.3339$) to glass and air at the interface ($n_{\text{air}}=1.0003$).

³⁹ P. Pallavicini; A. Donà; A. Taglietti; P. Minzioni; M. Patrini; G. Dacarro; G. Chirico; L. Sironi; N. Bloise; L. Visai; L. Scarabelli; *Chem. Commun.*, **2014**, 50, 1969-1971.

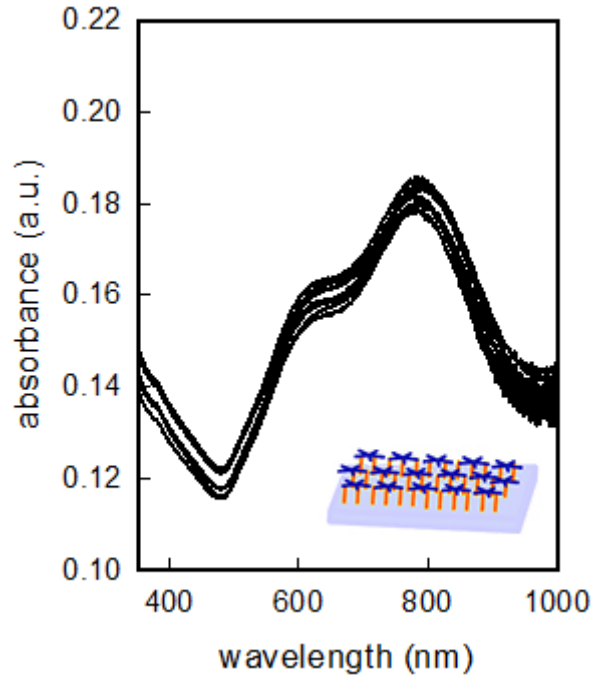


Figure 5: spectra of one representative preparation of eight samples of ZERO type glasses coming from one preparation jar.

As a result of this blue shift, type ZERO samples coming from different preparations were found to have LSPR maxima ranging from 770 to 800 nm, due to the mentioned variability of the original colloidal solutions of GNS used for the coating, with an absorbance of the long LSPR band ranging between 0.17 and 0.19. Samples with spectral features outside of these ranges were discarded (less than 10% of prepared samples). The total amount of metal grafted on the glass slide was measured, by fully oxidizing the GNSs monolayer with *aqua regia* and analyzing the obtained solution by ICP-OES (Inductively Coupled Plasma Optical Emission Spectroscopy). Typically, one slide for each preparation was analyzed. Both Au and Ag were determined, as the latter is present in the GNSs lattice in 10-15% atomic ratio vs Au, due to its use (with a similar proportion) in the seed-growth synthesis: the surface concentration of Au resulted to be 3.0(0.5) $\mu\text{g}/\text{cm}^2$, while Ag resulted in 0.33(0.05) $\mu\text{g}/\text{cm}^2$, with relatively low standard deviations accounting for reproducibility of preparations. As a further characterization, contact angle were measured for at least one glass sample for each preparation, obtaining a value of 37(4) $^\circ$.

As predicted, a gentle scratching, even with the soft surfaces of a tissue or a finger, leads to GNSs monolayer removal, visually indicated by disappearing of the blue colour on glass surface. Detachment and decolouring as observed also after one minute ultrasound

treatment, as can be seen in the image shown in Figure 8 in Chapter 2.1. Anyway, in absence of ultrasound treatment and carefully manipulating the samples, measures can be performed obtaining reproducible results.

2.2.3.2 COATING WITH SILICA

In a first step, the described uncoated ZERO samples were immersed in a MPTS solution: the thiol function of MPTS is expected to bind the gold surface, leaving the $-\text{Si}(\text{OCH}_3)_3$ moieties pointing outside and exposed to the solution, to serve as starting points on which silica growth may subsequently take place, as the groups can guide the reaction with sodium metasilicate to form a thin layer of SiO_2 on the nanoparticles layer, as reported in Chapter 2.1.^{31,32} After the MPTS treatment, we measured UV-Vis spectra on the glass slides observing a small red-shift of about 10(3) nm, caused by thiol binding to gold surface which changes the local refractive index. Contact angle increases to a value of 66(4)°, demonstrating that binding with MPTS was successful, and the surface now is hydrophobic because of alcoxysilane moieties exposed on the surface. At this point, coating with a silica layer was performed, following a reported method. As it was demonstrated by Rubinstein and colleagues,^{32,40} treatment of MPTS coated layer of gold nano-objects with a sodium silicate solution (see Paragraph 2.2.2.2 for experimental details) at a temperature of 90°, produces the growth of a silica layer with a rate of about 1 nm for hour of immersion. In order to obtain two different thickness, we used two immersion times: one hour, to obtain a ultrathin layer of an expected thickness of 1 nm (sample named ONE), and a more prolonged immersion (4 hours, named FOUR) which is expected to produce a thicker layer of about 4-5 nm, as we have demonstrated in Paragraph 2.2.2. The general strategy used to produce silica-protected GNSs layers is reported in Figure 6.

⁴⁰ Q. Wu; C. Luo; H. Yu; G. Kong; J. Hu; *Chemical Physics Letters*, **2014**, 608, 35-39.

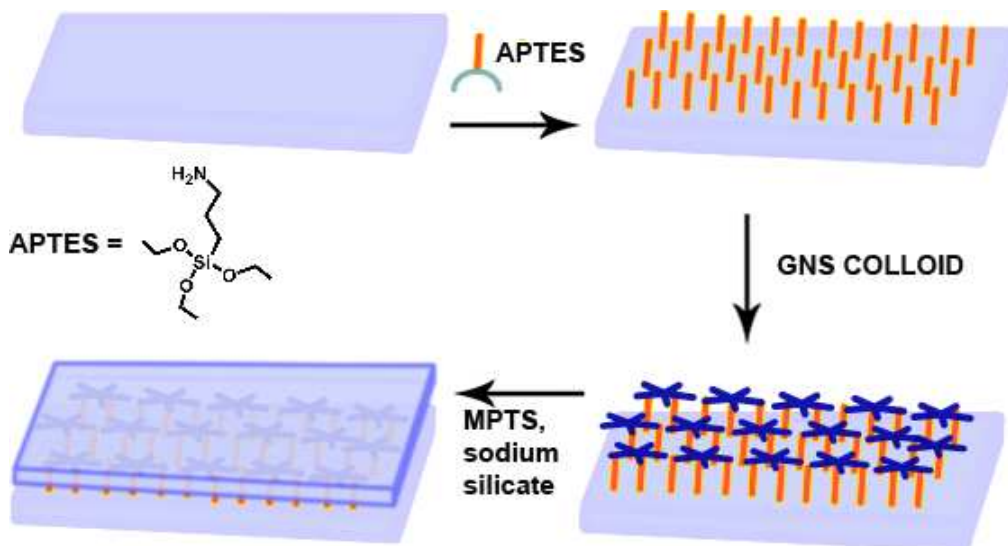


Figure 6: scheme of synthetic process of the ONE and FOUR type glasses.

Silica coating can be immediately perceived and demonstrated: when silica coated samples undergo an ultrasound treatment of 5 minutes, no change in colour or appearance (as shown in Figure 8 in Chapter 2.1) is observed. Even the scratching with a hard tip does not produce any degradation in the appearance of the coated glass, demonstrating that GNSs layer is now protected from detachment and mechanical degradation. Contact angle shifts to not measurable values ($<10^\circ$) indicating the presence of an elevated number of Si–OH groups which make the surface very hydrophilic. Once again, the total amount of metal grafted on the glass slides was measured, the already described method dissolving grafted GNSs in *aqua regia* and analyzing the obtained solution by ICP-OES. For ZERO and FOUR samples the surface concentration of Au resulted to be $2.8(0.5) \mu\text{g}/\text{cm}^2$, while Ag resulted in $0.30(0.05) \mu\text{g}/\text{cm}^2$, demonstrating that no sensible detachment and loss of GNSs happens during silica coating steps. UV-Vis spectrum of silica coated samples shows a red shift of the plasmonic features.

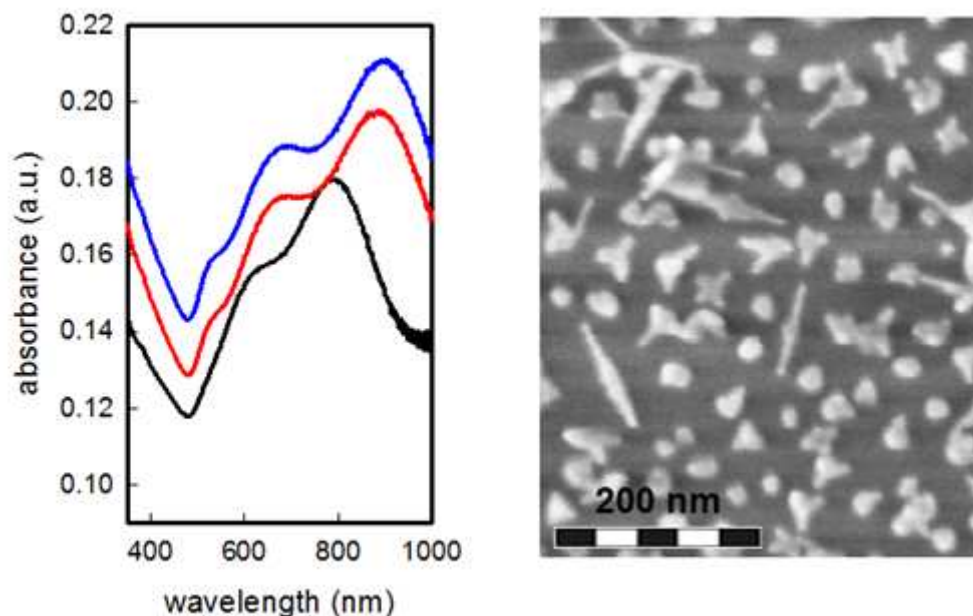


Figure 7: UV-Vis spectra of GNSs functionalized glass samples: ZERO sample (black line), ONE sample (red line); FOUR sample (blue line); on right HR-SEM image of the FOUR sample.

Typically, the LSPR maxima for the long band experience a red shift of about 80-100 nm as a consequence of SiO₂ coating, which can be slightly more pronounced for higher immersion times.^{41,32} The red shift is typical of gold nanoparticles when local refractive index (n) increase⁴² as consequence of the formation of the silica layer, which substitutes the mixed air/MPTS environment in the MPTS coated ZERO samples. It is worth of note that, apart the consistent red shift, LSPR bands aspect does not change, as already observed in Chapter 2.1, indicating that no appreciable variations in the GNSs morphology has happened. This was confirmed by HR-SEM imaging: Figure 7 represent the HR-SEM image of a FOUR sample and shows the homogeneous distribution of the unchanged GNSs objects. The coating process was found to be reproducible: only small differences in the measured spectra were found among ONE or FOUR samples, which are also due to the already observed differences among the parent ZERO samples (which may arise from the cited differences between the starting colloidal solutions). Anyway, the few samples having the long LSPR band centred out of the 870-910 nm range were discarded. UV-Vis spectra of some representative preparation batches after one or four hour silica coating treatments are reported in Figure 8: as can be clearly seen, reproducibility is observed not only between samples obtained from a single preparation vessel, but also between samples coming from different preparation batches: as an

⁴¹ T.A. Bendikov; A. Rabinkov; T. Karakouz; A. Vaskevich; I. Rubinstein; *Analytical Chemistry*, **2008**, 80, 19, 7487-7498.

⁴² K.M. Mayer; J.H. Hafner; *Chemical Reviews*, **2011**, 111, 6, 3828-3857.

example, Figure 8 reports the spectra obtained for some set of samples obtained from different preparation batches of ONE and FOUR samples.

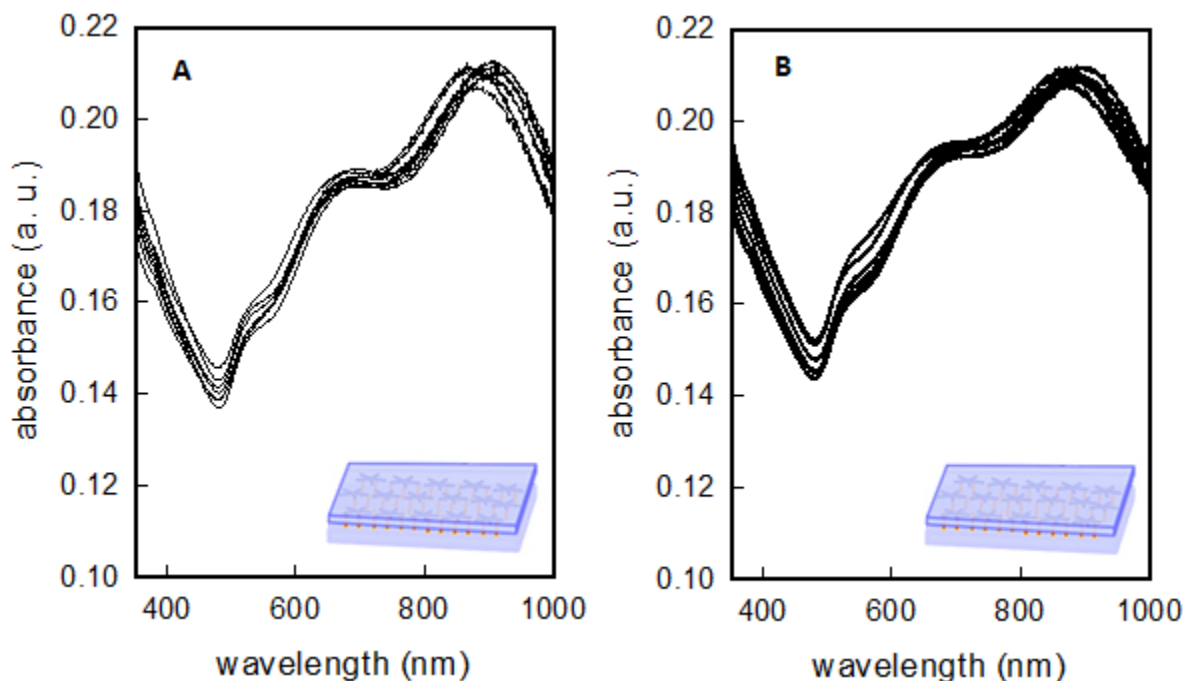


Figure 8: A) spectra of one representative preparation of samples of ONE type glasses come from different jars; B) spectra of different preparation of FOUR type glasses come from different jars;

2.2.3.3 SERS MEASURES: A PROOF OF CHEMICAL STABILITY OF CHIPS

As a first test of SERS substrates features, we decided to immerse ZERO type samples and FOUR type samples in an ethanol solution (10^{-3} M) of 7-mercapto-4-methylcoumarin, MMC, whose features as a Raman reporter in SERS based devices we recently described and that will be discussed in chapter 3.3 and 3.4.³⁷ Raman spectra of bulk MMC (which is reported in Figure 9a), is characterized by a high number of peaks spread in the whole measured energy region, and dominated by the stretching vibrational modes inside lactone and benzene rings. It is important to stress the fact that MMC was here chosen as a prototype of a contaminant possessing a strong Raman response with a complex fingerprint composed of several lines, coupled with a strong chemical affinity towards the gold nano-objects surfaces, by the means of formation of strong Au-S bonds, a molecule that could “chemisorbed” and not only “physisorbed” on the surface.¹⁸ In other words MMC was chosen as a model of a contaminant with a strong interfering signal and hard to remove from the SERS active surface of the chip.

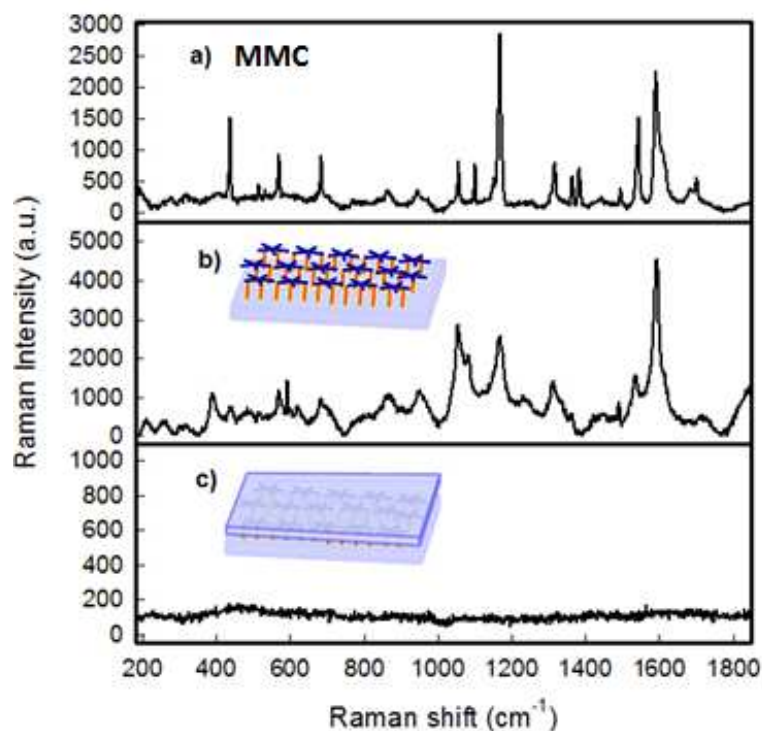


Figure 9: a) Raman spectra of solid MMC; b) SERS spectra obtained from a ZERO sample after immersion in 10^{-3} M solution of MMC followed by three cycles of washing; c) SERS spectra obtained from a FOUR sample after immersion in 10^{-3} M solution of MMC followed by three cycles of washing.

After one hour of immersion in a MMC ethanol solution, the SERS substrates were washed three times with 5 minutes immersions in fresh ethanol, in order to remove all the traces of the solution containing MMC and thus eliminate all the MMC molecules which were not “chemisorbed” to gold surfaces by means of S-Au bond. After these three washing cycles, the samples were gently dried under nitrogen flux and then the SERS spectrum was measured: it is showed in Figure 9. Presence of chemisorbed MMC, even after the three washing cycles, can be clearly observed.

This event can be explained only taking into account two obvious facts: i) MMC binds to gold surface of GNSs by means of the strong Au-S bond between MMC thiolic function and GNSs surface; ii) SERS effects is exerted on these MMC molecules by the close, nanostructured gold surface of GNSs. It is important to stress that even three washing cycles with EtOH are not enough to remove MMC chemically bound to the GNSs, and that the observable MMC SERS spectra is clearly signalling the presence of a strong and non-completely reversible interaction (the Au-S bond): in other words it denounces a pathway of interference and/or chemical degradation of the SERS active substrate,

caused by the irreversible reaction of unprotected noble metal nano-objects with functional groups of molecules dispersed in solution.

The SERS signal of MMC, even after the three washing cycles, is clearly observed in sample ZERO (Figure 9b) while no traces of the typical MMC Raman lines can be recognized in sample FOUR (Figure 9c). This fact demonstrated that even a thin silica coating prevent the formation of stable Au-S bond between MMC thiolic function and GNSs surface. In turn, without this oxide spacer, this bond cannot be removed even after three washing cycles with ethanol. Thus the silica coating protects the SERS active nanostructured substrates avoiding interferences and/or chemical degradation. In addition to mechanical inertness, a satisfying chemical stability, with complete separation of gold surface from reactive species in solution, is obtained with the silica coating process.

2.2.3.4 EFFECT OF THICKNESS OF SILICA COATING ON SERS RESPONSE

In order to investigate the applicability of the prepared functionalized glass samples as SERS substrates, the Raman signal of (R6G), a molecule widely used as a representative Raman probe, was measured for all kind of samples prepared. The SERS spectra of aqueous solutions with concentrations ranging between 1 and 100 μM were collected depositing 20 μL of R6G solution at a desired concentration on the SERS substrate, and spreading the drop on the functionalized surface by placing a “blank” (not functionalized) clean glass coverslip. In this way, a very thin film of solution is confined between two glass surfaces: a lower functionalized one and an upper blank (completely transparent) one.

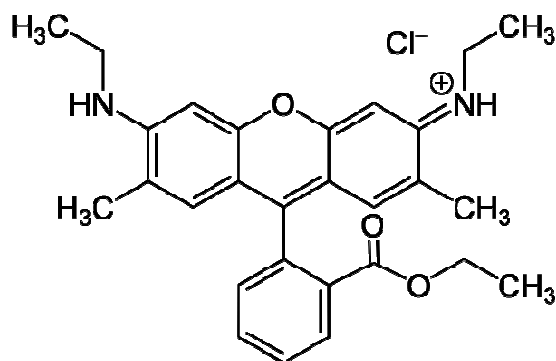


Figure 10: structure of Rhodamine 6G.

Table 1: assignment for Raman spectra of R6G molecule.⁴³

Wavenumber [cm ⁻¹]	610	770	1125, 1180	1310, 1575	1360, 1510, 1650
Vibration Mode	C-C-C Ring in plane	C-H Out of plane	C-H In plane bend	N-H In plane bend	C-C stretching

Rhodamine 6G molecule (Figure 10), containing two functional groups, a dibenzopyrene xanthene and a carboxyphenyl group tilted by about 90° with respect to the xanthene ring, exhibits an intense Raman yield, so this dye molecule has been widely used as SERS marker. The main Raman modes of R6G are peaked at around 614, 766, 1178, 1306, 1361, 1509, and 1647 cm⁻¹, corresponding to the CH, COC, and CC vibrations of aromatic rings. The different vibrational units responsible for the above mentioned peaks are detailed in Table 1, according to Watanabe et al.⁴³

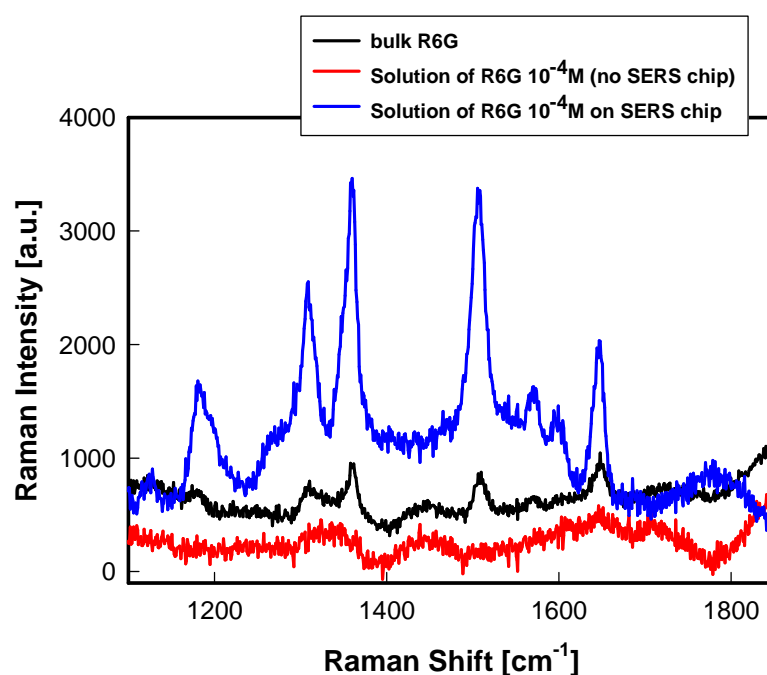


Figure 11: comparison between: a) Raman spectrum of bulk R6G, b) Raman spectrum of a solution 10⁻⁴ M of R6G in absence of a SERS ZERO type chip and c) Raman spectrum of a solution 10⁻⁴ M of R6G in presence of a SERS ZERO type chip.

⁴³ H. Watanabe; N. Hayazawa; Y. Inouye; S. Kawata; *J. Phys. Chem. B*, **2005**, 109, 5012-5020.

In Figure 11 the effect of enhancement in the region 1000-1900 cm^{-1} is clearly demonstrated. The SERS spectrum of 10^{-4} M of R6G dropped on ZERO chip (blue line) is compared to the signal from the same concentration of R6G dropped on a normal glass substrate and to the Raman spectrum from solid R6G (black line). R6G signals are well defined, and intensities do not change when the measure is performed on different zones of the same sample or in samples coming from different preparation batches. This fact has been verified and the results are reported in Figure 12-13-14, four SERS spectra obtained with 10^{-4} M, 10^{-5} M and 10^{-6} M solutions of R6G, obtained in four different positions on three different glass samples (one for every concentration used) is reported, accounting for good reproducibility of the measurements.

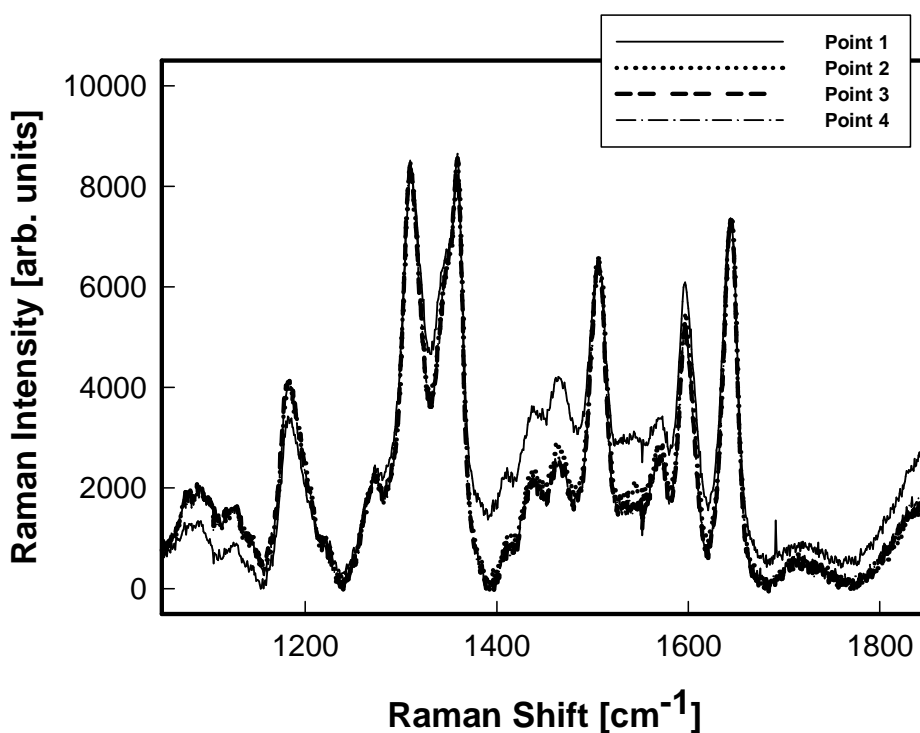


Figure 12: SERS spectra obtained with 10^{-4} M solutions of R6G on SERS ZERO type chip (four different positions on the same glass sample).

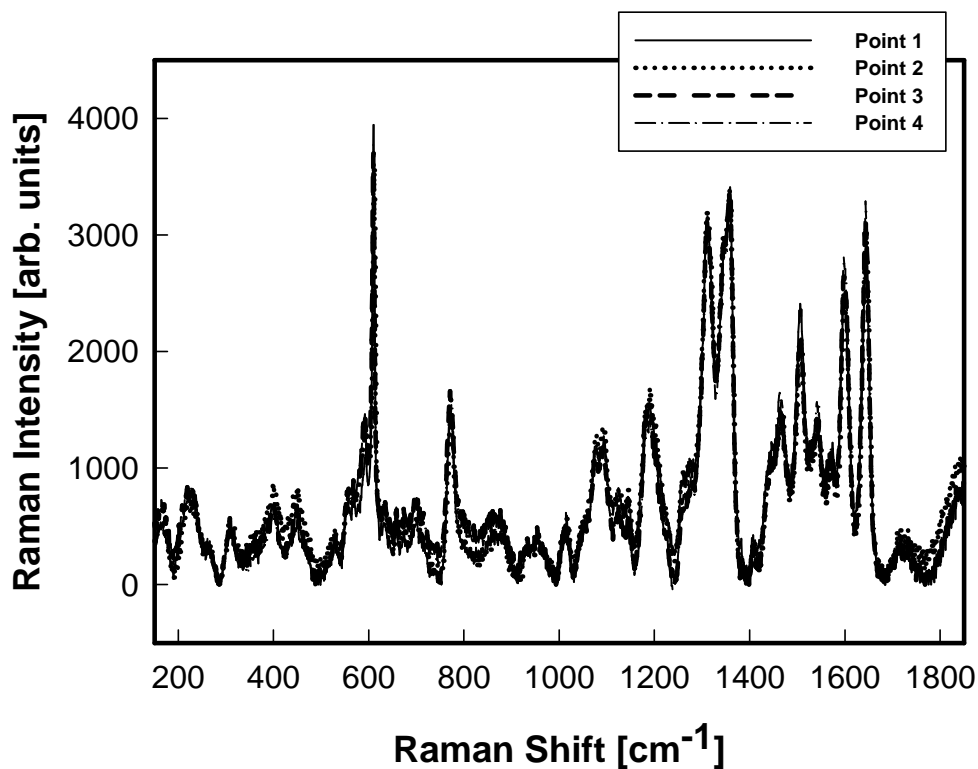


Figure 13: SERS spectra obtained with 10^{-5} M solutions of R6G on SERS ZERO type chip (four different positions on the same glass sample).

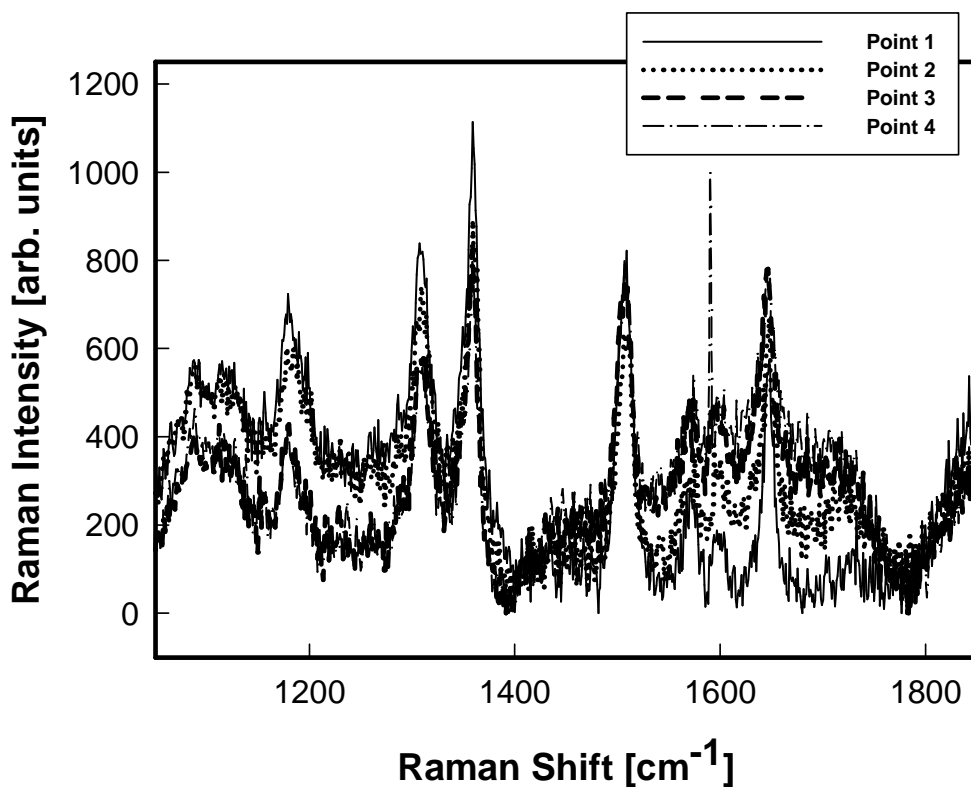


Figure 14: SERS spectra obtained with 10^{-6} M solutions of R6G on SERS ZERO type chip (four different positions on the same glass sample).

In Figure 15, the average spectrum of four SERS spectra obtained with 10^{-5} M solutions of R6G, coming from different preparations batches is reported, accounting for good reproducibility of the measurements.

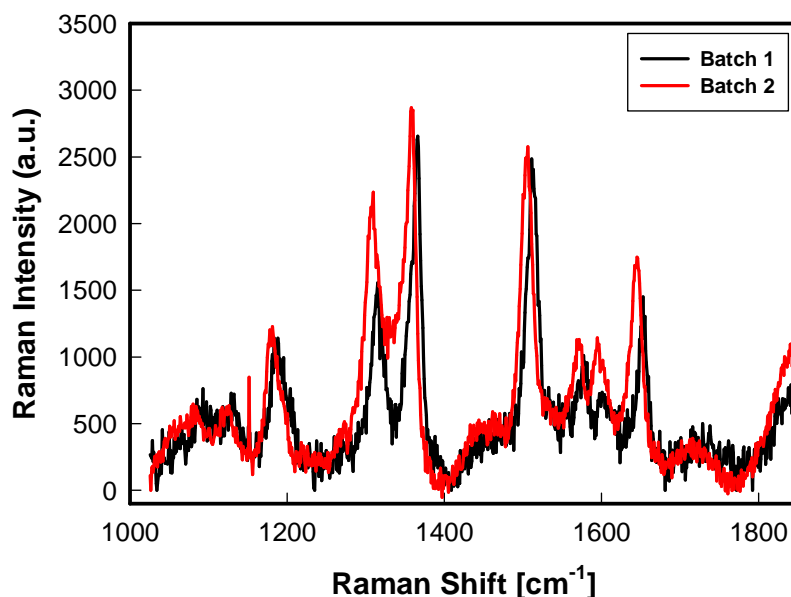


Figure 15: SERS spectra obtained with 10^{-5} M solutions of R6G on SERS ZERO type chip coming from two different preparation batches, realized from different starting colloids.

Measures were repeated on the ONE silica coated substrates. Presence of the thin layer of silica reduces but does not depress very strongly the SERS response. Figures 16 and 17 show a series of spectra obtained (in the same experimental conditions used for ZERO samples) for ONE samples in presence of 10^{-4} M and 10^{-5} M solutions of R6G. Once again reproducible spectra are obtained, while in all cases an obvious decrease in SERS intensity is observed when comparing the measures obtained for the same concentration of R6G in absence of silica coating.

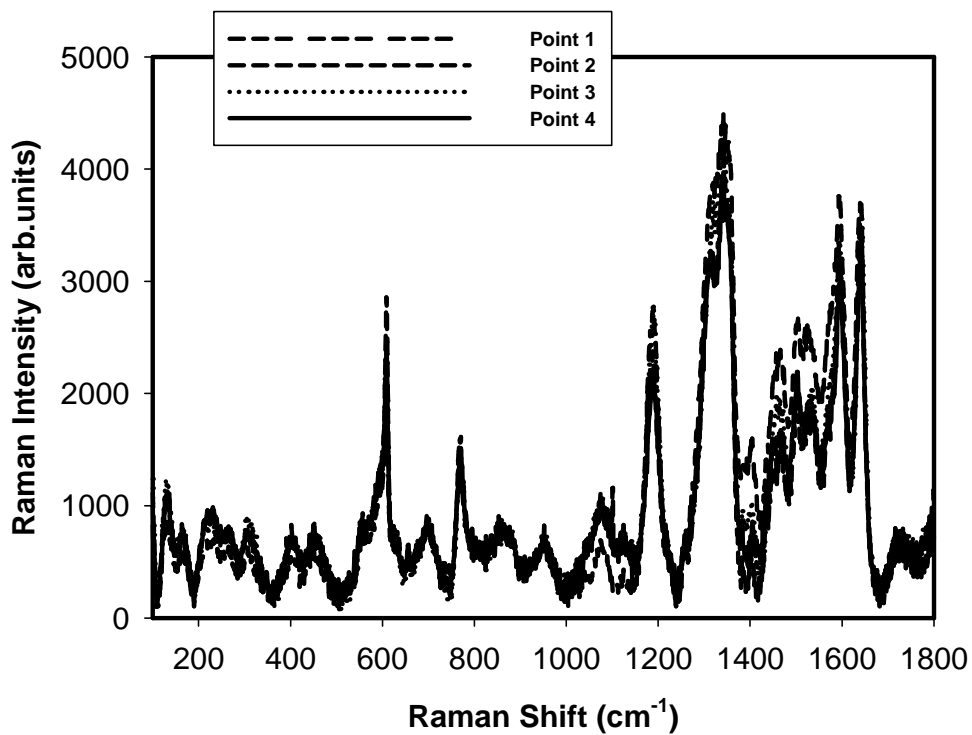


Figure 16: spectra of SERS response, with R6G 10^{-4} M, of a type ONE glass in four different positions.

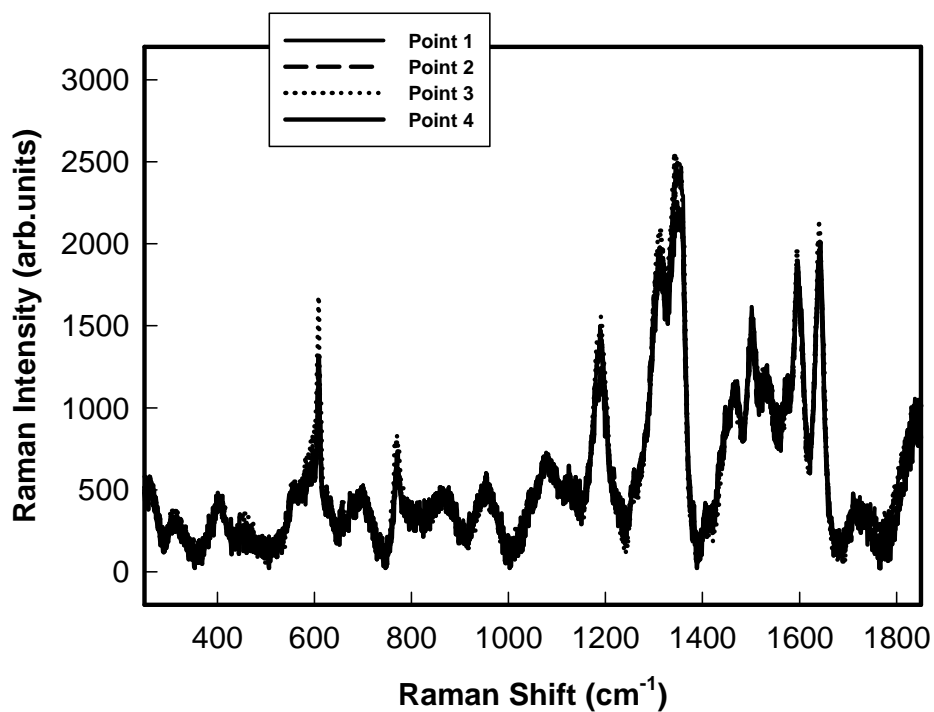


Figure 17: spectra of SERS response, with R6G 10^{-5} M, of a type ONE glass in four different positions.

Measures were repeated on the FOUR silica coated substrates. Presence of a more thick layer of silica than the ONE type, further reduces the SERS response. Figure 18 and 19 shows a series of spectra obtained (in the same experimental conditions used for ZERO samples) for FOUR samples in presence of 10^{-4} M and 10^{-5} M solutions of R6G. Once again reproducible spectra are obtained, while in all cases an obvious decrease in SERS intensity is observed when comparing the measures obtained for the same concentration of R6G in ONE type.

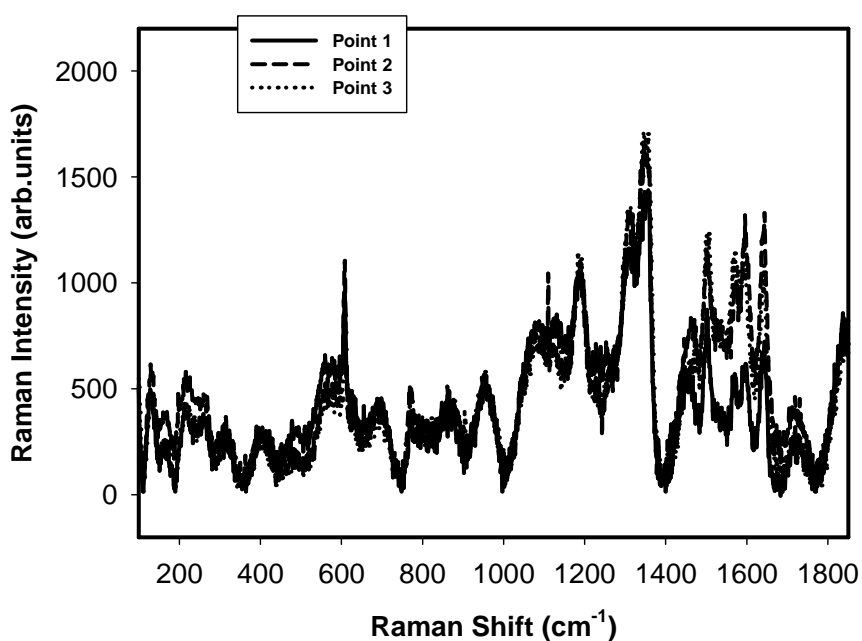


Figure 18: spectra of SERS response, with R6G 10^{-4} M, of a type FOUR glass in three different positions.

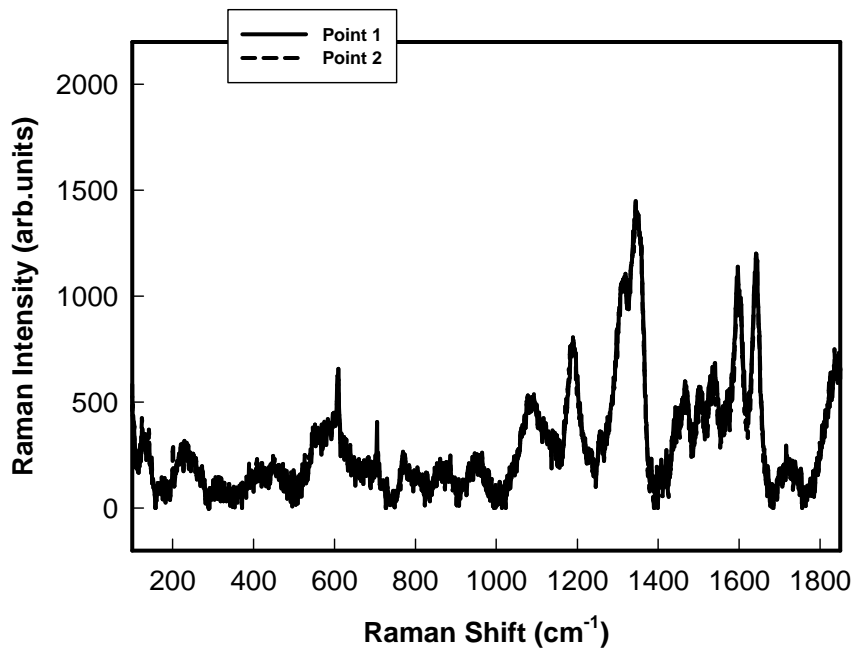


Figure 19: spectra of SERS response, with R6G 10^{-5} M, of a type FOUR glass in two different positions.

It is important to notice that a sensible difference is observed in the SERS spectra when comparing silica coated samples with the uncoated ones. Together with the reduction of intensity, a change in the spectra aspect is evident.

Anyway, as can be seen comparing spectra (with all the used concentrations) repeated in different zones of samples, intensities are very reproducible, and this finding demonstrates that not only we have an homogeneous GNSs coating, but that also the further added silica coating has an homogeneous thickness and does not alter the GNSs layer homogeneity.

In the case of FOUR samples, the SERS response is sensibly reduced. Anyway, it can be once again demonstrated that sampling on different zones of a sample yielded reproducible intensities of the R6G spectra, ensuring on the homogeneity of the silica coated SERS substrate. Even for coated samples, a good reproducibility is observed when using chips coming from different preparation batches: two examples are given in Figures 20 and 21.

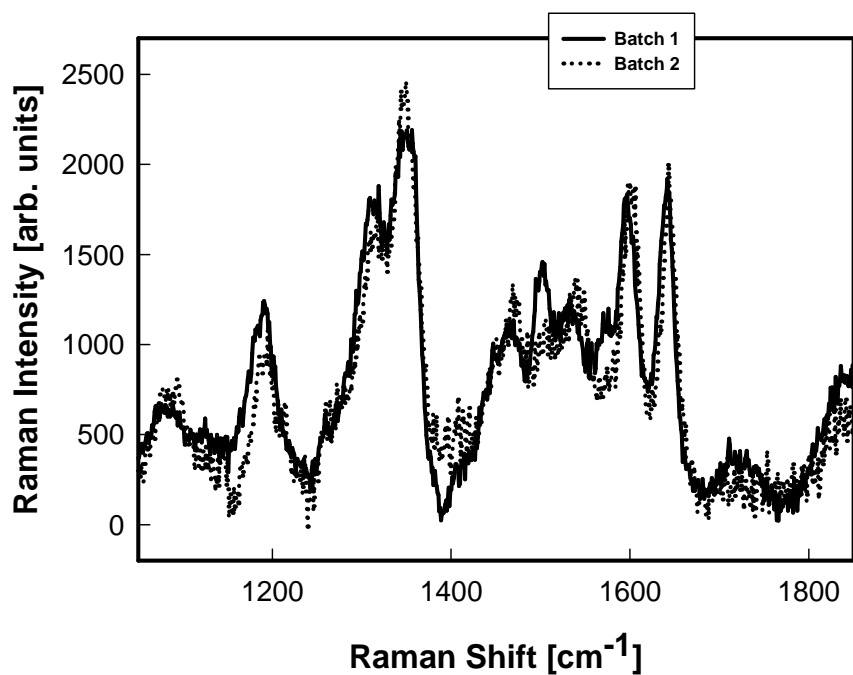


Figure 20: spectra of SERS response, with R6G 10^{-5} M, of two samples of type ONE glass coming from two different preparative batches.

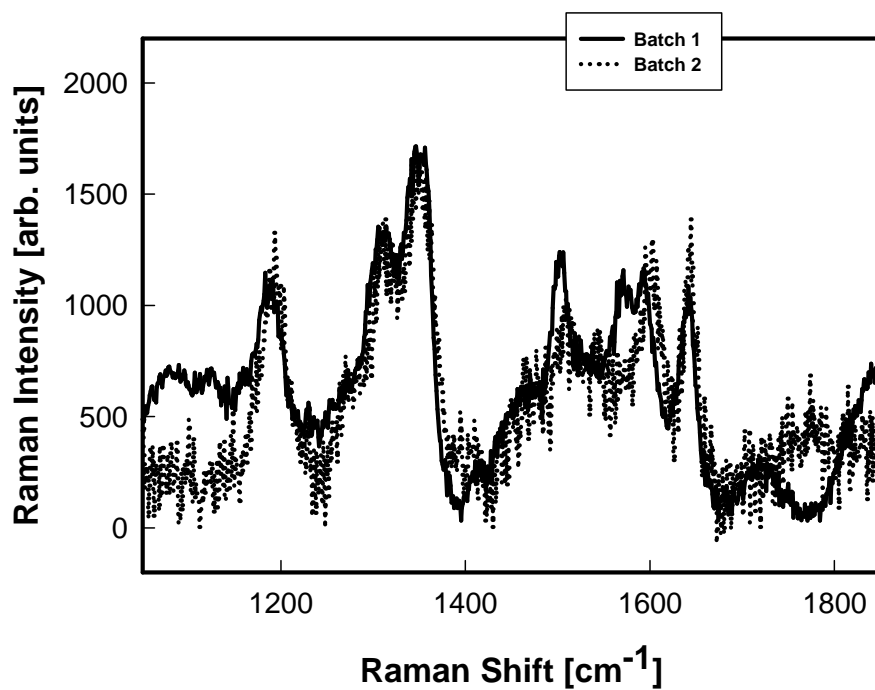


Figure 21: spectra of SERS response, with R6G 10^{-4} M, of two samples of type FOUR glass coming from two different preparative batches.

The overall results of these SERS measures can be summarized in Figure 22, where spectra for the three kind of samples are reported for the same R6G concentration (10^{-5} M) in the same experimental conditions.

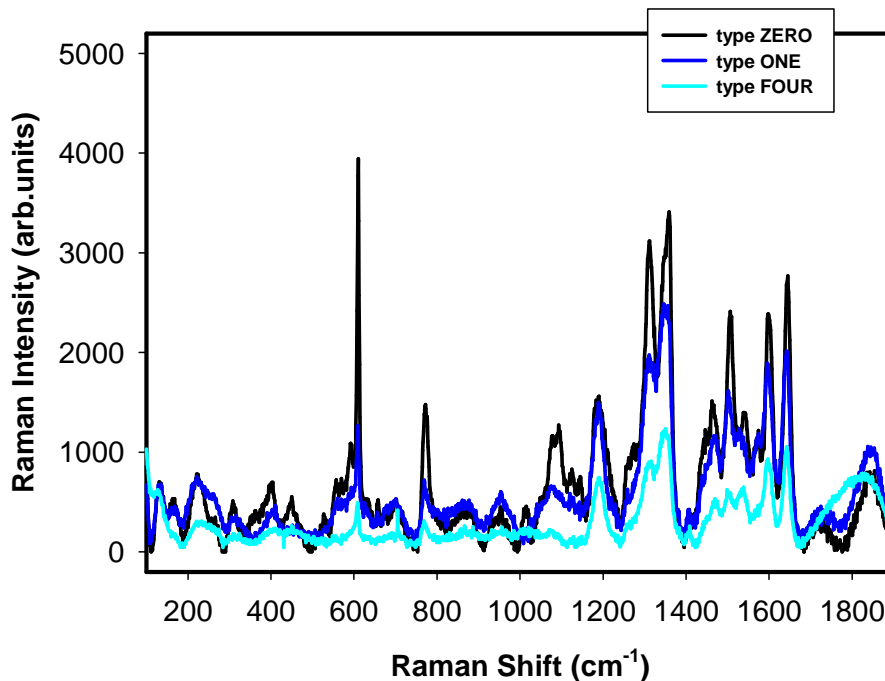


Figure 22: comparison of the SERS response, with R6G 10^{-5} M, of the different glass type: ZERO, ONE and FOUR.

Of course, the SERS yield of a specific Raman mode in the three different kind of samples can allow to extrapolate the dependence of SERS yield with the silica thickness. To do this, we calculated the integrated intensities of the Raman feature at 610 cm^{-1} for a set of SERS spectra obtained in identical experimental conditions, measured on the three kinds of samples. One lorentzian curve was used as the fitting function to derive the integrated intensities.

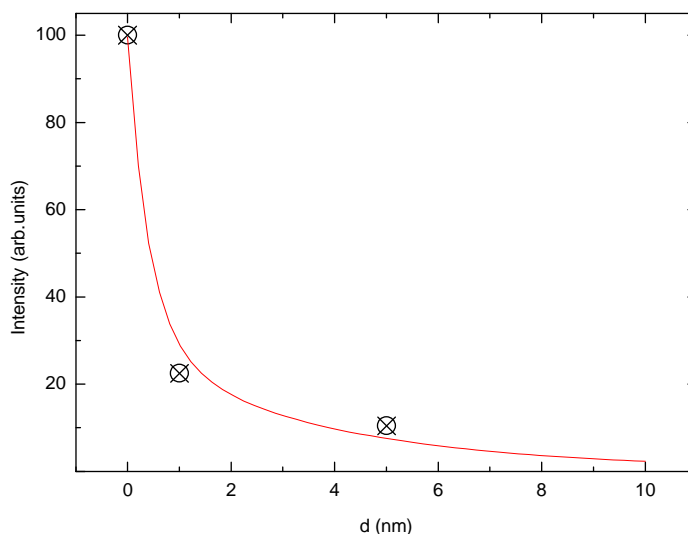


Figure 23: trend of the dependence of the normalized SERS yield with the silica thickness: the integrated intensity of the peak at 610 cm^{-1} is reported as a function of layer presumed thickness. The red line represents the expected electromagnetic enhancement as a function of distance from active surface according to equation (1), see text.

In Figure 23 the integrated intensities of the peak at 610 cm^{-1} , due to C-C-C ring in plane vibration, normalized to value obtained for ZERO sample, are plotted using as the independent variable the thickness, expressed in nm, of the silica layers in the three cases. These values has been considered as the minimum distances at which SERS enhancement take place in the three cases. The red line represent the out-put of the best fitting procedure where, according to Cotton et al.,⁴⁴ the following function has been used:

$$G_{em}(v_s) \sim [r/(r+d)]^{10} \quad (1)$$

In this formula $G_{em}(v_s)$ is the electromagnetic enhancement factor of a Raman mode at a given frequency v_s , r is the radius of the spherical nanoparticle and d the distance where a specific monolayer experiences the enhanced EM field. The experimental behaviour is well reproduced by a linear combination of two terms with two values for r , one accounting for the average curvature of the tip (4 nm) of a GNS and one accounting for the average radius of the larger central body of the nano-object (10 nm).⁴⁵ A good fit has been obtained using a weight for the smaller radius term 4 times greater than the other; this fact is the empirical proof of two different but cooperative effects: the abundance of

⁴⁴ T.M. Cotton; R.A. Uphaus; D. Mobius; *J. Phys. Chem.*, **1986**, 90, 6071-6073.

⁴⁵ B. Bassi; A. Taglietti; P. Galinetto; N. Marchesi; A. Pascale; E. Cabrini; P. Pallavicini; G. Dacarro; *Nanotechnology*, **2016**, 27, 265302-265313.

tips and the higher EF usually observed from sharp nano-objects.⁴⁶ The same agreement has been obtained also for the decreasing of SERS yield on higher energy modes (data not shown).

The observed behaviour indicates that only a very thin part of the LASER focus volume give sizeable SERS signal because molecular layers placed at distances greater than 10 nm from the nanoaggregates are practically SERS silent. We underline that quite recently a persistence of EF at longer distances, over 30 nm, has been reported and tentatively justified in terms of the spatial spread or depth of penetration to the dielectric of collective surface plasmon polaritons. In addition one has to consider that periodically some works report criticism on accepted explanations of SERS evidences and the risk of manage misconcepts in this field is extremely high.¹⁰ Best fitting results using equation (1) indicate that chemical enhancement is negligible even for “ZERO” samples and the behaviour is well reproduced by considering a pure EM contribution. These results allowed us to evaluate EF's. To estimate the SERS enhancement we used the following equation according to Le Ru et al.:¹¹

$$EF = (I_{SERS} / I_{RS}) \times (N_{RS} / N_{SERS}) \quad (2)$$

Where I_{RS} and I_{SERS} are the intensities of Raman and SERS peak of the same vibrational mode; N_{RS} and N_{SERS} are the numbers of R6G molecules respectively participating at the Raman and SERS phenomena in the two experiments. In this sense, the used formula is reminiscent of the SSEF definition given in paragraph 1.5.3.

For determination of N_{RS} and N_{SERS} , 10 μ L of R6G solution (10^{-3} M) was spread onto a blank glass slide with the diameter of 1 cm, while a more diluted R6G solution (1×10^{-4} M, 10 μ L) was dropped onto a ZERO substrates covering the same area. In both cases the drop was spread using a blank glass slide.

Some considerations are needed to explain the choice of R6G concentrations used to estimate EF factor. The comparison between Raman Spectroscopy and SERS signals are usually difficult and the first requirement is to be able to carefully control the experimental conditions. Just for this we used the same scattering geometry i.e. a sort of sandwich configuration. This allows to control the total volume of the drops. Then we choose 10^{-3} M concentration for Raman Spectroscopy experiments because this is the minimum value to obtain a sizeable signal in normal Raman experiments. We didn't use the same concentration in SERS to avoid contribution in SERS scattering from normal Raman process but on the other hand we selected 10^{-4} M to experience SERS in a similar

⁴⁶ K.S. Lee; M.A. El-Sayed; *J. Phys. Chem. B*, **2006**, 110, 19220– 19225.

concentration range thus avoiding SERS effects, sometimes unstable, from local hot spots. In this sense we are interested in the average and stable SERS response.

From the analyses on the peak at 610 cm^{-1} comparing SERS response from ZERO sample for a 10^{-4} M solution and normal Raman response for a 10^{-3} M solution, we obtain a value for the term ($I_{\text{SERS}}/I_{\text{RS}}$) equal to ~ 50 .

The term ($N_{\text{RS}}/N_{\text{SERS}}$) is strongly affected by the differences in scattering volumes, other than the factor 10 in concentration ratio. Due to the “sandwich” configuration the dimension that change in the two experiment is only the height of the beam contributing to the scattering. We have demonstrated that in the present case the SERS signal decreases dramatically with distance according to equation 1 (practically disappearing, see figure 23, at a distance longer than 10 nm) and thus we can consider that the effective volume, i.e. N_{SERS} , contributing to SERS signal is due to a 10^{-3} fraction of N_{RS} involved in normal Raman, being the whole thickness of the R6G dispersed drop calculated to be about 18 microns. More precisely, the ratio between the two heights should be $18000\text{ nm}/10\text{ nm} = 1.8 \times 10^3$. Considering the ratio in concentration, we obtain for ($N_{\text{RS}}/N_{\text{SERS}}$) a value of 1.8×10^4 and a total EF factor equal to $\sim 9 \times 10^5$ for the ZERO samples. We underline that this value is in good agreement with that reported in Le Ru et al..¹¹

2.2.3.5 TESTING REUSABILITY

Recyclable SERS-active substrates which can regenerate their activity after every cycle of measurements are highly desired, and different approaches have been proposed for cleaning of these SERS-active substrates. In a recent example, reusability was obtained regenerating a silica coated GNSs surface by means of washing with sodium borohydride solutions, which were able to remove every absorbed molecule by simply flowing into the capillary which were used for continuous online analysis.²⁹ As reusability should be a key feature for all SERS-active substrates, we tested in a very simple way the reusability of our samples, which derives directly from the mechanical and chemical inertness we have described in the previous section.

A freshly prepared ONE silica coated sample was used to measure the SERS spectra on 20 μL of a 10^{-4} M solution of R6G using the already described methodology. After the measure, the blank glass used as a cover was removed, and the SERS active substrate was simply washed under a flow of bi-distilled water and then treated in bi-distilled water with one minute of ultrasounds. At this point, a SERS spectra using 20 μL of water

was taken. After this, water was removed with a clean tissue, and then the substrate was reused with another portion of 10^{-4} M solution of R6G to take another SERS spectra. The results are reported in figure 24: as can be clearly observed, an almost identical spectra was obtained. The described procedure can be repeated several times without any change in behaviour.

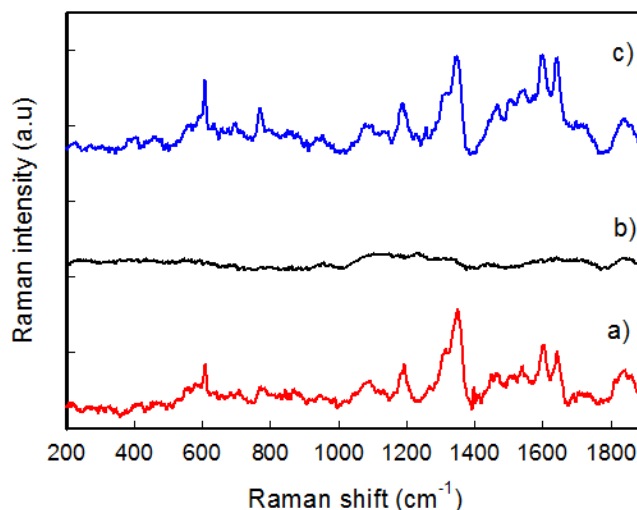


Figure 24: reusability of silica coated SERS substrate: a) SERS spectra of R6G 10^{-4} M on fresh new ONE substrate; b) spectra of water on same substrate after washing and sonication; c) SERS spectra of R6G 10^{-4} M on recycled substrate.

2.2.3.5 CONCLUSION

It is important to underline three facts: i) as described, the silica coating avoid contact with the solution, preventing chemical bonding of reactive molecules with the gold surface of nano-objects and ensuring mechanical resistance to washing, effects of ultrasounds, scratching; ii) in the same time, the presence of silica of a controlled thickness reduces but does not suppress SERS response; iii) homogeneity of GNSs grafting and of silica coating ensure reproducibility: taking the spectra of the same solutions in two positions of the SERS substrate before and after washing yields almost and identical response.

CHAPTER 3: GNSS: ADDING FUNCTIONS WITH TAILORED COATING

3.1 SENSING PB

3.1.1 INTRODUCTION

Detection of chemical and biological agents plays a fundamental role in biomedical, forensic and environmental sciences¹ as well as in anti-bioterrorism applications.² The development of highly sensitive, cost-effective, miniature sensors requires advanced technology coupled with fundamental knowledge in chemistry, biology, and material sciences.³ Such an example in this field is the design of metal ion sensors has long been a focus of research as it can provide on-site, real-time detection and quantification of beneficial and toxic metal ions in applications such as household and environmental monitoring, developmental biology, or clinical toxicology; as regard toxicology field, significant importance has been made in revealing trace of lead as a dangerous contaminant. Some 20 or 25 years ago, the pathological descriptions of lead toxicity consisted largely of clinically discernible effects and changes that could be seen in tissues under the microscope,⁴ at that time, permissible occupational exposure to lead was limited to a blood lead level of 70-80 µg/dL. Lead levels among people in the general population were 20-30 µg/dL, and levels in children above 40 µg/dL were recognized as indicative of lead toxicity. Nevertheless, over the past two decades there has been growing awareness and concern that toxic biochemical and functional effects were occurring at lower levels of exposure than those that produced overt clinical and pathological signs and symptoms. Some instances of disease associated with toxic lead level are: i) problems on cognitive and behavioural development of the central nervous system (CNS) on infants and children, ii) cardiovascular disease, iii) nephropathy and iv) renal adenocarcinoma.⁵ The major environmental sources of lead are: dust, soil, food, and water.⁶ As can be clearly understood, there is a strong and constant need to develop methods able to provide quick, inexpensive and on-site monitoring of lead presence in drinking waters and more generally in environment. While significant progress has been made in making fluorescent sensors,⁷ including Pb(II) sensors,⁸ few colorimetric metal

¹ D. Diamond; Principles of Chemical and Biological Sensors; John Wiley & Sons, Inc.: New York, NY, **1998**.

² M. Burnworth; S.J. Rowan; C. Weder; *Chem. Eur. J.*, **2007**, 13, 7828-7836.

³ O.R. Miranda; B. Creran; V.M. Rotello; *Curr. Opin. Chem. Biol.*, **2010**, 14, 728-736.

⁴ R.A. Goyer; B.C. Rhyne; *Int. Rev. Exp. Pathol.*, **1973**, 12, 1-77.

⁵ Robert A. Goyer; *Environmental Health Perspectives*, **1993**, 100; 177-187.

⁶ EPA. *Air Quality Criteria for Lead*; U.S. Environmental Protection Agency; Research Triangle Park, NC, **1986**.

⁷ R.Y. Tsien, R. Y.; *In Fluorescent Chemosensors for Ion and Molecule Recognition*, American Chemical Society: Washington, DC, **1993**, 538, 130-146.

⁸ Y. Lu; *Chem. Eur. J.*, **2002**, 8, 4588-4596.

sensors have been reported. A simple colorimetric sensor could eliminate or minimize most costs associated with instrumentation and operation in fluorescence detection and thus can make on-site, real-time detection easier.⁹

In this work, the already described gold nanostars (GNSs), having a mean hydrodynamic size of 40 nm, obtained using a seed-growth method using a zwitterionic surfactant (laurylsulfobetaine, LSB),¹⁰ were successfully coated with glutathione (GSH), in order to obtain a stable and purified solid product which can be easily stored and re-dissolved on need and upon exposure to micromolar concentrations of Pb²⁺ cation undergo a fast aggregation followed by the complete precipitation in about an hour. The subsequent disappearing of the intense LSPR extinction can, of course, be followed spectrophotometrically but, most importantly, can be easily detected with the naked eye. No signs of this event are noticed when other divalent cations are added to the colloidal suspension in the same condition. A careful investigation was performed to study this selectivity and the behaviour of aggregation as a function of time and Pb²⁺ cation concentration. Thanks to this approach an easy, rapid, instrument-free, visual detection of micromolar levels of Pb²⁺ can be obtained, showing a good selectivity towards other investigated metal cations.

In a classical supramolecular definition, a sensory system could be envisaged as a “selectivity signal” device, in which a receptor unit (selective for a specific analyte) is covalently/coordinationally bound to a signalling unit that is able to display a property whose magnitude changes substantially as a result of the interaction of the analyte with the receptor. For example, using as a signalling unit a chromophoric or fluorogenic moiety, the spectral features can be influenced by a binding event with the analyte, which happens in solution. Thus, any change which can be perceived by the naked eye¹¹ or with a simple instrument (spectrofluorimeter or UV-Vis spectrophotometer) is particularly precious, leading to quick qualitative determination of the presence of substances of interest, for example pollutants, poisons or relevant molecules in biological field.^{12,13} A completely different and interesting approach to colorimetric detection of analytes in solution comes from exploitation of the plasmonic features of noble metal nanoparticles.^{14,15,16} The use of these kind of probes for visual detection of ions has

⁹ I. Oehme; O.S. Wolfbeis; *Mikrochim. Acta*, **1997**, 126, 177-192.

¹⁰ A. Casu; E. Cabrini; A. Donà; A. Falqui; Y. Diaz-Fernandez; C. Milanese; A. Taglietti; P. Pallavicini; *Chem. Eur. J.*, **2012**, 18, 9381-9390.

¹¹ L. Fabbrizzi; P. Pallavicini; L. Parodi; A. Perotti; A. Taglietti; *J. Chem. Soc. Chem. Commun.*, **1995**, 23, 2439-2440.

¹² L. Fabbrizzi; M. Licchelli; G. Rabaioli; A. Taglietti; *Coord. Chem. Rev.*, **2000**, 205, 85-108.

¹³ N. Marcotte; A. Taglietti; *Supramol. Chem.*, **2003**, 15, 7-8, 617-625.

¹⁴ R. Elghanian; J.J. Storhoff; R.C. Mucic; R.L. Letsinger; C.A. Mirkin; *Science*, **1997**, 277, 5329, 1078-1081.

¹⁵ M.C. Daniel; D. Astruc; *Chem. Rev.*, **2004**, 104, 1, 293-346.

gained a huge attention in the last years. The development of colorimetric sensing devices based on the variation of LSPR rely usually on aggregation of opportunely functionalized nano-objects induced by binding of an analyte.^{17,18,19} The position of LSPR bands is sensibly influenced, in addition to several other features like size, shape, nature of the coating agent, solvent and media,²⁰ by interparticle distance,^{21,22} and thus aggregation usually produces a shift in plasmonic peaks, which can be easily measured by means of simple spectrophotometric apparatus, or even clearly perceived with naked eye. To obtain this kind of simple sensory systems for heavy metal cations, which can be contaminants with serious effects on human health, two features are important: i) the presence of a robust and protective coating agent on the surface of the nanoparticle to ensure stability and avoid precipitation in highly saline media,^{23,24} and some ii) binding property exerted by the same agent, to ensure a specific interaction with the specific cation, or at least a good degree of selectivity towards it. Furthermore, this molecule should be able to only partially fill the coordination demand of the cation, causing the cation itself to look for at least two coordinating moieties to complete its coordination sphere. If these conditions are verified, one can expect that the presence of cation in the colloidal suspension of the nanoparticle will cause cross-linking between them, resulting in an aggregation which could be perceived as a neat colour change of the colloidal suspension.

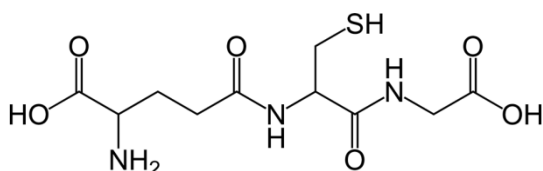


Figure 1: structure of glutathione.

Following this strategy, several examples have been presented in the recent past, based on spherical Ag and Au nanoparticles coated with different ligands: such oligo-DNA for Hg²⁺ detection,²⁵ histidine-based ligand for Fe³⁺,²⁶ cysteine for Cu²⁺,²⁷ just to name a few. One of

the most used ligands is glutathione (GSH) (Figure 1), which has several features which are strategic for the purpose: in addition to "mercapto" function, ensuring a robust binding to noble metal surfaces, GSH has two free-COOH groups and one NH₂ group

¹⁶ K. Saha; S.S. Agasti; C. Kim; X.N. Li; V.M. Rotello; *Chem. Rev.*, **2012**, 112, 5, 2739–2779.

¹⁷ E. Hutter; M.P. Pileni; *J. Phys. Chem. B*, **2003**, 107, 27, 6497–6499.

¹⁸ I. Tokareva; S. Minko; J.H. Fendler; E. Hutter; *J. Am. Chem. Soc.*, **2004**, 126, 49, 15950–15951.

¹⁹ A. Arduini; D. Demuru; A. Pochini; A. Secchi; *Chem. Commun.*, **2005**, 5, 645–647.

²⁰ C.W. Liu; C.C. Huang; H.T. Chang; *Langmuir*, **2008**, 24, 15, 8346–8350.

²¹ M.A. El-Sayed; *Acc. Chem. Res.*, **2001**, 34, 4, 257–264.

²² R. Elghanian; J.J. Storhoff; R.C. Mucic; R.L. Letsinger; C.A. Mirkin; *Science*, **1997**, 277, 5329, 1078–1081.

²³ E. Amato; Y.A.D. Fernandez; A. Taglietti; P. Pallavicini; L. Pasotti; L. Cucca; C. Milanese; P. Grisoli; C. Dacarro; J.M.F. Hechavarría; *Langmuir*, **2011**, 27, 15, 9165–9173.

²⁴ A. Taglietti; Y.A.D. Fernandez; P. Galinetto; P. Grisoli; C. Milanese; P. Pallavicini; *J. Nanoparticle. Res.*, **2013**, 15, 11, 1–13.

²⁵ S.J. Lee; M.S. Han; C.A. Mirkin; *Angew. Chem. Int. Edition*, **2007**, 46, 22, 4093–4096.

²⁶ J. Guan; L. Jiang; J. Li; W. Yang; *J. of Phys. Chem. C.*, **2008**, 112, 9, 3267–3271.

²⁷ W.R. Yang; J.J. Gooding; Z.C. He; Q. Li; G.N. Chen; *J. Nanosci. Nanotechnol.*, **2007**, 7, 2, 712–716.

ready to bind specific cations, with an affinity which can be tuned on the basis of the groups protonation and thus as a consequence of pH values.²⁸ Quite a lot of aspects have still to be explained on the features of these sensory systems, mainly from the point of view of the reasons of selectivity towards certain cations. Nevertheless, GSH-capped nanospheres have been used for detection of Ni²⁺,²⁹ As³⁺,³⁰ and Pb²⁺.^{31,32} Except a few examples, silver and gold nanoparticles used with this approach are of spherical size, even if in the last years some examples of anisotropical noble metal nanoparticles coated with GSH have been reported.^{33,34} Among the divalent cations worth of investigations, Pb²⁺ is of particular importance, as it is one of the most toxic for human health. Lead cation can also become a pollutant for drinking water. In the famous “lead in drinking water crisis” in Washington, DC, residents of the District of Columbia were subject to a high rise of lead cation concentration in drinking water, as a consequence of the change of disinfectant from free chlorine to chloramine in November 2000. This altered the water chemistry, causing the leaching of lead cations from lead line pipes and other plumbing materials. In some cases, lead concentration found in samples (taken during the leaching peak in early 2004) exceeded 300 ppb.^{35,36} As can be clearly understood, there is a strong and constant need to develop methods able to provide quick, inexpensive and on-site monitoring of lead presence in drinking waters and more generally in environment. As already stated several times, in our laboratory anisotropic gold nanoparticles (GNSs) based on seed-mediated growth approach, using a neutral surfactant, laurylsulphobetaine (LSB) have been widely characterized.¹⁰ Moreover, it was recently described a procedure to purify Ag nano-objects from unreacted species coming from the synthetic steps, by means of coating nano-objects with a self-assembled monolayer of GSH, which binds to noble metal nanoparticles surface with the sulphur atom of the thiolic function, followed by precipitation at a proper pH and centrifugation, yielding robust, purified AgNP to be used as antibacterial agents. On the basis of all these facts, it is described here a simple protocol in order to obtain purified and robust GNSs coated with GSH, which were then investigated in order to test the ability of the system to act a sensor for Pb²⁺ trace in solution. It will be demonstrated that a quick and selective visual

²⁸ R. Fu; J. Li; W. Yang; *J. Nanopart. Res.*, **2012**, 14, 929.

²⁹ H. Li; Z. Cui; C. Han; *Sens. Actuators B Chem.*, **2012**, 143, 1, 87–92.

³⁰ J.L. Li; L.X. Chen; T.T. Lou; Y.Q. Wang; *Acs Appl. Mater. Interfaces*, **2011**, 3, 10, 3936–3941.

³¹ L. Beqa; A.K. Singh; S.A. Khan; D. Senapati; S.R. Arumugam; P.C. Ray; *Acs Appl. Mater. Interfaces*, **2011**, 3, 3, 668–673.

³² F. Chai; C.A. Wang; T.T. Wang; L. Li; Z.M. Su; *Acs Appl. Mater. Interfaces*, **2012**, 2, 5, 1466–1470.

³³ C.V. Durgadas; V.N. Lakshmi; C.P. Sharma; K. Sreenivasan; *Sens. Actuators B Chem.*, **2011**, 156, 2, 791–797.

³⁴ H.K. Sung; S.Y. Oh; C. Park; Y. Kim; *Langmuir*, **2013**, 29, 28, 8978–8982.

³⁵ T.L. Guidotti; T. Calhoun; J.O.D. Cole; M.E. Knuckles; L. Stokes; C. Glymph; G. Lum; D.F. Goldsmith; L. Ragain; **2009**, 115, 695–701.

³⁶ M. Edwards; S. Triantafyllidou; D. Best; *Environ Sci. Technol.*, **2009**, 43, 5, 1618–1623.

response caused by aggregation of nanoparticles and subsequent precipitation are obtained with micromolar quantities of Pb^{2+} , even in the presence of other divalent cations.

3.1.2 EXPERIMENTAL DETAIL: SYNTHESIS AND CHARACTERIZATION

3.1.2.1 MATERIALS AND INSTRUMENTATION

Reagents

N-Dodecyl-N,N-dimethyl-3-ammonium-1-propanesulfonate (LSB) ($\geq 99.7\%$), Gold(III) chloride trihydrate ($\sim 30\text{wt}\%$ in HCl 99.99%), sodium borohydride (98%), L-ascorbic acid (AA) ($\geq 99\%$), silver nitrate (99.8%), sodium citrate ($\geq 99\%$), L-glutathione reduced (99%), Hepes, $\text{Cu}(\text{CF}_3\text{SO}_3)_2$, $\text{Cd}(\text{CF}_3\text{SO}_3)_2$, $\text{Ni}(\text{CF}_3\text{SO}_3)_2$, $\text{Co}(\text{CF}_3\text{SO}_3)_2$, $\text{Zn}(\text{CF}_3\text{SO}_3)_2$, $\text{Mn}(\text{CF}_3\text{SO}_3)_2$ and $\text{Pb}(\text{NO}_3)_2$ were purchased from Sigma–Aldrich. Reagents were used as received. Glass cuvettes were standard optical glass purchased from Hellman. All the preparation are made with bi-distilled water.

Instrumentation

UV-Vis Spectroscopy. All UV–Vis absorbance spectra of colloidal suspensions were taken with a Varian Cary 50 spectrophotometer in the range between 350 and 1100 nm, using a standard quartz cuvette with 1 cm optical path.

Transmission electron microscopy (TEM). Images were obtained on colloidal suspensions of GNSs-GSH adjusted at pH 3 and 7 in water soon after GSH addition, and on GNSs-GSH re-dissolved in 0.1 M Hepes at pH 7, after addition of Pb^{2+} ions at final concentration of 5 μM . All samples for TEM were prepared as described and immediately diluted 1:10 with bidistilled water, and soon deposited on Copper grids (300 mesh) covered with a Parlodion membrane and observed with a Jeol JEM-1200 EX II instrument, using a voltage of 80 kV.

Dynamic light scattering measurements (DLS). The measurements were performed with a Zetasizer Nano-ZS90 (source: polarized He–Ne laser, 30 mW output power, vertically polarized). In particular, hydrodynamic size and Zeta potencial measurements of GSH-GNSs at different pH values were estimated on eight samples of colloidal suspension brought at different pH values. To obtain the chosen pH value (ranging from 3.7 to 11), small quantities of standard solution of HNO_3 0.01 M or NaOH 0.05 M were added. Both

measurements of hydrodynamic size and Zeta potential were replicated three times for each pH value. DLS was also used to measure changes in GNSs-GSH hydrodynamic size in the presence of Pb^{2+} . These measurements were performed on 10 mL of colloidal suspension. To this samples, 0.005 mL of 10^{-3} M PbNO_3 10^{-3} M in water was added, to obtain a Pb^{2+} concentration of 0.5 μM . Immediately after addition (time zero), hydrodynamic measurements were registered. Then, on the same sample, hydrodynamic size of GNSs-GSH was recorded at different fixed time. Hydrodynamic size measurements were replicated three times for each established time. The influence of the increase in Pb^{2+} concentrations on aggregates formation rate was measured on four samples of GNSs-GSH colloidal suspension (10 mL buffered to pH 7 with 0.1 M Hepes) using DLS. The hydrodynamic diameter of colloidal particles was measured immediately after the addition of a certain amount of lead of a solution of PbNO_3 10^{-3} M in water, in order to have a final concentration in each sample, respectively, of 5×10^{-7} M, 10^{-6} M, 3×10^{-6} M and 5×10^{-6} M. After a lapse of five minutes from the addition of lead solution, hydrodynamic measurements were recorded again on each sample. The measurements were replicated three times for each concentration and established time.

3.1.2.2 GLASSWARE PRE-TREATMENT

All the glassware that come into contact with GNSs was always pre-treated before use: a wash in *aqua regia* for 30 minutes, then washed and filled with bi-distilled water and ultrasonicated for three minutes before discarding water. The bi-distilled water/ultrasound treatment was repeated three times. Then the glassware were dried in an oven for 1 hour at 140°C .

3.1.2.3 PREPARATION AND CHARACTERIZATION OF THE SENSORY SYSTEM

Preparation of GNSs

The seeds were prepared in a vial by adding 5.0 mL of LSB aqueous solution (0.2 M) and 5.0 mL of HAuCl_4 aqueous solution (5×10^{-4} M). Subsequently, 600 μL of an ice-cooled solution of NaBH_4 in water (0.01 M) were added to the pale yellow solution of AuCl_4^- obtained in the previous step. As prepared brown-orange solution was gently hand-shaken for a couple of second; this solution is efficient for the growth procedure of gold nanostar for 180 minutes from preparation if kept cold. The growth solution was

prepared with 50 mL of LSB solution in water at the same concentration chosen for the seed solution (0.2 M), 1800 μL of AgNO_3 in water (0.004 M), 50 mL of aqueous HAuCl_4 (5×10^{-4} M) and 820 μL of an aqueous L-ascorbic acid solution (0.078 M) mixed to obtain a colorless solution just after a few seconds of gentle mixing. Then 120 μL of seed solution were added to give a blue colour liquid, the intensity of which rapidly increased. The solution was allowed to react without agitation for 1 h.

Preparation, purification and re-dissolution of GNSs-GSH

Typically, a sample of GNSs (10 mL) was centrifuged for 25 minutes at 13000 rpm. Then the supernatant (colourless) was discarded, and the nano-objects pellet was completely re-dissolved in bi-distilled water (10 mL). GSH-coated GNSs suspension was prepared by adding GSH solution 0.001M (0.250 mL) in water to the GNSs colloidal suspensions and leaving the suspension standing for 1h. Then the sample was acidified with standard HNO_3 solution 0.01M in water to a pH value of about 3, in order to obtain precipitation of the GSH-capped GNSs. After centrifugation for 5 minutes at 5000 rpm and subsequent removal of the supernatant, the nano-objects were stored in glass vials. For further experiments, the stored GNSs-GSH were dissolved typically in 10 mL of 0.1 M Hepes buffer solution adjusted at pH 7, or in pure water, which was then adjusted to pH 7 with small aliquots of standard acid and base solutions.

Behaviour of GNSs-GSH with metal cations

Titration of 10 mL of colloidal suspension of GNSs-GSH, prepared as previously described, was performed adding increasing quantities of a stock solution of divalent cations. In a typical experiment, UV-Vis spectra for the colloidal suspension in the absence of added cation were registered, and then one spectrum was taken 10 s after every addition. For the mixed cations containing stock solutions, a first one, without Pb^{2+} , was prepared containing a total concentration of metal cations of 0.001 M (1.6×10^{-4} M for each cation). The second one, containing also Pb^{2+} , was once again prepared containing the same total concentration of metals (1.4×10^{-4} M for each cation). For time-related measurement, after taking a spectrum in the absence of cations, to 10 mL of colloidal suspension of GNSs-GSH, prepared as previously described, for each metal cation investigated a proper quantity of a stock solution was added, in order to have a final concentration of 3 μM . A spectrum was taken 30 s after mixing, then a second one

after 90 s. After these first spectra, all the following spectra were taken every 2 min. All UV–Vis absorbance spectra of colloidal suspensions were taken with a Varian Cary 50 spectrophotometer in the range between 350 and 1100 nm, using a standard quartz cuvette with 1cm optical path.

3.1.3 RESULT AND DISCUSSIONS

3.1.3.1 COATING OF GNSs WITH GLUTATHIONE

GNSs, synthesized with the seed-growth method described above¹⁰ are stabilized by the presence of LSB surfactant. After a first centrifugation step in order to remove excess of LSB and other reagents, a proper concentration of GSH (2×10^{-5} M) is added, the thiolic group of GSH easily deprotonates, and sulphur atom can directly bind to gold surface, bringing GSH to substitution of the remaining surfactant molecules. A first indication of this event can be obtained by a simple UV-Vis spectra, as reported in Figure 2.

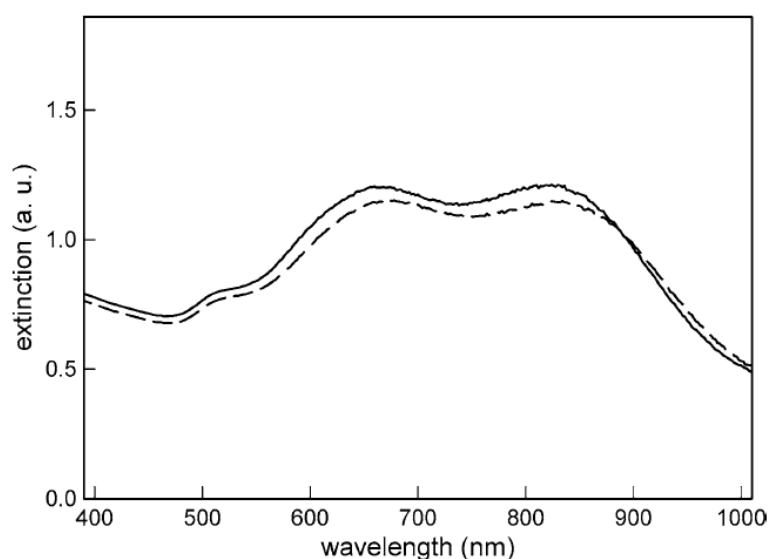


Figure 2: representative UV-Vis spectra of a colloidal suspension of GNSs: after centrifugation (solid line) and after GSH addition (dashed line)

The spectra of LSB stabilized GNSs are, as expected, composed of three plasmonic bands, reflecting the composition of objects mixture and the addition of GSH causes a moderate shift (about 8(3) nm) in the LSPR frequencies, a phenomenon which can be explained on the basis of the change of refractive index caused by thiolic coating agent. The GSH-coated GNSs were then characterized by means of DLS measurements. Z-potential at different pH was registered, obtaining a behaviour which is described in Figure 3 (black diamonds).

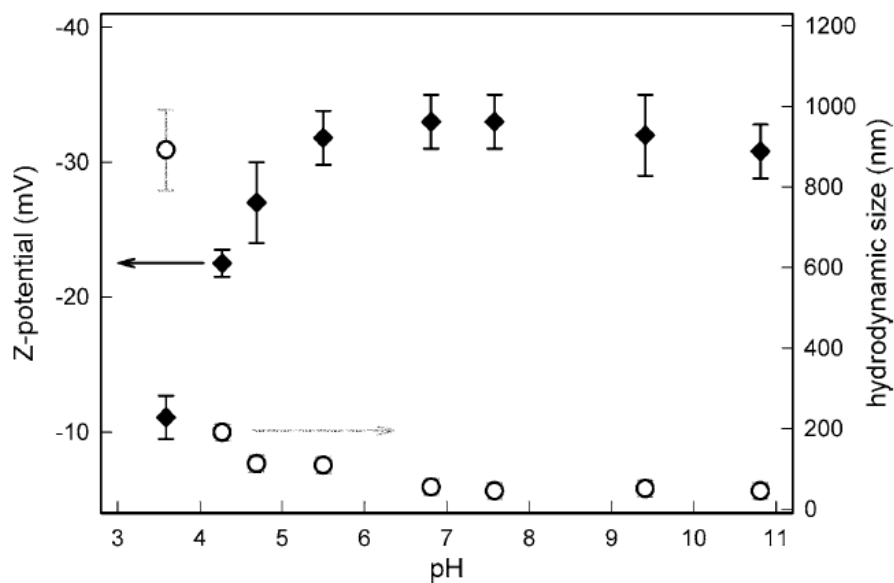


Figure 3: Z-potential (black diamond, left axis) and estimated hydrodynamic size (white circles, right axis) of a suspension of GNSs-GSH in water, with varying pH.

As can be clearly observed, at pH higher than 7 the GSH-coated GNSs have a distinctly negative and constant negative Z-potential (close to -30 mV), as a consequence of GSH net negative charges caused by the two carboxylate groups which are completely deprotonated. In these conditions, electrostatic repulsion ensures the colloid stability.^{23,24} On lowering pH, GSH is brought stepwise close to its zwitterionic form, and Z-potential is raised to less negative values. Under pH 4, precipitation of the colloid was visually perceived, and Z-potential was found to reach a value close to -10 mV. Thus, we decided to measure the hydrodynamic size of the objects. As colloidal suspensions here used are polydispersed systems of particles having different shape and size, it is obvious that values obtained from DLS measurement should just be regarded as an indication of the object sizes. Anyway, as can be seen in Figure 3 (white circles) the hydrodynamic size given by the instrument for neutral/basic pH is, as expected³⁷ of about 40(15) nm. When pH is brought under the value of 4.5, a sensible increase of the hydrodynamic size is observed, indicating the formation, at pH lower than 4, of aggregates with dimensions which can reach 1micron. The precipitation at these pH values is thus explained with the aggregation of the GNSs-GSH, promoted by: i) the reaching of an overall neutral charge around the particles ii) the electrostatic interactions between the coating layer and in particular to $\text{COO}^- \dots \text{NH}_3^+$ bond formation.^{23,24} Quick and quantitative precipitation of the colloid can thus be obtained simply reaching pH 3 by adding a few drops of nitric acid to

³⁷ G. Cavallaro; D. Triolo; M. Licciardi; G. Giammona; G. Chirico; L. Sironi; G. Dacarro; A. Donà; C. Milanese; P. Pallavicini; *Biomacromolecules*, **2013**, 14, 12, 4260–4270.

the colloidal suspension after GSH coating. These data were confirmed by TEM images as shown in Figure 4-5. Figure 3 shows the TEM images obtained on a GSH-coated colloid with pH adjusted to a value of 7. When the measurement is repeated on a colloid which was brought under pH 4 just before deposition on the TEM grid, a marked and quantitative aggregation of nano-objects is observed.

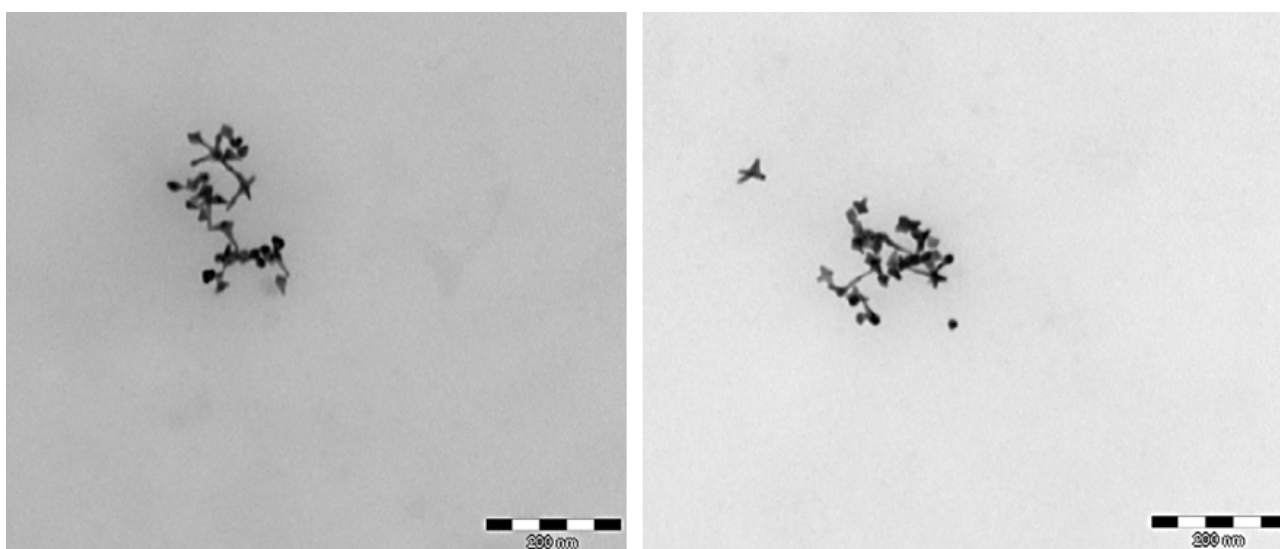


Figure 4: TEM images obtained from a colloidal suspension of GNSs-GSH adjusted at pH 7.

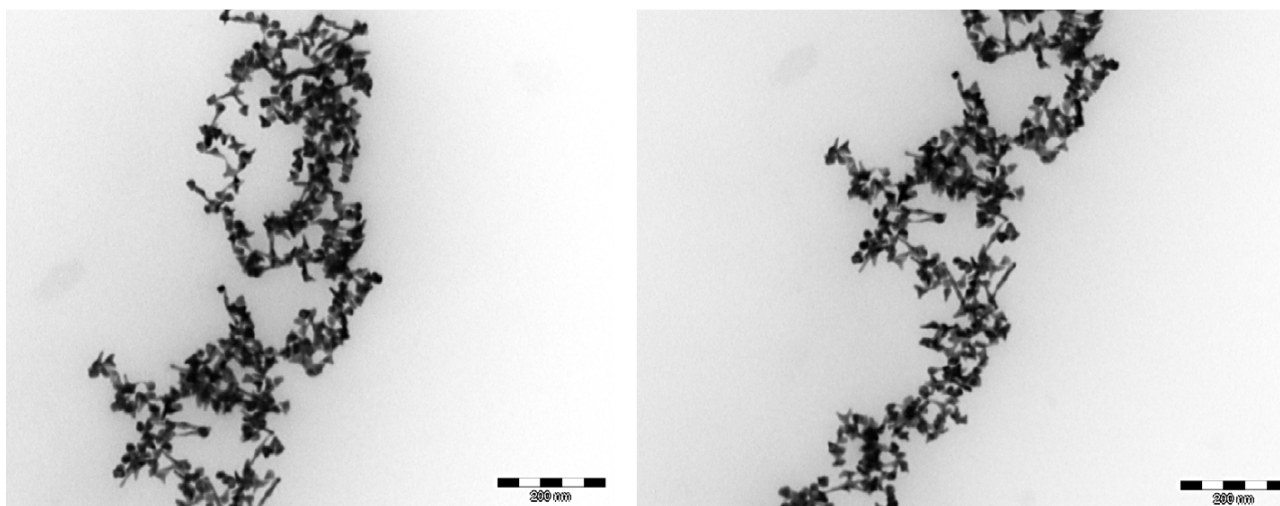


Figure 5: TEM images obtained from a colloidal suspension of GNSs-GSH adjusted at pH 4.

The phenomenon can be followed visually: it can be clearly noticed that, on lowering pH the suspension quickly decolours, as formation of large aggregates is expected to produce their fast sedimentation. Sedimentation or centrifugation of the coated NPs solution

brought to the appropriate pH value yields stable products, which can be separated and thus purified from reaction mixtures. In this way, GNSs-GSH can be obtained and stored as purified solid products, which can be re-dissolved in water buffered at pH 7 with 0.1 M Hepes.

3.1.3.2 BEHAVIOUR OF GNSs-GSH WITH METAL CATIONS: Pb^{2+} DETECTION

Re-dissolution of GNSs-GSH in 0.1 M Hepes at pH 7 gives a colloidal dispersion whose spectra show the expected LSPR bands, with only slight changes as compared to those observed prior to precipitation–purification treatments. The Z-potential in these conditions was measured using DLS, giving a value of -25(3) mV. We also tried to dissolve GNSs-GSH in different solvent systems. Attempts to use PBS buffer were unsuccessful. We noticed that spectrum of GNSs-GSH, immediately after re-dissolution in PBS, was completely different from the spectra obtained for freshly prepared GNS, for GNS freshly coated with GSH and for GNS-GSH in 0.1 M Hepes, which are, on the contrary, very similar. The expected three contributions to LSPR spectra were not present in the case of suspensions in PBS: we observed only wide, unstructured extinction spectra which is typical of aggregated samples, which was followed by a quick, complete sedimentation. The role of Hepes as stabilizing agent for gold nano-objects is not new to literature,³⁸ and indeed Hepes acts as a stabilizer of the reported GNSs colloidal suspensions. Infact, uptake in 0.1 M Hepes at pH 7 of native GNSs (after the standard centrifugation to eliminate reaction mixture and surfactant excess, but in the absence of GSH protection) produced a stable colloid, with no changes in spectrum or any other sign of aggregation, with a striking difference to what is observed with PBS, which once again, in a similar experiment, produces massive aggregation. I also tried to use non-buffered, bi-distilled water, but in this case the spectra obtained for re-dissolved GNSs-GSH were poorly reproducible, as aggregation is strongly influenced by pH of resulting suspension (as seen in Figure 5, aggregation begins for slightly acidic pH value). The pH value, when not controlled with a buffer, may vary a lot, as a result of small differences in the experimental setup like pH of water used for re-dissolution, the quantity of acid used for GNSs-GSH precipitation, the care and efficiency in the separation of precipitated GNSs-GSH from supernatant, just to name the more evident. Moreover, as already pointed out control of pH³⁹ value below 8 is essential to ensure that all $-NH_2$ groups are

³⁸ G.P. Villa; D. Bahena; A.R. Rodriguez; A. Ponce; M.J. Yacaman; *Metallomics*, **2013**, 5, 3, 242–250.

³⁹ L. Beqa; A.K. Singh; S.A. Khan; D. Senapati; S.R. Arumugam; P.C. Ray; *Acs Appl. Mater. Interfaces*, **2011**, 3, 3, 668–673.

protonated to $-\text{NH}_3^+$, and $-\text{COO}^-$ (whose preferences for Pb^{2+} are well known) is the only binding site in capping GSH molecules, in order to minimize interferences from other cations coordination. Moreover, in the absence of a buffer, adjusting pH, after resuspension of GNSs-GSH, to the chosen value of 7 with aliquots of standard acid or base is quite laborious and time consuming, leading sometimes to partial or complete colloid aggregation, and giving once again poorly reproducible samples. For all these reasons, use of an Hepes solution buffered at pH 7 was the obvious choice: anyway, we are planning further investigations to explain these aspects. When small aliquots of a stock solution of Pb^{2+} were subsequently added to a sample of the suspensions in 0.1 M Hepes, evident changes in the recorded spectra were noticed (as shown in Figure 6), suggesting the presence of a quick aggregation increasing with Pb^{2+} concentration.

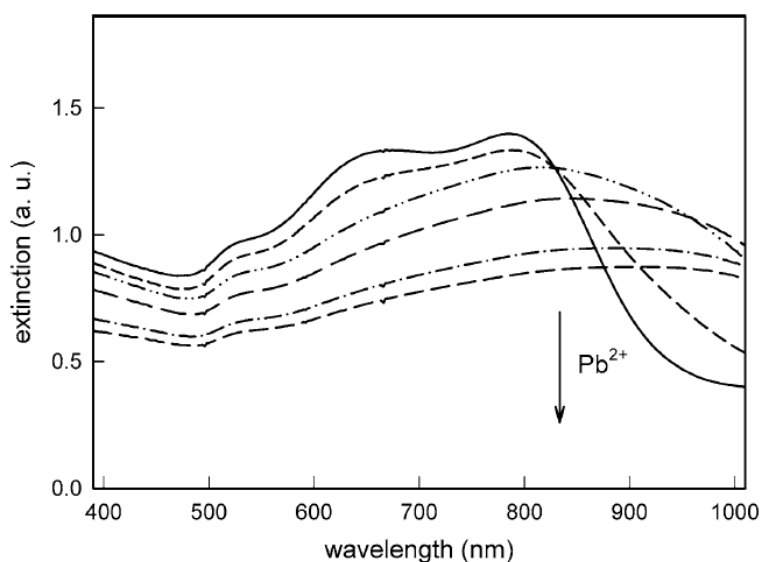


Figure 6: spectra of GNSs-GSH colloidal suspension (buffered to pH 7 with 0.1 M Hepes) before (full line) and after addition of increasing quantities of Pb^{2+} (from 1 to 5 μM final concentration).

After the titration, the suspension was allowed to stand and in one hour a massive precipitation could be observed visually, with almost complete decolouration: the suspension completely lost its intense blue colour. As can be seen in Figure 7 large aggregates are observed when Pb^{2+} is added to a colloidal suspension in Hepes buffered at pH 7 just before deposition on the TEM grid.

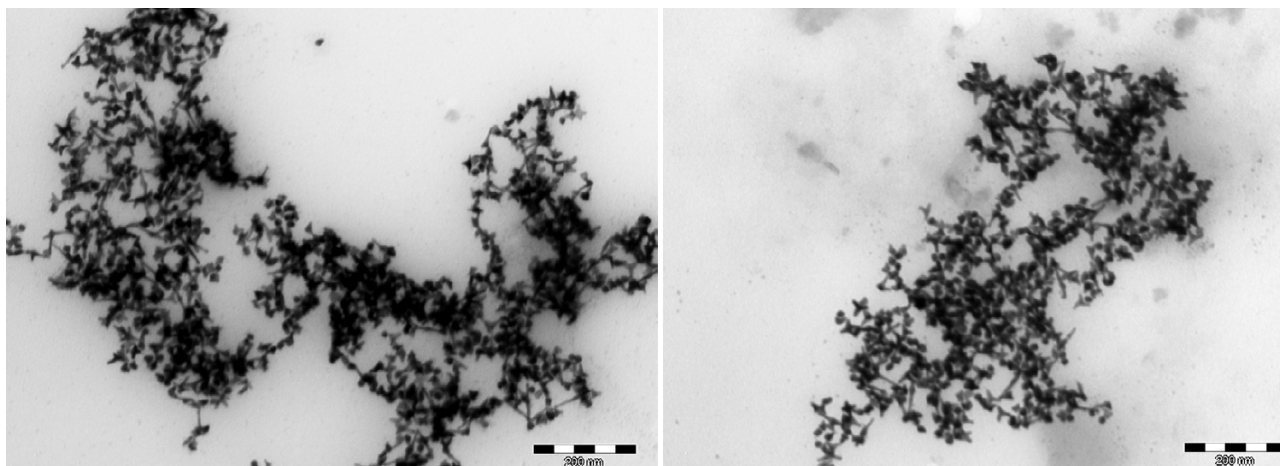


Figure 7: TEM images obtained from a colloidal suspension of GNSs-GSH in 0.1 M Hepes at pH 7, after addition of Pb^{2+} ions at to give a 5 μM concentration.

When the experiment was repeated with other bivalent cations, in the case of Ni^{2+} , Cu^{2+} and Co^{2+} negligible changes in spectra were noticed, while in the case of Mn^{2+} , Cd^{2+} and Zn^{2+} , small changes were noticed (as shown in Figure 8), suggesting a very limited aggregation, in any case not leading to noticeable precipitation in the following hours.

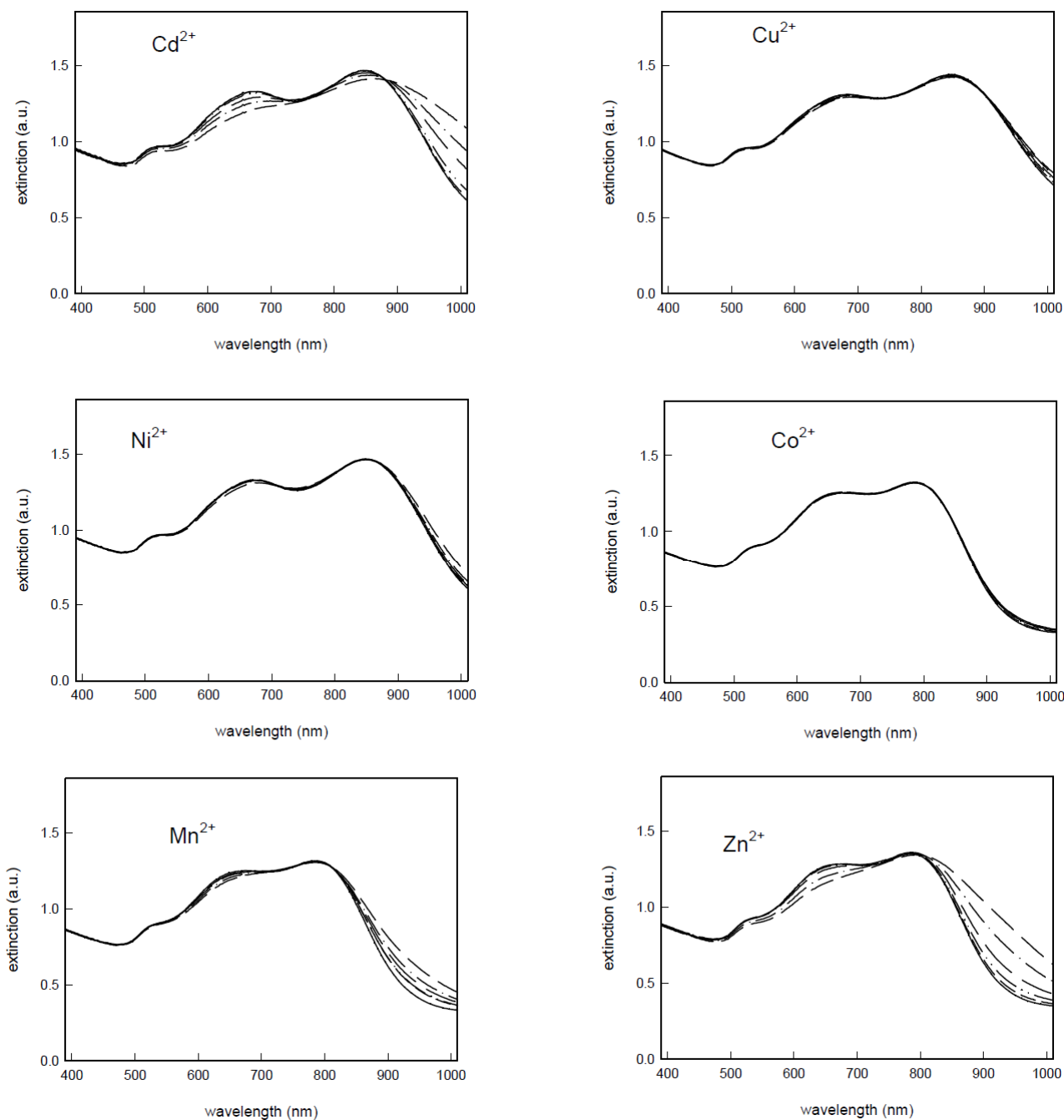


Figure 8: Spectra of GNSs-GSH colloidal suspensions (buffered to pH 7 with 0.1 M Hepes) before (full line) and after addition of increasing quantities of M^{2+} (from 1 to 5 μM final concentration).

Plot of the normalized extinction taken at the maximum of the long band (ranging between 790 and 850 nm, depending on GNSs preparation used) as a function of added metal cations is shown in Figure 7, indicating that only Pb^{2+} gives a clear signal of particle aggregation in the investigated concentration range.

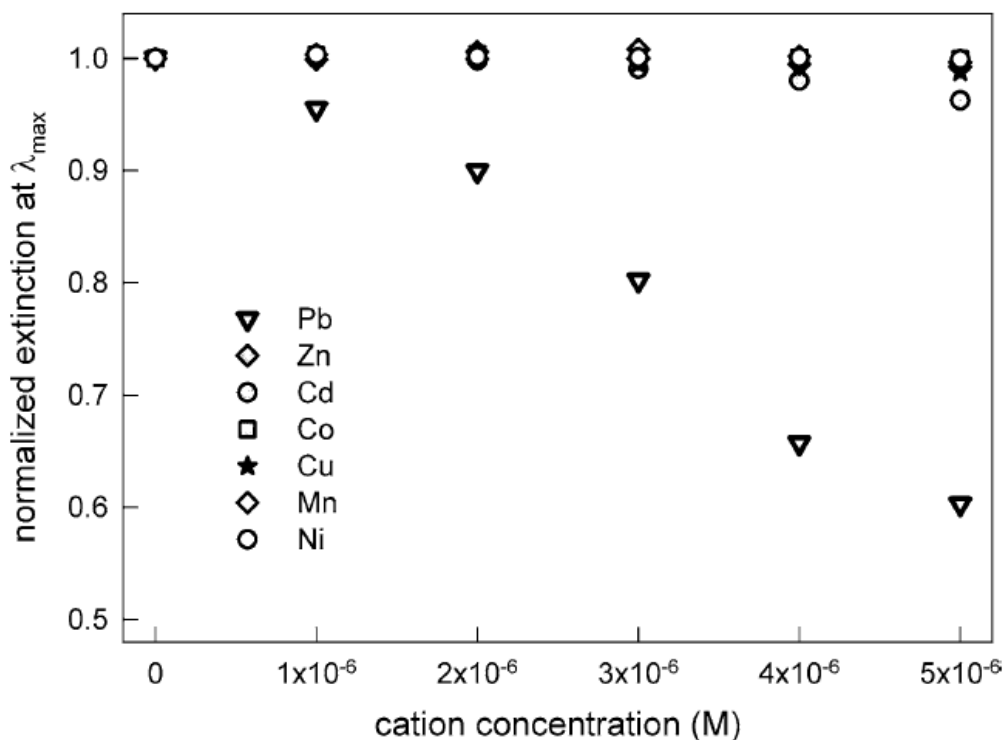


Figure 9: Plot of the normalized extinction of LSPR band (taken at the maximum of the long band, range 790–850 nm) for a GNSs-GSH colloidal suspension (buffered to pH 7 with 0.1 M Hepes) as a function of the concentration of M^{2+} in the suspension.

It has to be stressed the fact that no precipitation occur for all divalent cations considered: in the investigated range, only Pb^{2+} causes massive precipitation of the sample yielding a completely transparent solution in a couple of hours, while in the case of other investigated cations, negligible (Cu^{2+} , Ni^{2+} and Co^{2+}) or very limited (Zn^{2+} , Mn^{2+} and Cd^{2+}) changes in the LSPR spectra indicating aggregation are observed. Noteworthy, when aliquots of Pb^{2+} were added to a colloidal suspension obtained dissolving native GNSs (after a preliminary centrifugation to eliminate excess surfactants and reactants, but without GSH coating) in 0.1M Hepes at pH 7, no changes in GNSs spectrum or other aggregation signs were observed, demonstrating that GSH coating is the responsible of the reported aggregation upon cation addition. We then decided to follow the time evolution of GNSs-GSH colloidal suspension after the addition of fixed quantities of divalent metal cations. In order to do this, to identical samples of colloidal suspension of GNSs-GSH buffered at pH 7 in 0.1 M Hepes, stock solutions of cations were added to give a metal concentration of 3 μ M, and spectra evolution were followed. In Figure 10, the spectra evolution with time after Pb^{2+} addition is shown, while in Figure 11, as a representative example, the spectra evolution after Cd^{2+} addition is presented.

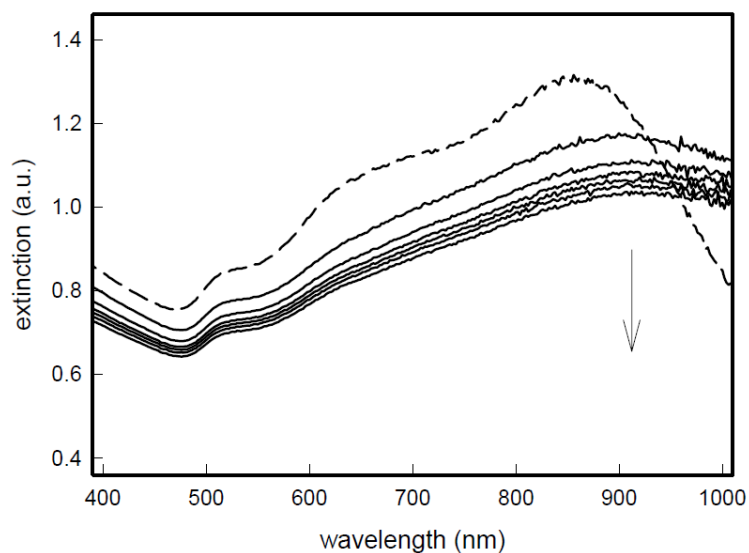


Figure 10: Spectra evolution, as a function of time, of GNSs-GSH colloidal suspension (buffered to pH 7 with 0.1 M Hepes) after addition of Pb^{2+} (concentration: $3 \mu\text{M}$). Spectra shown every 6 minutes. Dashed line: spectra of GNSs-GSH before cation addition.

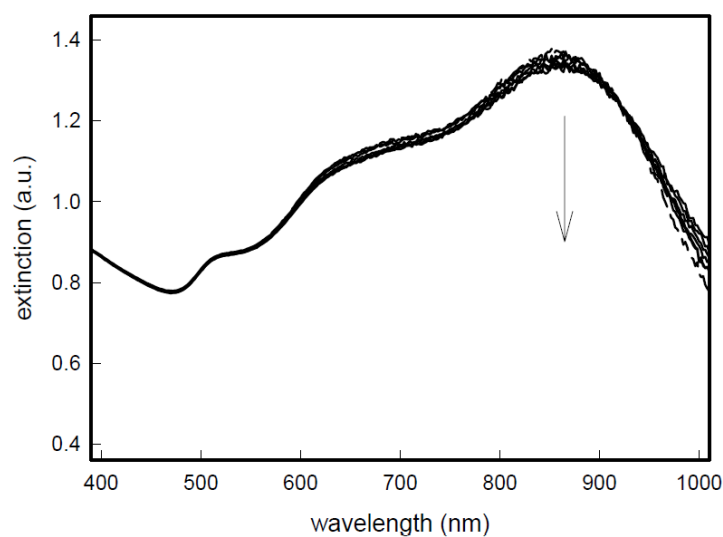


Figure 11: Spectra evolution, as a function of time, of GNSs-GSH colloidal suspension (buffered to pH 7 with 0.1 M Hepes) after addition of Cd^{2+} (concentration: $3 \mu\text{M}$). Spectra shown every 6 minutes. Dashed line: spectra of GNSs-GSH before cation addition.

Once again, spectra showed that at this concentration, and in the time range investigated (30 min) quantitative aggregation is observed only in the case of Pb^{2+} addition.

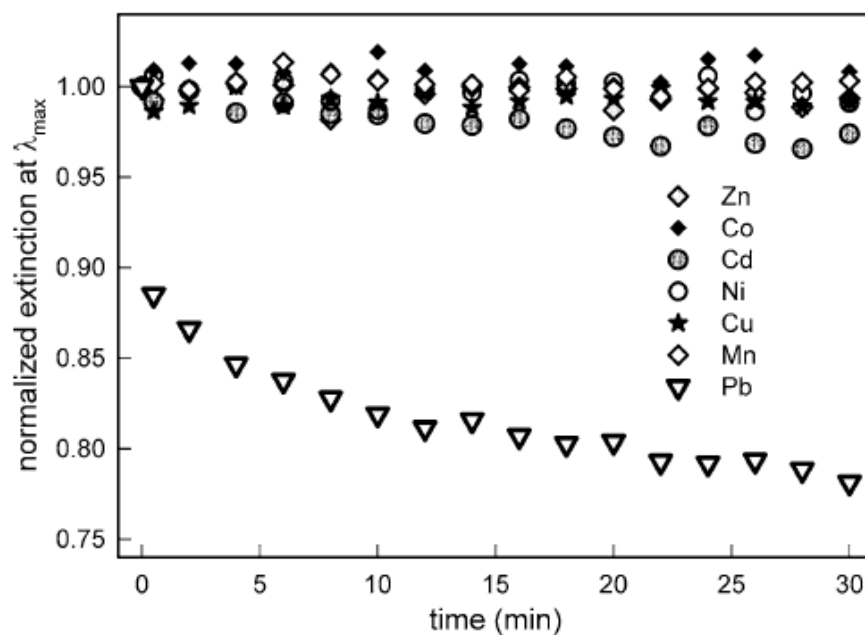


Figure 12: normalized extinction for the long band (850 nm) as a function of time, after addition of M^{2+} to a GNSs-GSH colloidal suspension (buffered to pH 7 with 0.1 M HEPES) at 3 μM concentration.

Plot of the normalized extinction value at the wavelength of LSPR maximum (measured before adding cation, for this whole set of preparation it was 850 nm) versus time for the experiments on all the cations investigated is given in Figure 12 as can be clearly observed, addition of Pb^{2+} gives an instantaneous decrease in the absorbance of the long LSPR band, indicating an aggregation, which proceeds with time, while very small effects are registered for other cations. Thus, at micromolar concentrations, only the presence of Pb^{2+} can be perceived instrumentally but, more importantly, also with naked eye, as a consequence of the strong decolouration of the colloidal suspension. Aggregation and subsequent precipitation are clearly visible as a neat decolouration in the time scale of less than one hour only in the case of Pb^{2+} addition: all other cations investigated do not give any visual response, and negligible instrumental signals, of their presence in solution in the investigated concentration range. It is worth of citation that in a precedent work⁴⁰ a similar system based on 5–8 nm diameter spherical gold nanoparticles coated with GSH was used to detect Pb^{2+} in a similar fashion, exploiting spectral changes of colloids upon aggregation. The main differences with this work are the following: i) in the cited work pH of colloidal suspension was neither controlled with a buffer nor adjusted ii) the presence of a certain amount of NaCl is necessary to promote sensible and quick aggregation and colour changes iii) no quick and quantitative precipitation is observed, if not in the presence of high quantities (100 μM) of Pb^{2+} . For

⁴⁰ F. Chai; C.A. Wang; T.T. Wang; L. Li; Z.M. Su; *Acs Appl. Mater. Interfaces*, **2010**, 2, 5, 1466–1470.

what concerns the two last points, we believe that the different behaviour is mainly due to differences in nanoparticles size and shape, which influence their surface area and subsequently the number of GSH molecules on the objects, which are responsible of the cross-linking between objects themselves as a result of Pb^{2+} complexation, and which causes the aggregation of the colloid.

GNSs described here have a mean size of 40 nm and branched shapes, resulting in strong increase of the particle surface area and of number of GSH molecules per object, and thus producing larger aggregations upon Pb^{2+} cation complexation, when compared to smaller spherical nanoparticles used in the cited work. As experiments described are showing the highest affinity for Pb^{2+} cation, we were interested to evaluate selectivity and competition towards other investigated divalent cations. To a sample of Hepes-buffered GNSs-GSH colloid, we added a stock solution containing Ni^{2+} , Cu^{2+} , Co^{2+} , Mn^{2+} , Cd^{2+} and Zn^{2+} , in order to obtain, in the colloidal suspension, a 3 μM concentration for each metal cation, with an overall M^{2+} concentration of 18 μM . Spectra (see Figure 13) of colloidal suspension were only slightly altered after addition of the “competing” cations, and, more importantly, precipitation was not observed, even after several (>12) hours.

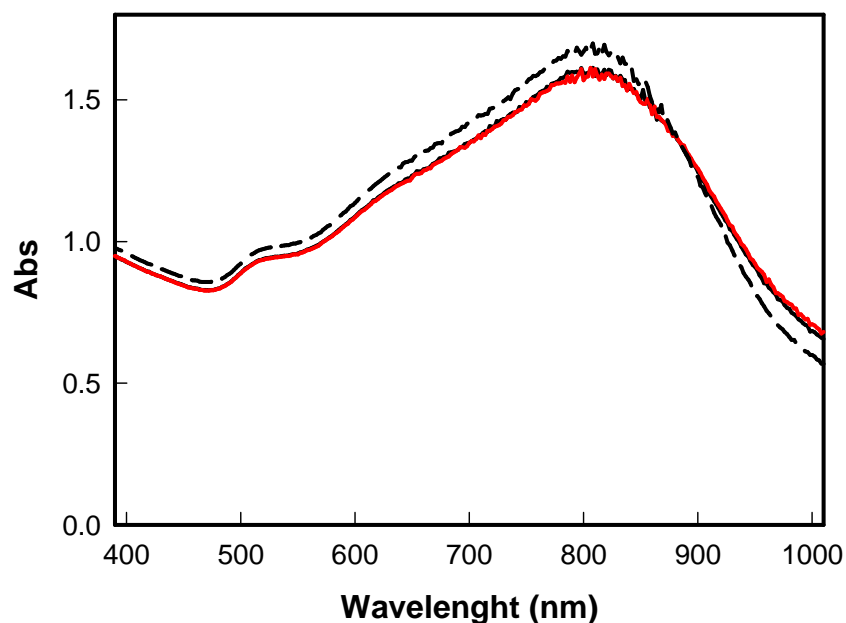


Figure 13: spectra of: i) AuNS-GSH colloidal suspension in 0.1M Hepes at pH 7 (dashed line); ii) same suspension immediately after addition of cation mix (Ni^{2+} , Cu^{2+} , Co^{2+} , Mn^{2+} , Cd^{2+} and Zn^{2+} , each one 3 μM , overall M^{2+} concentration 18 μM , solid black line); iii) same after three hours from cation mixture addition (solid red line).

The same experiment was repeated adding Pb^{2+} to the cation mixture, in order to obtain a final concentration of $3 \mu\text{M}$ of Pb^{2+} (corresponding to 240 ppb) and an overall $21 \mu\text{M}$ in divalent cations. In this case, a fast aggregation, identical to the one registered in the presence of $3 \mu\text{M}$ Pb^{2+} only (in the absence of any interfering cation) followed by quantitative precipitation in about one hour, as can be clearly seen in Figure 14, was observed.

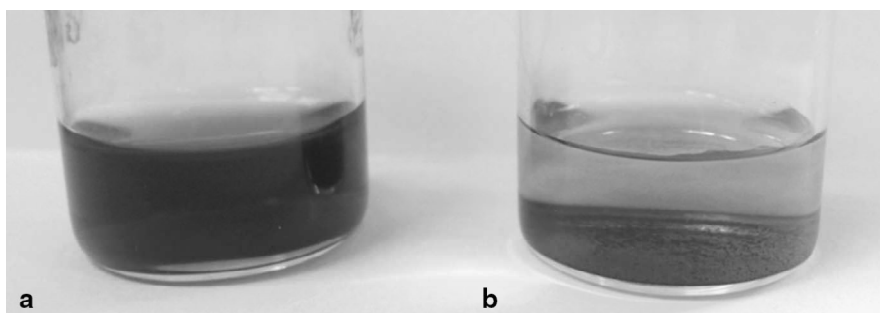


Figure 14: photograph of the GNSs-GSH colloidal suspension (in Hepes 0.1 M at pH 7) one hour after: a) the addition of Ni^{2+} , Cu^{2+} , Co^{2+} , Mn^{2+} , Cd^{2+} and Zn^{2+} , $3 \mu\text{M}$ each, overall M^{2+} concentration of $18 \mu\text{M}$; b) the same M^{2+} concentration, but in the presence also of $3 \mu\text{M}$ Pb^{2+} .

The same behaviour was observed when repeating the experiment on two samples of GNSs-GSH prepared dissolving solid GNSs-GSH in pure water and then carefully adjusting the resulting suspensions to pH 7 with aliquots of standard acid and base. Also, Z-potential was measured immediately after the addition of the divalent cation mixture ($3 \mu\text{M}$ in each divalent cation) to the suspensions in Hepes, in the absence and presence of Pb^{2+} , giving, respectively, values of $-26(5)$ and $-23(5)$ mV, values which are almost identical to the one observed for GNSs-GSH objects in the same pH conditions but in the absence of metal cations. In this way, we can rule out the idea that aggregation has to be related to a sensible variation in Z-potential caused by cation complexation (which could reduce the overall charge given by carboxylic and ammonium functions).

We also performed an experiment adding different quantities of Pb^{2+} ions to identical samples of a colloidal suspension in Hepes of GNSs-GSH made $18 \mu\text{M}$ in divalent cations mix ($3 \mu\text{M}$ each one). In order to try to minimize the effect of sedimentation and precipitation, which of course tends to grow with time, for each sample we performed spectra immediately after Pb^{2+} addition: spectra are shown in Figure 15.

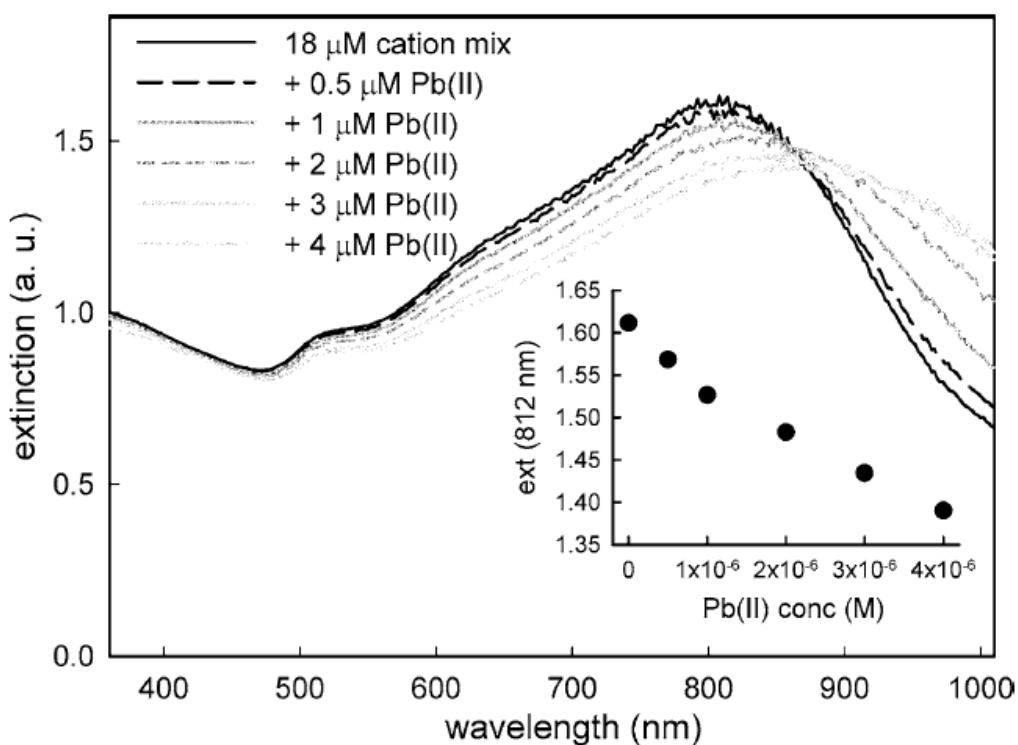


Figure 15: spectra of GNSs-GSH colloidal suspension (buffered to pH 7 with 0.1 M Hepes) after addition of: i) a cation mixture to give an overall M^{2+} concentration of 18 μM (solid black line); ii) 18 μM cation mix + increasing quantities of Pb^{2+} (see legend). Inset plot of absorbance for higher wavelength LSPR maximum (812 nm) as a function of Pb^{2+} concentration in the suspension.

It was observed that aggregation-induced decrease of the LSPR maximum has a linear dependence from lead concentration, even in the presence of competing cations (see inset of Figure 15). As can be seen, variations in LSPR bands which can be related to Pb^{2+} induced aggregation are obtained as a function of Pb^{2+} added, and a small spectral change can be observed even with sub-micromolar concentration (0.5 μM of Pb^{2+} , corresponding to 40 ppb) in the presence of quite higher concentration of other cations (overall 18 μM in M^{2+}). Quite interestingly, even for the case of the minimum added Pb^{2+} concentration (0.5 μM), precipitation of the colloidal suspension was observed after a few hours: in principle, Pb^{2+} presence in quantities lower than 50 ppb can be detected even in solutions containing distinctly higher quantities of other divalent cations. As already pointed out,⁴⁰ explanation of this preference towards Pb^{2+} cations is not straightforward: coordination of Pb^{2+} to binding functions of GSH is probably the most favourable in the pH conditions chosen for the assay. It has to be noticed that recently it was demonstrated that gold spherical nanoparticles coated with GSH show selectivity towards metal cations which changes as a function of pH.²⁸ Moreover, Hepes complexation of some of the investigated cations (such as Cu^{2+}) cannot be completely

excluded⁴¹ and could play a role in complex formation *equilibria*. Anyway, the experimental results give evidence of the fact that, in the described conditions, only Pb²⁺ is able to give a quantitative cross-linking of the GNSs-GSH objects leading to massive, visible aggregation and precipitation.

At this point, we decided to investigate the aggregation event caused by Pb²⁺ cations with DLS measurements of the hydrodynamic size of dispersed particles. As previously described, the colloidal dispersions used are polydispersed systems of particles with different shape and size, thus the reported values must be regarded as an indication of the mean object sizes, but once again some precious information can be obtained. Typically, DLS measurement on a GNSs-GSH colloid buffered at pH 7 with HEPES, gave a value of about 40(15) nm. The influence of increase in Pb²⁺ concentrations on aggregates formation rate was first measured. In this case, the mean hydrodynamic diameter of the dispersed colloidal particles was measured immediately after the addition of a certain amount of Pb²⁺ and after a lapse of 5 minutes.

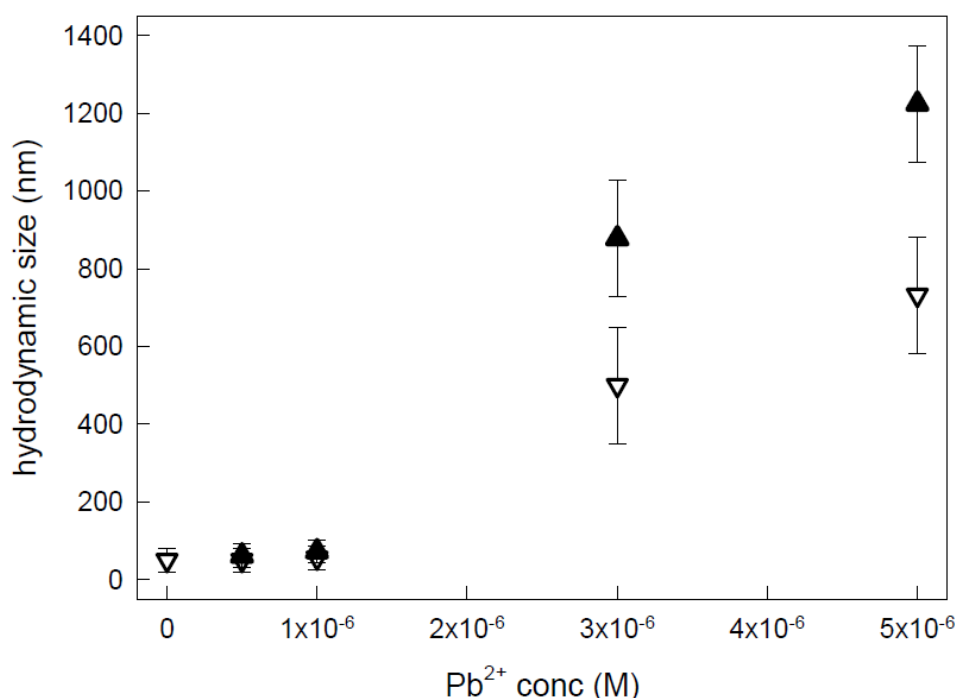


Figure 16: hydrodynamic size of GNSs-GSH colloidal suspension (buffered to pH 7 with 0.1M HEPES) as a function of Pb²⁺ concentration added, obtained with DLS immediately after addition (white triangles) and 5 minutes after the addition (black triangles).

⁴¹ M. Sokolowska; W. Bal; *J. Inorg. Biochem.*, **2005**, 99, 8, 1653–1660.

As can be seen from Figure 16, when Pb^{2+} concentration is higher than $1 \mu\text{M}$, aggregates are produced immediately, and also evolution to bigger aggregates get faster as concentration increases: with a $5 \mu\text{M}$ concentration, aggregates bigger than $1 \mu\text{m}$ grow instantly, explaining the complete precipitation occurring in a short time. On the other side, in a sample which was made $0.5 \mu\text{M}$ in Pb^{2+} , hydrodynamic size was determined as a function of time, observing a continuous increase of this value, as shown in Figure 17.

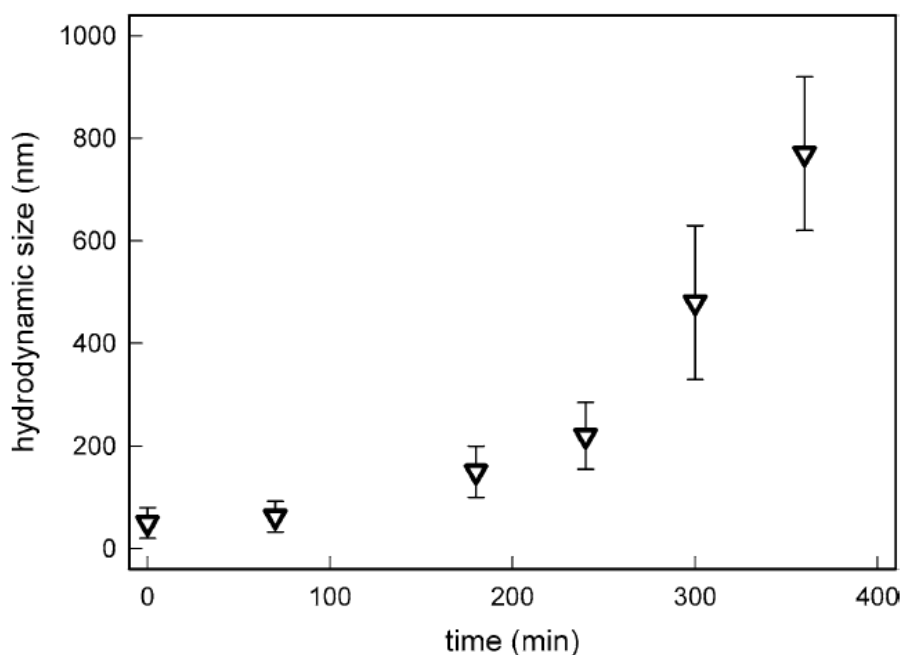


Figure 17: hydrodynamic size obtained from DLS measurements, as a function of time, of an GNSs-GSH suspension (buffered to pH 7 with 0.1 M HEPES) after addition of Pb^{2+} $0.5 \mu\text{M}$

Aggregation in these conditions seems to proceed quite slowly, but is able to produce, in a few hours, objects with a size which can undergo sedimentation and precipitation, as we visually perceived.

3.1.3.3 CONCLUSION

Thanks to the explained approach a method for coating GNSs with GSH was obtained, and this allowed to produce robustly coated anisotropic gold nano-objects, which can be easily purified from synthetic residual and surfactants, easily stored as a stable solid and re-dissolved on need in HEPES-buffered solution. We demonstrated that these GNSs-GSH,

when dissolved in 0.1 M HEPES buffer, offer a simple visual assay for micromolar Pb^{2+} detection at pH 7, based on their fast aggregation to micron-sized objects which quickly give sedimentation, giving a neat decolouration of the blue-coloured colloidal GNSs-GSH suspension. These phenomena can easily be detected with the naked eye, or followed with a simple UV-Vis spectrophotometer. The aggregation is not showed in the presence of all the other heavy metal cations investigated (Ni^{2+} , Cu^{2+} , Co^{2+} , Mn^{2+} , Cd^{2+} and Zn^{2+}), while is caused by sub micromolar Pb^{2+} concentration even in the presence of much higher concentration of the cited divalent cations which were considered as representative of possible interferents. This selectivity and the behaviour of aggregation as a function of time and of Pb^{2+} concentration, were assessed with careful investigations using mainly UV-Vis Spectrophotometry and DLS measurements. Further studies are in progress to fully understand the mechanism of selectivity and applicability to real biological and environmental samples.⁴²

⁴² A. D'Agostino; A. Taglietti; B. Bassi; A. Donà; P. Pallavicini; *J. Nanopart. Res.*; **2014**, 16, 2683-2694.

3.2 TAILORING OF GNS SURFACE FOR SERS TAG

3.2.1 INTRODUCTION

As we have told previously, Surface-Enhanced Raman Scattering (SERS) has seen in recent years a significant boost, mainly spurred by developments in LASER and detector technology and by an improved understanding of bottom-up synthetic methods.¹ Significant effort has been dedicated to understanding the fundamental physical laws at the basis of the phenomenon,² and to the development of sensing platforms and imaging approaches.³ Much less effort has been invested instead in identifying niches in which the use of SERS could benefit the medical field, as it has been primarily considered a tool for physical scientists. Very recently, however, the interest has shifted, and several seminal works have appeared, shedding a light on the use of SERS for in vivo medical applications, mainly in the oncology field.⁴ One of the reasons for this shift may be the improvement of LASER technology that has enabled the use of near infrared (nIR) LASERS for excitation with maximized light penetration depths and reduced tissue damage. However, perhaps the most important factor contributing to the first implementations of SERS in the medical field has been the introduction of the concept of SERS tag, an extension of what we previously called the “extrinsic SERS detection”.⁵

¹ H.D. Yu; M.D. Regulacio; E. Ye; M.Y. Han; *Chem. Soc. Rev.*, **2013**, 42, 6006-6018.

² E.C. Le Ru; E. Blackie; M. Meyer; P.G. Etchegoin; *J. Phys. Chem. C*, **2007**, 111, 13794-13803.

³ A.S. De Silva Indrasekara; S. Meyers; S. Shubeita; L.C. Feldman; T. Gustafsson; L. Fabris; *Nanoscale*, **2014**, 6, 8891-8899.

⁴ H. Karabeber; R. Huang; P. Iacono; J.M. Samii; K. Pitter; E.C. Holland; M.F. Kircher; *ACS Nano*, **2014**, 8, 9755-9766.

⁵ L. Fabris; *J. Opt.*, **2015**, 17, 114002-114013.

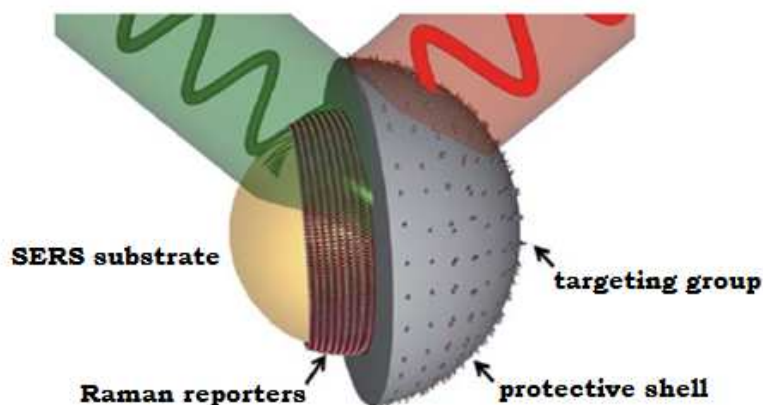


Figure 1: Components of a SERS tag: SERS substrate (e.g. gold nanoparticles), Raman reporters adsorbed onto its surface (the red self-assembled monolayer), protective shell, targeting group.

A SERS tag is a SERS-active nanoparticle-based system that, due to its size, can easily bind to or penetrate cells and label them with bright SERS signals; conceptually it plays a role in Raman microscopy that is similar to that of a fluorescent dye in fluorescence microscopy. Simply said, a SERS tag enables the indirect identification of a diseased tissue by following the SERS signal of the Raman reporter that is bound to the tag. As a consequence one does not need to rely, for identification, on the often extremely weak signals that are typical of biological tissues; in addition, SERS tags, if carefully synthesized and functionalized, can be mixed in suspension and enable the simultaneous detection of multiple targets (i.e., multiplexing) with high sensitivity and selectivity,⁶ as first suggested in a seminal work by Mirkin and co-workers.⁷ When using SERS tags, the targeted tissues are selectively labelled with single cell sensitivity and can, for instance, guide a surgeon in the identification of tumor margins during surgery, or a pathologist in the analysis of a histological specimen collected during biopsy. It is important to understand that not all medical procedures will benefit from the use of SERS tags, and therefore SERS should be envisioned as complementary to other medical imaging techniques, such as magnetic resonance imaging. SERS tags could find an ideal role in the detection of skin cancers, which do not require deep tissue penetration, in delineating tumor margins during surgery (for example in brain cancers)⁸, or for the endoscopic imaging of diseased tissues, where the LASER can be coupled to the endoscope, which provides a pathway for the backscattered light to the detector (e.g., in

⁶ L. Fabris; M. Schierhorn; M. Moskovits; G.C. Bazan; *Small*, **2010**, 6, 1550-1558.

⁷ Y.C. Cao, R. Jin; C.A. Mirkin; *Science* **2002**, 297, 1536-1540.

⁸ C.L. Zavaleta; B.R. Smith; I. Walton; W. Doering; G. Davis; B. Shojaei; M.J. Natan; S.S. Gambhir; *Proc. Natl. Acad. Sci. USA*, **2009**, 106, 13511-13521.

a colonoscopy).⁹ Other applications in which SERS tags can find an important niche entail the *ex vivo* analysis of specimens, such as the identification of biomarkers in blood or the detection of circulating tumor cells.¹⁰ What is also very promising, although not yet implemented in the medical field, is the fact that SERS tags can be easily functionalized with oligonucleotides¹¹ and could therefore, in principle, target gene fragments that are specific for each individual. Even though seemingly far in the future, these opportunities, taken together, promise to render SERS truly a personalized detection technique.

As shown in Figure 1 a SERS tag is composed of: i) one plasmonic nanoparticle (generally made of gold for medical applications as its toxicity effects have been addressed in greater detail compared to other metals),¹² ii) Raman reporter molecules possibly tightly bound to the nanoparticle, iii) a stabilizing layer to prevent coalescence and fouling (such as silica or polyethylene glycol, PEG), iv) one or more targeting moieties, which can provide the selectivity necessary to recognize a given target. SERS tags can be suspended in physiological solutions and injected in murine models via the tail vein to then follow via SERS their bio-distribution and targeting selectivity.¹³

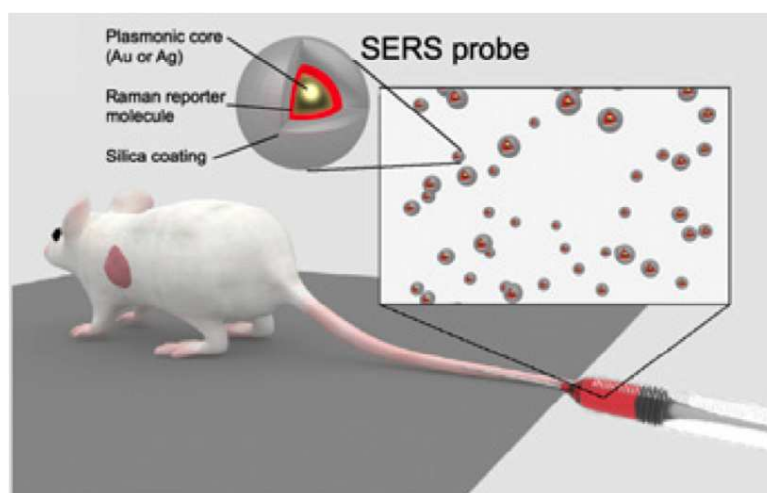


Figure 2: For *in vivo* analysis in murine models, the tags are injected in the animal via the tail vein and their biodistribution and specific tissue targeting are then followed using a SERS microscope.

Examples of ideal targeting molecules are antibodies and aptamers; antibodies are often chosen because of their availability for a wide range of targets, while aptamers

⁹ Y.W. Wang; S. Kang; A. Khan; P.Q. Bao; J.T.C. Liu; *Biomed. Opt. Express*, **2015**, 6, 3714-3724.

¹⁰ Z.A. Nima; M. Mahmood; Y. Xu; T. Mustafa; F. Watanabe; D.A. Nedosekin; M.A. Juratli; T. Fahmi; E.I. Galanzha; J.P. Nolan; A. Basnakian; V.P. Zharov; A.S. Biris; *Sci. Rep.*, **2014**, 4, 4752-4761.

¹¹ L. Fabris; M. Dante; T.Q. Nguyen; J.B.H. Tok; G.C. Bazan; *Adv. Funct. Mater.*, **2008**, 18, 2518-2514.

¹² N. Khlebtsov; L. Dykman; *Chem. Soc. Rev.*, **2011**, 40, 1647-1652.

¹³ C. Andreou; S.A. Kishore; M.F. Kircher; *J. Nucl. Med.*, **2015**, 56, 1295-1301.

(oligonucleotides that fold and bind to their targets with high specificity) are preferred because they are sturdier and less expensive, unfortunately they have not yet been developed for many targets. Effective SERS tags for cancer identification can recognize their specific targets with high sensitivity, selectively discriminate them from nonspecific ones, and retain their activity for at least 24 h in the biological environment. It is important to specify that, when thinking about SERS tags for cancer detection, the word target is meant to identify several objects: it can be a metabolite or protein biomarker in blood, a membrane protein on a specific cell, or a protein that can be specific for a cancerous tissue. SERS tags need also to be bright, that is, to identify their targets with high sensitivity. In order for this to happen the tags need to possess hot spots, that is, locations where the near field is significantly enhanced. Typical hot spots are tight junctions between metallic nanoparticles, or tips in anisotropic nanoparticles like those we have described in gold nanostars. The advantage of using GNSs is that their hot spots are “built in” and they can provide enhancement factors which can reach the order of 10^9 – 10^{10} , as a consequence of both plasmonic enhancements and of the so-called “lightning rod effect”.¹⁴ In order to fully understand how SERS tags work it is important to clearly comprehend the difference between direct and indirect detection in SERS. Direct (also known as label-free, or intrinsic, as explained above) SERS analyte detection takes advantage of the use of “naked” nanoparticles for the identification of the SERS spectral features typical of the analyte. This method is extremely powerful for the identification of analytes whose structure is rich in aromatic rings and unsaturated bonds, but can give rise to extremely weak signals for analytes that do not present these groups. As a result, when mixing a suspension of nanoparticles with a highly conjugated or aromatic analyte, a fingerprinting peak patterning, that is unique and assignable only to the analyte itself, can be recorded. Direct identification employing SERS is used only seldom in the medical field because of issues of opsonization (i.e., the effect by which nanoparticles are covered by a multilayer of proteins when suspended in biological fluids) that limit signal intensity, selectivity, and circulation times. The completely different approach to identification taken when using SERS tags (i.e., indirect detection, “extrinsic SERS detection”) is instead better suited for the highly heterogeneous environments that are studied in the medical field. In this approach, the target is recognized employing the targeting moieties bound to the nanoparticles. Following recognition, the SERS tag binds to the molecular target providing both identification and localization information. By mapping the area of interest with a Raman microscope, a SERS signal can then be recorded that belongs to the Raman reporter used, not the target. The presence of the

¹⁴ I. Baginskiy; T. Lai; L. Cheng; Y. Chan; K. Yang; R. Liu; M. Hsiao; C. Chen; S. Hu; L. Her; D.P. Tsai; *J. Phys. Chem. C*, **2013**, 117, 2396-2403.

target is only indirectly proven by the presence of the SERS signal of the reporter. As a consequence, indirect SERS detection needs not only to employ reliable targeting molecules, but also to drastically reduce non-specific binding of the tags, which would cause false positive results and therefore severe diagnostic repercussions.

The Nanoparticles

Ideally, SERS tags should be injected into the organism intravenously, applied during surgery in form of a gel to the area of interest, mixed to cell media during *in vitro* studies, or drop casted onto histo-pathological specimen during *ex vivo* tissue examination. When one takes into account these protocols, it becomes clear that, besides resistance to opsonization (as described above), the nanoparticles need to be non-cytotoxic, the Raman reporters need to be tightly bonded to the nanoparticle surface (ideally covalently), and need to be protected from enzymatic cleavage and acidic conditions that are typical of endosomal uptake in cells. Moreover, their size needs to be between 20 and 200 nm to allow cellular uptake and tissue extravasation while reducing toxicity, and they need to possess built-in hot spots for signal enhancement and brightness. To combine all these conditions in a single nano-structured tag is often a nontrivial task. As briefly mentioned before, gold nanoparticles have found much broader application in the medical field compared to other plasmonic nanoparticles (e.g., silver) because of their lower toxicity, moreover synthetic protocols to synthesize them from the bottom-up approach are better known; shape retention, especially for nanoparticles such as nanostars, plays an extremely important role in SERS, as features such as tips, besides being active as hot spots and lightning rod effect.

The Raman Reporter

Raman reporter molecules are a fundamental component of SERS tags because their SERS response provides indirect identification of a selected target. Specific features that characterize this kind of molecules are: i) high Raman cross sections to produce intense signal responses (generally the case of conjugated or aromatic molecules); ii) Raman spectra with a limited number of peaks to reduce peak overlap and improve selectivity in multiplexing experiments; iii) insensitivity to LASER light; iv) ability to bind to the metallic colloid. Generally speaking, traditional Raman reporters are aromatic molecules bind to the gold surface that can be fluorescent or not. Typical examples of Raman reporters include thiophenol, aminohexanethiol, naphthalene dithiol, mercaptobenzoic acid, 1,4-biphenyldithiol, rhodamine 6G and 7-mercapto-4-methylcoumarin and many

more.⁶ These molecules are small and rigid, covalently bind to gold, have high Raman cross sections, and are poorly fluorescent.

The Coating Layer

Surface coating for tags engineered for medical use is a fundamental component as it eliminates the adverse effects brought about by direct contact with physiological fluids (e.g., blood), which manifest themselves as opsonization and aggregation. There are three kinds of coatings that are generally employed: i) bio-molecules such as bovine serum albumin (BSA), ii) polymers, such as PEGs, and iii) glasses such as silica.¹⁵ Although one might be tempted to say that coatings of biological nature may be the best suited to provide stability while maintaining biocompatibility, one needs to remember that these molecules can only physically adsorb to the nanoparticle surface forming a protein corona, and not necessarily resist enzymatic cleavage by the organism, thus most likely losing their activity in a short time frame. The use of a biocompatible polymeric coating, such as PEG, gives the tag increased stability with retained biocompatibility, while at the same time providing it with chemical end groups that render it amenable to surface functionalization, which is important in order to strongly bind targeting moieties to the tag. PEG functionalization for example has shown to stabilize SERS tags during cellular uptake for over 24 h, which in turn leads to extended SERS activity in vitro and in vivo.¹⁶ Silica coating was the first coating to be developed for SERS tags, and has now been commercialized for quite some time. Silica shells can be grown following the traditional Stöber method with thicknesses that can be adjusted varying the amount of tetraethyl orthosilicate (TEOS) in ammonia.¹⁷

The Targeting Moieties

Targeting molecules allow the SERS tag to exclusively recognize the predetermined target, eliminating (or at worst drastically reducing) non-specific binding. It is extremely important to bind them to the tag so that targeting moieties for different targets bound to other tags are not exchanged when the particles are suspended in solution. The best way to do so is the creation of a covalent bond with the protective layer molecules, often taking advantage of synthetically added or native exposed pendant groups. One example is the use of pendant carboxylic moieties on PEG to create an amide bond with free amino groups in antibodies via EDC/sulfo-NHS chemistry. Other available binding

¹⁵ P. Khullar; V. Singh; A. Mahal; P.N. Dave; S. Thakur; G. Kaur; J. Singh; S.S. Kamboj; M.S. Bakshi; *J. Phys. Chem. C*, **2012**, 116, 8834-8843.

¹⁶ A.S. De Silva Indrasekara; B.J. Paladini; D.J. Naczynski; V. Starovoytov; P.V. Moghe; L. Fabris; *Adv. Healthcare Mater.*, **2013**, 2, 1370-1379.

¹⁷ W. Stöber; A. Fink; E. Bohn; *J. Colloid Interface Sci.*, **1968**, 26, 62-73.

chemistries, each of which are more or less appropriate depending on the system used are: i) direct adsorption, ii) binding of biotin-modified tags to avidin or streptavidin-modified nanoparticles, iii) click chemistry, iv) silane chemistry, or v) electrostatic interactions.⁵ Antibodies have found wide application in SERS tags because of their known affinity for a broad range of targets, but they suffer issues of sensitivity to manipulation and moreover, in the presence of a high number of targets, they suffer from cross reactivity. More recently, as we have previously seen, antibodies have started to be replaced by aptamers, which are sturdier and bind to their targets with equal if not higher selectivity.¹⁰ SERS detection using tags promises to truly become an important technology complementing existing techniques. Owing to its sensitivity, high target specificity allowed by the use of aptamers or antibodies, multiplexing capability (thus overcoming one of the major issues of fluorescence imaging), absence of photo-bleaching, limited or absent risks for health, easy synthesis and long stability of tags, SERS can, with an interdisciplinary approach, leave the laboratory and reach the hospital rooms.

Recently, the coating of nano-objects with monolayers of mixed thiols has bait attention because the deposition of Self-Assembled Monolayers (SAMs) on the surface of nanoparticles is a commonly applied technique used to impart or tune specific properties.^{18,19,20,21,22} Simply said this approach permit better performances compared to SAMs with a single coating agent and the tuning of the mixture composition allows the design of more sophisticated nano-devices.²³ Unfortunately there is also one big problem, as stated by a recent paper by Bell and colleagues²⁴: the control of the composition of the mixture bounded on the surface is not straightforward as it may seem at first sight, in fact, the ratio of the coating agents on surfaces usually derives from a complex function of several variables which hardly can be controlled such as: concentration, temperature, solvent features, etc., reflecting the different affinities of thiols for the gold surface,²⁵ as it was demonstrated by Whitesides^{26,27} for bulk noble metal surfaces. As it was discussed in the precedent paragraph, with a proper coating of nano-objects, the chosen molecules adsorbed on nano-scaled noble metal surfaces can undergo a strong enhancement of their Raman signals, producing the Surface Enhanced Raman Scattering (SERS) effect. The so called “SERS nanoparticles”²⁸ are showing great potential as imaging probes in biomedical applications, as we have just seen. Obviously, there is an increasing interest in the realization of novel SERS labels^{29,30} and SERS tags^{31,32} to be used *in vivo*. These attracting nano-devices must possess robustness (in order to be used in biological fluids), reproducibility and the possibility of a fine tuning of spectral signatures: all these properties are strictly related with the careful tailoring of the coating. Briefly, SERS advantages as optical labelling technique are due to the coupling of two features: a specific molecular spectral fingerprint contained in a Raman spectrum and the markedly enhanced cross-section of the SERS effect with values comparable with those

¹⁸ R.C. Van Lehn; A.A. Katz; *J. Phys. Chem. C*, **2013**, 117, 39, 20104-20115.

¹⁹ M. Mlambo; P.S. Mdluli; P. Shumbula; S. Mpelane; N. Moloto; A. Skepu; R. Tshikhudo; *Materials Research Bulletin*, **2013**, 48, 10, 4181-4185.

²⁰ C. Gentilini; L. Pasquato; *Journal of Materials Chemistry*, **2010**, 20 8, 1403-1412.

²¹ A. Centrone; Y. Hu; A.M. Jackson; G. Zerbi; F. Stellacci; *Small*, **2007**, 3, 5, 814-817.

²² A.M. Jackson; Y. Hu; P.J. Silva; F. Stellacci; *Journal of the American Chemical Society*, **2006**, 128, 34, 11135-11149.

²³ G. Wang; H.Y. Park; R.J. Lipert; *Analytical Chemistry*, **2009**, 81, 23, 9643-9650.

²⁴ A. Stewart; S. Zheng; M.R. McCourt; S.E.J. Bell; *Acs Nano*, **2012**, 6, 5, 3718-3726.

²⁵ P. Pallavicini; C. Bernhard; G. Dacarro; F. Denat; Y.D. Fernandez; C. Goze; L. Pasotti; A. Taglietti; *Langmuir*, **2012**, 28, 7, 3558-3568.

²⁶ C.D. Bain; G.M. Whitesides; *Journal of the American Chemical Society*, **1989**, 111, 18, 7164-7175.

²⁷ P.E. Laibinis; M.A. Fox; J.P. Folkers; G.M. Whitesides; *Langmuir*, **1991**, 7, 12, 3167-3173.

²⁸ C.L. Zavaleta; B.R. Smith; I. Walton; W. Doering; G. Davis; B. Shojaei; M.J. Natan; S.S. Gambhir; *Proc. Natl. Acad. Sci. U.S.A.*, **2009**, 106, 32, 13511-13516.

²⁹ Y.L. Wang; S. Schlucker; *Analyst*, **2013**, 138, 8, 2224-2238.

³⁰ J. Kneipp; H. Kneipp; A. Rajadurai; R.W. Redmond; K. Kneipp; *Journal of Raman Spectroscopy*, **2009**, 40, 1, 1-5.

³¹ K.K. Maiti; U.S. Dinish; A. Samanta; M. Vendrell; K.S. Soh; S.J. Park; M. Olivo; Y.T. Chang; *Nano Today*, **2012**, 7, 2, 85-93.

³² A. Samanta; S. Jana; R.K. Das; Y.T. Chang; *Rsc Advances*, **2014**, 4, 24, 12415-12421.

experienced in fluorescence analyses.³³ As described in detail above, SERS label should be made of: i) a noble metal nano-object, able to produce a strong enhancement of the Raman signal of a Raman active molecule, ii) a Raman reporter which has to be tightly held in proximity of the metal surface, and iii) a protecting layer that guard against the robustness of the nanoprobe in physiological conditions.³⁴ In addition, a recognition motif can be added³⁵ for sensing or theranostic purposes. In order to choose a nanoparticles which can be used as SERS substrate, branched nano-objects like gold nanostars are considered the best choice, as the presence of tips and edges acting as “hot spots” (or exploiting the “lightning rod” effect) may lead to a huge field enhancement of the scattering signal.³⁶ Thus, GNSs³⁷ have become an extremely popular kind of object for SERS applications, and several examples based on GNSs have been proposed to prepare SERS-encoded nanodevices³⁸ to give intracellular signals. GNSs are usually synthesized in presence of a surfactant, using a “classical” seed-growth approach,³⁷ but also surfactant-free methods³⁹ yielding very monodisperse objects and high quality tips have been proposed. In the construction of SERS nanotags, optimal ratios of Raman reporter and protecting agent must be respected, to offer the strongest protection coupled with the brightest signal: in a recent review³³ the issues concerning the proper amounts of polyethylenglicols (PEGs) and Raman reporter to be added on nano-objects surfaces were listed, evidencing the need of a careful investigation to control the coating conditions. Recently, a method for a precise and controlled coating of spherical silver nanoparticles (AgNPs) with mixed monolayers of thiols, was applied.⁴⁰ This approach is based on the determination, for a series of given thiols, of the minimum concentration in solution needed to give, in a post-synthetic coating, a monolayer of the thiol on the nanoparticles surface; these values were obtained from simple UV-Vis spectrophotometric titrations, exploiting the Localized Surface Plasmon Resonance (LSPR) shift which is caused by the thiol coating.⁴¹ Knowledge of these concentration values allowed to obtain a precise surface composition of a mixture of two thiols, simply

³³ L.A. Lane; X. Qian; S. Nie; *Chem. Rev.*, **2015**, 115, 10489–10529.

³⁴ B.M. DeVetter; S.T. Sivapalan; D.D. Patel; M.V. Schulmerich; C.J. Murphy; R. Bhargava; *Langmuir*, **2014**, 30, 29, 8931–8937.

³⁵ X. Qian; X.H. Peng; D.O. Ansari; Q.Y. Goen; G.Z. Chen; D.M. Shin; L. Yang; A.N. Young; M.D. Wang; S. Nie; *Nature Biotechnology*, **2008**, 26 1, 83–90.

³⁶ K. Kneipp; M. Moskovits; H. Kneipp; *Topics Appl. Phys.*, 103, Springer-Verlag Berlin Heidelberg, **2006**.

³⁷ A.G. Martinez; S. Barbosa; I.P. Santos; L.M. Marzan; *Current Opinion in Colloid & Interface Science*, **2011**, 16, 2, 118–127.

³⁸ A. Taglietti; Y.A.D. Fernandez; P. Galinetto; P. Grisoli; C. Milanese; P. Pallavicini; *Journal of Nanoparticle Research*, **2013**, 15, 11, 1–13.

³⁹ E. Amato; Y.A.D. Fernandez; A. Taglietti; P. Pallavicini; L. Pasotti; L. Cucca; C. Milanese; P. Grisoli; C. Dacarro; J.M.F. Hechavarría; V. Necchi; *Langmuir*, **2011**, 27, 15, 9165–9173.

⁴⁰ P. Pallavicini; G. Chirico; M. Collini; G. Dacarro; A. Dona; L. D'Alfonso; A. Falqui; Y.D. Fernandez; S. Freddi; B. Garofalo; A. Genovese; L. Sironi; A. Taglietti; *Chem Comm.*, **2011**, 47, 4, 1315–1317.

⁴¹ A. Casu; E. Cabrini; A. Dona; A. Falqui; Y.D. Fernandez; C. Milanese; A. Taglietti; P. Pallavicini; *Chem. Eur. J.*, **2012**, 18, 30, 9381–9390.

using, in the coating solutions, a linear combination of the two minimum concentrations needed to give a monolayer on the surface of colloidal dispersion. In this way, the final composition of the mixture of thiols detected on the nanoparticles surface was found to reflect the one used in solution, and the properties of the colloid could be controlled tuning the mixture composition in the post-synthetic coating. In this thesis we have described several times the synthesis of GNSs^{42,43} (seed-mediated growth approach, using LSB) and their features.

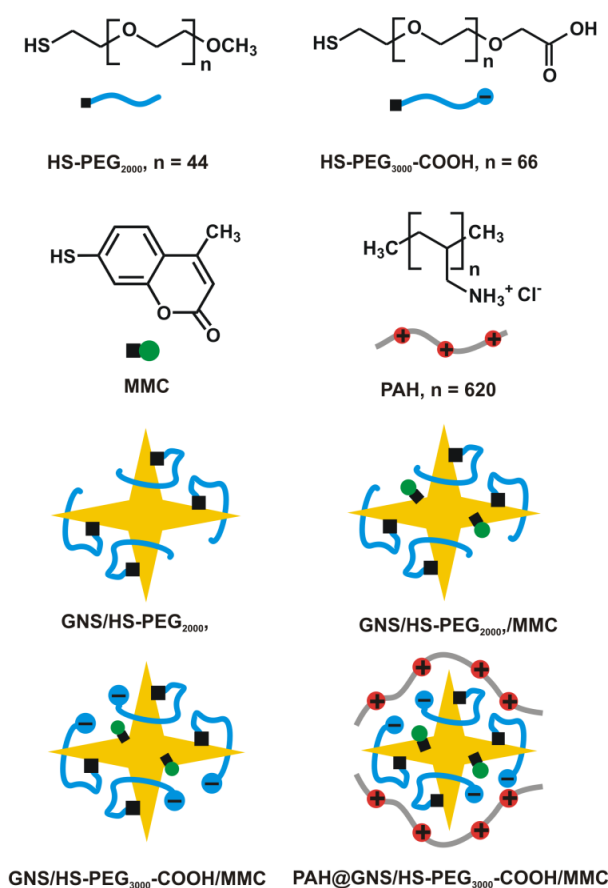


Figure 3: structures of PEGs, MMC and PAH polymer used in this work. The figure also includes pictorial sketches of GNSs with various coatings as prepared in this approach.

In this part of the work it will be proved how the coating of GNSs with mixtures of different thiols (see Figure 3) can be precisely controlled and tuned using a method which starts from a set of UV-Vis titrations. This approach allows to control the amount

⁴² P. Pallavicini; E. Cabrini; G. Cavallaro; G. Chirico; M. Collini; L. D'Alfonso; G. Dacarro; A. Donà; N. Marchesi; C. Milanese; A. Pascale; L. Sironi; A. Taglietti; *Journal of Inorganic Biochemistry*, **2015**, 151, 123–131

⁴³ N. Marchesi; C. Osera; L. Fassina; M. Amadio; F. Angeletti; M. Morini; G. Magenes; L. Venturini; M. Biggioggera; G. Ricevuti; S. Govoni; S. Caorsi; A. Pascale; S. Comincini; *Journal of Cellular Physiology*, **2014**, 229, 11, 1776–1786.

of 7-methyl-mercapto coumarin (MMC) introduced as a typical Raman reporter³⁸ on GNSs: MMC can be brought on the colloid surface in a precise quantity exploiting the robust S-Au bond, and mixed in different compositions with appropriate PEGs having a thiol moiety as an α -function; these kind of molecules are commonly used to protect nanoparticles from aggregation and to prepare SERS nanoparticles for biomedical applications.⁴¹ Moreover, the use of PEGs improve the biocompatibility and the cell-penetration abilities of NPs.⁴⁴ A general and reliable method to prepare robust and reproducible nanoparticles with intensity-tunable SERS responses, which linearly depends from the precisely controlled ratio between Raman reporter and thiolated PEG used, will be presented in the next pages. Furthermore it will be demonstrated the usability of the probes, on the basis of previous results, adding an additional external layer of polyallylamine hydrochloride (PAH) on negatively charged nano-objects in order to promote their penetration into SH-SY5Y neuroblastoma cells, investigating the biocompatibility of the samples and, more importantly, demonstrating their possible use as SERS tags in cells.

⁴⁴ F.S. Tautz; *Progress in Surface Science*, **2007**, 82, 9-12, 479-520.

3.2.2 EXPERIMENTAL DETAIL: SYNTHESIS AND CHARACTERIZATION

3.2.2.1 MATERIALS AND INSTRUMENTATION

Reagents

N-Dodecyl-N,N-dimethyl-3-ammonium-1-propanesulfonate (LSB) ($\geq 99.7\%$), Gold(III) chloride trihydrate ($\sim 30\text{wt}\%$ in HCl 99.99%), sodium borohydride (98%), L-ascorbic acid (AA) ($\geq 99\%$), silver nitrate (99.8%), PEG₂₀₀₀-SH (α -methoxy- ω -mercapto poly(ethylene glycol)), 7-mercapto-4-methylcoumarin $\geq 97\%$, poly(allylamine hydrochloride), ethanol ($\geq 99\%$), were all purchased from Sigma-Aldrich. HS-PEG₃₀₀₀-COOH (poly(ethylene glycol) 2-mercaptoethyl ether acetic acid) was purchased from RAPP polymere. Reagents were used as received. Glass cuvettes were standard optical glass cuvettes purchased from Hellma. All the preparation are made with bi-distilled water.

Instrumentation

UV-Vis Spectroscopy. UV-Vis spectra were taken on Cary 60 Varian, using poly(methyl methacrylate) cuvettes (optical path 1 cm). The wavelength scan range was 350-1100 nm.

Ultracentrifugation. Ultracentrifugation was carried out using the ultracentrifuge HermleZ366 with polypropylene 10 mL tubes.

Transmission electron microscopy (TEM). TEM images were taken with Jeol JEM-1200 EX II instrument on 10 μL colloidal solution drops, deposited on Copper grids (300 mesh) covered with a Parlodion membrane.

ICP-OES (inductively coupled plasma optical emission spectroscopy) analysis. The Au and Ag concentration were determined by ICP-OES on a ICP-OES OPTIMA 3000 Perkin Elmer instrument.

Dynamic light scattering measurements (DLS). The measurements were performed with a Zetasizer Nano-ZS90 (source: polarized He-Ne LASER, 30 mW output power, vertically polarized).

SERS measurements. SERS measurement were carried out at room temperature by using a Labram Dilor spectrometer equipped with an Olympus microscope HS BX40.

3.2.2.2 GLASSWARE PRETRATMENT

All the glassware that come into contact with GNSs was always pretreated before use: a wash in *aqua regia* for 30 minutes, then washed and filled with bi-distilled water and ultrasonicated for 3 minutes before discarding water. The bi-distilled water/ultrasound treatment was repeated 3 times. Then the glassware were dried in an oven for 1 hour at 140°C.

3.2.2.3 PREPARATION AND CHARACTERIZATION OF COATED GNSs

Preparation of GNSs

The synthesis of GNSs was carried out with the general synthetic method already described. In a typical synthesis, the seed solution was prepared in a vial. 5 mL of HAuCl_4 5×10^{-4} M in water were added to 5 mL of an aqueous solution of LSB 0.2 M. The mixture was gently hand-shaken and a pale yellow colour was obtained. Then were added 600 μL of a previously ice-cooled solution of NaBH_4 1×10^{-2} M in water. The mixture was gently hand-shaken and a orange-brown colour was obtained. The seed solution was kept in ice and used in few hours. The growth solution was prepared in a flask: 1800 μL of AgNO_3 4×10^{-3} M in water, 50 mL of HAuCl_4 5×10^{-4} M in water were added in this order to 50 mL of an aqueous solution of LSB 0.2 M. Then were added 800 μL of an aqueous solution of ascorbic acid 0.0788 M. The solution, after gentle mixing, became colourless. Soon after were added 120 μL of the seed solution. The solution was gently hand-shaken and a pink colour appeared and quickly changed to blue and became more intense. The samples were allowed to equilibrate for 1 h at room temperature. After one hour the samples were ultracentrifuged (13000 rpm, 25'), the supernatant discarded and the precipitates resuspended in 10 mL of bi-distilled water. UV-Vis of GNSs was recorded. Under these conditions, the used colloidal suspensions showed the main LSPR absorbance at 850 nm ($\sigma = 30$ nm) and the secondary LSPR absorbance at 650 nm ($\sigma = 20$ nm).

Spectrophotometric titrations of GNSs

A sample of GNSs (10 mL) as synthesized, were titrated using 10^{-3} M stock solutions of the desired thiol. Ethanol was used to prepare the MMC stock solution, while α -methoxy- ω -mercapto polyethylene glycol (HS-PEG₂₀₀₀) and poly(ethylene glycol) 2-mercaptoethyl ether acetic acid (HS-PEG₃₀₀₀-COOH) 10^{-3} M stock solutions were prepared in water. Titrations were carried until no changes in LSPR bands positions were registered. After each addition the solution was gently hand-shaken for three minutes before record UV-Vis spectrum.

Coating with mixed monolayers of thiols

To a chosen volume of GNSs suspension (10-100 mL), the proper amount of stock solution of the chosen thiols were added in order to obtain the desired mixture composition. In all cases, the overall concentration of the two thiols in the GNSs suspension was set to $1.1 \cdot 10^{-5}$ M. For example, the mixture containing 50% of MMC and 50% of HS-PEG₃₀₀₀-COOH was obtained making the final concentration in the GNSs colloidal suspension with $5.5 \cdot 10^{-6}$ M in MMC and $5.5 \cdot 10^{-6}$ M in HS-PEG₃₀₀₀-COOH. These mixtures were stirred for 1h at room temperature, then ultracentrifuged (13000 rpm, 25'). The supernatant was discarded and the precipitate re-dissolved in the same starting volume (10-100 mL) in bi-distilled water. Ultracentrifugation/re-dissolutions cycle was repeated three times. UV-Vis of coated GNSs was recorded. After the last ultracentrifugation, the pellets were re-dissolved in the amount of bi-distilled water calculated in order to obtain the desired concentration. Fluorescent spectra of supernatant after centrifugation steps were taken using Agilent Cary Eclipse Fluorescence Spectrophotometer and 1 cm path quartz cuvettes.

Coating with PAH

The pH of coated GNSs (10 mL) was regulated at the value of 7, with a small additions of HNO₃ 0.1 M. Z-potential was measured. Then, PAH [poly(allylamine) hydrochloride] was used: a solution 10^{-3} M in water was prepared and 100 μ L of this solution were added to 10 mL of the pre-treated GNSs samples and the mixture allowed to react for 1 h at room temperature. After 1 h, samples were ultracentrifuged and the precipitate was re-dissolved in the amount of bi-distilled water calculated in order to obtain the desired concentration. Z-potential of PAH modified nanoparticles was measured. Colloidal

stability was assessed for a sample of PAH coated GNSs prepared using PBS, as the medium used for cells culture was strongly absorbing in the visible region, overlapping with the LSPR spectra of colloids. After the centrifugation steps, a GNSs pellet was resuspended in PBS buffer, and UV-vis spectra monitored after 3, 24 and 120 hours.

ICP-OES (inductively coupled plasma optical emission spectroscopy) analysis

Samples of GNSs coated with the different coating systems were analysed after the typical 3-cycles ultracentrifugation/re-dissolution purification (four cycles in the case of PAH terminated samples) to check the Au concentration, and thus the one of GNSs in the colloidal suspension. After the last ultracentrifugation, the pellet was treated with 1 mL *aqua regia* and after complete reaction (1 hour) with 2 mL bi-distilled water. The Au and Ag concentration were determined by ICP-OES on a ICP-OES OPTIMA 3000 Perkin Elmer instrument.

SERS measurements

SERS measurements were carried out at room temperature by using a Labram Dilor spectrometer equipped with an Olympus microscope HS BX40. The 632.8 nm light from a He-Ne LASER was employed as excitation radiation. Pure colloidal samples (with Au concentrations of about 3.0×10^{-4} M, corresponding to 1.7×10^{-9} M of GNSs) were examined using a 10x objective with a 2.8 μm spot diameter while a 50x objective with a 1.5 μm laser spot diameter, was used for linear scanning and imaging on cells. The focus depth was about 150 μm and 15 μm for 10x and 50x respectively. The spectral resolution was about 1 cm^{-1} . The LASER power density was kept about $5 \times 10^5 \text{ W/cm}^2$ and $8 \times 10^4 \text{ W/cm}^2$ for colloidal samples and cells respectively. A cooled CCD camera was used as a detector and the typical integration times were about 20 s and the run was repeated 3 or 5 times. For the estimation of the SERS enhancement factor we compared the SERS signal of MMC from colloidal samples with Raman signal of MMC diluted at 10^{-2} M in ethanol. We estimated the analytical enhancement factor (AEF), defined as $\text{AEF} = (I_{\text{SERS}}/C_{\text{SERS}})/(I_{\text{RS}}/C_{\text{RS}})$, where I_{SERS} is the average intensity of the SERS signal for the analyte added at a concentration C_{SERS} and I_{RS} and C_{RS} are the corresponding values under normal Raman conditions. Because we use the same objective and the same LASER intensity when measuring the SERS signal and the normal Raman signal, we assume that the scattering volumes are the same in both experiments. The spectra used

for AEF estimation were obtained from an average over multiple runs and from different sample regions. In all cases the data were analyzed by a best fitting procedure using a lorentzian curve or a sum of lorentzian curves as the fitting function.

MTT assay

Mitochondrial enzymatic activity was estimated by the MTT [3-(4,5-dimethylthiazol-2-yl)-2,5-diphenyltetrazolium bromide] assay (Sigma-Aldrich, Milan, Italy). A cell suspension of 10000 cells/well in 100 μ l culture medium was seeded into 96-well plates. After each treatment (24 and 48 hours), the medium was substituted with fresh medium and then 10 μ l of MTT (final concentration equal to 1 mg/ml) were added to each well. After incubation at 37°C for 4 hours, the formed purple formazan crystals were solubilized in 100 μ l of lysis buffer (20% sodium dodecyl sulfate in 50% dimethylformamide) overnight at 37°C. Absorbance values were measured at 595 nm in a microplate reader (SynergyHT, BioTek Instruments, Inc.) and the results expressed as % with respect to the control value (100%). The data were subjected to analysis of variance (ANOVA) followed, when significant, by an appropriate *post-hoc* comparison test, as indicated in the figure legends. The differences were considered statistically significant when p values ≤ 0.05 .

3.2.3 RESULT AND DISCUSSIONS

3.2.3.1 NATIVE GNSs CHARACTERIZATION

GNSs were synthesized according to the described pathway (Paragraph 1.3.1) using LSB surfactant.⁴⁵ The absorption spectrum of this kind of preparation was already described in detail.

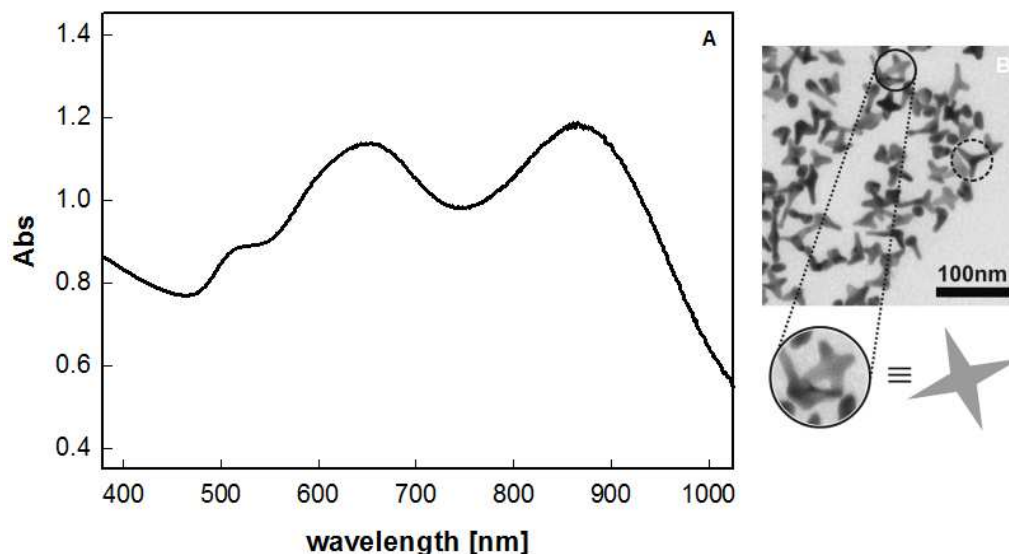


Figure 4: A) UV-Vis spectrum of a typical GNSs colloid used in this part of the work B) TEM images of the GNSs used.

As mentioned before, the spectrum reflecting the composition of nano-objects mixture and can be quite precisely tuned changing the concentration of the ascorbic acid. In this part of the work, the position of the long band was tuned close to 850(30) nm (a typical UV-Vis spectrum is shown in Figure 4A). A Transmission Electron Microscopy (TEM) image of a typical colloid preparation used in this work is reported in Figure 4B.

3.2.3.2 GNSs TITRATION

After the purification of GNSs from excess of LSB by ultracentrifugation, we have performed a series of UV-Vis spectrophotometric titrations in order to quantify the amount of the chosen thiols needed to obtain a molecular SAM on GNSs surfaces. The

⁴⁵ A. Casu; E. Cabrini; A. Donà; A. Falqui; Y.D. Fernandez; C. Milanese; A. Taglietti; P. Pallavicini; *Chem. Eur. J.*, **2012**, 18, 9381-9390.

principle behind this approach is based on the fact that the position of the long LSPR band of the colloid, will shift upon the addition of thiols, since the effective refractive index experienced by the GNSs will change^{39,44,43} by substituting the expressly labile surfactant coating layer given by LSB with the much stronger Au-S bond. When the coating with the desired thiol is complete, i.e. when no more molecules of thiols can be added to the surface of the nano-objects, the position of the LSPR long band will not further shift upon thiol addition, reaching a plateau. Therefore, the minimum amount of thiol molecules needed to reach the almost complete coating of the colloid with a SAM can be determined from the plot of the wavelength shift vs the quantity of the thiol added to the colloidal suspension.

Experimental UV-Vis data show that upon the addition to a suspension of standard colloid of GNSs of a stock solution of each of the investigated thiols (MMC, HS-PEG₂₀₀₀, HS-PEG₃₀₀₀-COOH), the long LSPR peak red-shifted. A representative titration of a typical colloid GNSs with MMC is reported in Figure 5, as well as the titration profile obtained, evidencing the plateau reached by the wavelength of the “long band” in one representative experiment. Representative titrations obtained with HS-PEG₂₀₀₀ and HS-PEG₃₀₀₀-COOH are reported in Figure 6 and 7.

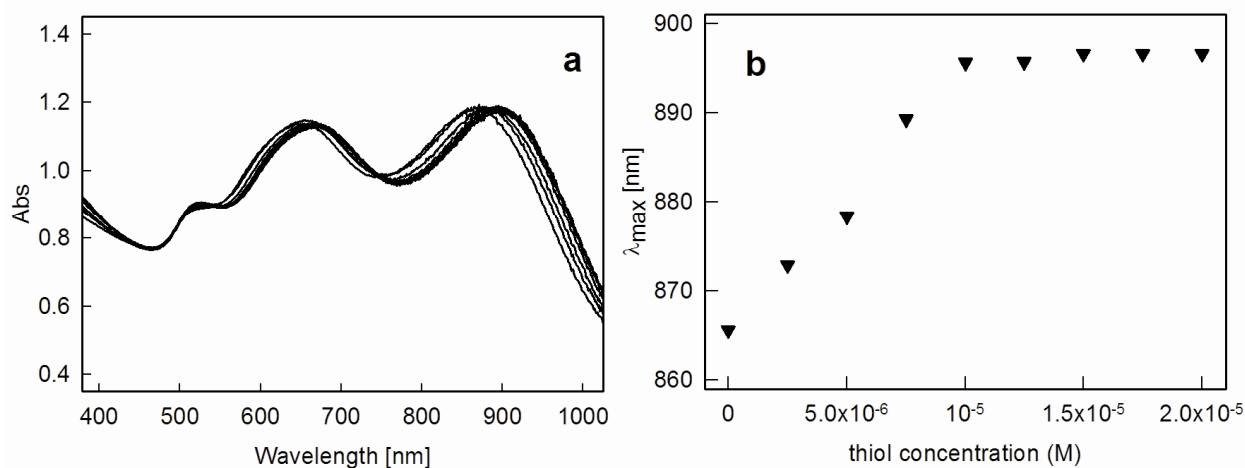


Figure 5: representative titration of a standard GNSs colloidal suspension with a stock solution of MMC: a) spectra obtained upon addition of increasing quantities of MMC; b) titration profile showing the red shift of the position of the LSPR long band as a function of MMC added.

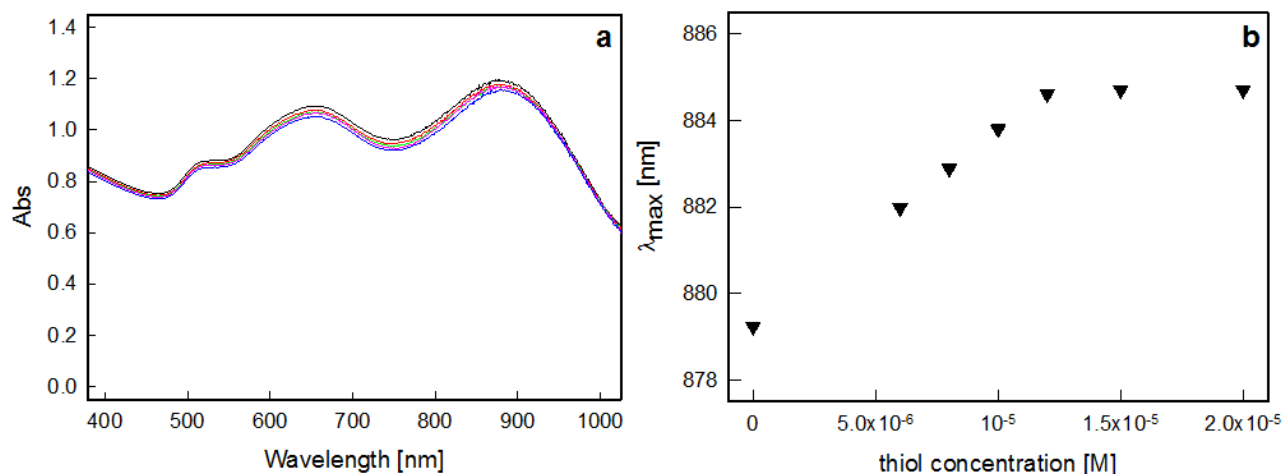


Figure 6: representative titration of a standard GNSs colloidal suspension with a stock solution of HS-PEG₂₀₀₀: a) spectra obtained upon addition of increasing quantities of HS-PEG₂₀₀₀; b) titration profile showing the red shift of the position of the LSPR long band as a function of HS-PEG₂₀₀₀ added.

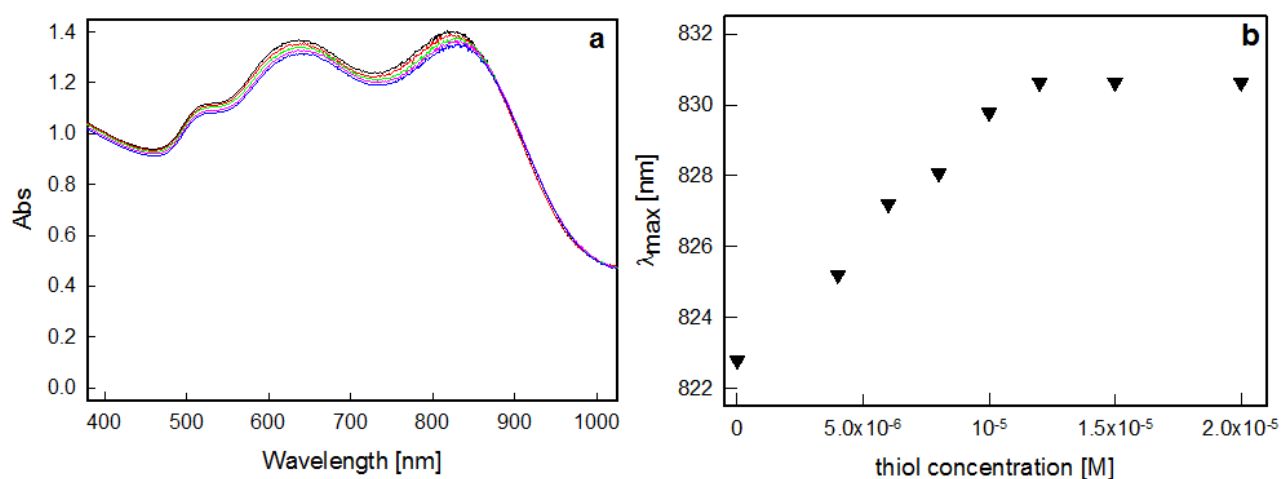


Figure 7: representative titration of a standard GNSs colloidal suspension with a stock solution of HS-PEG₃₀₀₀-COOH: a) spectra obtained upon addition of increasing quantities of HS-PEG₃₀₀₀-COOH; b) titration profile showing the red shift of the position of the LSPR long band as a function of HS-PEG₃₀₀₀-COOH added.

For each thiol, at least five titrations were performed, calculating the maximum wavelength shift obtained for the “long band” (i.e. the difference between the starting value and the one reached at the plateau) and the concentration of the thiol needed to reach the plateau. Data are reported in Table 1, with standard deviations.

Table 1: LSPR red shift observed after the addition of different thiols used in this work, and the concentrations needed to reach this maximum LSPR red shift value at the plateau.

Thiol	Δ at plateau [nm]	Thiol concentration [M]
MMC	30 \pm 4	1.1 \pm 0.2 $\times 10^{-5}$
HS-PEG ₂₀₀₀	8 \pm 2	1.1 \pm 0.2 $\times 10^{-5}$
HS-PEG ₃₀₀₀ -COOH	7 \pm 3	1.1 \pm 0.2 $\times 10^{-5}$

It is worth of note, from the data reported in Table 1 and from the spectra of the Figures above, that the LSPR shift obtained upon exhaustive coating with MMC is considerably larger than the shifts obtained with the two thiolated PEGs investigated. A similar phenomenon was already observed for AgNPs coated with MMC⁴⁰ when compared to AgNPs coated with other molecules having a thiolic function like glutathione or cysteine.⁴¹ This larger red shift might be due to the fact that MMC is an aromatic molecule, able to undergo coupling between the molecular orbitals and the plasmonic states of the colloid, affecting both the LSPR frequency and the electronic properties of the organic molecules adsorbed on the metal surface.^{46,47} Also, the hydrophobic character of MMC is expected to cause a sensible change of the effective refractive index experienced by the coated nanoparticles, when LSB (in the case of GNSs) is substituted by MMC, and this effect is known to influence the position and intensity of LSPR absorption.⁴⁸ Anyway, it is important to observe that all the three investigated thiols gave the same value of concentration in solution necessary to give a monolayer on the standard colloid used, i.e. 1.1(0.2) $\times 10^{-5}$ M. This behaviour has probably to be ascribed to the fact that the three molecules investigated are able to access the same number of reactive sites on gold surface, and that once bound occupy the same available space.

3.2.3.3 CHARACTERIZATION OF GNSs COATED WITH MIXED MONOLAYERS

At first, we have investigated variable compositions of coating solutions by changing the molar ratio between MMC and HS-PEG₂₀₀₀, but keeping an overall concentration of thiols of 1.1 $\times 10^{-5}$ M, which was found to be the concentration needed to obtain a SAM on the standard colloid for each one of the used thiols. At this overall concentration, it is

⁴⁶ E. Hutter; J.H. Fendler; *Advanced Materials*, **2004**, 16, 19, 1685-1706.

⁴⁷ E.C. Cho; J. Xie; P.A. Wurm; Y. Xia; *Nano Letters*, **2009**, 9, 3, 1080-1084.

⁴⁸ E. Vogel; W. Kiefer; *Fresenius Journal of Analytical Chemistry*, **1998**, 361, 6-7, 628-630.

reasonable to foresee an unchanged transfer of the molar ratio from the solution to the colloidal suspension, obtaining a SAM composition with a known mixture of the two thiols. If this approach works well, the red shift observed for the LSPR long band ($\Delta\lambda_{\text{mix}}$) for a given mixture composition, in presence of a random arrangement of the thiols on the surface, should be a linear combination of the shifts observed for the formation of a SAM with each single thiol ($\Delta\lambda_a$ and $\Delta\lambda_b$ as determined from the titrations showed in the previous paragraph, see Table 1), obeying to the relationship expressed in equation (1):

$$\Delta\lambda_{\text{mix}} = X_a\Delta\lambda_a + (1-X_a)\Delta\lambda_b \quad (1)$$

where X_a is the fraction of thiol “a” used in the coating mixture and $1-X_a$ obviously is the fraction of thiol “b” in the mixture.

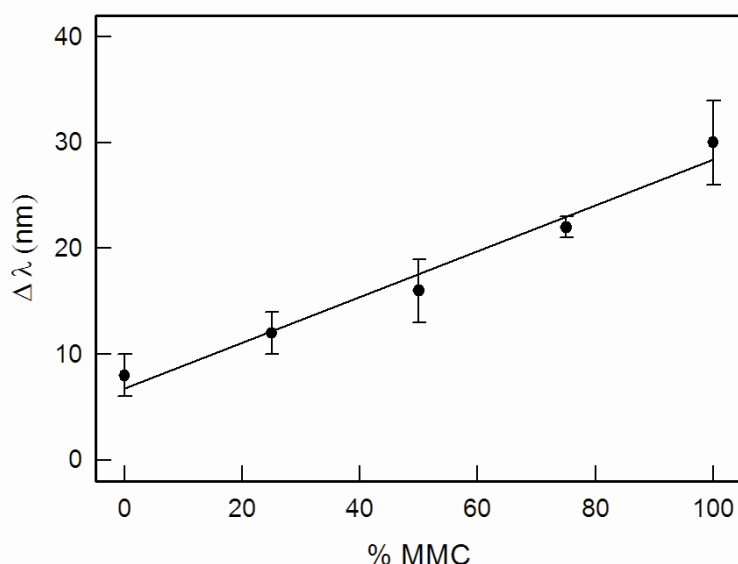


Figure 8: LSPR shift ($\Delta\lambda$) of the GNSs long band upon coating, as a function of the composition of the thiols (MMC and HS-PEG₂₀₀₀) stock solution used, expressed as MMC percentage in a stock solution having an overall thiol concentration of 1.1×10^{-5} M. Each point represents the mean value of at least three preparations. The regression line has $r^2 = 0.975$.

Figure 8 reports the values of $\Delta\lambda_{\text{mix}}$ obtained for five different compositions (at least three preparations and measurements for each composition investigated) of the coating mixture using MMC and HS-PEG₂₀₀₀. A linear relationship ($r^2 = 0.975$) is found between the red shift observed for the LSPR long band and the mixture composition, confirming that equation (1) is verified with $\Delta\lambda_a = 8(2)$ nm (the red shift observed at the plateau in the case of the formation of a SAM of HS-PEG₂₀₀₀) and $\Delta\lambda_b = 30(4)$ nm (the red shift observed at the plateau in the case of the formation of a SAM of MMC). The same experiments (consisting of at least three preparations and measurements for each composition) were

repeated with the coating mixtures composed of MMC and HS-PEG₃₀₀₀-COOH, and once again we found that the LSPR shift observed for a given mixtures obeys to a linear ($r^2=0.986$) combination of the red shift observed for the formation of a SAM with MMC and the one observed for HS-PEG₃₀₀₀-COOH. Again, as can be seen in Figure 9, equation 1 is verified with $\Delta\lambda_a=7(3)$ nm (the red shift observed at the plateau in the case of the formation of a coating layer of HS-PEG₃₀₀₀-COOH) and $\Delta\lambda_b=30(4)$ nm (the red shift observed at the plateau in the case of the formation of a coating layer of MMC).

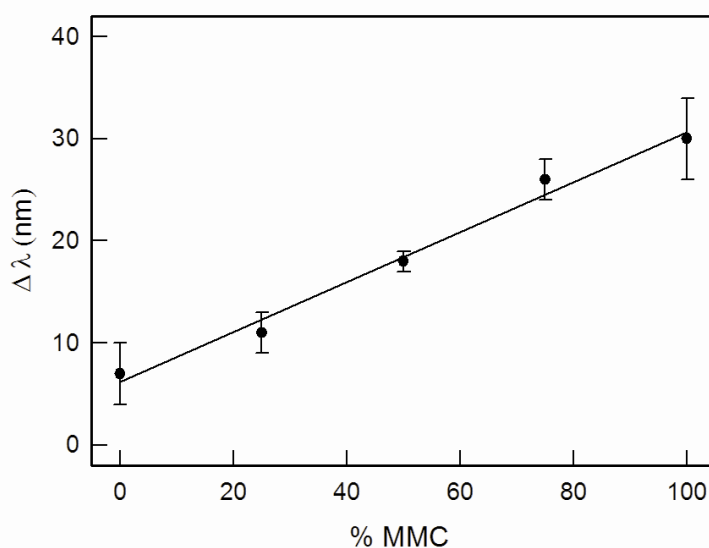


Figure 9: LSPR shift ($\Delta\lambda$) of the GNSs long band upon coating, as a function of the composition of the thiols (MMC and HS-PEG₃₀₀₀-COOH) stock solution used, expressed as MMC percentage in a stock solution having an overall thiol concentration of 1.1×10^{-5} M. Each point represents the mean value of at least three preparation. The regression line has $r^2=0.986$.

We can therefore conclude that the compositions of a mixed monolayer obtained following the described approach reflects the composition of the thiols solutions used. After the described coating and after a first ultracentrifugation step, fluorescence spectra were measured on the supernatant solutions obtained from all the samples: no presence of fluorescent MMC ($\lambda_{exc}=350$ nm, $\lambda_{em}=400$ nm) was observed, demonstrating that all the Raman reporter molecules added to the colloidal suspension were bound to GNSs surfaces as already suggested by the UV-Vis titrations. These results agree with recently published works,^{24,40} confirming that the use of stock solutions of coating agents having concentrations close to the values needed for full-coverage with a monolayer allows to control the composition of modifiers layer on nanoparticles surfaces. In other words, one must take the care to have, in the coating solution of the two modifiers, an overall thiol concentration which does not exceed the maximum quantity requested to give a monolayer according to the spectro-photometric titration monitoring the LSPR shift.

This method seems particularly precious especially in all those cases where surface area is unknown or difficult to calculate: by following the described procedure, a precise control of surface concentration of different functions can be obtained without knowing surface area of the colloidal suspension or the area occupied by the single coating molecule. The only value needed is the turning point of the spectro-photometric titrations of the two (or, in principle, more than two) component of the desired mixture. In all the studied systems, after the coating process, stability of the coated colloids were investigated by three cycles of centrifugation/solvent-discharge/pellet uptake in bi-distilled water, each cycle followed by registration of UV-Vis spectra. In all cases, except for the case of 100% MMC coating, coated GNSs were found completely stable, as the LSPR features of the spectra (band position and intensity) were not altered after each centrifugation step (for an example regarding the 25% MMC and 75% HS-PEG₃₀₀₀-COOH coating mixture see Figure 10).

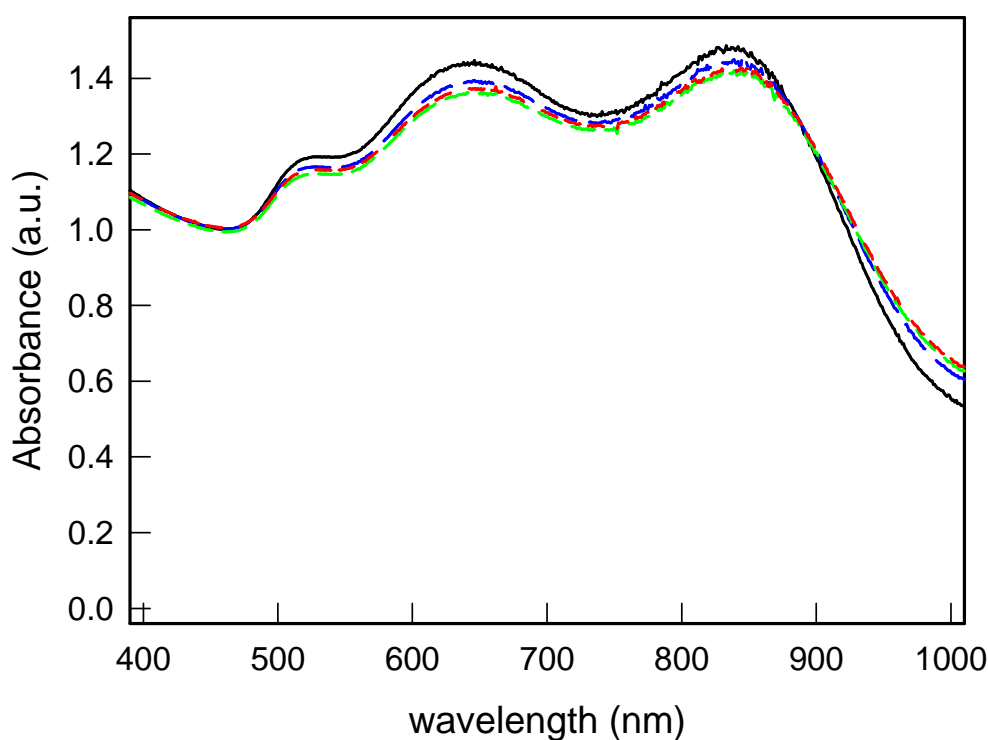


Figure 10: Spectra of a sample of GNSs coated with a 25% MMC and 75% HS-PEG₃₀₀₀-COOH mixture (black line); the same after one centrifugation and redissolution step (blue line); the same after a three centrifugation and redissolution step (green line); the same after the final coating with a PAH layer (red line).

As a further proof of stability, fluorescence spectra measured on the supernatant solutions obtained from the samples after every centrifugation step was measured. Supernatant solutions did not show the presence of MMC demonstrating that all the

added Raman reporter was bound tightly to the GNSs surface and not released in solution, evidencing the robustness of the SERS labels. Only in the case of the coating with 100% MMC, after the first centrifugation step, an irreversible aggregation of the colloid was observed: trying to re-dissolve the solid obtained, we obtained an almost flat LSPR spectra, losing the peculiar features typical of this anisotropic objects mixture. It is worth of note, anyway, that also small fractions of HS-PEG₂₀₀₀ or HS-PEG₃₀₀₀-COOH (for example in samples coated with 25% of HS-PEG and 75% MMC) ensure an excellent stability of GNSs. For each kind of prepared sample, Au concentration after the three ultracentrifugation steps was checked by ICP-OES analysis giving, as already observed for similar coatings with PEGs, values close to 3.0×10^{-4} M (0.06 mg/mL), which correspond to a GNSs concentration of about 2.0×10^{-9} M, considering an average mass of 5×10^{-17} g/GNS, as previously reported.⁴²

3.2.3.4 PAH COATING OF GNSs COATED WITH MIXED MONOLAYERS

To allow cellular uptake of coated GNSs and to test them as labels for cellular SERS imaging, a further coating with a positively charged layer was performed. For example, it was shown that PAH-coated gold nanospheres (diameter 18 nm) can enter into SK-BR-3 breast cancer cells, indicating the need of a positively charged coating to promote internalization, as the same nanoparticles with neutral or negative surface charge did not show any internalization using the same cells.⁴⁹ Moreover, exploiting the two-photon luminescence of GNSs and using confocal laser scanning microscopy, we recently demonstrated that when GNSs are coated with a SAM of PEGs they do not enter SH-SY5Y cells, while when overcoated with a layer of PAH they massively penetrate into the cytoplasm causing, when used at high concentrations, cell death, as evidenced by dramatic changes in cell morphology.⁴² Thus, GNSs coating with the mixed monolayer (MMC and HS-PEG₃₀₀₀-COOH) objects were further coated with a layer of PAH, in order to promote their internalization in SH-SY5Y cells and test their use as potential SERS probes. This can be easily done by adding PAH to the coated GNSs colloid at pH adjusted to a value of 7, as in these conditions all the carboxylic functions are deprotonated, while PAH is mostly protonated. As a consequence of this coating, as expected, we observed the Z-potential switching from about -15 mV for the COO⁻ terminated GNSs, to a value of about $+40$ mV for the PAH coated GNSs (see values in Table 2).

⁴⁹ E. Vogel; A. Gbureck; W. Kiefer; *Journal of Molecular Structure*, **2000**, 550, 177-190.

Table 2: Z-potential values (mV) at pH 7 of SERS tags (GNSs coated with MMC and HS-PEG₃₀₀₀-COOH) with different coating compositions, before and after coating with PAH, and after coating with PAH followed by one ultracentrifugation/supernatant-discarding/re-dissolution cycle.

	Before coating with PAH	After coating with PAH	After coating with PAH and centrifugation
75% MMC 25% HS-PEG-COOH	-17 ± 4	44 ± 6	43 ± 6
50% MMC 50% HS-PEG-COOH	-14 ± 5	46 ± 6	40 ± 5
25% MMC 75% HS-PEG-COOH	-16 ± 4	47 ± 5	44 ± 6
100% HS-PEG-COOH	-19 ± 3	45 ± 5	42 ± 3

PAH coating did not affect the LSPR spectra of GNSs, indicating the absence of any change in shape or any aggregation phenomenon (see Figure 11). In order to eliminate unbound PAH, we processed these samples with one further ultracentrifugation/supernatant-discarding/re-dissolution cycle, and measured Z-potentials observing no sensible changes in the values after this steps (see values in Table 2), indicating a good stability of PAH terminal coating and an overall stability of the probes. Also in this case, Au concentration of the final samples was checked by ICP-OES analysis giving the value of about 3.0×10^{-4} M (0.06 mg/mL).

Stability of coated GNSs was further tested by measuring the variations of LSPR spectra of a PAH@GNSs|MMC|HS-PEG₃₀₀₀-COOH sample (prepared with a mixed monolayer composed of 25% of MMC and 75% of HS-PEG₃₀₀₀-COOH) when dissolved in PBS buffer.

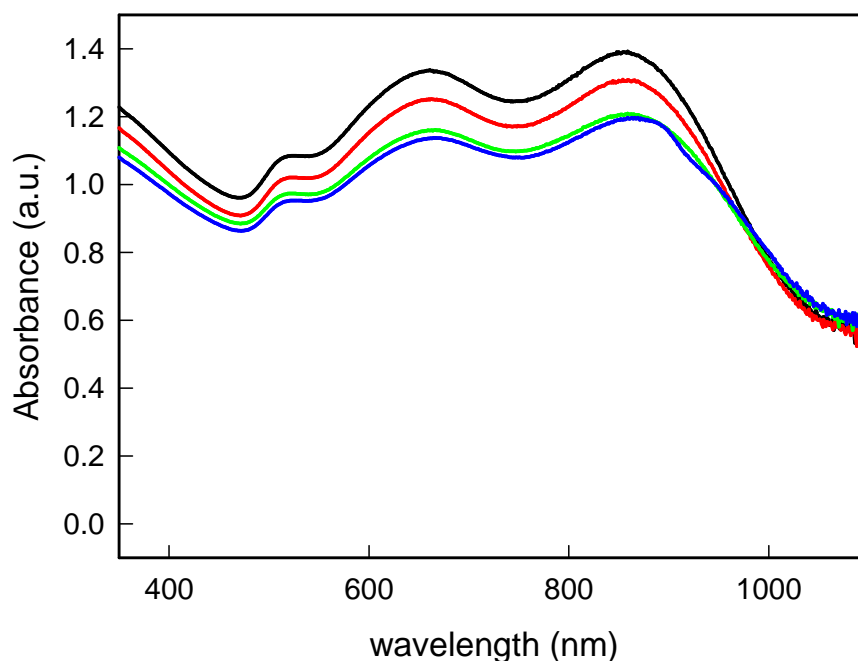


Figure 11: spectra of a) a sample of PAH@GNSs|MMC|HS-PEG₃₀₀₀-COOH prepared with a mixed monolayer composed of 75% of HS-PEG₃₀₀₀-COOH and 25% of MMC (black line) dissolved in PBS; b) the same after 3 hours (red line); c) the same after 24 hours (green line); d) the same after 5 days (blue line).

Extinction spectra show that LSPR shape and position remained unchanged (see Figure 11). Only an intensity decrease over the whole range is observed in the first hours after dissolution. This variation could be ascribed to a partial, slow and reversible aggregation caused by high salinity media and suggested by the observation of a small amount of sediment after 5 days, which completely re-dissolves upon a few seconds of ultrasounds treatment. Anyway, the persistence of LSPR features allows to exclude irreversible aggregation, flocculation phenomena and/or changes of nano-objects morphology, thus indicating the good stability of the SERS tags.

3.2.3.5 SERS MEASUREMENTS ON COLLOIDAL SUSPENSIONS OF GNSs

Raman spectra were measured on colloidal suspensions of GNSs coated with the chosen mixtures as described previously, re-dissolving in bi-distilled water the pellets obtained after purification with the centrifugation steps. In a typical experiment, the concentration of coated GNSs was approximately 1.7×10^{-9} M, as calculated from gold concentrations detected by means of ICP-OES.⁴² The Raman spectrum of MMC has been already well

interpreted.^{50,51} The Raman yield is dominated by the stretching vibrational modes inside lactone and benzene rings. The most pronounced features in the Raman spectra of MMC are the bands at ~ 1170 , 1597 and 1544 cm^{-1} . The latter can be attributed to vibrations involving the in-plane C=C stretching of the lacton ring and to the modes of the benzene ring. Vibrations involving C–H bending mixed with C–C and C–O deformation give rise to the bands in the 1000 – 1350 cm^{-1} region. In particular the intense bands at 1170 cm^{-1} can be assigned to the “triangular” and to the symmetric benzene ring “breathing” vibrations including the in-plane deformations of the C(O)–O group of the molecule. SERS data were acquired for all samples in the energy region between 1000 – 1900 cm^{-1} just to record the main Raman modes.

In Figure 12 are compared the SERS spectra from samples with different coating but with the same MMC amount, i.e. 75%.

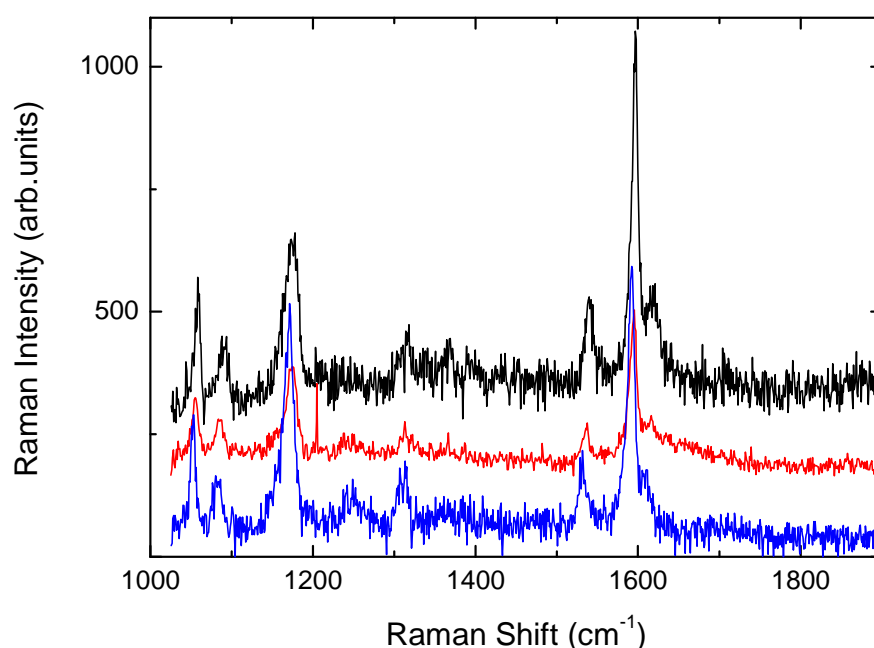


Figure 12: SERS spectra of colloidal suspensions of GNSs obtained with different coating systems: 75% MMC and 25% HS-PEG₂₀₀₀ (black line); 75% MMC and 25% HS-PEG₃₀₀₀-COOH (red line); 75% MMC and 25% HS-PEG₃₀₀₀-COOH with further PAH coating (blue line).

We notice that the different coatings have negligible effect on Raman features in term of line shape and intensity ratio between different Raman modes. The coating seems to

⁵⁰ V. Sortur; J. Yenagi; J. Tonannavar; V.B. Jadhav; M.V. Kulkarni; *Spectrochim. Acta Mol. Biomol. Spectrosc.*, **2008**, 71, 2, 688-694.

⁵¹ A.M. Alkilany; C.J. Murphy; *Journal of Nanoparticle Research*, **2010**, 12, 7, 2313-2333.

affect weakly the peak energies, inducing a small softening passing from GNSs coated with MMC and HS-PEG₂₀₀₀ to PAH coated sample. According to the literature,⁵² from these data it has been possible to estimate the analytical enhancement factor (AEF) comparing the integrated intensity of the mode at around 1590 cm⁻¹ in the SERS spectrum of colloidal samples and the same mode measured from a solution of 10⁻² M of MMC in ethanol. For the sample of GNSs coated with the 75% MMC and 25% HS-PEG₂₀₀₀ we obtained an AEF of the order of 10⁵. Thus, we performed a complete characterization of SERS response of a set of samples with different MMC amounts and coating systems.

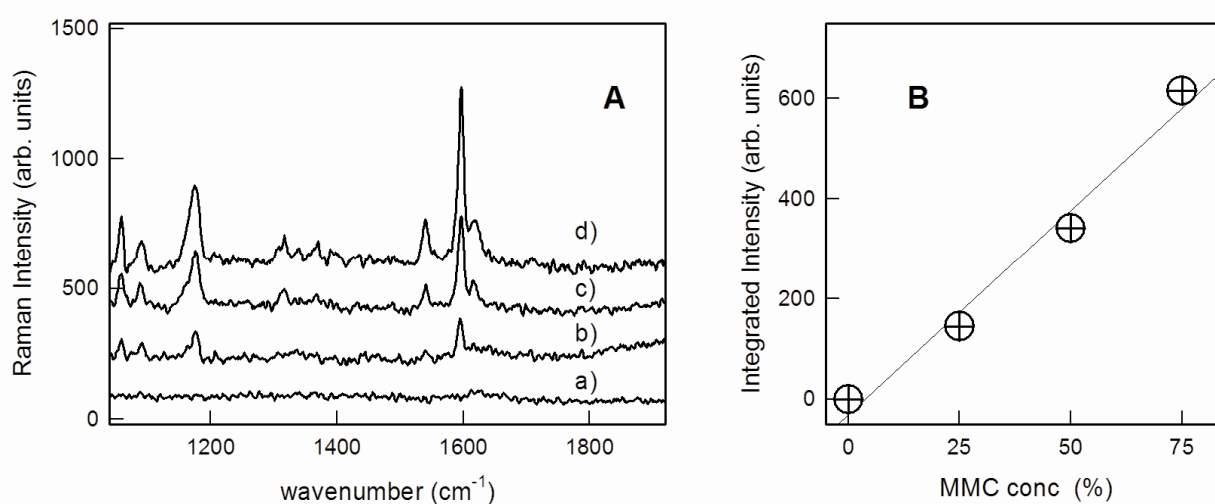


Figure 13: A) SERS spectra of colloidal suspensions of GNSs coated with MMC and HS-PEG₂₀₀₀ obtained with different coating solutions: a) 100% HS-PEG₂₀₀₀; b) 25% MMC and 75% HS-PEG₂₀₀₀; c) 50% MMC and 50% HS-PEG₂₀₀₀; d) 75% MMC and 25% HS-PEG₂₀₀₀; B) integrated intensity of peak at 1595 cm⁻¹ as a function of MMC fraction in the coating mixtures.

The SERS spectra for the series GNSs|MMC|HS-PEG₂₀₀₀ are reported in Figure 13A, while in Figure 13B the integrated intensity for the in-plane C=C stretching peak at 1595cm⁻¹ is reported as a function of MMC concentration in the starting coating mixture.

⁵² E.C. Le Ru; E. Blackie; M. Meyer; P.G. Etchegoin; *J. Phys. Chem. C*, **2007**, 111, 13794.

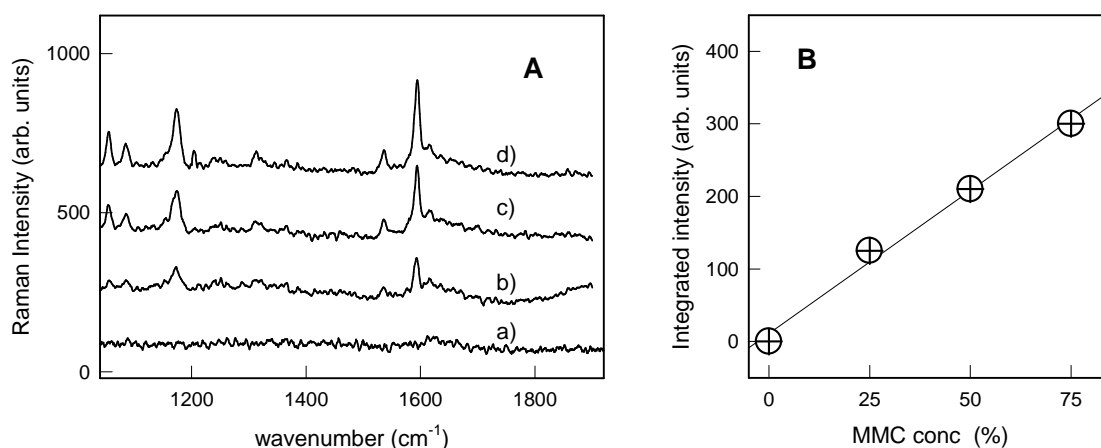


Figure 14: A) SERS spectra of colloidal suspensions of GNSs coated with MMC and HS-PEG₃₀₀₀-COOH obtained with different coating solutions: a) 100% HS-PEG₃₀₀₀-COOH; b) 25% MMC and 75% HS-PEG₃₀₀₀-COOH; c) 50% MMC and 50% HS-PEG₃₀₀₀-COOH; d) 75% MMC and 25% HS-PEG₃₀₀₀-COOH; B) integrated intensity of peak at 1595 cm⁻¹ as a function of MMC fraction in the coating mixtures.

The same set of measurements was repeated for the systems GNSs|MMC|HS-PEG₃₀₀₀-COOH (see Figure 14) and PAH@GNSs|MMC|HS-PEG₃₀₀₀-COOH (see Figure 15).

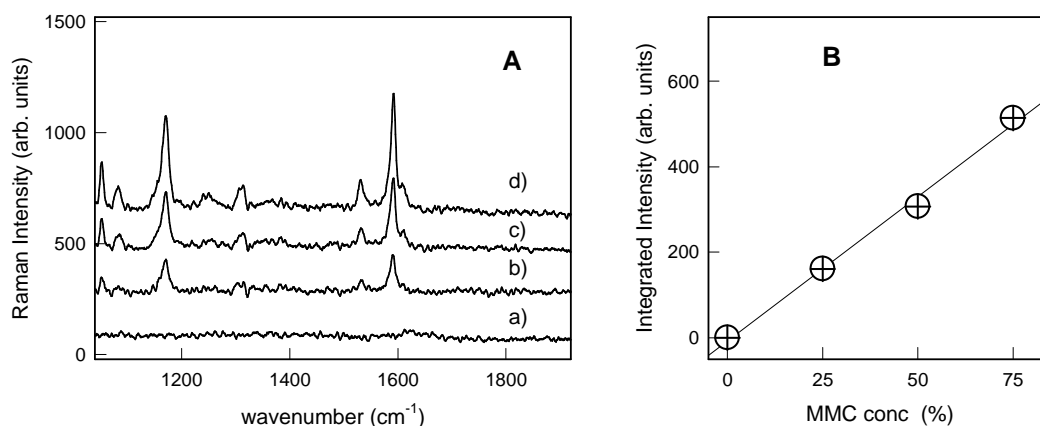


Figure 15: A) SERS spectra of colloidal suspensions of PAH@GNSs|MMC|HS-PEG₃₀₀₀-COOH obtained with different thiol coating solutions: a) 100% HS-PEG₃₀₀₀-COOH; b) 25% MMC and 75% HS-PEG₃₀₀₀-COOH; c) 50% MMC and 50% HS-PEG₃₀₀₀-COOH; d) 75% MMC and 25% HS-PEG₃₀₀₀-COOH; B) integrated intensity of peak at 1595 cm⁻¹ as a function of MMC fraction in the thiols coating mixtures.

As it can be clearly observed in all cases, the SERS signal increases linearly with the fraction of MMC used in the coating mixture, as already observed for the behaviour of long LSPR band red shift. The change of coating PEG and the final coating with the PAH layer does not affect the linear dependence of SERS label signal with the fraction of MMC

used in the mixture. These results point out once again that a controlled quantity of Raman reporter can be introduced in the coating shell, the intensity of the Raman response can be regulated on need, and it is possible to control the surface concentration of two different functions: the signalling (given by the Raman reporter) and the protecting one (given by PEG thiols).

3.2.3.6 BIOCOMPATIBILITY STUDIES

As recently demonstrated,⁴² pegilated GNSs are fairly biocompatible with SH-SY5Y cells at all concentrations used, while a decrease in viability is observed upon introduction of a external PAH layer. PAH, on the other side, is necessary to obtain cellular uptake by means of endocytosis. The explanation is that the negatively charged cell surface interacts with the positively charged PAH coated constructs,⁵³ promoting internalization of GNSs in cells, eventually leading to cytotoxicity caused by probable membrane disruption. Thus, we decided to check the biocompatibility limits for PAH@GNSs|MMC|HS-PEG₃₀₀₀-COOH system (50% MMC and 50% HS-PEG₃₀₀₀-COOH coating, mixture called “MMC 50%”), as we intended to further demonstrate the internalization of these PAH coated GNSs in SH-SY5Y cells by means of SERS mapping. Cells were incubated with concentrations of these SERS labels of 1.25, 2.5, 5.0, 10, 25, 50 and 100 µg Au/mL, using contact times with cells of 24 and 48 hours. The cell viability was then evaluated by the MTT assay. Results in terms of cell viability (% surviving fraction) are reported in Figure 16, showing that, as expected, a sensible reduction of viability is observed for high concentrations (>25 µg Au/mL) of PAH overcoated GNSs and mostly for long (48 hours) exposure times.

⁵³ E. Vogel; W. Kiefer; *Fresenius Journal of Analytical Chemistry*, **1998**, 361, 6-7, 628-30.

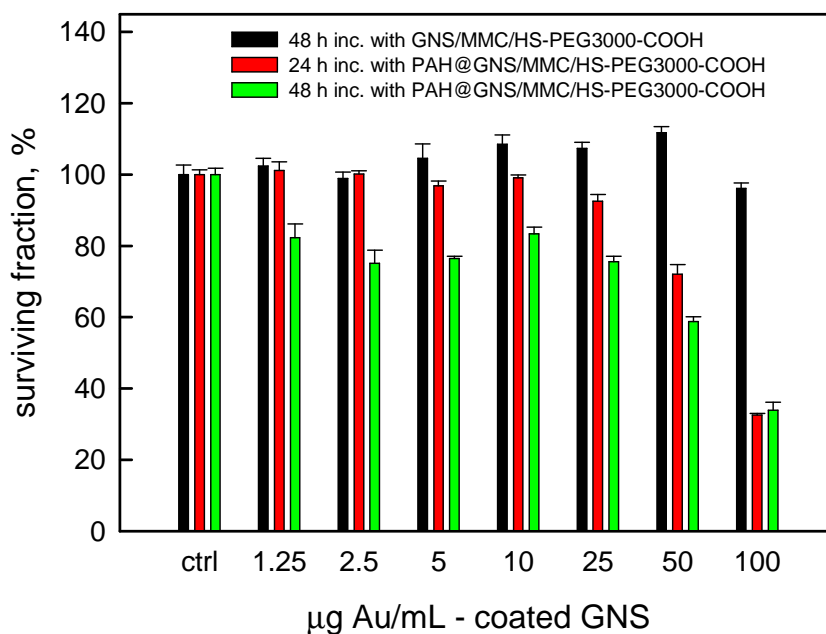


Figure 16: surviving SH-SY5Y fraction after: 48 hours treatment with GNSs|MMC(50%)|HS-PEG₃₀₀₀-COOH (50%) (black bars), 24 hours treatment with PAH@GNSs|MMC(50%)|HS-PEG₃₀₀₀-COOH(50%) (green bars), 48 hours treatment with PAH@GNSs|MMC(50%)|HS-PEG₃₀₀₀-COOH(50%) (red bars). Surviving fractions are given as a function of concentration of GNSs expressed as µg of added gold.

As a reference, an MTT test was performed incubating the cells for 48 hours with GNSs|MMC|HS-PEG₃₀₀₀-COOH (MMC 50%) system: in absence of PAH no reduction of viability was observed, suggesting the absence of internalization. Comparison of these data with those previously reported seems also to indicate that the substitution of a certain amount of HS-PEG₃₀₀₀-COOH on GNSs surface with MMC does not cause any change in the viability, as expected on the basis of the fact that cell damage is mainly caused by PAH promoted internalization.

3.2.3.7 SERS IMAGING IN CELLS

Imaging studies were carried out on the SH-SY5Y cells, exploiting the SERS signals offered by MMC in the coating layer of GNS. As a first experiment, we treated the cells with PAH@GNS/MMC/HS-PEG₃₀₀₀-COOH (MMC 50%) as representative of partially cytotoxic (and, as previously demonstrated, cell penetrating) GNS, and with GNS/MMC/HS-PEG₃₀₀₀-COOH (MMC 50%), as an example of completely biocompatible GNS unable to penetrate in cells. In both cases, incubation was done for 24 h contact time using a GNS concentration of 50 µg Au/mL. After contact with GNS, and washing

with phosphate-buffered saline (PBS) to remove all GNS not adhering to cells and not internalized, plated cells were fixed and prepared for microRaman measurements.

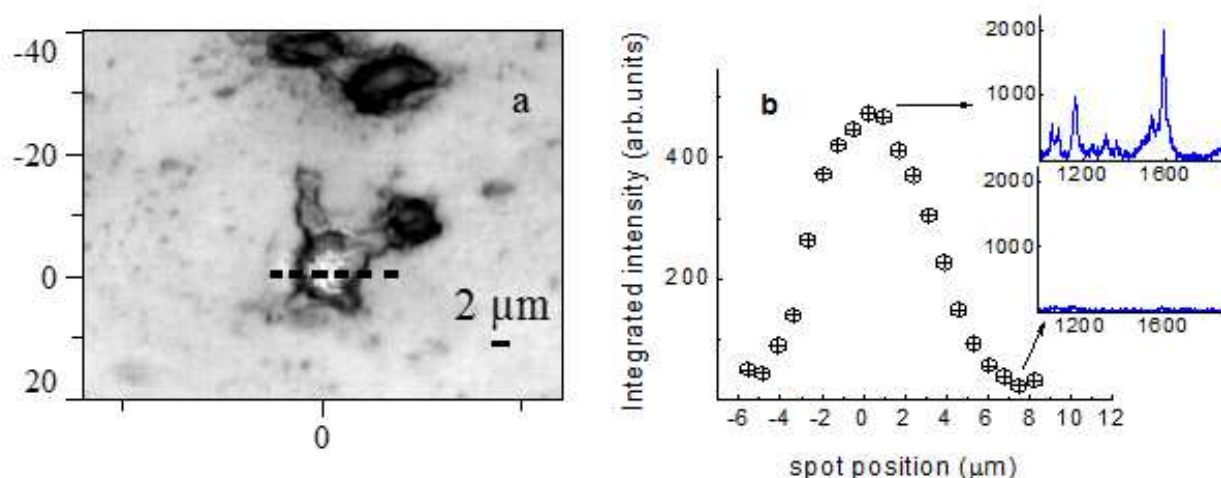


Figure 17: a) bright field image of SH-SY5Y cells incubated for 24 hours with 50 µg/mL of PAH@GNS/MMC/HS-PEG₃₀₀₀-COOH SERS label (MMC 50%); b) integrated intensity of SERS signal profile obtained using the Raman signal of MMC at 1595 cm⁻¹ scanning along the dashed line (length: 14.0 µm) evidenced in figure 17a. In the two insets, typical spectra obtained inside (upper spectrum) and outside (lower spectrum) the cell.

In the case of contact with the GNS/MMC/HS-PEG₃₀₀₀-COOH colloidal suspension (i.e. in absence of PAH final coating) no signal, except for the very weak, not enhanced Raman fingerprint of cell was observed. This means that there is no GNS internalization or binding to membrane: GNS are simply washed away with PBS and any SERS signal from the MMC cannot be found. A completely different behaviour is observed for the cell samples incubated with a 50 µg Au/mL colloidal suspension of PAH@GNS/MMC/HS-PEG₃₀₀₀-COOH (MMC 50%). A scanning of the Raman signal across the cell along the red line (Figure 17a) has been realized and from all the spectra, by best-fitting analyses, the integrated intensities of the MMC peak at 1595 cm⁻¹ has been extrapolated. The results are plotted in Figure 17b: the intensity is negligible outside the cell, while it is maximum inside of it. The FWHM of the Raman yield profile is about 5.5 µm and as the used laser spot has a diameter of 1.6 µm, one can conclude that the signal is present only inside the cell. The strength of the Raman signals, as well the morphology of cells, which appear smaller and roundish reflecting a cellular suffering condition as also indicated by a reduced viability at these concentrations of PAH coated GNS, suggested to repeat the experiment incubating the cells at a lower concentrations of SERS labels, in order to obtain an internalization process with a limited damage and, at the same time, allowing SERS measurements.

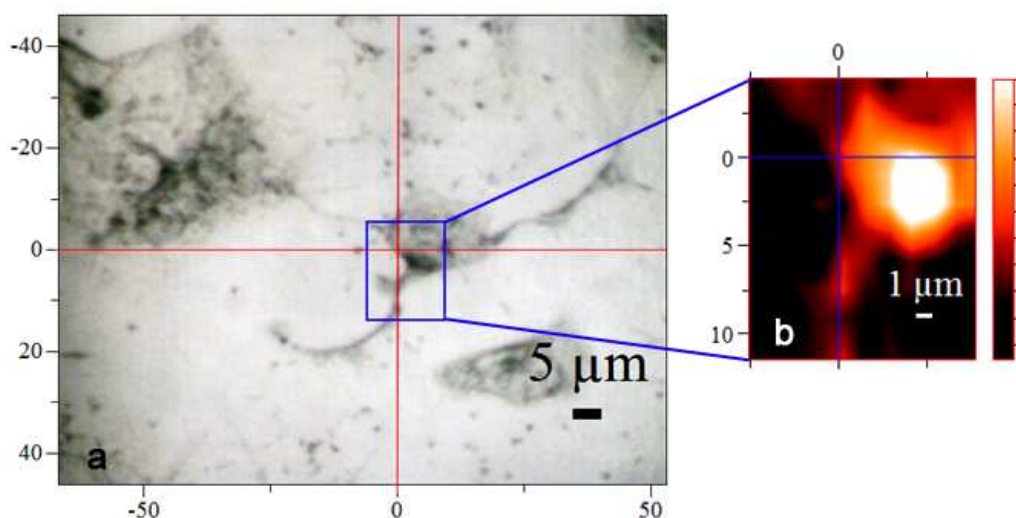


Figure 18: a) bright field image of SH-SY5Y cells incubated for 24 hours with 10 µg/mL of PAH@GNS/MMC/HS-PEG₃₀₀₀-COOH (MMC 50%) SERS label; b) SERS image obtained mapping the area of 14.0 x 17.4 µm² evidenced in the blue rectangle, using the Raman signal of MMC at 1595 cm⁻¹

Figure 18a reports a bright field image of a SH-SY5Y cell coming from a sample which was incubated for 24 hours with 10 µg Au/mL PAH@GNS/MMC/HS-PEG₃₀₀₀-COOH (MMC 50%), while in figure 6b the result of 2D Raman mapping of the region within an area of 14.0 x 17.4 µm² evidenced by the blue rectangle is shown. The colour map is derived again using the integrated intensities of the same Raman mode at 1595 cm⁻¹ described above. One can appreciate almost a perfect correspondence between optical and SERS images, which demonstrates internalization of SERS labels as well as their very good signal to noise ratio. In addition, also in this case the Raman features typical of the MMC structure are the lonely detected, as the coating shell is thick enough to avoid field effects to be exerted on the cellular surrounding components. Thus, only MMC SERS signature is observed, demonstrating that coated GNS have been uptaken by the cell, as the preparation was washed with PBS and all the nano-objects not adhering to the cells or not internalized were removed.

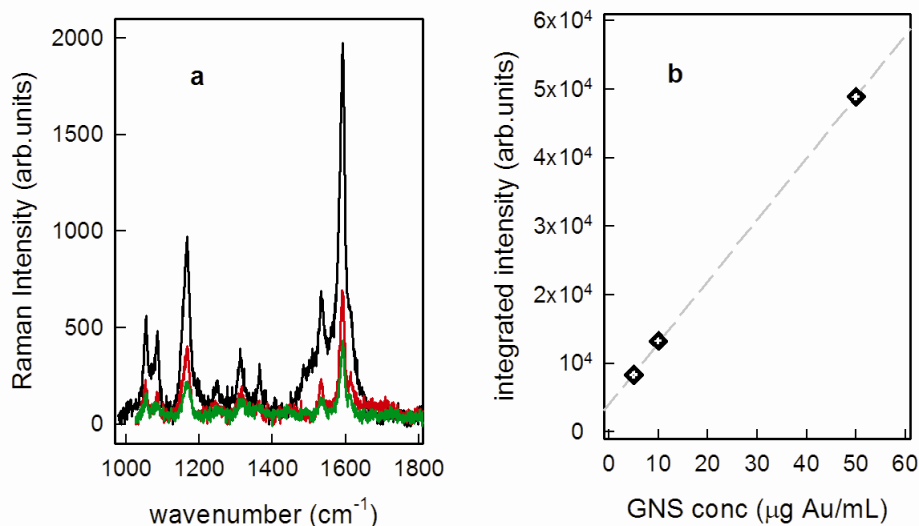


Figure 19: a) SERS spectra from SH-SY5Y cells incubated for 24 hours with 50 (black line), 10 (red) and 5 (green) $\mu\text{g/mL}$ of PAH@GNS/MMC/HS-PEG₃₀₀₀-COOH (MMC 50%); b) Integrated intensities of the Raman mode at 1595 cm^{-1} vs. the SERS label concentration (expressed as Au concentration) used in the incubation step: the dashed line is a guide to the eye.

Finally, we compared the SERS responses from SH-SY5Y cells samples incubated for 24 hours with respectively 5, 10 and 50 $\mu\text{g Au/mL}$ of the PAH@GNS/MMC/HS-PEG₃₀₀₀-COOH (MMC 50%) colloid. For these experiments we selected, for each sample, the region inside the cell exhibiting the most intense SERS response. In this region, the SERS signal was sampled over a small area and thus an average spectrum was derived. The results are reported in figure 19. The Raman yield scales almost perfectly with the SERS label concentration used during the incubation steps, and as reported in figure 19b, it is directly proportional to this concentration, confirming the reproducibility of the imaging experiments described and the reliability of the prepared SERS labels in the cellular environment.

3.2.3.8 CONCLUSION

A new family of SERS tags, based on thiols-coated GNSs was designed and carefully investigated by varying the composition of different coating mixtures of thiols, in which one of the component (MMC) acts as the Raman reporter, while the other (a PEG thiol) is used to impart to GNSs the stability and robustness needed in physiological conditions. Compositions of the coating mixtures were precisely controlled with a method here fully explained, based on simple spectro-photometric titrations exploiting LSPR shifts due to the changes of effective refractive index experienced by the GNSs upon substitution of

the labile LSB coating layer with the much stronger Au-S bond. The whole procedure allowed to modulate the intensity of the signal of the SERS labels, in the same time ensuring an overall nanoprobe stability: using the proper synthetic conditions, a precise concentration of the mixture components can be obtained in the surface coating layer. The further coating of negatively charged SERS devices with a positive PAH layer does not change their behaviour, while the functionalization with positive charges has effects on biocompatibility and cell penetrating abilities, confirming previous data⁴² found using two photon luminescence. Using concentrations and incubation times in which PAH terminated GNSs are still fairly biocompatible allowed the SERS mapping and visualization of cell morphology. Further developments directed to equip these kind of SERS nanotags with a recognition moiety, to achieve selectivity towards a specific cellular target are currently ongoing in our laboratory, and a prototype example will be described in the next chapter.

3.3 SERS TAGS AS THERANOSTIC DEVICES

3.3.1 INTRODUCTION

In addition to therapeutic purposes, nanomedicine formulations have in recent years also been increasingly employed for imaging applications. Moreover, paralleled by advances in chemistry, biology, pharmacy, nanotechnology, medicine and imaging, several different systems have been developed in the last decade in which disease diagnosis and therapy are combined. These so-called nano-theranostics contain both a therapeutic function (or agent) and an imaging function (or agent) within a single formulation, and they can be used for different purposes. Nanomedicine formulations have also been more and more used for imaging applications as well as, in recent years, for theranostic approaches. In the last years an explosive development of a variety of nanotechnology platforms to diagnose and treat cancer has been reported.^{1,2} Compared with traditional molecular-based contrast agents or therapeutic drugs, this new nanomedicine paradigm enables a highly integrated design that incorporates multiple functions, such as cell targeting or ultra-sensitive imaging and therapy, in one system. Multi-functional nanomedicine holds considerable promise as the next generation of medicine that enables the early detection of disease, simultaneous monitoring and treatment and targeted therapy with minimal toxicity. Tumor heterogeneity and adaptive resistance remain formidable challenges to therapy, and treatment of cancer requires the ability to address these two intrinsic properties of this complex disease. Theranostic was coined originally as a term to describe a treatment platform that combines a diagnostic test with targeted therapy based on the test result.³ Up to now, scientists define theranostic nanomedicine as an integrated nano-therapeutic system which can diagnose, deliver targeted therapy and monitor the response to therapy; this integration of capabilities is critical addressing the challenges of cancer heterogeneity and adaptation. As a platform technology, nanomedicine has the advantage of being able to target multiple tumor markers and deliver multiple agents simultaneously for synergy in addressing the challenges of cancer heterogeneity and adaptive resistance. In the following pages it will be shown the study of a prototype of theranostic device in which the imaging features are ensured by SERS.

¹ M. Ferrari; *Nat. Rev. Cancer*, **2005**, 5, 161-171.

² D. Peer; J.M. Karp; S. Hong; O.C. Farokhzad; R. Margalit; R. Langer; *Nat. Nanotechnol.*, **2007**, 751-760.

³ S. Warner; *Scientist*, **2004**, 18, 38-39.

The labeling of nanoparticles, such as nanorods, quantum dots and nanostars has been the subject of intensive research in the last decade.^{4,5,6} In the same years, Raman-based nanoparticles, as a class of emerging labels, have been attracting considerable attention.^{7,8,9,10} As it was already told, conventional Raman scattering spectroscopy is a rather insensitive technique for analyte detection, while the peculiar features of SERS made it increasingly investigated during past years for imaging purposes: as it has already described, SERS spectroscopy is a method by which the Raman efficiency can be greatly enhanced,¹¹ by adsorbing Raman-active molecules onto the surface of metal nanoparticles.^{12,13}

In the previous chapter it was described how a SERS tag can be realized having a peculiar attention in the rational control of the coating layer, in order to be able to tune the quantities of a Raman-active molecule, called Raman reporter, and of a protective agent (owing to the class of PEG thiols) used to impart biocompatibility. The SERS tag we have described in previous chapter, anyway, had, in principle, a very poor selectivity, as the ability to bind to cell membranes was essentially due to the aspecific interaction of positive PAH layer with the negatively charged cell membrane. Recalling the complete definition of SERS tag given at the beginning of Chapter 3.2, a typical SERS tag consists of a metal nanoparticle, a Raman reporter bound to the metal surface of the nanoparticle and a biocompatible layer around the metal nanoparticle and the Raman active molecule, and, desirably, a targeting fragment able to specifically recognize the desired target. Thus, one should add a targeting function in order to precisely address the device towards the desired target, for example a cancer cell. We decided to start to pursue this task in most simple way, i.e. using a thiolated PEG bringing, at the opposite end to the one having the thiol function, a reactive function, and we decided for a primary amine group, which can be easily reacted with a carboxylic function by formation of an amidic bond.

⁴ S.P. Mulvaney; M.D. Musick; C.D. Keating; M.J. Natan; *Langmuir*, **2003**, 19, 4784-4790.

⁵ L. He; M.D. Music; S.R. Nicewarner; F.G. Salinas; S.J. Benkovic; M.J. Natan; C.D. Keating; *Am. Chem. Soc.*, **2000**, 122, 9071-9077.

⁶ Z.F. Ma; S.F. Sui; *Angew Chem. Int. Ed.*, **2002**, 41, 2176-2179.

⁷ I. Khan; D. Cunningham; R.E. Littleford; D. Graham; W.E. Smith; D.W. McComb; *Anal. Chem.*, **2006**, 78, 224-230.

⁸ D.S. Grubisha; R.J. Lipert; H.Y. Park; J. Driskell; M.D. Porter; *Anal. Chem.*, **2003**, 75, 5936-5941.

⁹ W.E. Doering; S.M. Nie; *Anal. Chem.*, **2003**, 75, 6171-6177.

¹⁰ Y.C. Cao; R.C. Jin; J.M. Nam; C.S. Thaxton; C.A. Mirkin; *J. Am. Chem. Soc.*, **2003**, 125, 14, 676-683.

¹¹ E.C. Le Ru; M. Meyer; P.G. Etchegoin; *J. Phys. Chem. B*, **2006**, 110, 1944-1951.

¹² A. Campion; P. Kambhampati; *Chem. Soc. Rev.*, **1998**, 27, 241-248.

¹³ S. Chan; S. Kwon; T.W. Koo; L.P. Lee; A.A. Berlin; *Adv. Mater.*, **2003**, 15, 1595.



Figure 1: structure of the polyethylene glycol used in this work.

The idea is to coat nanostars once again with a mixture of two thiols: as we have described, coating can be sharply controlled using a method allowing to place on the GNS surface a precise amount of 7-Mercapto-4-methylcoumarin (MMC), the Raman reporter, mixed in precise molar ratios with HS-PEG₃₀₀₀-NH₂, to protect NPs from aggregation and impart biocompatibility. This controlled coating will ensure to give the GNS maximum stability and biocompatibility, coupled to a good SERS response, which intensity in principle can be modulated. Following this approach, the SERS device coated with this modular approach will expose to the environment primary amines ready to react. Subsequently, a target molecule able to recognize a predetermined target, avoiding or drastically reducing the possibility of forming non-specific bonds, must be bound on the surface of the mixed monolayer. We have chosen folic acid, since typically many types of tumor cells overexpress receptors for folic acid and folate. To make a few examples, among cell lines which overexpress folate receptors one can remember Hela cells,¹⁴ OV-167¹⁵ and GP-38.¹⁶ Moreover, folic acid has of two carboxylic functions, which can be coupled easily with amine termination of HS-PEG₃₀₀₀-NH₂. Following this approach, we will show that is possible to found a reliable and reproducible procedure for the synthesis of a SERS tag specific for cancer cells overexpressing folate receptors, based on our GNSs: in other words this device should be able to selectively bind to cancer cells and reveal them by SERS imaging.

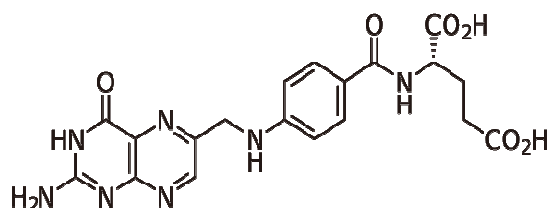


Figure 2: structure of the folic acid.

¹⁴ S. Wang; P.S. Low; *Journal of Controlled Release*, **1998**, 53, 1–3, 39–48.

¹⁵ R. Bhattacharya; C.R. Patra; A. Earla; S. Wang; A. Kataryaa; L. Lu; J.N. Kizhakkedathu; M.J. Yaszemski; P.R. Greipp; D. Mukhopadhyay; P. Mukherjee; *Nanomedicine*, **2007**, 3, 3, 224–238.

¹⁶ P.C. Elwood; *J. Biol. Chem.*, **1989**, 264, 14893-14901.

In addition to this, we must recall what already reported in Chapter 1.6: GNSs show an efficient photo-thermal effect, which can be used to kill bacteria cells. It sounds clear that the GNSs at the core of the described SERS tag, once bound to the cancer cells by means of the specific recognition of folate moieties by the proper receptors, can be irradiated with a nIR LASER source, and that the local hyperthermia generated by the described photo-thermal effect could be used to damage and possibly kill the cancer cells.

We will thus show that by combining the properties of SERS detection and imaging to the possibility of generating a localized heating (in order to damage the cells to which SERS tag is tied), the described system may be considered a prototype of theranostic device, based on the typical features of our GNSs, and easy to build and use thanks to the peculiar approach in the coating steps that we developed.

3.3.2 EXPERIMENTAL DETAIL: SYNTHESIS AND CHARACTERIZATION

3.3.2.1 MATERIALS AND INSTRUMENTATION

Reagents

Triton-X100 (laboratory grade), N-Dodecyl-N,N-dimethyl-3-ammonium-1-propanesulfonate (LSB) ($\geq 99.7\%$), Gold(III) chloride trihydrate ($\sim 30\text{wt}\%$ in HCl 99.99%), sodium borohydride (98%), L-ascorbic acid (AA) ($\geq 99\%$), silver nitrate (99.8%), PEG₂₀₀₀-SH (α -methoxy- ω -mercapto poly(ethylene glycol)), 7-mercapto-4-methylcoumarin $\geq 97\%$, poly(allylamine hydrochloride), ethanol ($\geq 99.8\%$), sodium hydroxide ($\geq 98\%$), nitric acid (1N), folic acid ($\geq 97\%$), triethylamine ($\geq 99\%$), N-(3-dimethylaminopropyl)-N-ethylcarbodiimide (EDC) ($\geq 99\%$), N-hydroxysuccinimide (98%), dimethylsulfoxide anhydrous (DMSO) ($\geq 99\%$), dimethylsulfoxide (DMSO) ($\geq 99\%$) N,N'-dicyclohexylcarbodiimide, 99% were all purchased from Sigma-Aldrich. HS-PEG₃₀₀₀-COOH (poly(ethylene glycol) 2-mercaptoethyl ether acetic acid) was purchased from RAPP polymere. Reagents were used as received. Glass cuvettes were standard optical glass cuvettes purchased from Hellman. All the preparation are made with bi-distilled water.

Instrumentation

UV-Vis Spectroscopy. UV UV-Vis spectra were taken on Cary 60 Varian, using poly(methyl methacrylate) cuvettes (optical path 1 cm) or quartz micro cuvette (optical path 1 cm). The wavelength scan range was 250-1100 nm.

Ultracentrifugation. Ultracentrifugation was carried out using the ultracentrifuge HermleZ366 with polypropylene 10mL tubes. The speed was 13000 rpm.

Dynamic light scattering measurements (DLS). The measurements were performed with a Zetasizer Nano-ZS90 (source: polarized He-Ne laser, 30 mW output power, vertically polarized).

ICP-OES (inductively coupled plasma optical emission spectroscopy) analysis. The Au concentration was then determined by ICP-OES on a ICP-OES OPTIMA 3000 Perkin Elmer instrument.

Transmission electron microscopy (TEM). TEM images were taken with Jeol LEM-1200 EX II instrument on 10 μ L colloidal solution drops, deposited on Copper grids (300 mesh) coated with a Parlodion membrane.

SERS measurements. SERS measurement were carried out at room temperature by using a Labram Dilor spectrometer equipped with an Olympus microscope HS BX40.

IR Spectroscopy. IR spectra were taken on FT-IR spectrum 100 Perkin Elmer.

Photothermal measurements. The photothermal effect was evaluated with Thermocam FLIR E40 using a L808P200 Thorlabs as a laser ($\lambda = 808$ nm).

3.3.2.2 GLASSWARE PRE-TREATMENT

All the glassware that come into contact with GNSs or sGNSs was always pre-treated before use: a wash in *aqua regia* for 30 minutes, then washed and filled with bi-distilled water and ultrasonicated for 3 minutes before discarding water. The bi-distilled water/ultrasound treatment was repeated 3 times. Then the glassware were dried in an oven for 1 hour at 140°C.

3.3.2.3 PREPARATION AND CHARACTERIZATION OF THERANOSTIC DEVICE

Synthesis of Gold Nanostar (GNSs)

The seeds were prepared in a vial by adding 5.0 mL of LSB aqueous solution (0.2 M) and 5.0 mL of HAuCl₄ aqueous solution ($5 \cdot 10^{-4}$ M). Subsequently, 600 μ L of an ice-cooled solution of NaBH₄ in water (0.01 M) were added to the pale yellow solution of AuCl₄⁻ obtained in the previous step. As prepared brown-orange solution was gently hand-shaken for a couple of second; this solution is efficient for the growth procedure of gold nanostar for 180 minutes from preparation if kept cold. The growth solution was prepared with 50 mL of LSB solution in water at the same concentration chosen for the seed solution (0.2 M), 1800 μ L of AgNO₃ in water (0.004 M), 50 mL of aqueous HAuCl₄

(0.001 M) and 820 μL of an aqueous L-ascorbic acid solution (0.078 M) mixed to obtain a colourless solution just after a few seconds of gentle mixing. Then 120 μL of seed solution were added to give a blue colloid, the intensity of which rapidly increased. The solution was allowed to react without agitation for 1 h. The colloidal suspensions were stored in the preparation flask, maintained in the dark and used within 7 days from preparation.

Synthesis of Shrunked Gold Nanostar (sGNSs)

The seeds were prepared in a vial by adding 5.0 mL of TritonX-100 aqueous solution (0.1 M) and 5.0 mL of HAuCl_4 aqueous solution (5×10^{-4} M). Subsequently, 600 μL of an ice-cooled solution of NaBH_4 in water (0.01 M) were added to the pale yellow solution of AuCl_4^- obtained in the previous step. As prepared brown-orange solution was gently hand-shaken for a couple of second; this solution is efficient for the growth procedure of gold nanostar for 180 minutes from preparation if kept cold. The growth solution was prepared with 50 mL of TritonX-100 solution in water at the same concentration chosen for the seed solution (0.1 M), 2500 μL of AgNO_3 in water (0.004 M), 50 mL of aqueous HAuCl_4 (5×10^{-4} M) and 2000 μL of an aqueous L-ascorbic acid solution (0.0788 M) mixed to obtain a colourless solution just after a few seconds of gentle mixing. Then 600 μL of seed solution were added to give a blue colloid, the intensity of which rapidly increased. The solution was allowed to react without agitation for 1 h. The colloidal suspensions were stored in the preparation flask, maintained in the dark and used within 7 days from preparation.

Spectrophotometric titration of GNSs

A 10 mL of GNSs as synthesized were titrated using 10^{-3} M stock solution in water of HS-PEG₃₀₀₀-NH₂. Titration were carried until no changes in LSPR bands positions were registered. After each addition the solution was gently hand-shaken for 3 minutes before record UV-Vis spectrum.

Coating of GNSs and sGNSs with mixed monolayers of thiols

To a chosen volume of GNSs or shrunked GNSs colloid (10-100 mL), a proper amount of stock solution of the chosen thiols were added in order to obtain the desired mixture

composition: the mixture containing 25% of MMC (in ethanol) and 75% of HS-PEG₃₀₀₀-NH₂ (in water) was obtained making the final concentration in the colloidal suspension 2.5×10^{-6} M in MMC and 7.5×10^{-6} M in HS-PEG₃₀₀₀-NH₂. These mixtures were stirred for one night at room temperature, then ultra-centrifuged (13000 rpm, 25°). The supernatant was discarded and the precipitate re-dissolved in the same starting volume (10-100 mL) of bi-distilled water. Ultracentrifugation/re-dissolutions cycle was repeated 3 times. UV-Vis of coated nano-objects was recorded. After the last ultracentrifugation, the pellets were re-dissolved in the amount of bi-distilled water calculated in order to obtain the desired concentration.

Reaction with targeting group: folic acid

A solution of folic acid 10^{-3} M in DMSO was prepared and were added: 600 μ L of EDC solution 0.1 M (in DMSO) and 600 μ L of NHS solution 0.1M (in DMSO). The mixture allowed to react for 1 h at room temperature. To this solution were added 9 mL of coated GNSs or sGNSs concentrated 10x. Then the acidity of the solution was adjusted pH to 8 value with triethylamine. The mixture was allowed to react for one night under gently stirring and then ultra-centrifuged (13000 rpm, 25°). The supernatant was discarded and the precipitate re-dissolved in the same starting volume (10-100 mL) of bi-distilled water at pH = 8. Ultracentrifugation/re-dissolutions cycle was repeated 2 times. UV-Vis and Z potential of nano-objects was recorded. After the last ultracentrifugation, the pellets were re-dissolved in the amount of bi-distilled water calculated in order to obtain the desired concentration.

Synthesis of aminated-folic acid

486 mg of anhydrous folic acid was first dissolved in 30 mL of anhydrous DMSO under nitrogen atmosphere. 140 mg of N-Hydroxysuccinimide (NHS) and 250 mg of dicyclohexylcarbodiimide (DCC) were then added under stirring. Subsequently, the reaction flask was shielded from light by using aluminum foil. The reaction was then allowed to proceed for 24 h at room temperature under nitrogen atmosphere. After that, the white precipitates, i.e. the by-product dicyclohexylurea, were removed by filtration. The yellow DMSO solution of the NHS-folate was then stored at -20 °C for further use. The above NHS-folate solution was slowly dropped, into a vial that contains the mixture of 60 mg of HS-PEG₃₀₀₀-NH₂ and 139 μ l of triethylamine in 5 mL of anhydrous DMSO at

room temperature. The reaction was allowed to proceed for another 24 h under nitrogen atmosphere and the vial was covered with aluminum foil during the whole course of the reaction. The final yellow reaction mixture was filtered and distilled. In order to functionalized 10 mL of GNSs, 44 μ L of this final product were used.

MTT assay

Mitochondrial enzymatic activity was estimated by the MTT [3-(4,5-dimethylthiazol-2-yl)-2,5-diphenyltetrazolium bromide] assay (Sigma-Aldrich, Milan, Italy). The day before the experiment, a cell suspension of 10000 cells/well in 100 μ L culture medium (DMEM+10%FBS+ 1x Pen Strep) was seeded into 96-well plates. After each treatment with GNSs or sGNSs (24 hours), the medium was substituted with 100 μ L of fresh medium and then 100 μ L of MTT (final concentration equal to 1 mg/ml in cold PBS) were added to each well. After incubation at 37°C for 4 hours, the formed purple formazan crystals were solubilized in 100 μ L of Lysis Buffer (20% sodium dodecyl sulfate in dimethylformamide/water 1:1) overnight at 37°C. Absorbance values were measured at 595 nm in a microplate reader (SynergyHT, BioTek Instruments, Inc.) and the results expressed as % with respect to the control value (100%). The data were subjected to analysis of variance (ANOVA) followed, when significant, by an appropriate post-hoc comparison test, as indicated in the figure legends. The differences were considered statistically significant when p values <0.05.

ICP-OES analysis

Samples of coated GNSs or sGNSs were analysed after the typical 3-cycles ultracentrifugation/re-dissolution purification to check the Au concentration. After the last ultracentrifugation, the pellet was treated with 1 mL *aqua regia* and after complete reaction (1 hour) with 2 mL bi-distilled water.

Evaluation of the photothermal effect

The evaluation of the photothermal effect was realized irradiating 100 μ L of the colloidal samples (GNSs or sGNSs) positioned into 96-well plates, with a laser (100 or 500 mW for 10 minutes); the variation of the temperature was registered with a thermocam.

Preparation of SERS tags for SERS measurement

100000 cells were seeded on a rounded glass (\varnothing 2 cm) positioned over a petri dish (\varnothing 35 mm), 2 mL of medium (DMEM+ 10%FBS+ 1x Pen Strep) were added and left overnight at 37°C. The next day the medium was substituted with 2 mL of the samples colloid (50 μ g/mL of GNSs or sGNSs in medium) and left 24 hours at 37°C, after this time the sample was washed two times with PBS (1x). Then the cells were immobilized with ethanol (70%) for 20 minutes and with formaldehyd (4%) for other 20 minutes. Then the cells were washed with PBS (1x) for two times and then the petri was filled with 2 mL of bi-distilled water.

Preparation of SERS tags for evaluation ad theranostic device

30000 cells were seeded on a rounded glass (\varnothing 1 cm) blocked with poly-L-lisina over a petri dish (\varnothing 35 mm), 2 mL of medium (DMEM+ 10%FBS+ 1x Pen Strep) were added and left overnight at 37°C. The next day the medium was substituted with 2 mL of the samples colloid (50 μ g/mL of GNSs or sGNSs in medium) and left 24 hours at 37°C, after this time the sample was washed two times with PBS (1x) and finally the petri was filled with 2 mL of PBS (1x). Then the rounded glass were irradiated with laser (500 mW – 10 minutes) and photographed through a traditional optical microscope.

3.3.3 RESULT AND DISCUSSION

3.3.3.1 NATIVE GNSs AND SHRUNKEN GNSs

GNSs were synthesized according to the described approach (Paragraph 1.3.1).¹⁷

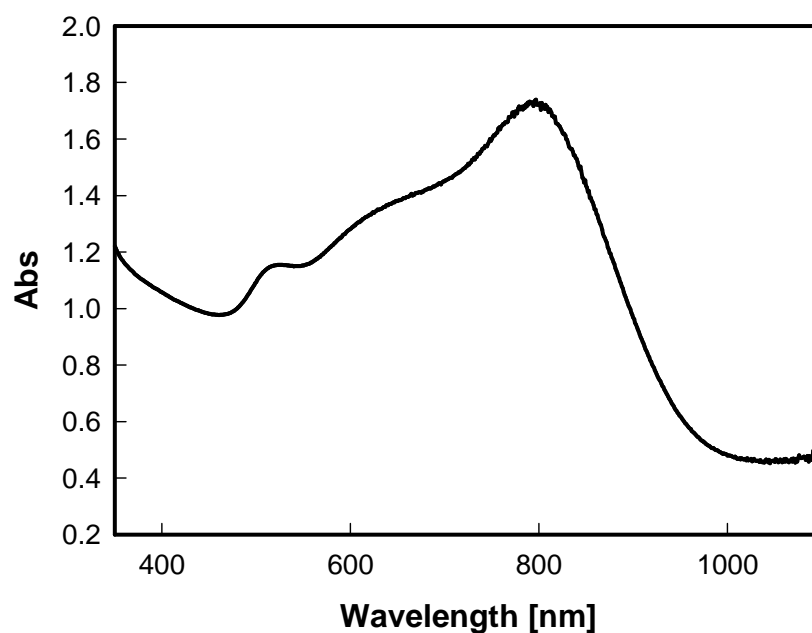


Figure 3: UV-Vis spectrum of a typical GNSs colloid used in this work.

As mentioned before, the spectrum reflects the composition of the nano-objects mixture, and can be quite precisely tuned changing the concentration of the ascorbic acid. In this part of the work the position of the long band was tuned close to 800 nm. On the other side, shrunked GNSs (sGNSs) were synthesized according to the described approach (Paragraph 1.3.2) following a modified seed growth method, based on TRITON-X100 surfactant.¹⁸ These reduced GNSs, as expected, feature two intense LSPR (see Figure 4): the “short” one and the “intermediate”, fuse together, resulting a band that fall in the 530 – 560 nm range, while a long band is shifted in UV-Vis region in the 900 – 1000 nm range. Thanks to this modified approach, nano-spheres and regular 5-branched gold nanostars with 2.8 AR were obtained, with the long band falling in the biological window,

¹⁷ A. Casu; E. Cabrini; A. Donà; A. Falqui; Y.D. Fernandez; C. Milanese; A. Taglietti; P. Pallavicini; *Chem. Eur. J.*, **2012**, 18, 9381-9390.

¹⁸ P. Pallavicini; A. Donà; A. Casu; G. Chirico; M. Collini; G. Dacarro; A. Falqui; C. Milanese; L. Sironi; A. Taglietti; *Chem. Commun.*, **2013**, 49, 6265-6267.

thus resulting with ideal features for biological applications that require internalization into the cells.

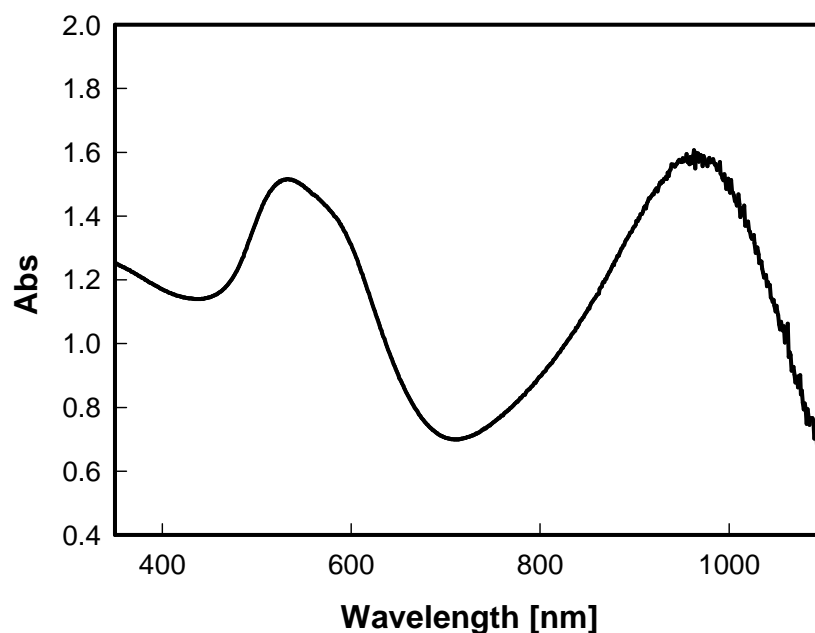


Figure 4: UV-Vis spectrum of a typical sGNSs colloid used in this work.

3.3.3.2 TITRATION OF GNSs AND sGNSs WITH HS-PEG₃₀₀₀-NH₂

After the purification of GNSs or sGNSs from excess of surfactant (LSB or TRITON-X100) a series of spectrophotometric titrations were performed in order to determine the amount of HS-PEG₃₀₀₀-NH₂ needed to obtain a molecular SAM on nanostar surface. The principle behind this approach was explained in detail in Paragraph 3.2.3.2. Briefly, it is based on the fact that the position of the long LSPR band of the colloid will shift upon the addition of thiol,^{19,20} since the effective refractive index experienced by the nano-objects will change by substituting the labile surfactant coating layer given by LSB or TRITON-X100 with the much stronger Au-S bond. As expected, the experimental UV-Vis data show that upon the addition of a stock solution of HS-PEG₃₀₀₀-NH₂ (10⁻³ M in water) the long LSPR peak of GNSs and sGNSs red-shifted. A representative titration of typical colloid of GNSs is reported in Figure 5 together with the titration profile which was

¹⁹ H. Yuan; C.G. Khoury; H. Hwang; C.M. Wilson; G.A. Grant; V.D. Tuan; *Nanotechnology*, **2012**, 23, 075102.

²⁰ E. Amato; Y.A.D. Fernandez; A. Taglietti; P. Pallavicini; L. Pasotti; L. Cucca; C. Milanese; P. Grisoli; C. Dacarro; J.M.F. Hechavarria; V. Necchi; *Langmuir*, **2011**, 27, 15, 9165–9173.

obtained, evidencing the plateau reached by the wavelength of the “long band” in one representative experiment.

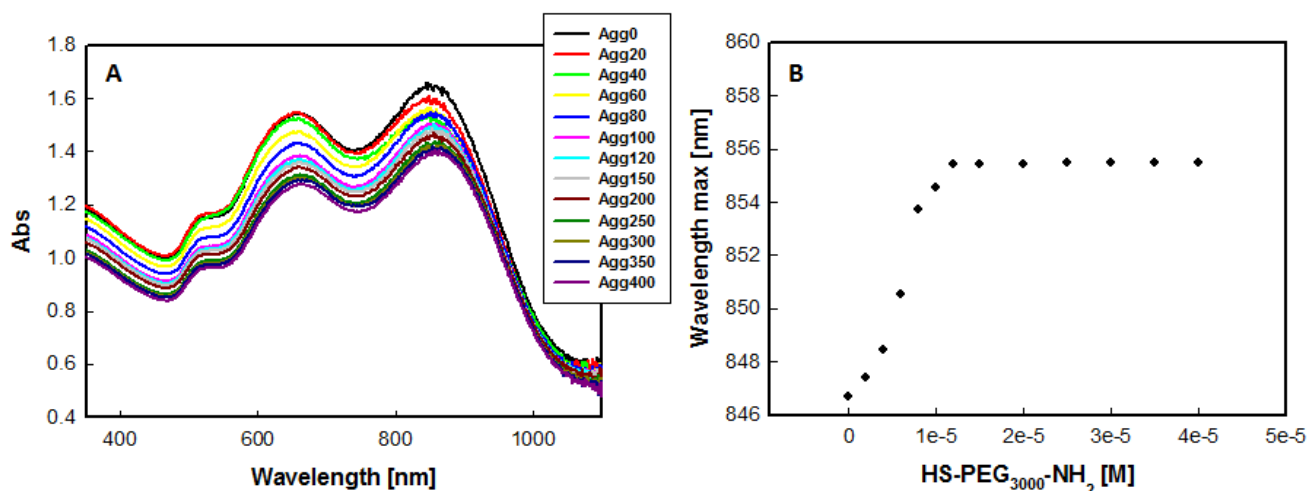


Figure 5: representative titration of a GNSs colloidal suspension with a stock solution of HS-PEG₃₀₀₀-NH₂: A) spectra obtained upon addition of increasing quantities of HS-PEG₃₀₀₀-NH₂; B) titration profile showing the red shift of the position of the long LSPR band as a function of HS-PEG₃₀₀₀-NH₂ added.

Table 1: concentration of HS-PEG₃₀₀₀-NH₂ observed in three different titration on GNSs.

	HS-PEG ₃₀₀₀ -NH ₂ [M]
Titration 1	1.1 x 10 ⁻⁵
Titration 2	1.0 x 10 ⁻⁵
Titration 3	1.3 x 10 ⁻⁵
Mean value	1.1 x 10⁻⁵
STD DEV	2 x 10 ⁻⁶

Table 1 evidences that all the three titrations gave similar value of concentration in solution necessary to give a monolayer on the GNSs colloid, i.e. $1.1 \times 10^{-5} \pm 2.0 \times 10^{-6}$ M. This value is in agreement with previous titrations of GNSs with other type of thiols (see Paragraph 3.2.3.3);²¹ this behavior has probably to be ascribed to the fact that thiols investigated are able access the same number of reactive sites on gold surface and that once bound occupy the same available space. The red-shift observed is between 6 and 9 nm, similar values were found with other PEGs thiols.

²¹ B. Bassi; A. Taglietti; P. Galinetto; N. Marchesi; A. Pascale; E. Cabrini; P. Pallavicini; G. Dacarro; *Nanotechnology*, **2016**, 27, 265301.

In a previous work regarding sGNSs²² we found the same value of concentration both for HS-PEG₃₀₀₀-NH₂ and 7-mercapto-4-methylcoumarin (MMC). This experimental data show that both GNSs and sGNSs need a similar value of thiol concentration in solution to give a coating monolayer on their colloid surfaces.

3.3.3.3 COATING WITH A MIXED MONOLAYER OF HS-PEG₃₀₀₀-NH₂ AND MMC

At this point, keeping an overall concentration of thiols of about 1.1×10^{-5} M (which was found to be the concentration needed to obtain a monolayer on the two standard colloids for each one of the used thiol), coating of colloidal suspensions with mixed monolayers was investigated. This approach (see Paragraph 3.2.3.3) imply that the red-shift observed for the long LSPR band ($\Delta\lambda_{\text{mix}}$) for a given composition, in presence of a random arrangement of the thiols on the surface, results to be a linear combination of the shifts observed for the formation of a monolayer with each single thiol ($\Delta\lambda_{\text{PEG}}$ and $\Delta\lambda_{\text{MMC}}$). Figure 6 shows the spectra of GNSs colloid coated with different mixed monolayer of MMC and HS-PEG₃₀₀₀-NH₂. Increasing percentage of MMC, as expected, causes a more pronounced red shift, which should be a linear combination of the shifts observed for the monolayers obtained with each single thiol.

²² S. Bertani; *Sintesi e separazione di nanostelle d'oro di dimensioni ridotte e morfologia controllata*; Master Thesis in Chemistry, **2014-2015**.

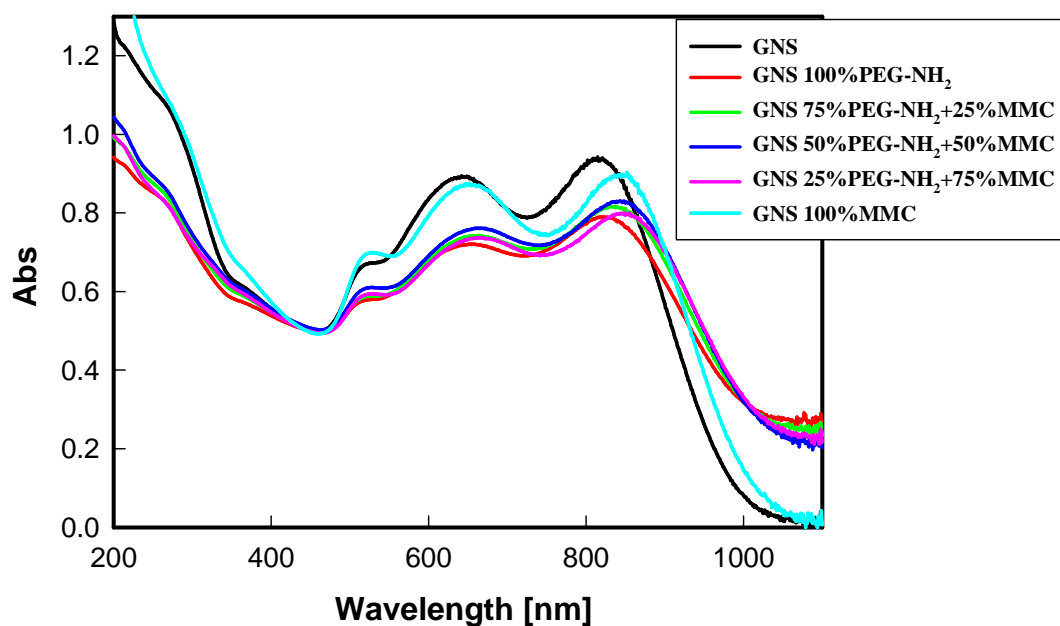


Figure 6: UV-Vis Spectra of colloids of GNSs coated with different mixed monolayer of MMC and HS-PEG₃₀₀₀-NH₂.

Table 2: summary of all red-shift recorded for different composition of the mixed monolayer on GNSs.

Monolayer Composition	Red-shift [nm]
100% HS-PEG ₃₀₀₀ -NH ₂	7.9
75% HS-PEG ₃₀₀₀ -NH ₂ +25% MMC	19.2
50% HS-PEG ₃₀₀₀ -NH ₂ +50% MMC	27.2
25% HS-PEG ₃₀₀₀ -NH ₂ +75% MMC	30.9
100% MMC	31.0

As already observed, in Table 2 we see that a more pronounced red-shift is found when coating with MMC that HS-PEG-NH₂, an evidence which is due to the fact that MMC is an aromatic molecule, able to undergo coupling between the molecular orbitals and the plasmonic states of colloid, and also from the fact that the hydrophobic character of MMC is expected to cause a sensible change of the effective refractive index experienced by the coated nanoparticles, when LSB is replaced by MMC, and this effects is known to influence the position and intensity of LSPR absorption.²³

²³ E. Vogel; W. Keifer; *Fresenius Journal of Analytical Chemistry*, **1998**, 361, 6-7, 628-630.

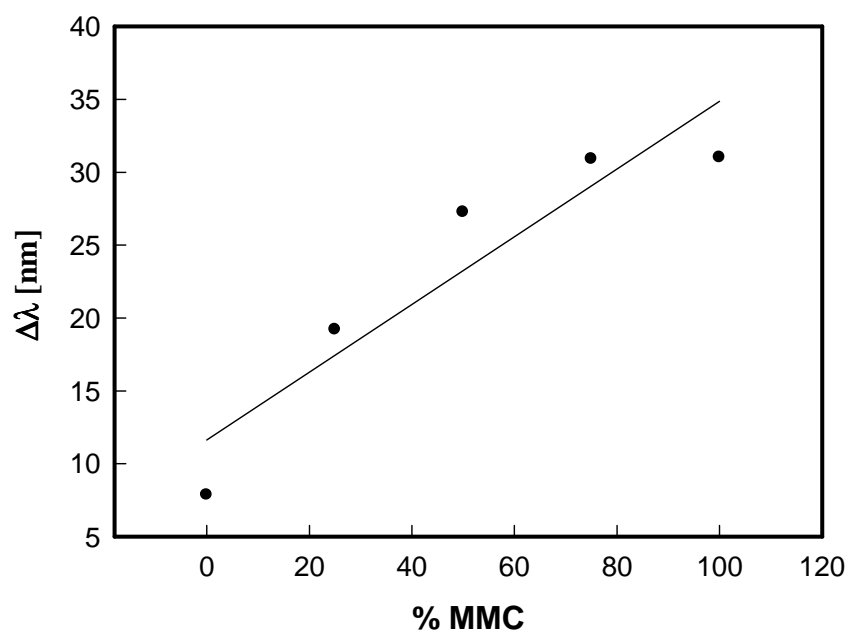


Figure 7: relationship between the percentage of MMC and the $\Delta\lambda_{\text{mix}}$ of the GNSs coated with different mixed monolayers of MMC and HS-PEG₃₀₀₀-NH₂.

Anyway, as can be observed from Figure 7, the relationship between the percentage of MMC and the $\Delta\lambda_{\text{mix}}$ of the long LSPR band of the GNSs coated with different mixed monolayers is not linear. There is an apparently striking difference with the data shown paragraph 3.2.3, where the linearity is observed. The reason, anyway, is quite simple: these are preliminary data, and the graph represents a single set of measure on a single set of GNSs with varying mixed monolayers concentrations. A single set of measures could be affected by several kind of systematic errors, due for example to some imprecision in the concentrations of the coating stock solutions or to the concentrations of the colloidal suspensions, which could affect all the results. Data reported in figure 8 and 9 of paragraph 3.2.3 resulted from the mean values obtained from at least 3 repeated measures of $\Delta\lambda_{\text{mix}}$, and the same number of titrations must be repeated here to confirm linearity. Anyway, there is no reason why linearity should not be confirmed, as it will be demonstrated also by the following paragraph. The same approach was in fact used on sGNSs, and even in this case spectra of samples coated with different compositions of mixed monolayer (with an overall concentration of $1.1 \cdot 10^{-5}$ M of thiols) on sGNSs were investigated (see Figure 8).

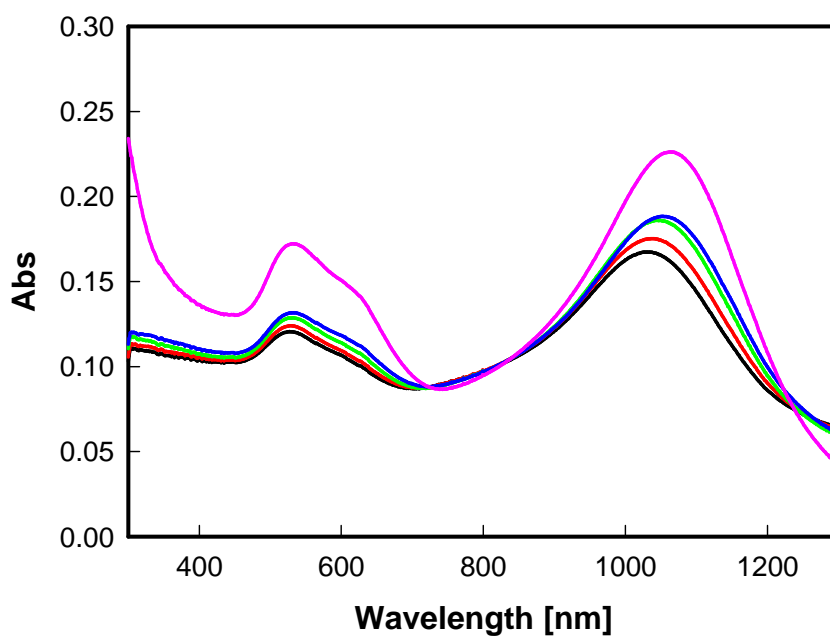


Figure 8: UV-Vis Spectra of colloids of shrunk GNSs coated with different mixed monolayer of MMC and HS-PEG₃₀₀₀-NH₂.

Figure 9 corroborates the linear relationship between the percentage of MMC and the $\Delta\lambda_{\text{mix}}$ of the long LSPR of the sGNSs coated with different mixed monolayers.

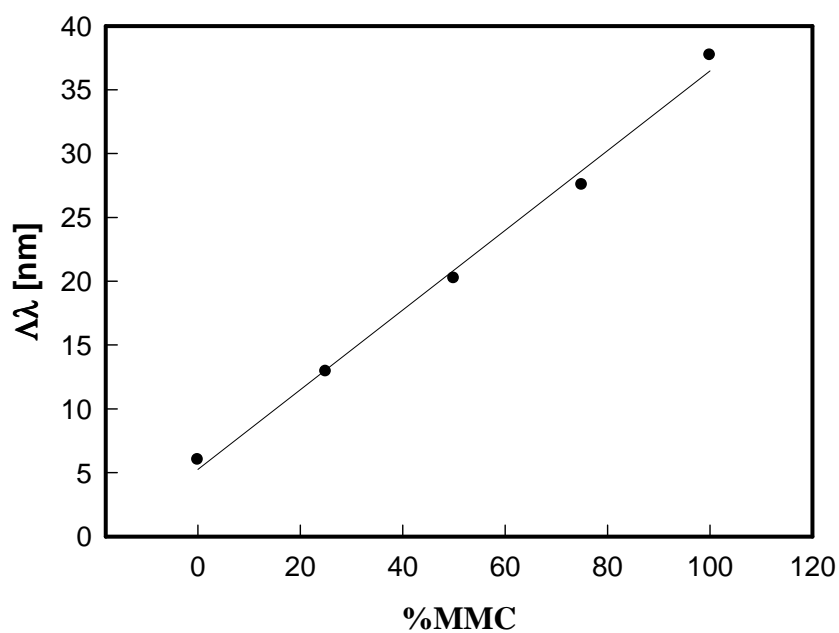


Figure 9: relationship between the percentage of MMC and the $\Delta\lambda_{\text{mix}}$ of the shrunk GNSs coated with different mixed monolayers of MMC and HS-PEG₃₀₀₀-NH₂.

Table 3: summary of all red-shift recorded for different composition of the mixed monolayer on sGNSs.

Monolayer Composition	Red-shift [nm]
100% HS-PEG ₃₀₀₀ -NH ₂	6.1
75% HS-PEG ₃₀₀₀ -NH ₂ +25% MMC	12.9
50% HS-PEG ₃₀₀₀ -NH ₂ +50% MMC	20.2
25% HS-PEG ₃₀₀₀ -NH ₂ +75% MMC	27.5
100% MMC	37.7

These results agree with recently published work on GNSs,²¹ confirming that the use of stock solutions of coating agents (MMC and HS-PEG₃₀₀₀-NH₂) having concentrations close to the value needed to full-coverage with a monolayer allow to control the composition on nanoparticles surface. By following the described method, a quite precise control of surface concentration of different functions can be obtained without knowing surface area of the colloidal suspension or the area occupied by the single coating molecule. In all the studied system, after the coating process, stability of the coated colloids were investigated by three cycles of centrifugation/solvent discharge/pellet uptake in bi-distilled water. In all cases, once again, except for the preparation of 100% MMC coatings, coated GNSs and sGNSs were found stable, and the LSPR's shape or position did not change after each centrifugation step. As mentioned in the Paragraph 3.3.1, the two types of nanostars (GNSs and sGNSs) were investigated as possible prototypes of SERS tags with a theranostic activity, using a coating made of 75% HS-PEG₃₀₀₀-NH₂ and 25% MMC, in order to guarantee the maximum stability of the system and an intense SERS signal of MMC, even if the presence of only 25% of HS-PEG₃₀₀₀-NH₂ can ensure enough stability.

3.3.3.4 RELATIONSHIP BETWEEN Z POTENTIAL AND PH

Nanoparticles in a colloidal suspension usually carry a charge. When the surface of the NPs is coated with a SAM, it may exhibit chemical groups that can ionize to produce a charged surface, which will depend on pH of the suspension. Quantification of the charge on the GNSs or sGNSs surface, for example, is an important feature, because it will determine many of the properties of the suspensions. The boundary between the edge of this solvated layer and bulk liquid is termed as the “shear plane” and the Z-potential is

defined like the electrostatic potential calculated in the shear plane. The value of the Z-potential is strictly related with the stability of the colloid and can provide informations about the coating. In order to study the variations of the charge of the monolayer in relation to the pH of the suspension, a Z-potential titration (pH between 3 and 9) was designed for: i) nanostars coated with 100% HS-PEG₃₀₀₀-NH₂ and ii) nanostars coated with 75% HS-PEG₃₀₀₀-NH₂ and 25% of MMC. Using this approach it will be possible to have precious information on the coatings of the nano-objects surfaces, and on their modification after the reactions which can be performed on the exposed functional groups. In Figure 10 (black dots), GNSs coated with 100% of HS-PEG₃₀₀₀-NH₂ showed high values of Z-potential at acidic pH (un-coated GNSs usually show a Z pot.=-15 mV). In these conditions, in fact, the surface of the nano-objects is positively charged as the terminal amino groups of the PEG are protonated, becoming -NH₃⁺.

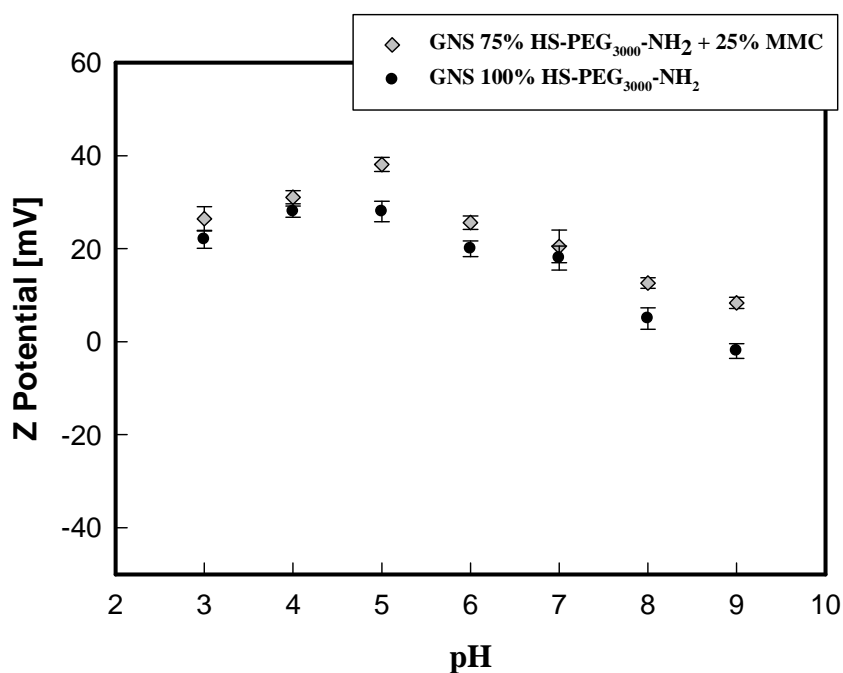


Figure 10: Z-potential titrations of GNSs coated with 100% HS-PEG₃₀₀₀-NH₂ (black dots) or with a mixed monolayer composed of 75% HS-PEG₃₀₀₀-NH₂ and 25% of MMC (grey diamonds).

Increasing the value of pH (obtained with small additions of NaOH) the Z-potential decreases as we deprotonate them back to free amino functions. Moreover, reaching basic pH values GNSs are not stable because the weak repulsions (surface are no more positively charged) fail to avoid aggregation and coagulation phenomena.

As shown in Figure 10 (grey diamonds) a similar trend is observed when moving to the GNSs coated with 75% HS-PEG₃₀₀₀-NH₂ and 25% of MMC: substitution of part of the PEG with MMC does not cause any sensible change in the behavior. The presence of a small amount of MMC in the monolayer does not affect the positive charge of the surface of GNSs at neutral/acidic pH.

Table 4: summary of the values of Z potential obtained for coated GNSs at different pH values.

	pH 3	pH 4	pH 5	pH 6	pH 7	pH 8	pH 9
GNSs 100% HS-PEG₃₀₀₀-NH₂ Z Potential (mV)	22.1±1.9	28.3±1.2	27.5±2.2	20.1±1.7	18.9±2.6	5.3±2.3	-2.1±1.6
GNSs 75% HS-PEG₃₀₀₀-NH₂ + 25% MMC Z Potential (mV)	26.4±2.6	31.1±1.4	38.1±1.5	18.7±1.4	20.5±3.5	12.6±1.1	8.3±1.1

The same experiment was performed on sGNSs, as shown in Figure 11. Even in this case, when the sGNSs were coated with 100% HS-PEG₃₀₀₀-NH₂, they showed the expected trend with pH variation, also in the case when the titration was repeated on sGNSs coated with 75% HS-PEG₃₀₀₀-NH₂ and 25% of MMC. Thus, even in this case, the presence of MMC in the mixed monolayer does not affect the charge of the surface of the nano-objects.

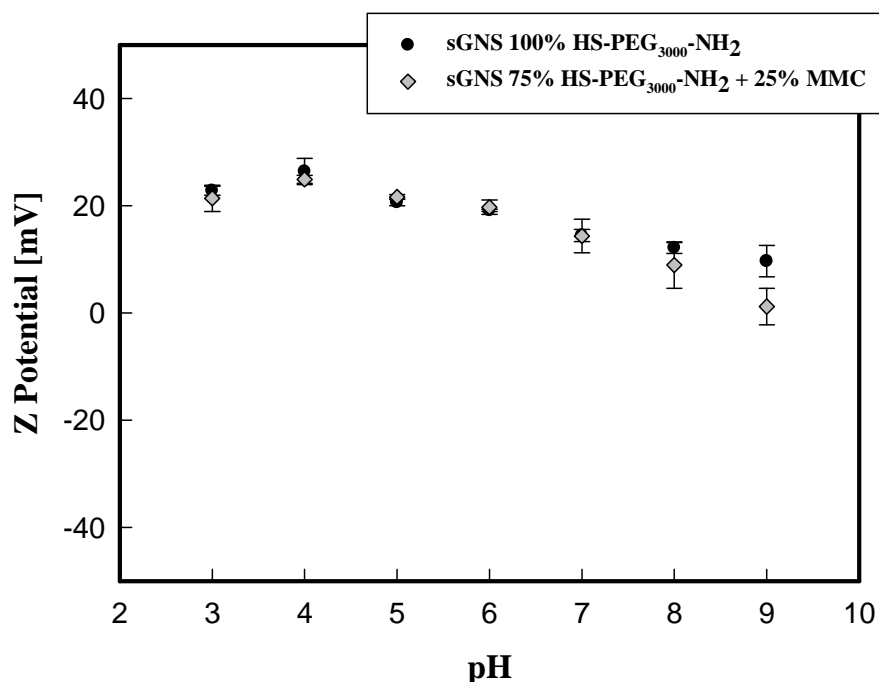


Figure 11: Z-potential titrations of sGNSs coated with 100% HS-PEG₃₀₀₀-NH₂ (black dots) or with a mixed monolayer composed of 75% HS-PEG₃₀₀₀-NH₂ and 25% of MMC (grey diamonds).

Table 5: summary of the values of Z potential obtained for coated sGNSs at different pH values.

	pH 3	pH 4	pH 5	pH 6	pH 7	pH 8	pH 9
sGNSs 100% HS-PEG₃₀₀₀-NH₂ Z Potential [mV]	22.8±0.8	26.4±2.4	20.6±0.6	19.1±0.2	14.4±1.1	12.1±1	9.6±2.9
sGNSs 75% HS-PEG₃₀₀₀-NH₂ + 25% MMC Z Potential [mV]	21.4±2.4	24.9±0.7	21.7±0.4	19.7±1.3	14.4±3.1	8.9±4.3	0.01±3.42

3.3.3.5 EVALUATION OF SERS RESPONSE OF THE SERS TAG

As can be noticed in Figure 12, the Raman spectrum of GNSs coated with a simple monolayer of HS-PEG₃₀₀₀-NH₂, as expected, does not show any peaks because PEG were not Raman active molecules. Instead, in the spectrum of GNSs coated with a mixed monolayer of 75% HS-PEG₃₀₀₀-NH₂ and 25% of MMC was visible the typical fingerprint of the Raman Reporter, in particular two peaks: the first one at 1600 cm⁻¹ related to symmetric stretching in plane of the C=C bond and the second one at 1170 cm⁻¹ related to the breathing of the benzenic ring.

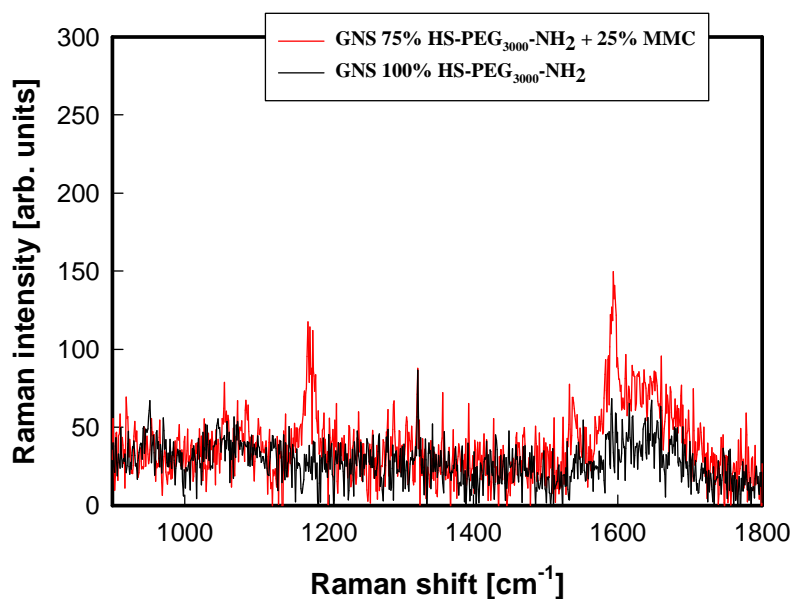


Figure 12: Raman spectra of GNSs coated with 100% HS-PEG₃₀₀₀-NH₂ (black line) and with 75% HS-PEG₃₀₀₀-NH₂ and 25% MMC (red line).

The same measurements were made on shranked GNSs coated with simple monolayer of HS-PEG₃₀₀₀-NH₂ and with 75% HS-PEG₃₀₀₀-NH₂ and 25% MMC. Even in this case, the first kind of coating does not show any peak, instead in the second type of coating exhibited the typical fingerprint of MMC, see Figure 13.

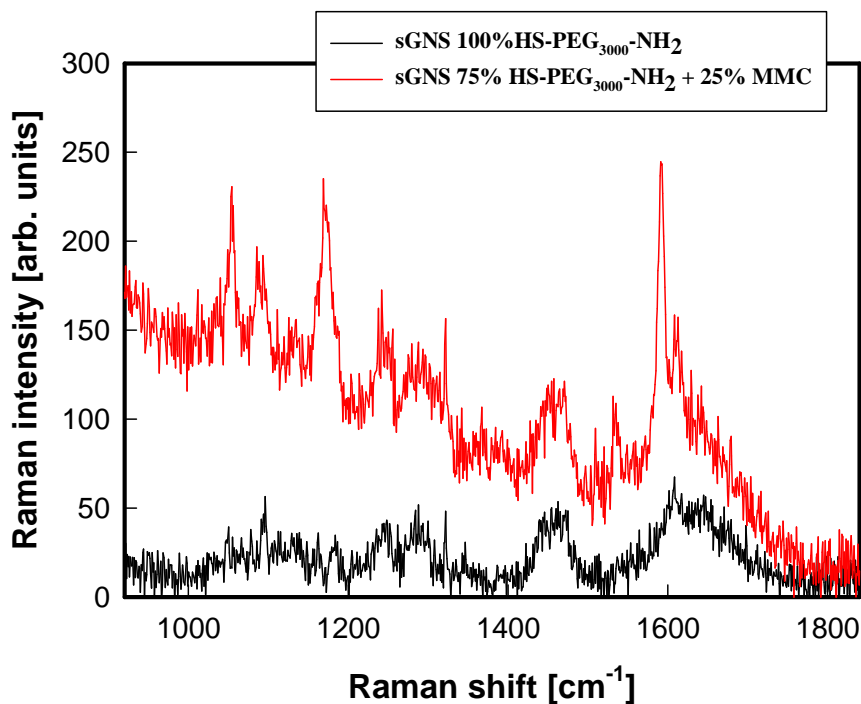


Figure 13: Raman spectra of shranked GNSs coated with 100% HS-PEG₃₀₀₀-NH₂ (black line) and with 75% HS-PEG₃₀₀₀-NH₂ and 25% MMC (red line).

Both spectra of GNSs or sGNSs coated with mixed monolayer (75% HS-PEG₃₀₀₀-NH₂ and 25% MMC) proved that MMC was bound on the surface of nano-objects with a strong Au-S bond and was possible to detect it through Raman spectroscopy thanks to the SERS effect carried out to nanostar. It is important to stressed that the simple Raman spectrum of a solution 2.75×10^{-6} M, in absence of nanoparticles was not significant.

3.3.3.6 FUNCTIONALIZATION WITH FOLIC ACID

The GNSs coated with the mixed monolayer composed of 75% HS-PEG₃₀₀₀-NH₂ and 25% MMC were further functionalized with folic acid. The folic acid was equipped to the GNSs by means of the coupling reactions described in paragraph 3.3.2.3. After this synthetic step, the colloid of coated nanostar was centrifuged twice, and the precipitate characterized by UV-Vis and DLS.

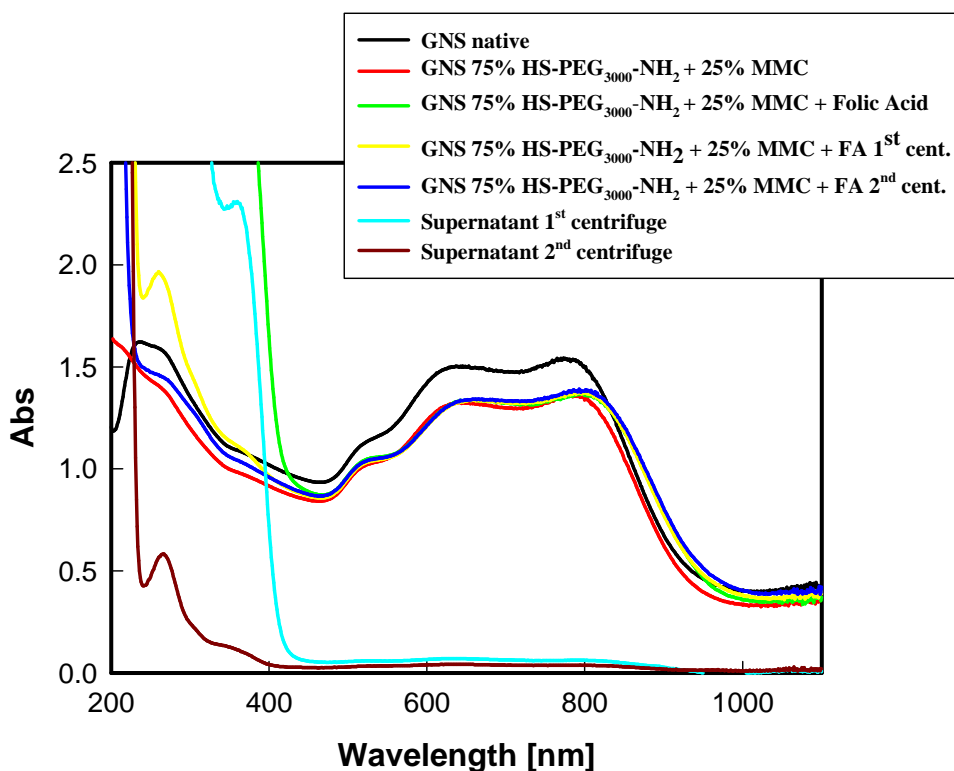


Figure 14: UV-Vis spectra coming from preparation of the GNSs SERS tag.

Figure 14 summarize the UV-Vis spectra obtained after each synthetic step of the preparation of the SERS tag. It is important to underline the presence of a red-shift of the long band of GNSs after the coupling reaction with folic acid (blue line), with an average value of 20(1) nm if compared to the native colloid (represented by the black line). This means that after coupling reaction the long band has shifted of more 10 nm whne compared to the GNSs coated with the mixed monolayer (red line). This further red shift does not change after two cycle of centrifugation, suggesting that it is due to the reaction of amino surface groups with folic acid, and that the amidic bond between them is, as expected, stable. Another indication of the success of the functionalization is the presence of two weak shoulders, which are due to typical absorption of folic acid, at 260 and 360 nm in the spectrum of the final SERS tag after two centrifugation steps. On the other side, we found presence of unbound folic acid in the supernatants after each centrifugation step.

The coated GNSs colloids were also characterized with DLS before and after the coupling reaction: the positive value of Z-potential = 29.6(2.6) mV (pH=5) found for the GNSs coated only with the mixed monolayer (a positive value due to the protonation of amino groups) became negative after the reaction with folic acid and two cycle of centrifugation, reaching a Z-potential of -26.6(1.2) mV (pH=8), indicating the presence of an anionic

function: as can be clearly seen in the structure of folic acid, there are two carboxylic functions. As only one of the two is expected to react for each molecule, the other one is reasonably able to impart a negative Z-potential to the nano-objects at neutral/basic pH.

The same coupling reaction with folic acid was performed with shrunk GNSs. Figure 15 summarizes all the UV-Vis spectra registered after each synthetic step of the preparation of the final SERS tag. Even in this case a red-shift of the long band of sGNSs occurred after the coupling reaction with folic acid, with an average value of 20(1) nm, and after two cycle of centrifugation both the shape and the position of the LSPR does not modify, confirming a firm binding of folic acid to amino groups brought on sGNSs. Another proof of this is once again the presence of the two weakshoulders at 260 and 360 nm in the spectrum of the final SERS tag.

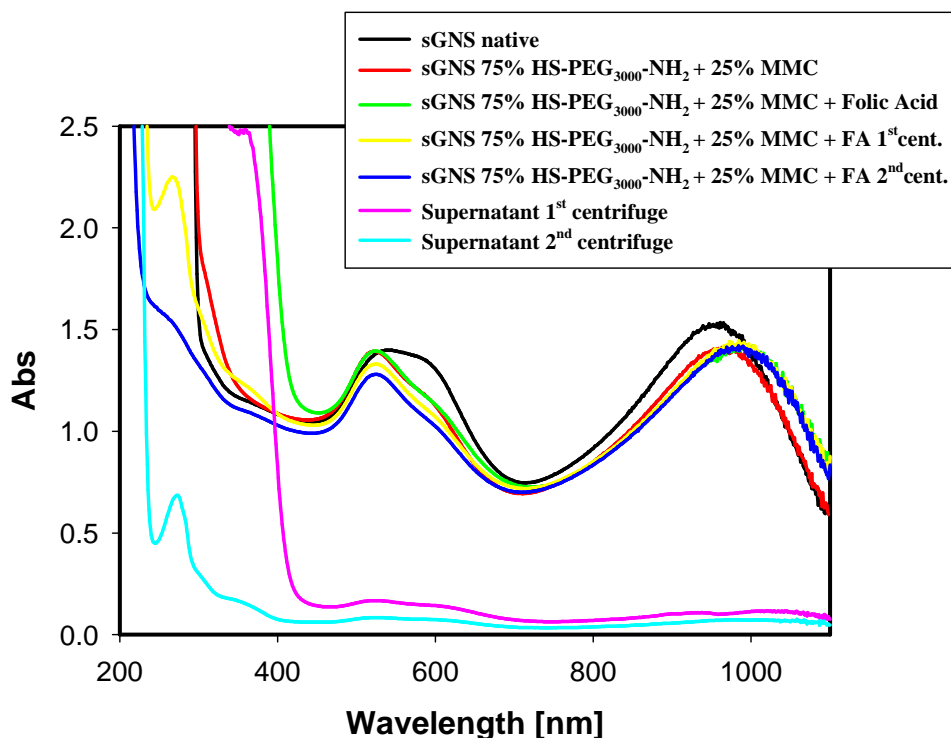


Figure 15: UV-Vis spectra about each step of the preparation of the sGNS SERS tag.

Even in this case the coated sGNSs colloid were characterized with DLS before and after the coupling reaction: the positive value of Z-potential = 30.8(3.6) mV (pH=5) of the GNSs coated only with the mixed monolayer (thanks to the protonated aminic group of the PEG) became negative after the reaction with folic acid and two cycle of centrifugation, Z-

potential = -28.4(1.0) mV (pH=8), thanks to a carboxylic group present on the targeting group.

3.3.3.7 RELATIONSHIP BETWEEN Z POTENTIAL AND pH OF FINAL SERS TAG

To confirm the functionalization with folic acid, a study of the relationship between Z-potential and pH was performed on GNSs SERS tags and sGNSs SERS tags.

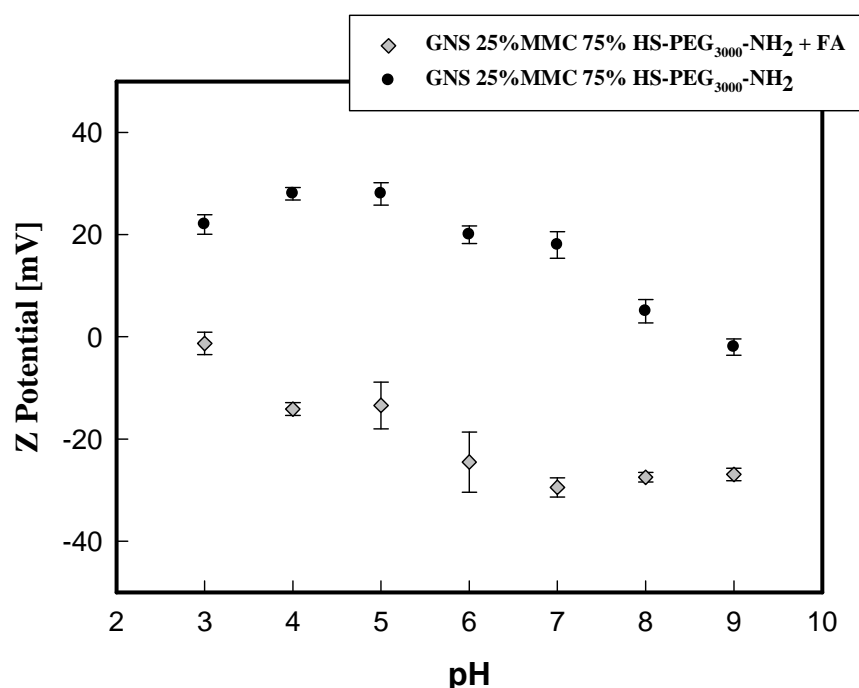


Figure 16: Z-potential titrations of GNSs coated with 25% MMC 75% HS-PEG₃₀₀₀-NH₂ (black dots) or with 25% MMC 75% HS-PEG₃₀₀₀-NH₂ and folic acid (grey diamonds).

Table 6: summary of the values of Z-potential of coated GNSs at different pH.

	pH 3	pH 4	pH 5	pH 6	pH 7	pH 8	pH 9
Z-potential [mV]	-1.3±2.1	-14.1±1.2	-13.4±4.5	-27.9±5.9	-29.5±1.9	-27.5±0.9	-26.9±1.2

In Figure 16 are reported two titration of GNSs coated with: i) 25% MMC - 75% HS-PEG₃₀₀₀-NH₂ (black dots) and with ii) 25% MMC - 75% HS-PEG₃₀₀₀-NH₂ coupled to folic acid, i.e. the final SERS tag (grey diamonds).

The final GNSs SERS tag shows, as expected, weakly positive values of Z-potential at acidic pH (as the exposed carboxylic functions of folic acid are in the acidic form, with a

pK_a placed around 4). With the increase of pH values, the Z-potential decreases to negative values, as an effect of the deprotonation of the carboxylic groups. The evident difference between the two titrations represents in the graph confirms that the coupling reaction has happened, changing the chemical groups exposed by the surface: from the amino groups to one of the two $-COOH$ groups of folic acid (the other one being involved in the formation of amidic bond). The same behavior is observed for the SERS tag obtained from sGNSs, as evidenced by the titrations presented in Figure 17.

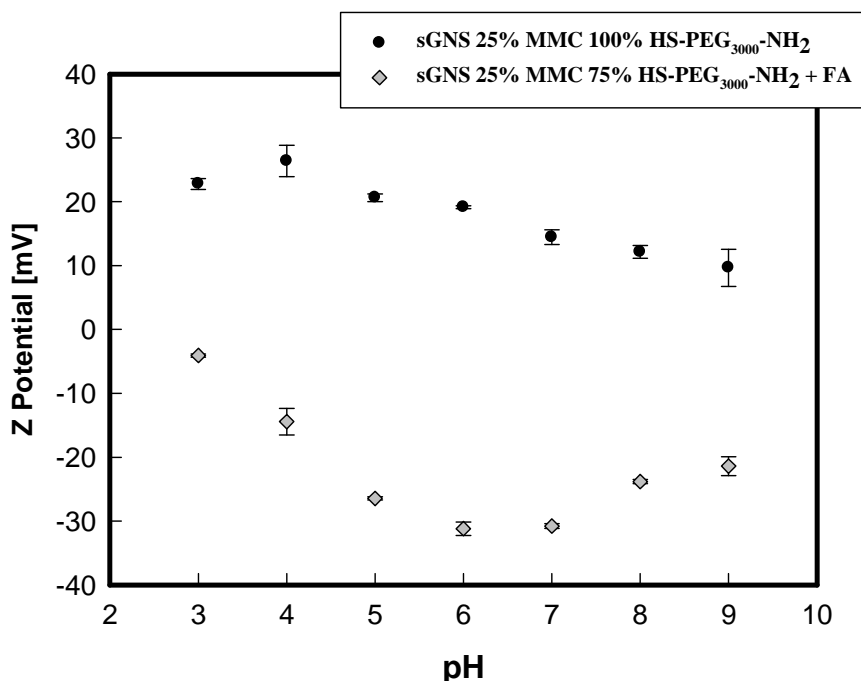


Figure 17: titrations of shranked GNSs coated with 25% MMC 75% HS-PEG₃₀₀₀-NH₂ (black dots) or with 25% MMC 75% HS-PEG₃₀₀₀-NH₂ and folic acid (grey diamonds).

Table 7: summary of the values of Z-potential of coated sGNSs at different pH.

	pH 3	pH 4	pH 5	pH 6	pH 7	pH 8	pH 9
Z-potential [mV]	-4.1±0.2	-14.4±2.1	-26.4±0.2	-31.2±1.2	-30.8±0.3	-23.8±0.3	-21.3±1.4

3.3.3.8 FT-IR CHARACTERIZATION

At this point, the presence of conjugated folic acid on nanoparticles surfaces is suggested by: i) the red-shift of the long LSPR band after coupling reaction and two cycle of centrifugation, ii) the presence of the two typical bands of folic acid (260 and 360 nm) in the spectrum of the final SERS tag and iii) the change of the Z-potential from positive to negative values after the functionalization and two cycle of centrifugation. In order to obtain an additional proof, FT-IR spectra were taken for: bulk folic acid, bulk HS-PEG₃₀₀₀-NH₂, GNSs coated with 100% HS-PEG₃₀₀₀-NH₂ and GNSs coated with 100% HS-PEG₃₀₀₀-NH₂ reacted with folic acid.

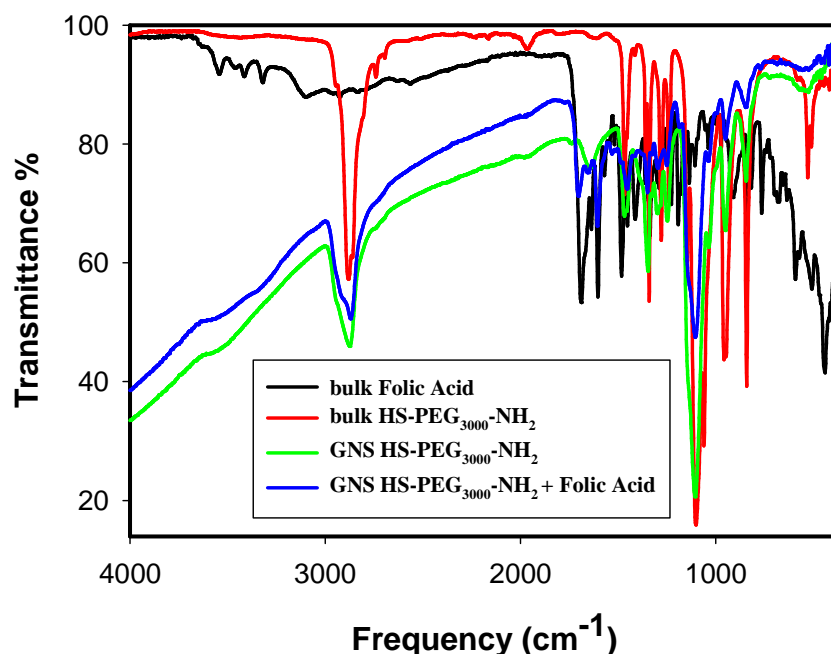


Figure 18: FT-IR spectra of: bulk folic acid (black line), bulk HS-PEG₃₀₀₀-NH₂ (red line), GNSs HS-PEG₃₀₀₀-NH₂ (green line) and bulk HS-PEG₃₀₀₀-NH₂ and folic acid (blue line).

A comparison between FT-IR spectra of this four sample was studied (see Figure 18). The peaks that fall at 1700 cm⁻¹ and 1608 cm⁻¹ can be ascribed respectively to the stretching of the C=O bond and the bending of N-H from an amide group. These peaks could be ascribed both to amide already present in the structure of folic acid or from the one coming from the coupling reaction, but in any case confirms the presence of folic acid on the nano-device.²⁴

²⁴ H.X. Xia; X.Q. Yang; J.T. Song; J. Chen; M.Z. Zhang; D.M. Yan; L. Zhang; M.Y. Quin; L.Y. Bai; Y.D Zhao; Z.Y. Ma; *J. Mater. Chem. B*, **2014**, 2, 1945-1953.

In Figure 19 is possible to appreciate a detail of the spectral zone containing these peaks.

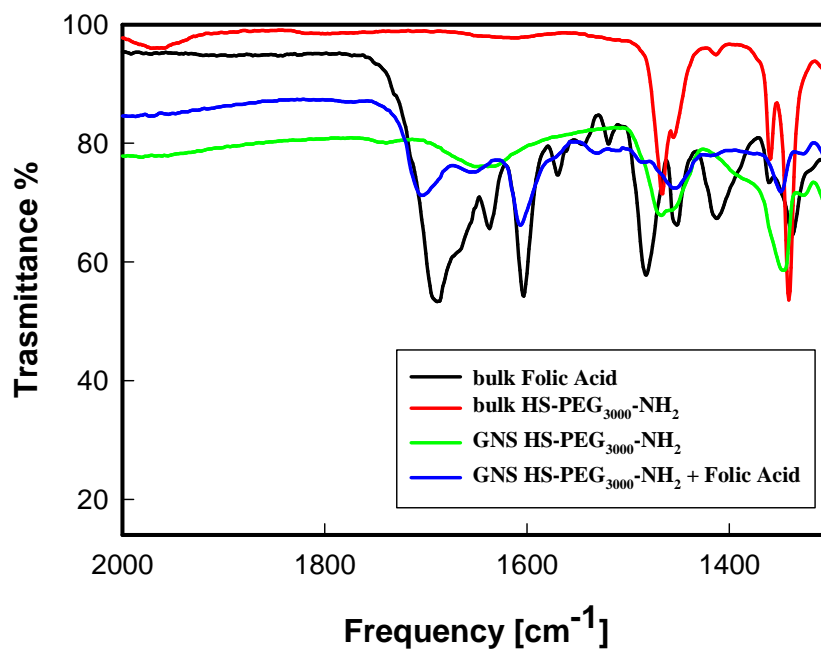


Figure 19: a detail of spectra reported in Figure 18.

3.3.3.9 SERS RESPONSE AFTER FUNCTIONALIZATION WITH FOLIC ACID

After functionalization with folic acid the SERS response was measured again.

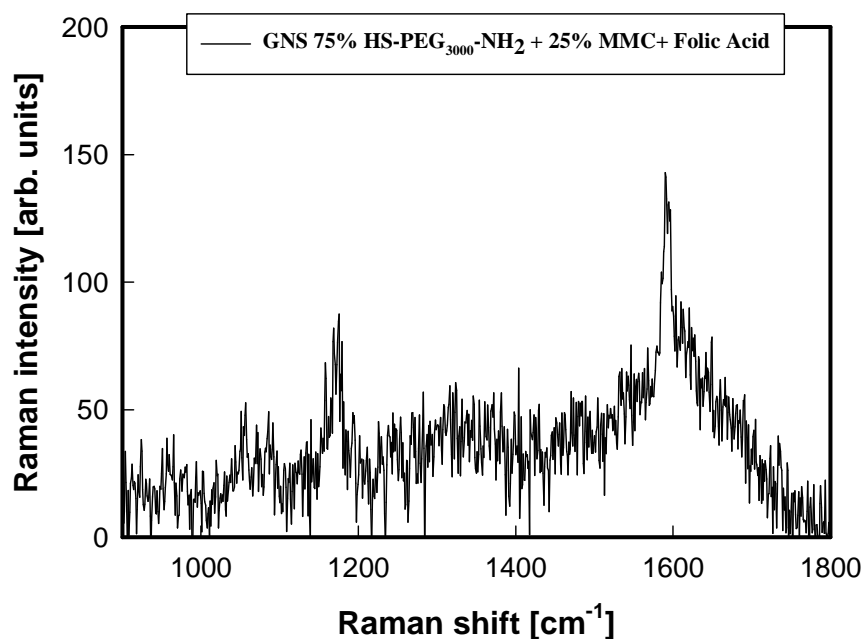


Figure 20: Raman spectrum of final GNSs SERS tag (75% HS-PEG₃₀₀₀-NH₂ 25% MMC and folic acid).

The Figure 20 show the Raman spectrum of the final SERS tag realized with GNSs coated with 75% HS-PEG₃₀₀₀-NH₂ 25% MMC and conjugated with folic acid, as can be observed the two typical peaks of MMC at 1600 cm⁻¹ and at 1170 cm⁻¹ are still present.

The Figure 21 shown the Raman spectrum of the final SERS tag realized with sGNSs coated with 75% HS-PEG₃₀₀₀-NH₂ 25% MMC and conjugated with folic acid: also in this case the two typical peaks of the Raman reporter at 1600 cm⁻¹ and at 1170 cm⁻¹ can be observed.

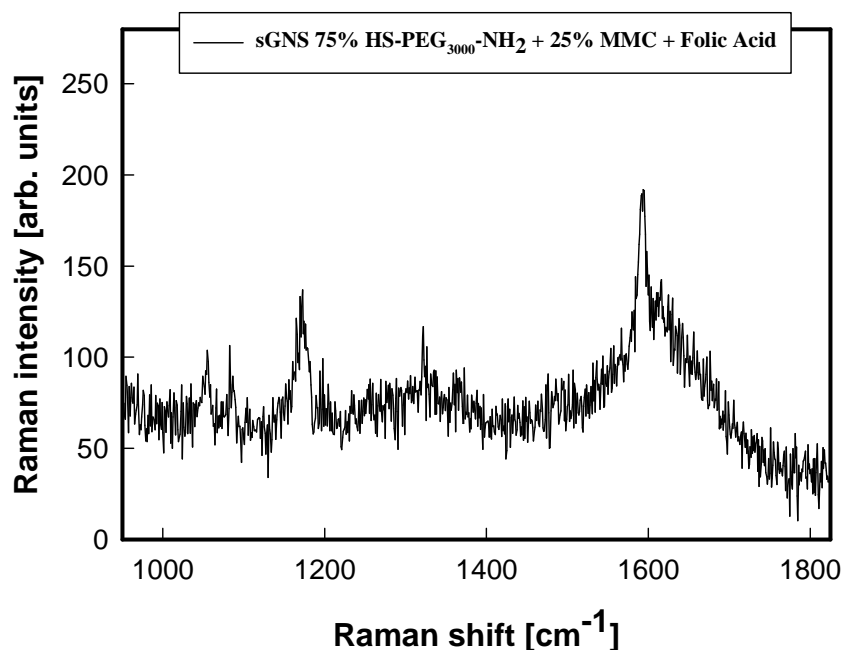


Figure 21: Raman spectrum of final shranked GNSs SERS tag (75% HS-PEG₃₀₀₀-NH₂ 25% MMC and folic acid).

Thus, in both cases, the typical response of Raman signal of MMC was found unaltered, showing that the reaction steps used for the further functionalization with folic acid of the surface of nano-devices did not affect the SERS performance of the SERS tags.

3.3.3.10 TEM CHARACTERIZATION OF sGNS SERS TAGS

In a previous work²² sGNSs coated with PEG₂₀₀₀-SH were characterized by Transmission Electron Microscopy (TEM), as can be seen in Figure 22A. One can notice the presence of a majority of regular reduced nanostars and a minor quantity of spheres.

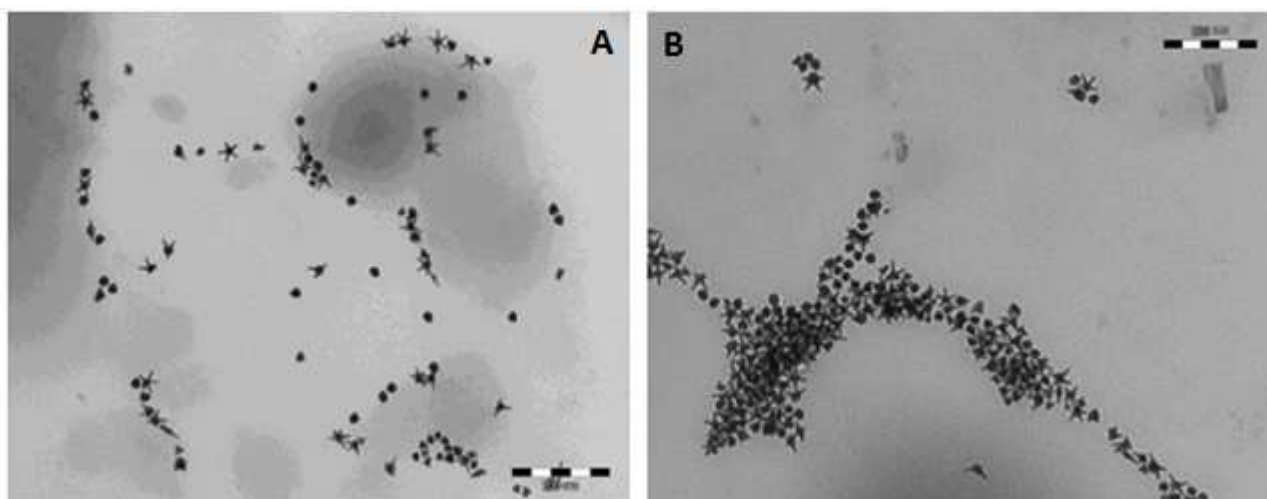


Figure 22: TEM images of: A) shrunken GNSs coated with PEG₂₀₀₀-SH and B) shrunken GNS coated with 75% HS-PEG₃₀₀₀-NH₂ 25% MMC and folic acid. Scale bar: 200 nm.

A sample of sGNS based SERS tags (sGNSs coated with 75% HS-PEG₃₀₀₀-NH₂ 25% MMC and conjugated with folic acid) were analyzed by TEM. As can be seen in Figure 22B, the morphology of the colloid is identical to the one observed in image 22A, so we can state that all the synthetic steps performed on the surface of the nano-objects did not affect the morphology and the size distribution of the colloid.

3.3.3.11 AN ALTERNATIVE PATHWAY: REACTION BETWEEN HS-PEG-NH₂ AND FOLIC ACID FOR SUBSEQUENT FUNCTIONALIZATION OF GNSs

As an alternative pathway to the reaction between NH₂ groups placed on GNSs and folic acid, we decided to try a similar reaction in solution between HS-PEG₃₀₀₀-NH₂ and folic acid, in order to use the resulting molecule to coat the nanostars. The reaction is described in Paragraph 3.3.2.3. NMR spectrum of the product is reported in Figure 23.

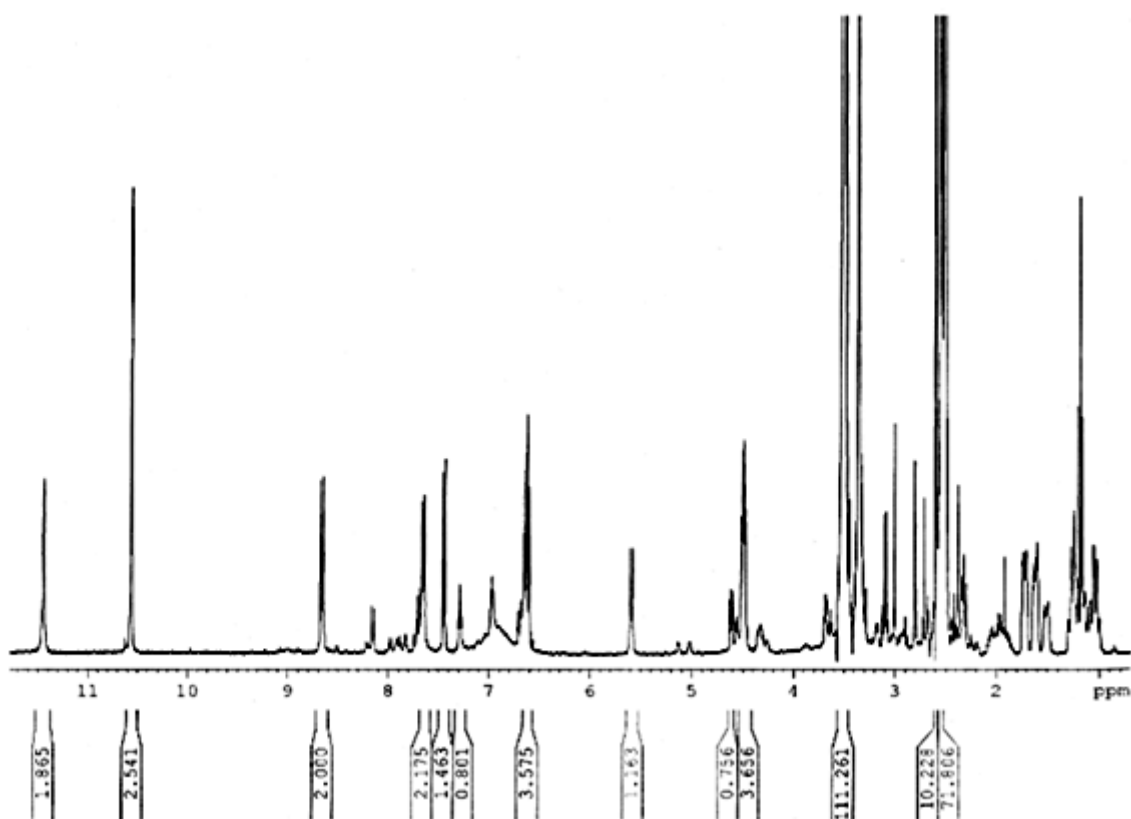


Figure 23: NMR spectrum of HS-PEG₃₀₀₀-NH₂ bonded to folic acid.

As can be seen from the spectrum, two signals at 6.97 and 7.20 ppm suggest the existence of two different amidic functions, generated between the aminic group of the PEG and the two carboxylic groups of the folic acid, which thus seem to show a similar reactivity. At 3.5 ppm it can be observed the signal of the PEG's strand. Unfortunately, this alternative path has turned out to be ineffective, as treatment of nanostars with the obtained molecule produced unstable colloidal suspensions: this fact can be probably ascribed to the incomplete purification of the reaction products. Anyway the NMR spectra showed us that both carboxylic groups of the folic acid are able to react with the aminic group of the used PEG.

3.3.3.12 EVALUATION OF THE PHOTOTHERMAL EFFECT

As described in detail in Chapter 1.6, one of the most charming properties of gold nanoparticles is the ability of plasmon oscillation to relax non-radiatively, and the conversion of this component into heat on the time scale of picoseconds. Thanks to this advantageous skill it is possible to cause localized hyperthermia in the immediate

proximity of nanostars, when they are properly irradiated with a LASER. As one of the aims of this work is to take advantage of this skill in order to burn specific cancer cells that overexpress folate receptors, one of the first step was the evaluation of the photothermal effect given by the final GNSs or sGNSs based SERS tags in colloidal suspensions. We used LASER's irradiation conditions similar to those that will be used for the evaluation of damages produced by irradiation of cells exposed to the prototypes of theranostic devices based on the SERS tags.

First of all, a sample of 100 μL of a native colloid of GNSs was irradiated with a LASER at 808 nm using a power of 100 mW for 10 minutes (LASER's spot = 1 mm^2 , 10.0 W/cm^2 of irradiance), the thermogram is presented in Figure 24a. The value of ΔT was 7.96 $^\circ\text{C}$. In the same experimental conditions, a sample of 100 μL of GNSs coated with 75% HS-PEG₃₀₀₀-NH₂ 25% MMC and conjugated with folic acid (the first of our final SERS tag), was irradiated. In this case the value of the ΔT was 5.82 $^\circ\text{C}$ (Figure 24b). The small difference between the two values can be ascribed to differences existing in the absorbance values at 808 nm of the two investigated samples of colloids: the second one has passed through several synthetic/centrifugation steps and during these steps colloid concentrations were only roughly normalized. Thus, concentrations are not the same, and absorbance too are different, and this cause the differences in temperature increase, as it of course depends from the quantity of radiation absorbed.

It is also important to underline that the registered hyperthermia giving these values reflects a "macroscopic" warming of all the volume of the liquid sample: anyway we hypnotize that hyperthermia in the immediate proximity of nanostars should be sensibly higher.

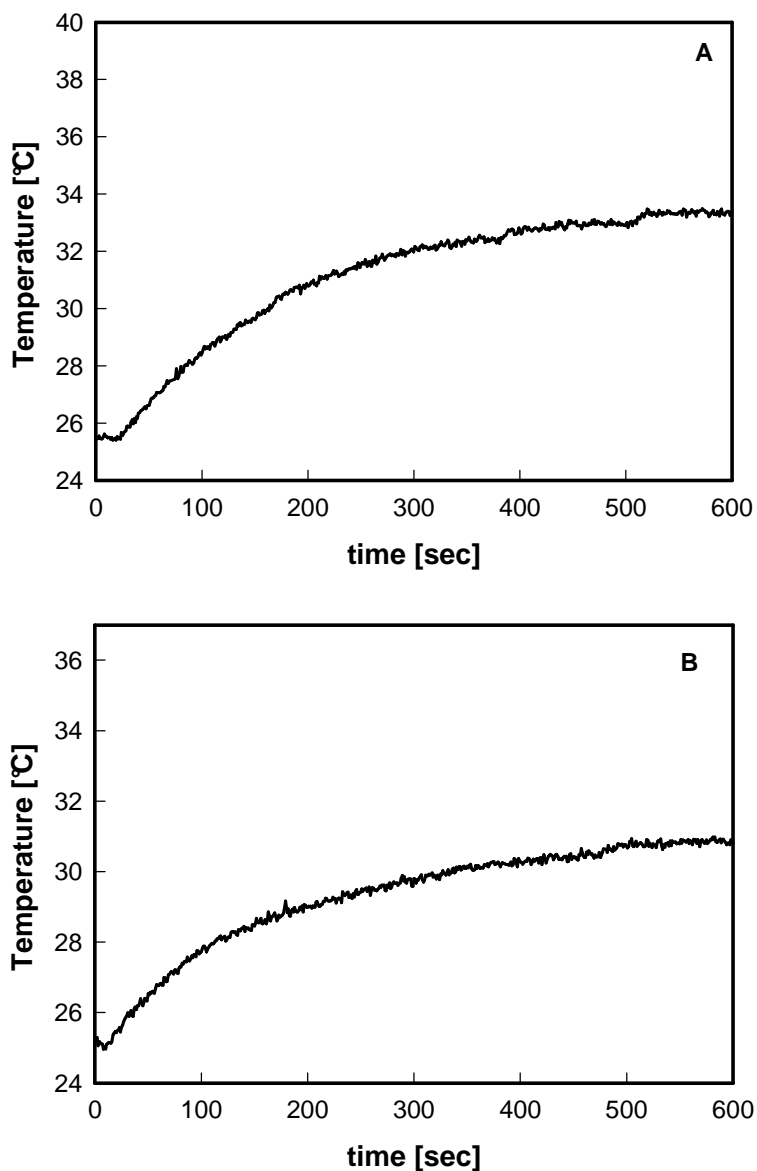


Figure 24: thermograms of: A) native GNSs irradiated at 100 mW for 10 min and B) GNSs coated with 75% HS-PEG₃₀₀₀-NH₂ 25% MMC irradiated at 100 mW for 10 min.

Then, the measurement was repeated on 100 μ L of GNSs coated with 75% HS-PEG₃₀₀₀-NH₂ 25% MMC and folic acid, after a 10 fold dilution, in order to simulate a situation in which after the incubation of cells with the SERS tag (*vide infra*), an imperfect washing has left a relatively huge amount of GNSs in the experiment environment. The sample was irradiated at 500 mW (50.0 W/cm² of irradiance) for 10 min, the same LASER's parameters that will be used during the experiment on HeLa cells that will be described later. In this case we found a ΔT of 5.15 °C.

It is important to stress the fact that even in the worst case (that will not be reached in our experiments) of an huge quantity of SERS tag unbound to cells but present in the

experiment environment, this “macroscopic” hyperthermia value reached by the whole sample will be not high enough to produce a generalized damage to investigated cells: in our design, only nano-devices bound to cell membranes are expected to cause a localized hyperthermia in the “nano” region, high enough to damage the targeted cells.

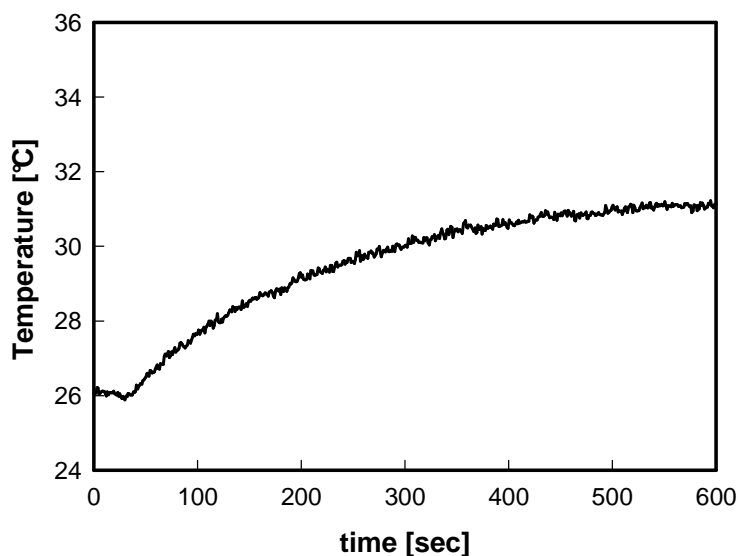


Figure 25: thermograms of diluted GNSs coated with 75% HS-PEG₃₀₀₀-NH₂ 25% MMC and folic acid irradiated at 500 mW for 10 min.

The evaluation of the photothermal response was conducted also on sGNSs, obtaining results almost identical to those described for GNSs.

3.3.3.13 CYTOTOXICITY OF SERS TAG

The MTT Cell Proliferation Assay measures the cell proliferation rate and conversely, when metabolic events lead to apoptosis or necrosis, the reduction in cell viability. Measurement of cell viability and proliferation forms the basis for numerous in vitro assays of a cell population’s response to external factors. The reduction of tetrazolium salts is now widely accepted as a reliable way to examine cell proliferation. The yellow tetrazolium MTT (3-(4, 5-dimethylthiazolyl-2)-2,5-diphenyltetrazolium bromide) is reduced by metabolically active cells, in part by the action of dehydrogenase enzymes, to generate reducing equivalents such as NADH and NADPH. The resulting intracellular purple formazan can be solubilized and quantified by spectrophotometric means (595 nm).

In order to evaluate the cytotoxicity of the final SERS tag (GNSs coated with 75% di HS-PEG-NH₂ 25% MMC and folic acid) towards HeLa cells, a MTT assay was designed. Before this, an ICP-OES analysis was realized on the SERS tag in order to evaluate the concentration of gold. The value found is 1.9×10^{-4} M (0,037 mg/mL), that corresponds to a GNSs concentration of 1.2×10^{-9} M (the estimate average mass is 5×10^{-17} g/GNS, see Chapter 1.3). Thanks to this information the MMT experiment was performed: the GNS SERS tags were suspended into the medium in order to obtain the concentrations of 5, 10, 25, 50, 100 µg/mL. The values of cells viability are reported in Table 8.

Table 8: values of HeLa cells viability for each concentration of GNS SERS tags.

	CTR	5.0 µg/mL	10 µg/mL	25 µg/mL	50 µg/mL	100 µg/mL
Cells viability [%]	100.0 ± 1.3	91.9 ± 2.0	96.5 ± 1.7	97.9 ± 1.6	98.1 ± 0.8	97.4 ± 1.4

For each concentration used the cells viability is decisively high, so the SERS tag is entirely biocompatible in the investigated range. This measure allowed also to choose the appropriate concentration of SERS tag for the incubation experiments: the maximum value of 100 µg/mL has been excluded because a precipitation phenomenon was observed in to the well during the MTT test, thus the value 50 µg/mL was chosen.

3.3.3.14 IMAGING OF HELA CELLS WITH GNSs SERS TAGS

The SERS tag described so far should be able to recognize and bind cancer cell that overexpress folate receptors. HeLa cells are a cell type in an immortal cell line used in scientific research that present this features, so they could be used in order to evaluate the ability of our final SERS tag to recognize and localize them (i.e. produce an imaging function), thanks to the relative SERS signal.

The GNSs SERS tags equipped with folic acid were prepared as indicate in Paragraph 3.3.2.3, and used for incubation of HeLa cells for 24 hours at 37°C. Then, the cells were washed three times with PBS and the petri filled with bi-distilled water. After this, the SERS response was evaluated along a line (15 points separate each other from 1.5 µm, the membrane placed in the position between 12 and 15 µm) that started outside the cell

and then continued inside the cell. The measure is summarized in the graph reported in Figure 27.

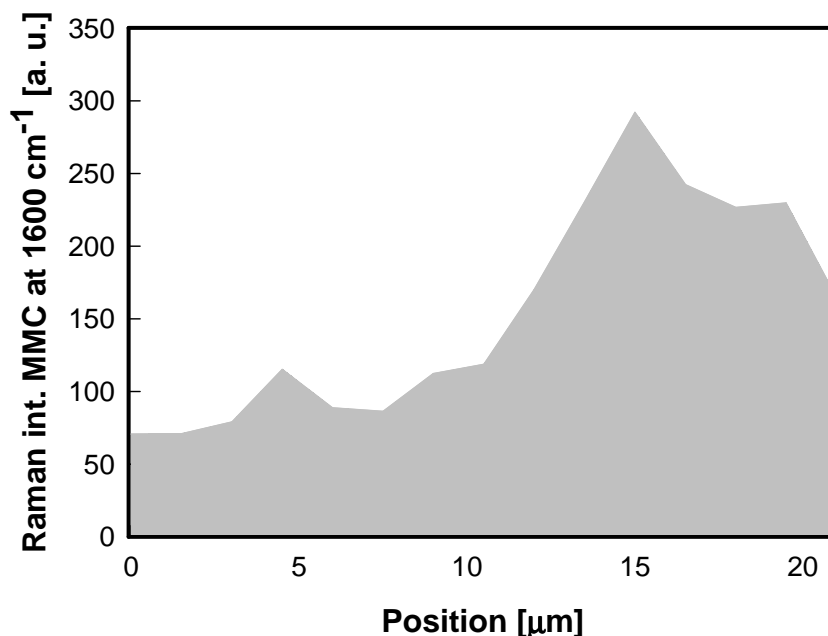


Figure 27: SERS response of GNS SERS tags evaluated along a line (15 points separate each other from 1.5 μm) after incubation of HeLa cells with the SERS tag.

As can be seen the MMC signal at 1600 cm^{-1} is very intense in the position between 12 and 15 μm , in correspondence to the membrane of the cell, while it was slightly smaller inside the cell (position $> 15\text{ }\mu\text{m}$). Outside the cell the signal is completely absent, as expected, and one can only observe almost flat spectra over the whole investigate range. The variation of the MMC signal evidenced in Figure 27 is a proof of the fact that the SERS tag is able to recognize and bind the overexpressed folate receptors of the HeLa cells, otherwise the SERS tag should have been washed away during the three washing cycles with PBS after incubation. The fact that the signal is found at a maximum value on the membrane zone depends on the sampling geometry of the Raman spectrometer, but indeed demonstrates that the SERS tag is bound on the membrane of the investigated cell.

In addition to this measure, a bi-dimensional mapping was recorded, taking several spectra along a rectangular area that include a portion of space taken inside and a portion taken outside of a HeLa cell (see Figure 28).

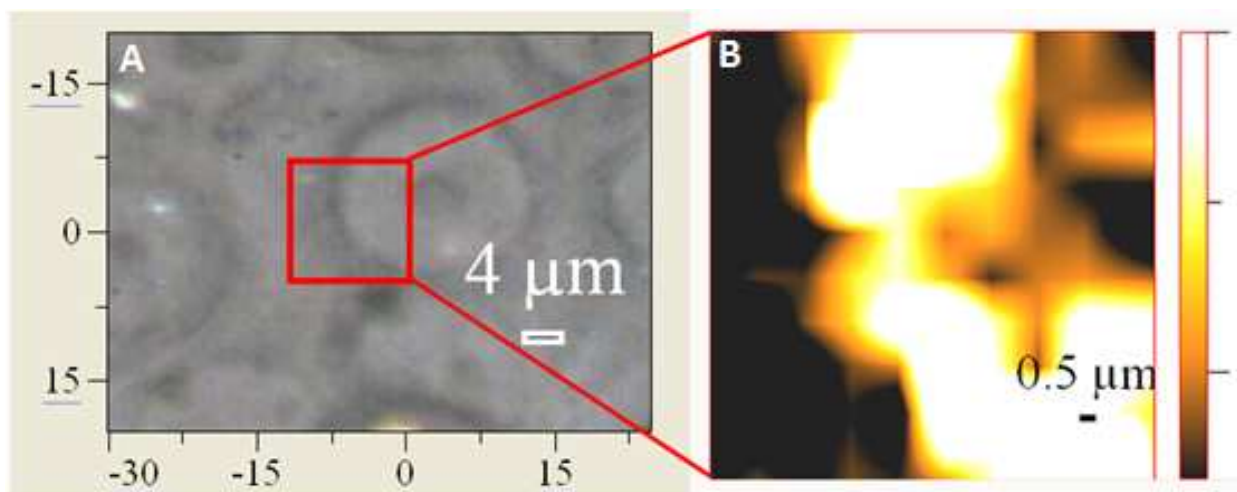


Figure 28: A) image of HeLa cells incubated with GNS SERS tags, characterized at micro-Raman spectroscopy: the red rectangular delimit the area which was mapped with the microRaman; B) image of the distribution of the integrated intensity of the MMC Raman signal at 1600 cm^{-1} , recorded in the red rectangular area.

As can be seen from Figure 28, when mapping the area included in the red rectangle, one can notice the absence of the signal outside the cell, while a clear signal (brightness is proportional to the intensity of the signal by the SERS tag) is found in the part corresponding to the cell, with a very high intensity on the cell margin corresponding to the membrane part of a HeLa cell.

3.3.3.15 IMAGING OF HELa CELLS WITH SHRUNKED GNSS SERS TAGS

The same experiment described in the previous Chapter, was realized using sGNS SERS tags. In this case, thanks to the reduced dimensions of the nano-objects, an internalization of the SERS tag was expected. Even in this case sGNS SERS tags equipped with folic acid were prepared as indicate in Paragraph 3.3.2.3, and incubated with HeLa cells for 24 hours at 37°C . Then, the cells were washed three times with PBS and the petri filled with bi-distilled water. The SERS response was evaluated in the same way explained in the precedent chapter, and the response is shown in the Figure 29.

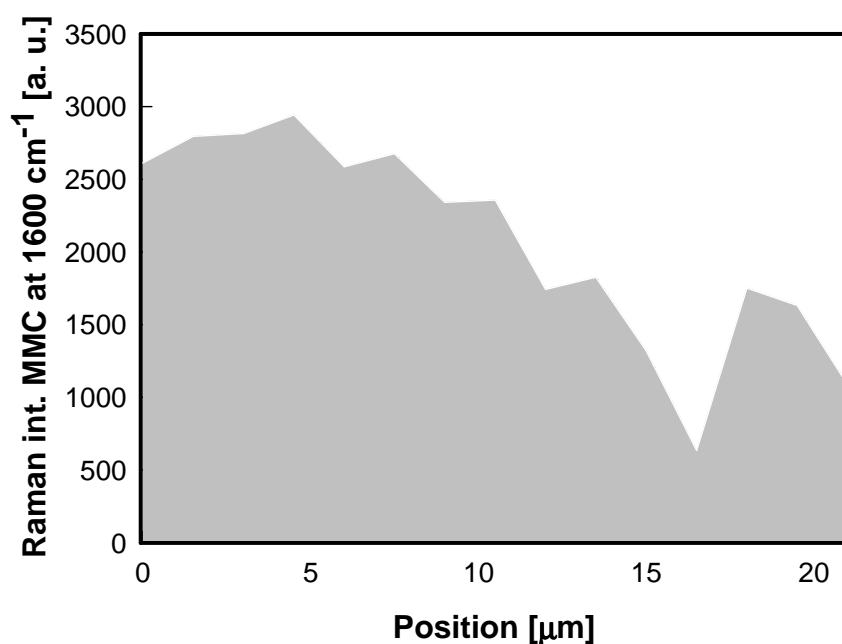


Figure 29: SERS response of sGNS SERS tags evaluated along a line (15 points separate each other from 1.5 μm) after incubation of HeLa cells with the SERS tag.

As can be seen, the MMC signal at 1600 cm^{-1} is quite intense in any analyzed position, and seems to decrease inside the cell. This unexpected behavior is probably caused by the uniform adhesion of the colloid all over the experiment environment, including the glass support, which could not be removed even after three washings with PBS. The result is therefore not very encouraging: additional investigation is required to understand the reasons which have caused it. For this reason, the following experiments were performed using only GNSs based SERS tags and devices.

3.3.3.16 IMAGING HELa CELLS IN ABSENCE OF FOLIC ACID

In order to obtain another proof of the selectivity of the GNS SERS tags, the same experiment described in Paragraph 3.3.3.14 was repeated in the same conditions, but in absence of the folic acid targeting group. For this task we used GNSs coated with a mixed monolayer of 75% HS-PEG-COOH and 25% MMC. We choose this kind of coating because it equips the nanostars with a carboxylic group, thus giving the nano-device similar surface chemicals properties, mainly from the point of view of Z potential.

Thus, this kind of GNSs should not be able to recognize and bind specific cancer cells overexpressing folate receptors. Once again HeLa cells were incubated with the SERS tags for 24 hours at 37°C. Then, the cells were washed three times with PBS and the petri filled with bi-distilled water. After this, the SERS response was evaluated along a line (15 points separate each other from 1.5 μm , the membrane placed in the position between 12 and 15 μm) that started outside the cell and then continued inside the cell; the response is show in the Figure 30.

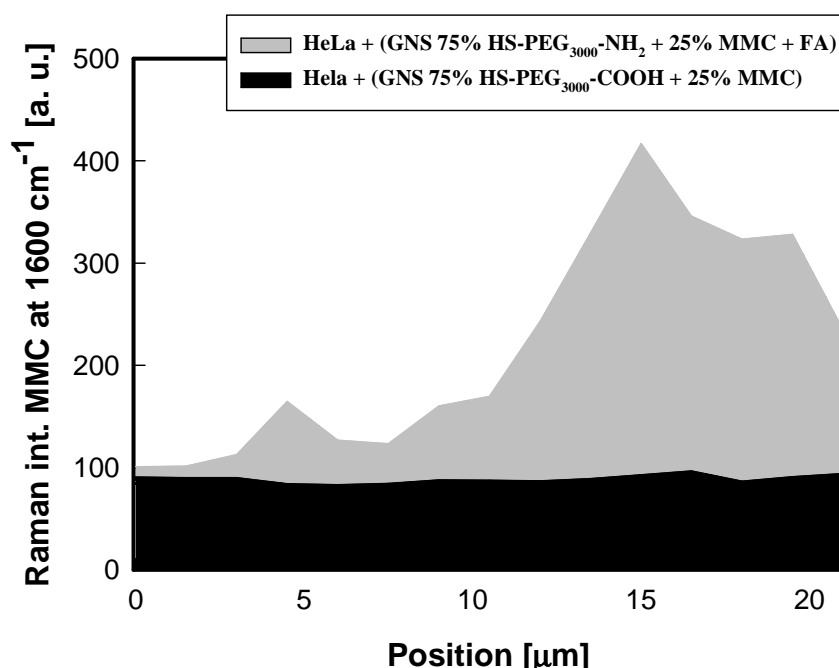


Figure 30: comparison between: SERS response of GNS SERS tags evaluated along a line (15 points separate each other from 1.5 μm) (grey area) and SERS response of GNSs coated with 75% HS-PEG-COOH and 25% MMC (15 points separate each other from 1.5 μm) (black area) after incubation of HeLa cells with the SERS tags.

In the graph, the measure obtained in presence of folic acid functionalization is reported from Figure 30 (grey area) and compared with the measure obtained with the SERS tag “finished” with the simple carboxylate coating: in this second case no signal of MMC is found, indicating that all the SERS tag was removed by PBS washing, and no binding to HeLa cells was taking place in absence of the targeting group.

3.3.3.17 IMAGING OF DI TCN1 CELLS WITH GNS SERS TAGS

In order to obtain another proof of the role of folic acid as targeting group and of the selectivity of our SERS tags, the same experiment described in Paragraph 3.3.3.14 was repeated in the same conditions using the same GNS SERS tags with a different cells line: DI TCN1 cells. This kind of cells are astrocytes with fibroblast shape that do not overexpress folate receptors. Even in this case, the SERS tags were incubated with HeLa cells for 24 hours at 37°C. The SERS response was evaluated analyzing 3 points (outside, inside the cell and on the membrane), and the result is shown in Figure 31.

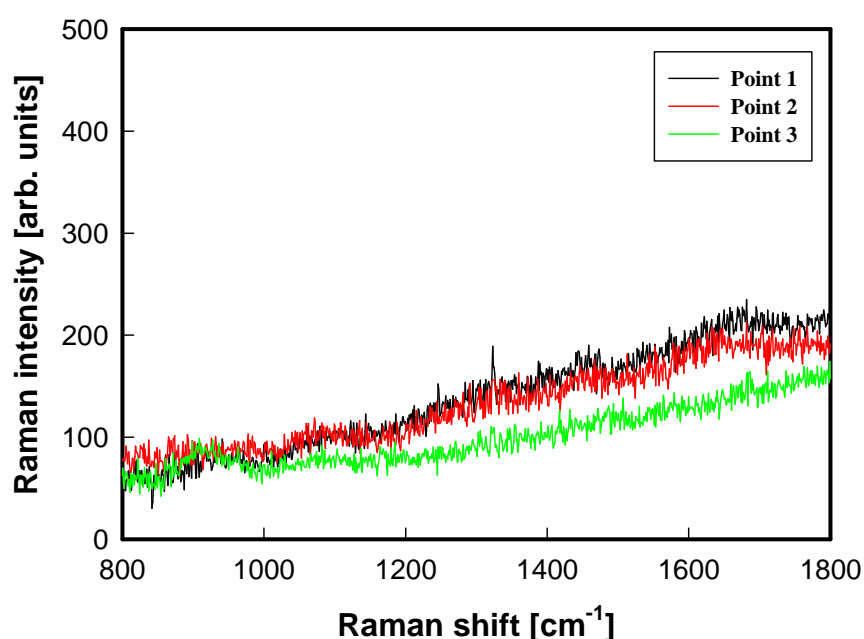


Figure 31: SERS response of GNS SERS tags evaluated in three different points (inside, outside and on the membrane of a DI TCN1 cell).

As expected, no SERS signal from MMC can be found in any of the regions investigated: the SERS tags were washed away during the three washing with PBS, as this kind of cells lack folate receptor and no binding of SERS tags is possible.

In Figure 32 the results of the imaging experiments are summarized by showing the spectra obtained with a Raman spectra performed exactly on the membrane zone in the three described imaging experiments performed with GNSs based devices.

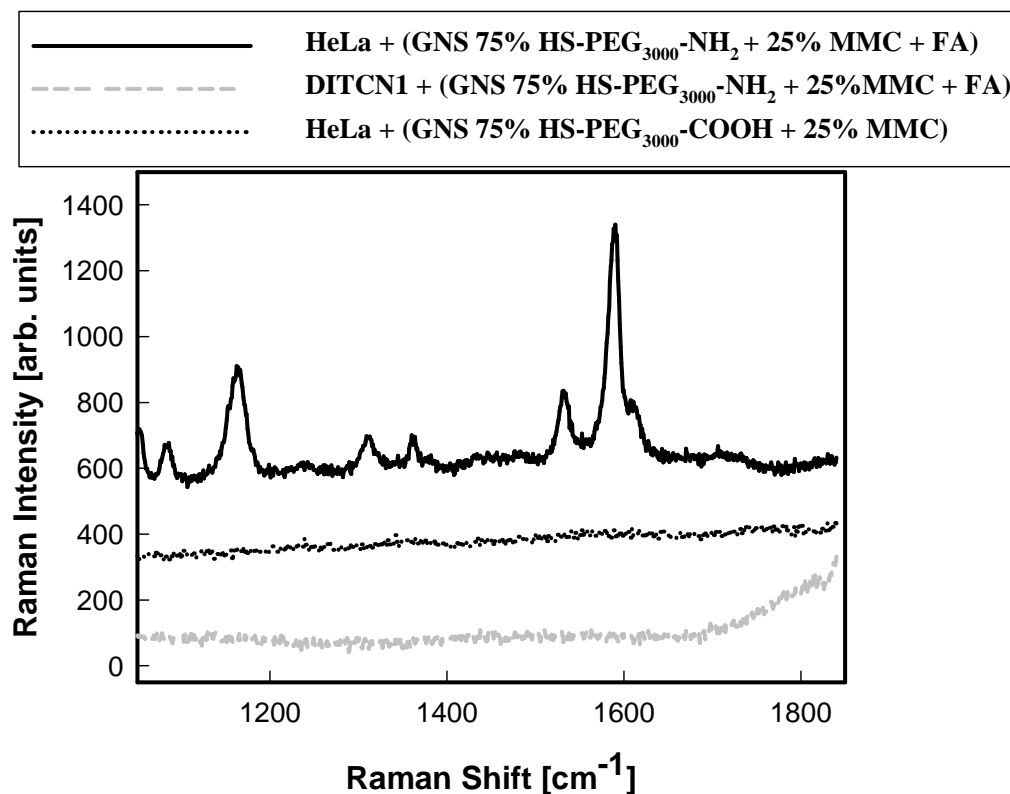


Figure 32: comparison between: SERS response found on the membrane of the cells in the three imaging experiments. (black line) HeLa incubated with GNS SERS tags; (black dotted line) DI TCN1 incubated with GNS SERS tags; (grey dotted line) HeLa incubated with GNSs SERS tags without pending folic acid.

As can be seen in Figure 32, the typical fingerprint of MMC of the SERS tags was detected only on the membrane of the HeLa cancer cells, while this signal is absent in the spectra obtained in the other two experiments. In these last two cases, no presence of SERS tags on cells membrane is observed as no binding between folate and proper receptors can take place: in one case (COOH finished SERS tags) we lack the folate moiety, in the other (DI TCN1 cells) we lack the folate receptors. The folic acid conjugated SERS tags can thus be considered selective for cancer cells overexpressing folate receptors.

3.3.3.18 EVALUATION OF THE PHOTO-THERMAL EFFECT ON HELA CELLS

The term "theranostics" represent a combination of therapy and diagnostics in the same device, addressed, for example, to treat and image efficiently cancer cells with a single tool. As the imaging features of the SERS tag were demonstrated with the experiments described in the previous paragraph, at this stage we decided to investigate the ability of GNS SERS tags to damage the HeLa cancer cells, which can be easily recognized and bound by the tags themselves, by means of hyperthermia induced by the GNSs typical photo-thermal effect.

The experiment was designed as described in Paragraph 3.3.2.3. Briefly, HeLa cells were incubated for 24 hours at 37°C with the SERS tags, washed three times with PSB in order to remove all unbound SERS tags, and then irradiated with a LASER source having a wavelength of 808 nm, using a power of 200 mW and a spot of 1.0 mm², thus giving an irradiance of 50 W/cm². As controls, the following samples were considered: i) HeLa cells incubated for 24 hours at 37°C without GNS SERS tags, before irradiation; ii) HeLa cells incubated for 24 hours at 37°C without GNS SERS tags, after irradiation with a LASER at 808 nm wavelength ; iii) HeLa cells incubated for 24 hours at 37°C with GNS SERS before irradiation. All these control samples allow to verify the damage eventually caused by the LASER irradiation, alone or by the incubation with SERS tags, even if this last eventuality is ruled out by MTT test results. All samples (with or without SERS tags, before and after irradiation) were observed with the optical microscope.

In the Figure 33 is reported the photography of the first control sample: the HeLa cells incubated for 24 hours at 37°C without GNS SERS tags before the irradiation with a LASER at a wavelength of 808 nm. As can be clearly observed, there is an uniform distribution of the HeLa cells: it is important to underline that the morphology of the cells reflect the health of the population, in fact, when there is a cellular suffering the shape went from an ellipsoidal to a more roundish shape. The image suggests that the cells were growth in optimal conditions.

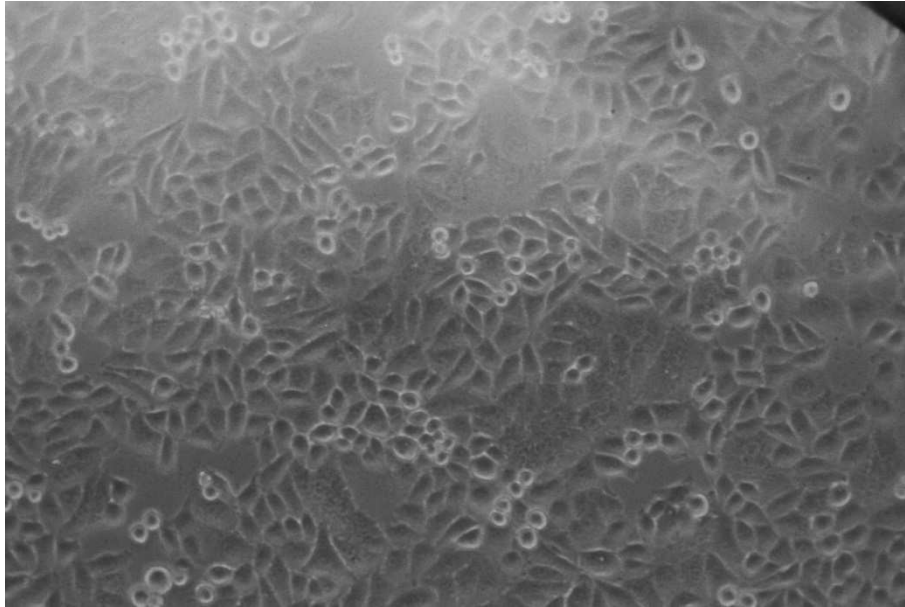


Figure 33: photography of HeLa cells incubated for 24 hours at 37°C without GNS SERS tags.

The same control sample was irradiated in three close points of 1 mm² area with a 808 nm LASER at 500 mW of power (50 W/cm² of irradiance) for 10 minutes each one. After the irradiation the sample was observed through a optical microscope (see Figure 34). As can be seen, the simple treatment with the LASER, even at very high irradiance, in absence of SERS tag, does not provoke any suffering (which should result in a change of shape) of the HeLa cells.

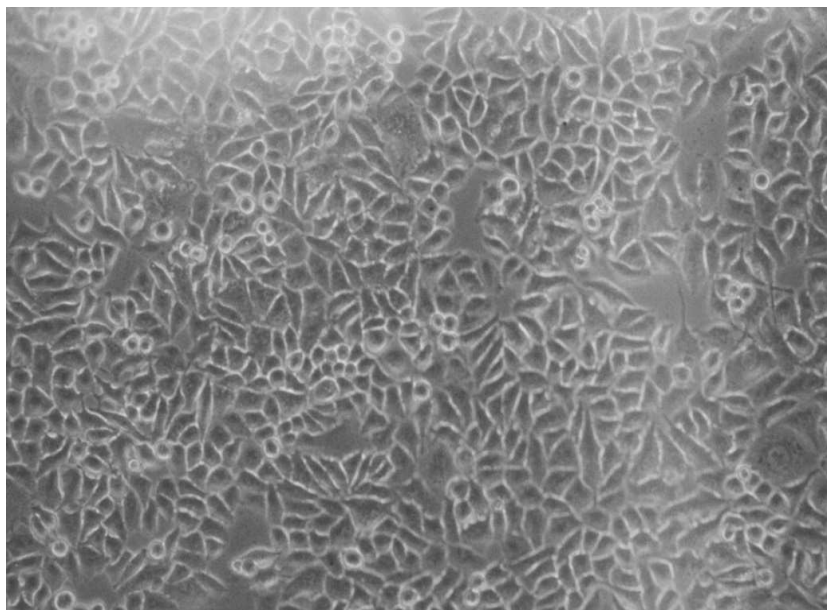


Figure 34: photography of HeLa cells incubated for 24 hours at 37°C without GNS SERS tags, after irradiation with 808 nm LASER, irradiance of 50 W/cm²

Finally, a sample of HeLa cells incubated for 24 hours at 37°C with GNS SERS tags was irradiated in the same conditions (after three washing with PBS in order to eliminate the un-bounded SERS tags). After that, the sample was once again photographed through an optical microscope. As can be seen from the Figure 35, there is a radical change of the morphology of the HeLa cells from ellipsoid to a roundish shape, demonstrating that the cancer cells were seriously damaged by the photo-thermal effects exerted by the SERS tags, which were bound at their membranes as demonstrated by the SERS imaging experiments.

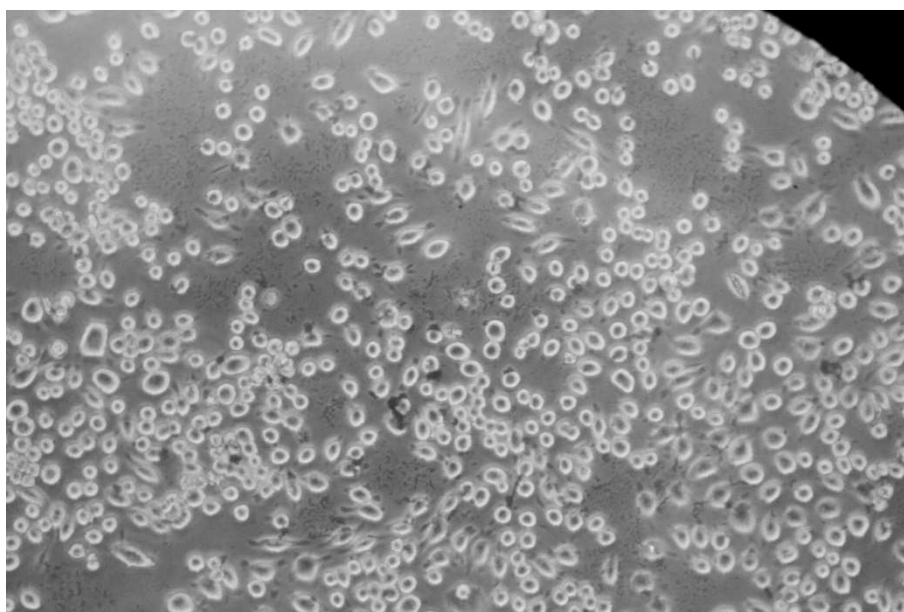


Figure 35: photography of HeLa cells incubated for 24 hours at 37°C with GNS SERS tags and after irradiation with 808 nm LASER, irradiance of 50 W/cm².

This experiment prove that the GNS SERS tags are able to recognize and selectively bind HeLa cancer cells and thanks to this proximity is possible to destroy them through irradiation with an appropriate LASER, this event in fact provoke a localized heating called “photo-thermal effect” which is typical of gold anisotropic nano-objects.

3.3.3.20 CONCLUSION

We coated GNSs with a mixture of two thiols, sharply controlling the surface composition, using a method that allowed us to place on the GNS surface a precise amount of 7-Mercapto-4-methylcoumarin (MMC), the Raman reporter, mixed in precise molar ratios with HS-PEG₃₀₀₀-NH₂, to impart biocompatibility. This controlled coating,

which takes place in one step, gave the GNSs maximum stability and biocompatibility, ensuring a good SERS response, and in principle can be exploited to modulate the intensity of the signal. Subsequently, a target molecule able to exclusively recognize a predetermined target, avoiding or drastically reducing the possibility of forming non-specific bonds, was successfully bound on the surface of mixed monolayer: we have chosen folic acid, since typically many types of tumor cells over express receptors for folic acid and folate. Due to the presence of two carboxylic functions, which can be coupled with aminic termination of HS-PEG₃₀₀₀-NH₂, it was possible to found a reliable and reproducible procedure for the synthesis of the SERS tag, and step by step characterization with several techniques was performed. After demonstrating the efficient recognition and binding of the SERS tags to HeLa cells by means of SERS spectroscopy, we investigated the effect of a LASER treatment when SERS tags are bound to HeLa cells. Preliminary results show that upon laser irradiation in the nIR, our GNS based device produce an intense localized hyperthermia which causes a serious damage to investigate HeLa cells.

In conclusion, by combining the properties of SERS detection and imaging to the possibility of generating a localized heating in order to damage the cells to which SERS tag is tied, the described system may be considered a prototype of theranostic (diagnostic and therapeutic) device, based on the typical features of our GNSs.

CHAPTER 4: CONCLUSIONS

Conclusions relating to each one of the parts of the work reported in this thesis can be found at the end of each chapter which described the single investigation (see paragraphs 2.1.3.4, 2.2.3.5, 3.1.3.3, 3.2.3.8 and 3.3.3.20).

Some words, anyway, could be spent to recapitulate the path that was successfully followed during the three years of Ph.D. research.

Gold has been the object of long-standing fascination since antiquity, for its supposed (at the time) medicinal properties and for its ornamental value. In the past two decades or so, numerous advances in the chemical synthesis of gold nanoparticles with anisotropic shapes have opened up an enormous number possibilities in sensing, bio-imaging, antibacterial and theranostic devices, SERS chips, just to name a few, in a plethora of possible different applications. In these three years I tried to hold some of these different fields simultaneously, taking advantage of what in my opinion is one of the most fascinating class of nano-objects: gold nanostars. The different parts described can be summarized in three vast categories: i) glass substrates provided with antibacterial or SERS skills, ii) colloids equipped with appropriate functionalization for sensing application of heavy metals, iii) SERS tags developed for bio-sensing, imaging and therapy.

I believe this work demonstrated once again that Richard Feynman was absolutely right when stating *“there is plenty of room at the bottom”*. In the same time, having so largely talked about these brand new shining gold (nano) stars, it was demonstrated that there is also plenty of space in the landscape of a new (nano) golden future: *“going for gold”* in nanotechnology, nanochemistry and nanomedicine has never been so exciting.

Acknowledgment

I must be thankful to all the people who collaborated at this strongly interdisciplinary work:

University of Pavia - Drug Science Department: *A. Pascale, P. Grisoli and N. Marchesi.*

University of Pavia - Physics Department: *P. Galinetto and M. Patrini.*

University of Milano-Bicocca - Physics Department: *G. Chirico, L. D'Alfonso and L. Sironi.*

University of Florence - Department of Chemistry "Ugo Schiff" and CSGI: *E. Fratini.*

University of Liverpool - School of Biomedical Sciences (Biomedical EM Unit): *A.J. Beckett, I.A. Prior.*

University of Liverpool - Open Innovation Hub for Antimicrobial Surfaces: *M. Moritz, I. Sorzabal-Bellido, A. Susarrey-Arce, E. Latter, R. Raval and Y.A. Diaz-Fernandez.*